$\pi^+\pi^-$ electroproduction off protons in deuterium: measurements of quasi-free cross sections and kinematic probing of final state interactions

by

Iuliia Skorodumina

Specialist Degree
Lomonosov Moscow State University, 2012

Submitted in Partial Fulfillment of the Requirements

for the Degree of Doctor of Philosophy in

Physics

College of Arts and Sciences

University of South Carolina

2021

Accepted by:

Ralf Gothe, Major Professor

Fred Myhrer, Committee Member

Steffen Strauch, Committee Member

Viktor Mokeev, Committee Member

Tracey L. Weldon, Interim Vice Provost and Dean of the Graduate School

Acknowledgement

First, I would like to thank my advisor, Ralf Gothe, for his guidance and support during my PhD program, and for encouraging me to pursue my ideas.

I am very grateful to Gleb Fedotov for his assistance to this work and for his great help along the way.

I would like to thank my dissertation committee, Fred Myhrer, Steffen Strauch, and Viktor Mokeev, for taking the time to review this work.

I am also thankful to my colleagues, Evan Phelps, Ye Tian, Arjun Trivedi, Gary Hollis, Nick Tyler, Chris McLauchlin, and Krishna Neupane.

Finally, I thank the University of South Carolina, the CLAS Collaboration, and the National Science Foundation, without which this work would not have been possible.

Abstract

In this study, the process of $\pi^+\pi^-$ electroproduction off protons bound in deuterium nuclei is explored. The exploration is performed through the analysis of experimental data on electron scattering off the deuteron target, collected in Hall B at Jefferson Lab with the CLAS detector. As a main result, the set of integrated and single-differential cross sections of the reaction $\gamma_v p(n) \to p'(n')\pi^+\pi^-$ is obtained. The cross sections are extracted in the quasi-free regime, which implies that only events not affected by final state interactions are subject to selection. The measurements are performed in the kinematic region of the invariant mass W from 1.3 GeV to 1.825 GeV and photon virtuality Q^2 from 0.4 GeV^2 to 1 GeV^2. Sufficient experimental statistics allows narrow binning, i.e. 25 MeV in W and 0.05 GeV^2 in Q^2, while maintaining an adequate statistical uncertainty. The extraction of quasi-free cross sections is accompanied by the kinematic probing of FSI between the reaction final hadrons and the spectator neutron in the aforementioned exclusive channel. In this probing the distributions of missing quantities are used in order to investigate the relative spread of events with FSI along the reaction phase space, trace the difference of FSI manifestations in different reaction topologies, reveal details on alterations of the hadron momentum in FSI, and isolate FSI contributions of various final hadrons. The performed examination is also capable of retrieving information on some underlying FSI mechanisms, among which the process of resonance formation in the intermediate state of pion-neutron interactions is particularly remarkable.

Table of contents

List of tables

List of figures

Chapter 1

Introduction

Exclusive reactions of meson photo- and electroproduction off protons are intensively studied in laboratories all over the world as a very powerful tool for the investigation of nucleon structure and the principles of strong interaction. These studies include the extraction of various observables through the analysis of experimental data as well as subsequent theoretical and phenomenological interpretations of the extracted observables [1–3].

By now exclusive reactions off the free proton have been studied in considerable detail, and a lot of information on differential cross sections and different single and double-polarization asymmetries with almost complete coverage of the reaction phase-space is available. A large part of this information came from the analysis of data collected in Hall B at Jefferson Lab with the CLAS detector [4, 5].

Meanwhile, reactions occurring in photon and electron scattering off nuclei are less extensively investigated, i.e. experimental information on these processes is scarce and mostly limited to inclusive measurements of total nuclear photoproduction cross sections [6–8] and nucleon structure function F_2 [9–11].

The available inclusive data, however, exhibit some surprising peculiar features not fully elucidated over the years, which are now attracting significant scientific attention. Specifically, the nuclear photoproduction cross section (per nucleon) turns out to be less pronounced and damped in strength compared with the cross section off the free proton. This effect manifests itself differently depending on the invariant mass

(W) range, i.e. the $\Delta(1232)$-resonance peak is damped, but still evident for all nuclei, however, the second resonance region becomes somewhat less pronounced and damped for the deuteron and strongly suppressed and structureless for all heavier nuclei.

A similar effect is observed in the behavior of the nucleon structure function F_2, which in the case of the deuteron shows moderate damping and flattening [10] and completely loses its structure, when measured off carbon [11] (compared with the free proton structure function [12]). A fact of particular interest is that the intensity of this effect increases as Q^2 grows, i.e. as $Q^2 = 3$ GeV^2 is reached, the structure function F_2 becomes almost flat even for the deuteron [11]. These peculiar features cannot just be explained by the Fermi motion of nucleons in the nucleus and are thought to be an indication that nucleons and their exited states, bound inside the nuclear medium, may be subject to some modifications of their properties [6–8, 13, 14].

This phenomenon, which is still not fully understood, generates lots of debates among scientists, triggering efforts to describe the processes that happen in reactions off bound nucleons. These studies rely heavily on experimental data, which at the moment are mostly limited to inclusive measurements [6–11] and lack information on exclusive reactions. This information, however, is crucial, since various exclusive channels have different energy dependencies and different sensitivity to reaction mechanisms. This situation causes a strong demand for exclusive measurements off bound nucleons, and the deuteron, being the lightest and weakly-bound nucleus, is the best target for initiating these efforts.

This study represents a thorough exploration of the process of charged double-pion electroproduction off protons bound in deuterium nuclei. The exploration has been performed through the analysis of experimental data on electron scattering off the deuteron target, collected with the CLAS detector [4]. The description of the detector and target setup is given in Chapter 2 together with information on the data format and the overall analysis structure.

The experimental measurements have been performed in the second resonance region, where the double-pion production plays an important role, i.e. the channel opens at the double-pion production threshold at $W \approx 1.22$ GeV, contributes significantly to the total inclusive cross section for $W \lesssim 1.6$ GeV, and starts to dominate all other exclusive channels for $W \gtrsim 1.6$ GeV.

In general, experimental identification of exclusive multi-particle final states is a rather sophisticated task, which requires certain analysis techniques to be elaborated and established. This was carried out over the last twenty years as different studies of double-pion production off the free proton were being performed [15–23], and currently a solid framework for such studies is in place. For this particular study, focused on the $N\pi\pi$ final state, this framework laid the foundation. However, the deuteron as a target introduces some specific issues, which are external to the free proton data analysis and originate from (a) Fermi motion of the initial proton and (b) complex effects of the final state interactions due to the presence of a spectator nucleon. This caused some difficulties that were encountered and needed to be overcome during the analysis and, therefore, in this study special attention is paid to detailed description of these issues.

As this study represents the first attempt of detailed investigation of the double-pion exclusive reaction occurring off nucleons in nuclei, its objectives are multifaceted.

The main goal of this study is to obtain the set of integrated and single-differential cross sections of the reaction $\gamma_v p(n) \rightarrow p'(n')\pi^+\pi^-$. The cross section measurements are performed in the kinematic region of the invariant mass W from 1.3 GeV to 1.825 GeV and photon virtuality Q^2 from 0.4 GeV^2 to 1 GeV^2. Sufficient experimental statistics allows narrow binning, i.e. 25 MeV in W and 0.05 GeV^2 in Q^2, while maintaining an adequate statistical uncertainty. The cross sections are extracted in the quasi-free regime, which implies that only events not affected by final state interactions were selected.

The whole enterprise of the cross section extraction is presented in Chapters 3 through 7, which encompass the selection of quasi-free events, the cross section calculation framework, the description of the corrections applied to the cross sections, as well as the procedures of normalization verification and uncertainty estimation.

To exploit opportunities offered by this experiment in their full capacity, the main analysis is accompanied by the complementary examination of FSI effects in the investigated exclusive channel, which is presented in Chapter 9. The main focus of this examination is set on events affected by FSI, which were lacking attention throughout the main analysis being attributed to the background. These events, meanwhile represent a fruitful ground for probing FSI and revealing their features and manifestations.

Another objective of this study stems from the Fermi motion that initial protons undergo in deuterium nuclei. The fact that the initial proton is not at rest introduces several unaccustomed peculiarities into the analysis, which were not relevant for free proton studies, such as Fermi smearing of some kinematic quantities (e.g. W and missing masses), blurring of the boundaries of the W versus Q^2 distribution, alterations in the common procedure of the Lab to CMS transformation, etc. To deal with these issues, special methods and techniques have been developed during this study, which enrich the conventional analysis framework elaborated in numerous free proton studies [15–23].

As a matter of fact, effects of the initial proton motion turned out to be tightly interwoven with many analysis aspects. For this reason, it was found hard to address them in an isolated Chapter without introducing much repetition. Therefore, the description of the analysis peculiarities that originate from the Fermi motion is scattered throughout the thesis. Some of them are also addressed in a separate study [24], which accompanies this analysis.

It is also worth mentioning that this study benefits from a very fortunate circumstance; namely from the fact that the corresponding cross sections of the

same exclusive reaction off the free proton have been recently extracted from CLAS data [22, 23]. These free proton measurements were performed under the same experimental conditions as in this study, including the beam energy value and the target setup. For the majority of $(W,\,Q^2)$ points, the statistical uncertainty combined with the model dependent uncertainty ($\delta_{\text{stat, mod}}^{\text{tot}}$) is on a level of $\sim$1%-3% for the free proton integral cross sections and on a level of $\sim$4%-6% for the quasi-free integral cross sections obtained in this study. Being performed in the same experimental configuration, both measurements have identical binning in all kinematic variables and similar inherent systematic inaccuracies.

The free proton study [22, 23], therefore, naturally sets the standard for this particular study, being used as a reference point for many analysis components. This unique advantage allows not only the reliability verification of those analysis aspects that are similar for experiments of free and bound protons, but also for a deeper understanding of those that differ. The latter include the effects of initial proton motion and final state interactions.

Additionally, a direct comparison of the cross sections extracted in this study with their free proton analogues from Ref. [22, 23] may represent a promising further step in the investigation of the double-pion exclusive channel. Such comparison can provide experimentally the best possible opportunity to explore distinctions between the $\pi^+\pi^-$ electroproduction off protons in deuterium and the corresponding reaction off free protons. In this way, a condition-independent estimation of contribution from events with FSI to the total number of reaction events can be accomplished along the entire reaction phase-space. Based on this, other potential reasons that may contribute to the difference between the cross section sets can be explored, which includes possible in-medium modifications.

Chapter 2

Experiment

The experiment of the electron scattering off deuterium nuclei, that provides data for this study, was conducted at JLab Hall B as a part of the "e1e" run period. A longitudinally polarized electron beam of 2.039 GeV energy was produced by the Continuous Electron Beam Accelerator Facility (CEBAF) and then scattered off the 2-cm-long liquid deuterium target, which was located in the center of the CEBAF Large Acceptance Spectrometer (CLAS) [4]. This state of the art detector covered a good fraction of the full solid angle and provided efficient registration of the final-state particles originating from the scattering process.

2.1   Detector setup

The CLAS design is based on a toroidal magnetic field, which is generated by six superconducting coils arranged around the beamline. The magnetic field bends charged particles toward or away from the beam axis (depending on the particle charge and the direction of the torus current) but leaves the azimuthal angle essentially unchanged. The magnet coils naturally separate the detector into six areas, the so-called "sectors", each functioning as an independent magnetic spectrometer. Each sector includes four sub-detectors: Drift Chambers (DC), Čerenkov Counters (CC), Time-of-Flight System (TOF), and Electromagnetic Calorimeters (EC) [4]. A view of the detection system in the direction of the beam (cut through the target region) is given in Fig. 2.1.
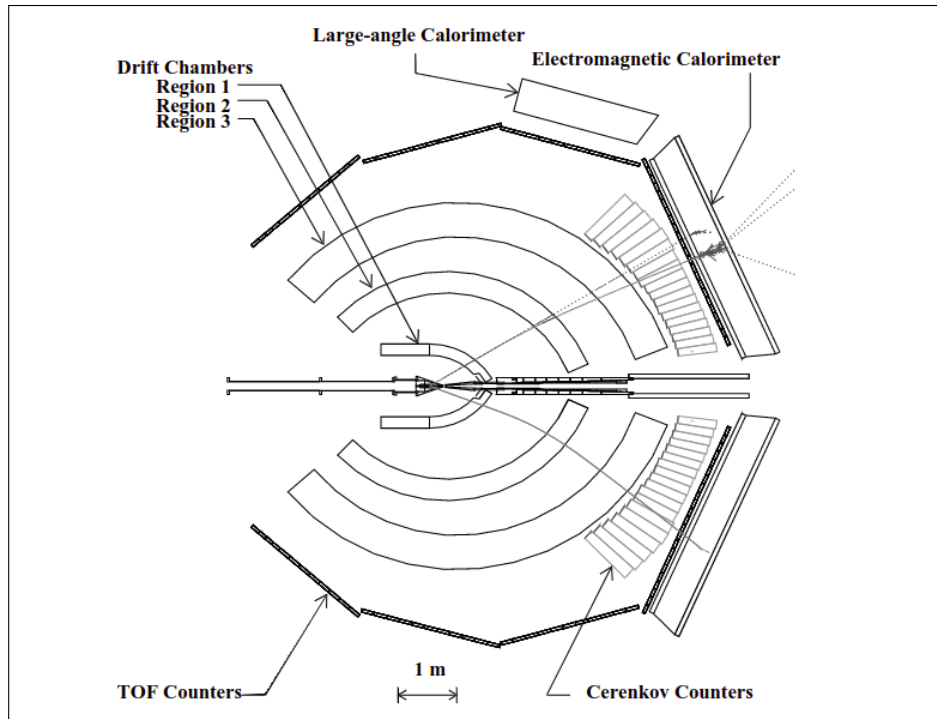
Figure 2.1: A schematic top view of the CLAS detector cut along the beam line. Typical photon, electron, and proton tracks (from top to bottom) from an interaction in the target are superimposed on the figure. The figure is taken from Ref. [4]
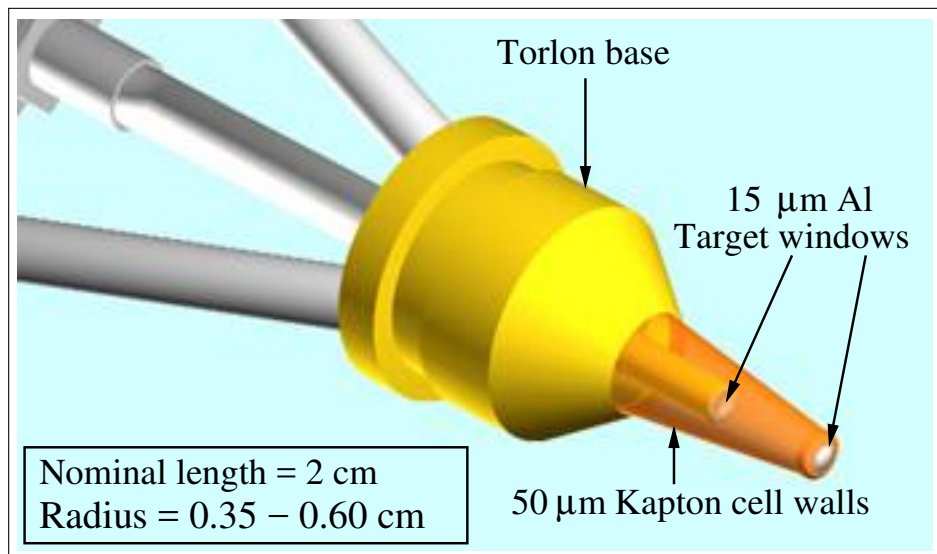
Figure 2.2: The target cell and its support structure used during the "e1e" run period [25]. The figure is taken from Ref. [23].

The azimuthal coverage for CLAS is limited only by the magnet coils and approximately 90% at large angles and 50% at forward angles [26]. The coverage in the polar angle is from 8° to 45° for the Čerenkov Counters and Electromagnetic Calorimeter and from 8° to 142° for the Drift Chambers and the Time-of-Flight system.

The Drift Chambers are located within the region of the magnetic field, which bends the trajectories of the charged particles traveling through. The Drift Chambers perform the particle tracking, allowing the determination of the particle momentum from the curvature of its trajectory. Other sub-detectors are located outside the magnetic field region, which means that having left the DC, the charged particles move further along a straight line.

The Čerenkov Counters are located right behind the DC and serve the dual function of triggering on electrons and separating electrons from pions [27].

The TOF scintillators are located radially outside the Drift Chambers and the Čerenkov Counters but in front of the Calorimeters [28, 29]. Their alignment and relative positioning with respect to other detector sub-systems is shown in Fig. 2.1. The Time-of-Flight system measures the time when a particle hits a TOF scintillator, thus allowing for the determination of its velocity. With the help of the particle momentum known from the DC, its mass can then be determined, which means that the particle can be identified.

The main functions of the Electromagnetic Calorimeter are triggering on and detection of electrons at energies above 0.5 GeV, detection of photons at energies above 0.2 GeV (allowing for the π^0 and η reconstructions from their 2γ decays), and detection of neutrons [26].

The six CLAS sectors are equipped with a common data-acquisition (DAQ) system that collects the digitized data and stores the information for later off-line analysis.

2.2 Target setup

The target design was specific for the "e1e" run period [25]. The setup of the target cell with its support structure is presented in Fig. 2.2. For this particular part of the "e1e" run period, the target cell was filled with liquid deuterium.

The conical shape of the target (with the diameter varying from 0.35 to 0.6 cm) serves the purpose of effective extraction of gas bubbles, which are formed in the liquid target content due to the heat that either originates from the beam and/or comes from outside through the target walls. Due to the conical shape, the bubbles are drained upwards and into a wider area of the target thus clearing the beam interaction region and allowing the boiled deuterium to be effectively delivered back to the cooling system to be condensed.

The interaction region of the target was 2-cm-long. The target cell had 15-μm-thick aluminum entrance and exit windows. In addition, an aluminum foil was located 2.0 cm downstream of the target. This foil was made exactly to the same specifications as the entry/exit windows of the target cell and served for both the estimation of the number of events that originated in the target windows and the precise determination of the target z-position along the beamline. See also Sect. 3.4.3 for more details.

2.3 Experimental data

The measurements are attributed to the "e1e" run period that lasted from November 2002 until January 2003. This run period included several experiments with different beam energies (1 GeV and 2.039 GeV) and different target cell contents (liquid hydrogen and liquid deuterium). This study is devoted to the experiment conducted with the 2-cm-long liquid deuterium target and a 2.039 GeV polarized electron beam.

All data collected with the CLAS detector is stored in a specific format, which is the BOS format [30, 31]. The information on the detector response to particles passing through is recorded for each event and sorted into a set of BOS banks. The original BOS files store the data in terms of "raw" signals (like TDC, ADC). These "raw" files are then "cooked" with the reconstruction software (recsis), which converts the detector response to the variables that characterize the events directly, i.e. the particle momentum, the track coordinates, timing, etc. This information is also stored in BOS banks. However, since the cooking process introduces new variables, the structure of the "cooked" BOS files is different from that for the "raw" files. The "cooked" data is stored in various formats including BOS files and ROOT ntuples. In this analysis the latter were used.

2.4   Data analysis using the CLAS software

Events corresponding to the investigated reaction $ep(n) \rightarrow e'p'(n')\pi^+\pi^-$ are distinguished among all other registered events through the event selection procedure, described in detail in Chapter 3. The selected exclusive events, however, represent only a part of the total number of events produced in the reaction, while the remainder were not registered due to (i) geometrical holes in the detector acceptance and (ii) less than 100% efficiency of particle detection within the detector acceptance. Therefore, to extract the reaction cross sections, the experimental event yield should be adjusted for the geometric acceptance and detection efficiency, thus accounting for the lost events.

In order to determine the overall detector efficiency, a Monte Carlo simulation is typically performed. In this analysis, double-pion events are generated with TWOPEG-D, which is an event generator for the double-pion electroproduction off a moving proton [24]. These events are hereinafter called "generated" events.

The generated events are passed through a standard multi-stage procedure of simulating the detector response [4]. At the first stage the interaction of the generated events with the CLAS detector is simulated. For this purpose, the GSIM package (GEANT SIMulation) is used. GSIM incorporates information about the detector geometry and materials with their electromagnetic properties, magnetic fields, target material and geometry, etc. It propagates all the particles through the CLAS detector from the vertex produced by the event generator and provides the detector response in terms of the same "raw" signals as the actual CLAS detector does.

Although the GSIM package includes all the detector geometry and properties, it still does not properly reproduce the resolution of the drift chambers and the TOF system. For that reason the GSIM Post Processor (GPP) is used to better match the resolution as well as to include the effects of a less-than-perfect detector response (due to broken drift wires, problematic phototubes, etc.). The latter effects are unique for a particular run period, and therefore the information on the detector imperfections is usually provided along with the data files to be then used in the GPP. Meanwhile, the GPP parameters intended to adjust the resolution (DC and TOF smearing factors) are typically determined individually during a particular analysis as the resolution depends on the kinematics and hence on the experimental conditions. This analysis employs the same values of the resolution related GPP parameters as the study [22, 23] in which the double-pion cross sections off the free proton are measured under the same experimental conditions.

At the final stage, GPP output files are "cooked" using the same reconstruction software that was used for the real data (recsis). Events that survive after the "cooking" process are hereinafter called "reconstructed" Monte Carlo events. They are analyzed in the same way as real experimental events.

Chapter 3

Event selection

In the initial analysis step, all collected events are subject to a standard event pre-selection[1], which is performed using specific variables from the BOS banks [30, 31]. Firstly, to ensure that particles within an event were properly reconstructed, the number of geometrically reconstructed particles (*gpart*) is required to be greater than zero for each event. The *gpart* variable is extracted from the variable $NPGP$ in the HEVT bank according to the following relation,

$$NPGP = (\text{Number of final reconstructed particles}) \times 100 + gpart. \qquad (3.0.1)$$

Then, to exclude from consideration out-of-time particles, the status word *stat* (which corresponds to the variable *Status* in the EVNT bank) is required to be greater than zero for each particle candidate.

For each event the electron candidate is defined as the first in time particle that gives signals in all four parts of the CLAS detector (DC, CC, TOF, and EC), which means that the variables *DCStat*, *CCStat*, *SCStat*, and *ECStat* from the EVNT bank should be greater than zero. To select hadron candidates, signals only in two sub-detectors (DC and TOF) are required, i.e. the variables *DCStat* and *SCStat* from the EVNT bank should be greater than zero.

Finally, all particle candidates should have an appropriate charge, i.e. the variable *Charge* from the EVNT bank is required to be ±1 depending on the candidate type.

---

[1] See also Ref. [32].

The particle candidates that survive this event preselection are then subject to further detailed selection, which is described below.

3.1 Electron identification

First, the Electromagnetic Calorimeter (EC) and Čerenkov Counter (CC) responses need to be examined, to reveal good electrons among all electron candidates and to separate them from electronic noise, accidentals and the π^- contamination.

3.1.1 Electron selection in the EC

According to [33], the overall EC resolution as well as uncertainties from the EC output summing electronics lead to fluctuations of the EC response near the hardware threshold. Therefore, to select only reliable EC signals, a minimal cut on the scattered electron momentum $P_{e'}$ should be applied in the software. The value of this cut is chosen according to the relation (3.1.1) suggested in [33],

$$P_{e'}^{min} \text{ (in MeV)} = 214 + 2.47 \cdot V_{th} \text{ (in mV)}, \qquad (3.1.1)$$

where V_{th} is the calorimeter threshold voltage.

For "e1e" run $V_{th} = 100$ mV, which results in $P_{e'}^{min} = 461$ MeV.

Then, the so-called sampling fraction cut is applied to eliminate part of the pion contamination. To develop this cut, the fact that electrons and pions have different energy deposition patterns in the EC is used. An electron produces an electromagnetic shower, where the deposited energy E_{tot} is proportional to the scattered electron momentum $P_{e'}$, while a π^- loses a constant amount of energy per scintillator (~2 MeV/cm) independently of its momentum. Therefore, for electrons the quantity $E_{tot}/P_{e'}$ plotted as a function of $P_{e'}$ should follow the straight line that is parallel to the x-axis and located around the value $1/3$ on the y-axis, since electrons lose about $2/3$ of their energy in lead sheets (in reality this line has a slight slope).

13
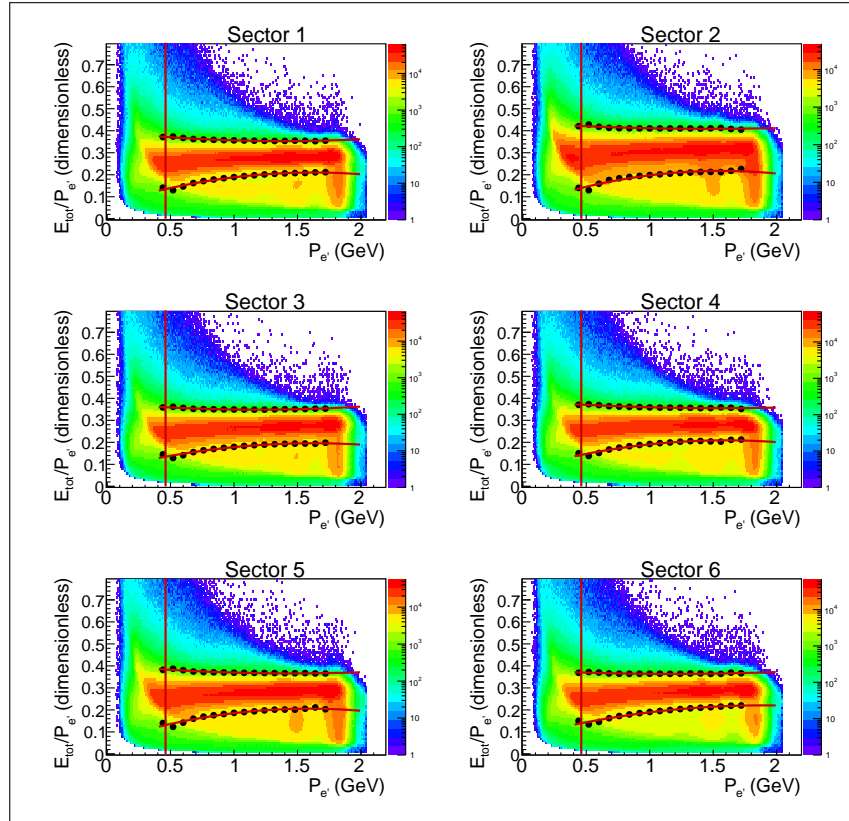
Figure 3.1: Sampling fraction distributions for the data. The six plots correspond to the six CLAS sectors. The vertical red line at $P_{e'} = 0.461$ GeV shows the EC threshold cut. Black points correspond to the positions of Gaussian fit maxima $\pm 3\sigma$ for different X-slices of the 2D histograms. These points are fit by a second order polynomial, the resulting functions are shown by the red curves. Events between the red curves are selected for further analysis.
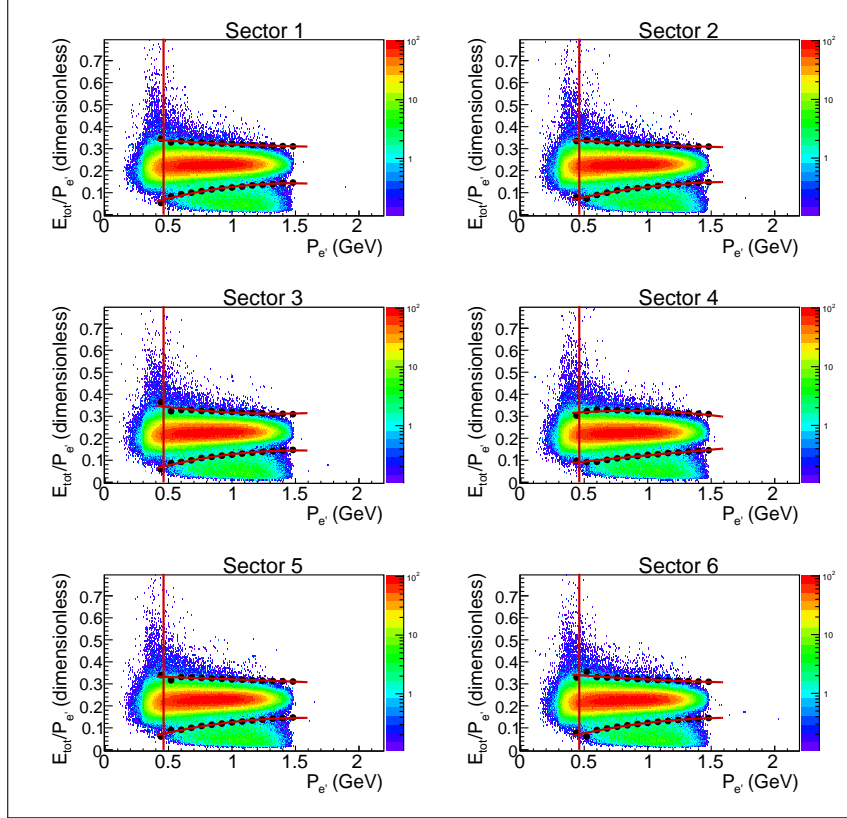
Figure 3.2: Sampling fraction distributions for the reconstructed Monte Carlo events. The six plots correspond to the six CLAS sectors. The vertical red line at $P_{e'} = 0.461$ GeV shows the EC threshold cut. Black points correspond to the positions of Gaussian fit maxima $\pm 3\sigma$ for different X-slices of the 2D histograms. These points are fit by a second order polynomial, the resulting functions are shown by the red curves. Events between red curves are selected for further analysis.

In Fig. 3.1 the total energy deposited in the EC divided by the particle momentum is shown as a function of particle momentum. The six plots correspond to the six CLAS sectors. Events between the red curves are selected as good electron candidates for further analysis. The vertical red line at $P_{e'} = 0.461$ GeV shows the EC threshold cut. The upper and lower red curves are obtained in the following way: X-slices of the 2D histograms are fit by Gaussians. In this way points that correspond to the positions of the fit maxima $\pm 3\sigma$ are obtained. These points are shown by black circles in Fig. 3.1. They determine the upper and lower boundaries for the cut. Finally, to obtain smooth curves, all points are fit by a second order polynomial.

Cuts on the minimal electron momentum and on sampling fraction are applied both to the experimental and reconstructed Monte Carlo events. Since the Monte Carlo simulation does not reproduce electromagnetic showers well enough, the sampling fraction distributions for the simulation are slightly lower than for the data. EC cuts for the simulation, obtained using the same procedure as for the data, are shown in Fig. 3.2. These plots contain no events with $P_{e'} > 1.5$ GeV since only double-pion events were generated, while for the data events with $P_{e'} > 1.5$ GeV exist since Figure 3.1 was plotted for inclusive electrons.

3.1.2 Electron selection in the CC

To improve the quality of the electron candidate selection and π^-/e^- separation, a Čerenkov counter is used [27]. As shown in [34], there is a contamination in the measured CC spectra that manifests itself as a so-called single-photoelectron peak, which is actually located at a few photoelectrons (see the distributions shown in black in Fig. 3.5). The main source of this contamination are accidental coincidences of PMT noise signals with measured pion tracks [34]. The goal of CC cuts is to separate the spectrum of good electron candidates (it corresponds to the main maximum of the photoelectron distribution) from the single-photoelectron peak, but at the same

time to minimize the loss of good events. As seen in Fig. 3.5 (black curves), where photoelectron distributions are plotted, the single-photoelectron peak is rather pronounced and it significantly overlaps with the spectrum of good electron candidates. Thus the elimination of this contamination is not a straightforward task and a special procedure has been developed for this purpose.

The following set of CC cuts was applied:

- fiducial cut,

- φ_{cc} matching cut,

- θ_{cc} matching cut,

- geometrical cut that removes inefficient zones, and

- standard procedure of dealing with the single-photoelectron peak contamination based on the fit of the photoelectron distributions by the modified Poisson function.

All these cuts, except the last one, are defined in the so-called "CC projective plane" [34]. This is an imaginary plane behind the CC where the Čerenkov radiation would arrive if its polygonal (due to reflections in the mirror system) path from the emission point to the PMT was substituted by a straight line preserving the initial propagation direction and the total distance traveled [27, 34]. The polar and azimuthal angles $(\theta_{cc}, \varphi_{cc})$, which are defined in this projective plane, are not directly available in the BOS banks [30]. Therefore, some calculations are made to derive these angles from the variables available in the DCPB bank. Figure 3.3 illustrates these calculations.

The CC projective plane is defined in the sector reference coordinate system, i.e. the sector is bisected in the middle by the xz-plane with the z-axis directed along the beam line. In this reference system the equation of the projective plane is the following (according to Ref. [34]),

$$Ax + By + Cz + D = 0,$$

$$A = -0.000785, \quad B = 0,$$

$$C = -0.00168, \quad D = 1, \tag{3.1.2}$$

$$\vec{S} = (A, B, C),$$

where $\vec{S}$ is a vector perpendicular to the projective plane.

In Fig. 3.3 the particle track in the DC is shown by the thin dashed curve. Since the particle moves through a magnetic field in the DC, the track is curved. Having left the magnetic field region of the DC, the particle moves further along a straight line, tangential to a curved DC track in the point of its intersection with the CC. The unit vector that defines the direction of this tangent is known from the DCPB bank $\vec{n} = (n_x, n_y, n_z) = (\text{CX\_SC, CY\_SC, CZ\_SC})$. In Fig. 3.3 the vector $\vec{t}$ is pointing this direction and goes from the SC hit point to the CC projective plane.
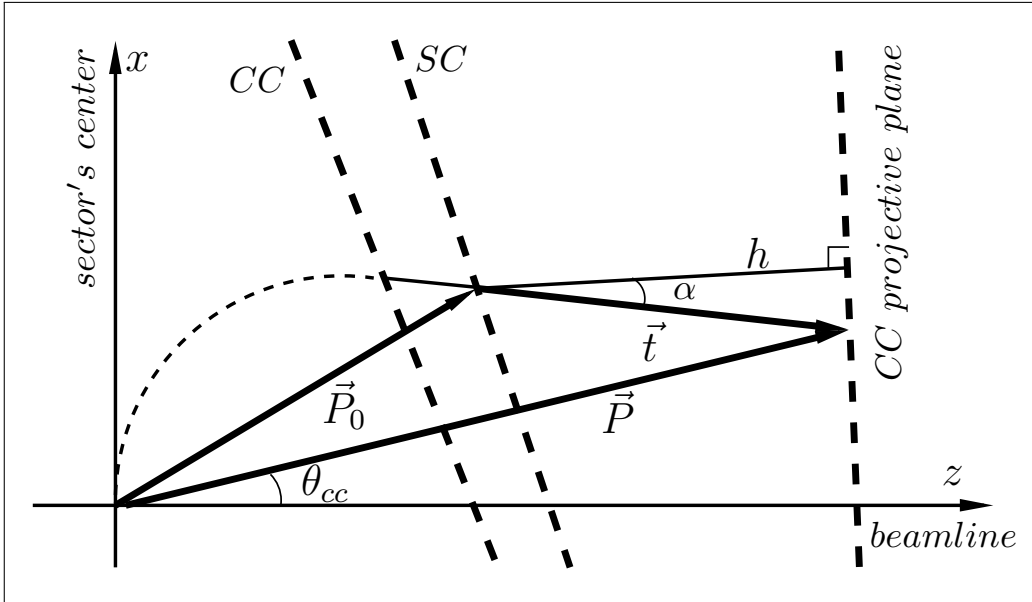
Figure 3.3: Illustration for the calculation of the polar θ_{cc} and azimuthal φ_{cc} angles in the CC projective plane (see text for details).

The $(\theta_{cc}, \varphi_{cc})$ angles in the projective plane are determined by the vector $\overrightarrow{P} = \overrightarrow{P_0} + \overrightarrow{t}$, where $\overrightarrow{P_0}$ is a vector that goes from the vertex to the point of the track intersection with the SC. Its components are known from the DCPB bank[2] $\overrightarrow{P_0} = (p_x^0, p_y^0, p_z^0) = (\text{x\_SC, y\_SC, z\_SC})$.

The vector $\overrightarrow{t}$ can be defined as

$$\overrightarrow{t} = |\overrightarrow{t}| \cdot \overrightarrow{n} = \frac{h}{\cos\alpha} \cdot \overrightarrow{n}, \tag{3.1.3}$$

where $\overrightarrow{n}$ is the unit vector in the $\overrightarrow{t}$-direction defined above, while h is the distance from the SC hit point to the CC projective plane, which is given by[3]

$$h = \frac{|(\overrightarrow{S} \cdot \overrightarrow{P_0}) + D|}{|\overrightarrow{S}|}, \tag{3.1.4}$$

where $\overrightarrow{S}$ is the vector normal to the CC projective plane defined by Eq. (3.1.2).

In turn $\cos\alpha$ can be calculated as

$$\cos\alpha = \frac{|(\overrightarrow{S} \cdot \overrightarrow{n})|}{|\overrightarrow{S}|}, \tag{3.1.5}$$

since $\overrightarrow{S}$ is directed along h and $\overrightarrow{n}$ is directed along $\overrightarrow{t}$.

This leads to the following expression for the vector $\overrightarrow{t}$,

$$\overrightarrow{t} = |\overrightarrow{t}| \cdot \overrightarrow{n} = \left| \frac{(\overrightarrow{S} \cdot \overrightarrow{P_0}) + D}{(\overrightarrow{S} \cdot \overrightarrow{n})} \right| \cdot \overrightarrow{n} = \left| \frac{A \cdot p_x^0 + B \cdot p_y^0 + C \cdot p_z^0 + D}{A \cdot n_x + B \cdot n_y + C \cdot n_z} \right| \cdot \overrightarrow{n}. \tag{3.1.6}$$

---

[2] In the DCPB bank both $\overrightarrow{n}$ and $\overrightarrow{P_0}$ are defined in the sector reference frame.

[3] This is a standard relation for the distance from the point (given here by the vector $\overrightarrow{P_0}$) to the plane $Ax + By + Cz + D = 0$.

Then, obtaining the required vector $\overrightarrow{P}$ as the sum of $\overrightarrow{P_0}$ and $\overrightarrow{t}$, one can finally calculate the angles θ_{cc} and φ_{cc} as

$$\theta_{cc} = \arccos\left(\frac{P_z}{|\overrightarrow{P}|}\right),$$
$$\varphi_{cc} = \arctan\left(\frac{P_y}{P_x}\right).$$

(3.1.7)

The angle φ_{cc} defined by Eq. (3.1.7) is determined with respect to the center of each sector. This means that $\varphi_{cc} = 0$ is the middle of the sector, $\varphi_{cc} < 0$ is on the left side of the sector, and $\varphi_{cc} > 0$ is on its right side.

One should also define the variables *CC segment number* (that indicates which segment has been hit) and *index* (that indicates which PMT has fired). They are taken from the CCPB bank *Status* variable according to the following relation,

$$Status = 10 \times (\text{CC segment number}) + 1000 \times (1 + index),$$

(3.1.8)

where *index* is 1 for right PMTs, -1 for left PMTs, and 0 when both PMTs have fired.

After all needed variables have been defined, all the cuts from the list specified above can be implemented.

First of all the fiducial cut in the CC plane is applied. The shape of this cut is taken from [35] and is given by

$$\theta_{cc} > 7.0 + 0.0032 \cdot \varphi_{cc} + 0.0499 \cdot \varphi_{cc}^2,$$
$$\left(\frac{\theta_{cc} - 45.5^o}{34.5^o}\right)^2 + \left(\frac{\varphi_{cc}}{21^o}\right)^2 \leq 1,$$
$$\left(\frac{\theta_{cc} - 45.5^o}{1.75^o}\right)^2 + \left(\frac{\varphi_{cc}}{21^o}\right)^2 > 1, \text{ and}$$
$$\theta_{cc} < 45^o.$$

(3.1.9)

Then the so-called φ_{cc} and θ_{cc} matching procedures (based on the studies [34] and [36]) are performed. The idea of this matching is quite simple: there must be one-to-one correspondence between the angles in the CC plane (which are calculated based on the information from the DC) and PMT signals in the CC for real events, while background noise and accidentals should not show such correlation.

The principle of the φ_{cc} matching cut is the following: when the track is on the right side of the CC segment, the right PMT should be fired, and vice versa. Therefore, if $\varphi_{cc} < 0$, the *index* defined in Eq. (3.1.8) is required to be -1 and if $\varphi_{cc} > 0$, the *index* is required to be 1. Events that do not satisfy these conditions are removed. All events with *index* $= 0$ are kept.
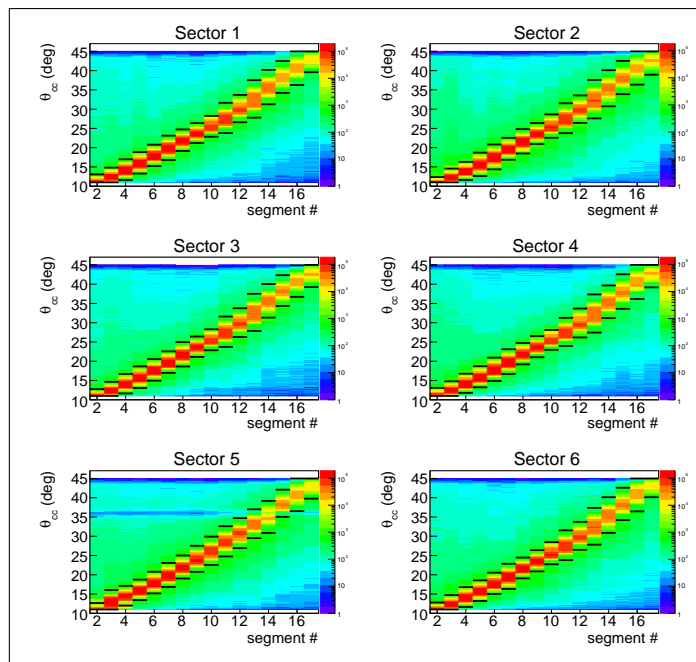
Figure 3.4: θ_{cc} versus segment distributions for six CLAS sectors. Events between the horizontal black lines are treated as good electron candidates.

In order to perform θ_{cc} matching, the θ_{cc} versus segment number cut should be done. Figure 3.4 shows θ_{cc} versus segment distributions for the six CLAS sectors. Event distributions in each segment have been plotted as a function of θ_{cc} and fit by

21

Gaussians. The horizontal black lines correspond to the positions of the fit maxima $\pm 4\sigma$. Events between these black lines are treated as good electron candidates.

The influence of φ_{cc} and θ_{cc} matching cuts on the photoelectron distributions is demonstrated in Fig. 3.5, where the distributions before matching cuts are plotted in black, distributions after the φ_{cc} matching are plotted in red, and after the subsequent θ_{cc} versus segment cut are plotted in blue. As seen in Fig. 3.5 both these cuts reduce the single-photoelectron peak, but leave the main part of the spectrum unchanged. The same φ_{cc} and θ_{cc} matching cuts are also applied to the reconstructed Monte Carlo events.

The accidental noise and pion background are not the only source of the single-photoelectron peak contamination. The peak also partially corresponds to electrons that hit some specific geometrical zones with low CC efficiency. When an electron hits such a zone the number of detected photoelectrons turns out to be significantly less than expected. This leads to the fact that the region of the photoelectron spectrum, which corresponds to the low number of photoelectrons, appears to be overpopulated by events. Since low efficiency zones are distributed inhomogeneously in the CC plane and the Monte Carlo simulation do not reproduce them properly, it is better to remove them from the consideration completely. For this purpose a special geometrical cut is established.

This geometrical cut is done in the following way. Distributions φ_{cc} versus θ_{cc} are plotted for each CLAS sector (see Fig. 3.6, upper frame) with the quantity (3.1.10) as a color code.

$$\frac{number\ of\ events\ inside\ (\theta_{cc}, \varphi_{cc})\ bin\ with\ more\ than\ five\ photoelectrons}{total\ number\ of\ events\ inside\ (\theta_{cc}, \varphi_{cc})\ bin}$$

(3.1.10)

This quantity varies from zero to one and shows the proportion of electron candidates with number of photoelectrons greater than five inside a $(\theta_{cc}, \varphi_{cc})$ bin. The

value for this criterion (five photoelectrons) was chosen rather arbitrarily, since its only purpose is to facilitate the separation of inefficient zones (which correspond mostly to low numbers of photoelectrons) from the regular zones (which correspond to the full photoelectron spectrum).

The curved vertical stripe in sector five in Fig. 3.6 corresponds to an inefficient zone that will be discussed further in Sect. 3.4.1.
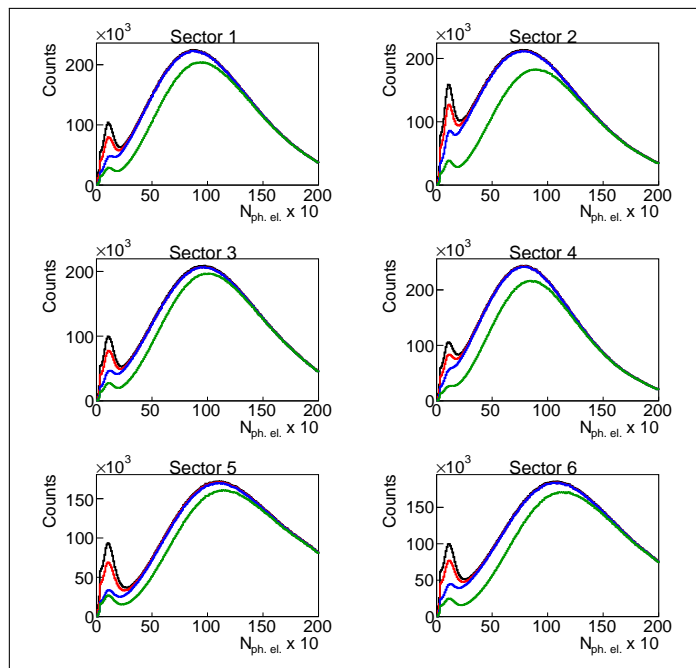
Figure 3.5: Influence of different CC cuts on the distributions of the number of photoelectrons multiplied by ten for the six CLAS sectors. Black curve – only fiducial cut in the CC plane is applied, red curve – the φ_{cc} matching cut is added, blue curve – the θ_{cc} matching cut is added, and green curve – the geometrical cut in the CC plane that removes inefficient zones is finally added.

For further analysis only fiducial areas with a ratio (3.1.10) greater than the certain threshold value are selected. This threshold value was chosen to be 0.7, 0.65, 0.7, 0.65, 0.8, and 0.8 for sectors 1, 2, 3, 4, 5, and 6, respectively. Since inefficient zones are not identical for various CLAS sectors (see Fig. 3.6), different threshold values are needed for them. Geometrical zones, which are selected for further analysis, are shown in black in the lower plots of Fig. 3.6. All zones shown in white are treated as inefficient

and are removed from the analysis. As seen in Fig. 3.6, there is an inefficient zone in the middle of each sector. This is expected since two CC mirrors are joined here.

The threshold values for the ratio (3.1.10) were chosen in order to keep the balance between the intention to reduce the amount of low efficient zones as much as possible and the desire to preserve most of the statistics. The influence of this geometrical cut on the photoelectron distributions in different sectors is demonstrated in Fig. 3.5, where the distributions after the cut are plotted in green. As was expected, this cut leads to some reduction in the low lying part of the photoelectron spectrum, including the region of the single-photoelectron peak, and leaves the high lying part of the spectrum unchanged.

This geometrical cut is fully based on the experimental data. It acts as a fiducial cut, because it simply removes certain geometrical regions in the CC plane. This means that it can be safely applied to the Monte Carlo simulation, too. Thus, the same geometrical regions (shown in white in the lower plots in Fig. 3.6) are removed both for the experimental and reconstructed Monte Carlo events.

After the geometrical cut discussed above is applied, the single-photoelectron peak appears to be significantly smaller and better separated from the main spectrum, but still remains (see Fig. 3.5). Therefore, in order to completely get rid of this contamination, the standard procedure should then be applied [17].

To apply the standard procedure of dealing with the single-photoelectron peak contamination, the photoelectron distributions are plotted for each PMT on the left and right sides of each CC segment and for each CLAS sector (see Fig. 3.7).

In Fig. 3.7 the red lines show the cuts that are made in order to eliminate events under the single-photoelectron peak. The cut position is individually optimized for each PMT in each sector. The distributions of events, for which both right and left PMTs have fired ($index = 0$) are not subject to this cut, since their contamination caused by the single-photoelectron peak is assumed negligible.

24
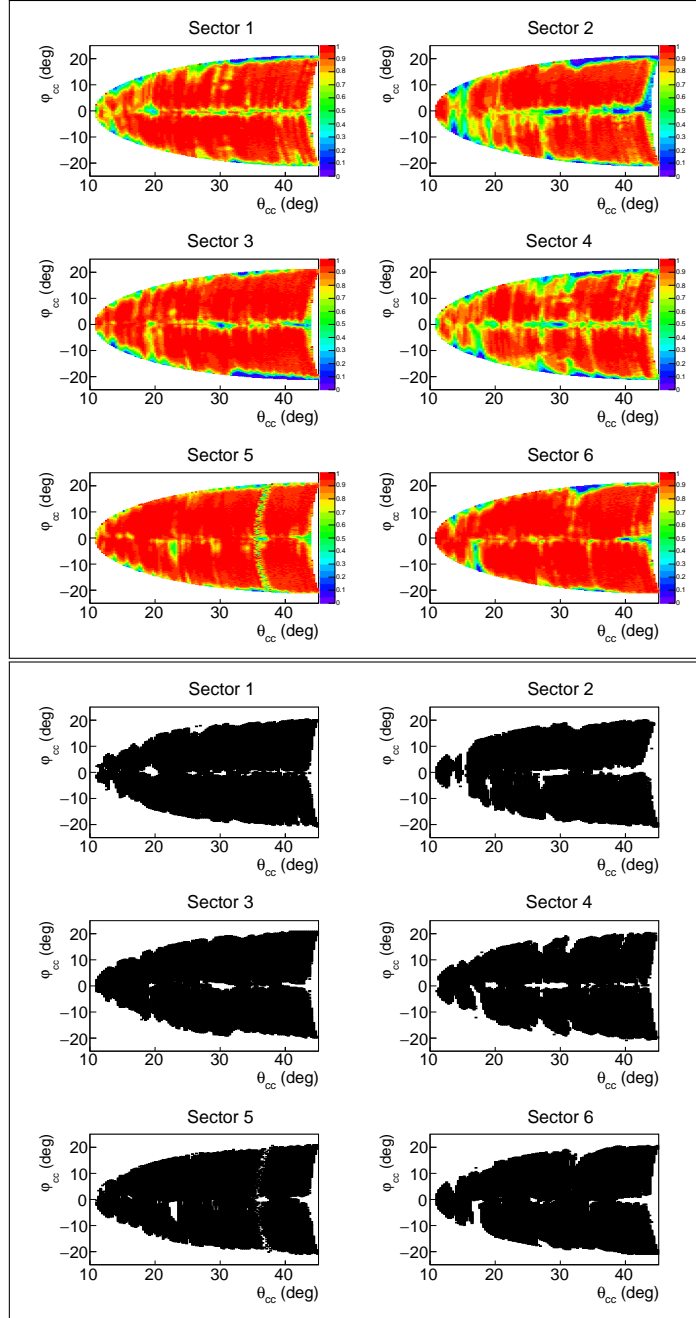
Figure 3.6: Upper frame: Distributions of the quantity (3.1.10) as a function of the polar θ_{cc} and azimuthal φ_{cc} angles in the CC plane for the six CLAS sectors. This quantity varies from zero to one and shows the proportion of electron candidates with number of photoelectrons greater than five inside a $(\theta_{cc}, \varphi_{cc})$ bin. Lower frame: Black zones correspond to the fiducial areas with the ratio (3.1.10) greater than 0.7, 0.65, 0.7, 0.65, 0.8, and 0.8 for sectors 1, 2, 3, 4, 5, and 6, respectively. These zones are selected for further analysis. All zones shown in white are treated as inefficient and removed from the analysis.

Since the Monte Carlo does not reproduce photoelectron distributions well enough, the cut shown by the red lines in Fig. 3.7 is applied only to the data. To recover the good electrons that were cut off in this way, a special procedure is applied. The part of the distributions on the right side of the red line is fit by the function (3.1.11), which is a slightly modified Poisson distribution.

$$y = P_1 \left(\frac{P_3^{\frac{x}{P_2}}}{\Gamma\left(\frac{x}{P_2} + 1\right)} \right) e^{-P_3}, \tag{3.1.11}$$

where P_1, P_2, and P_3 are free fit parameters.
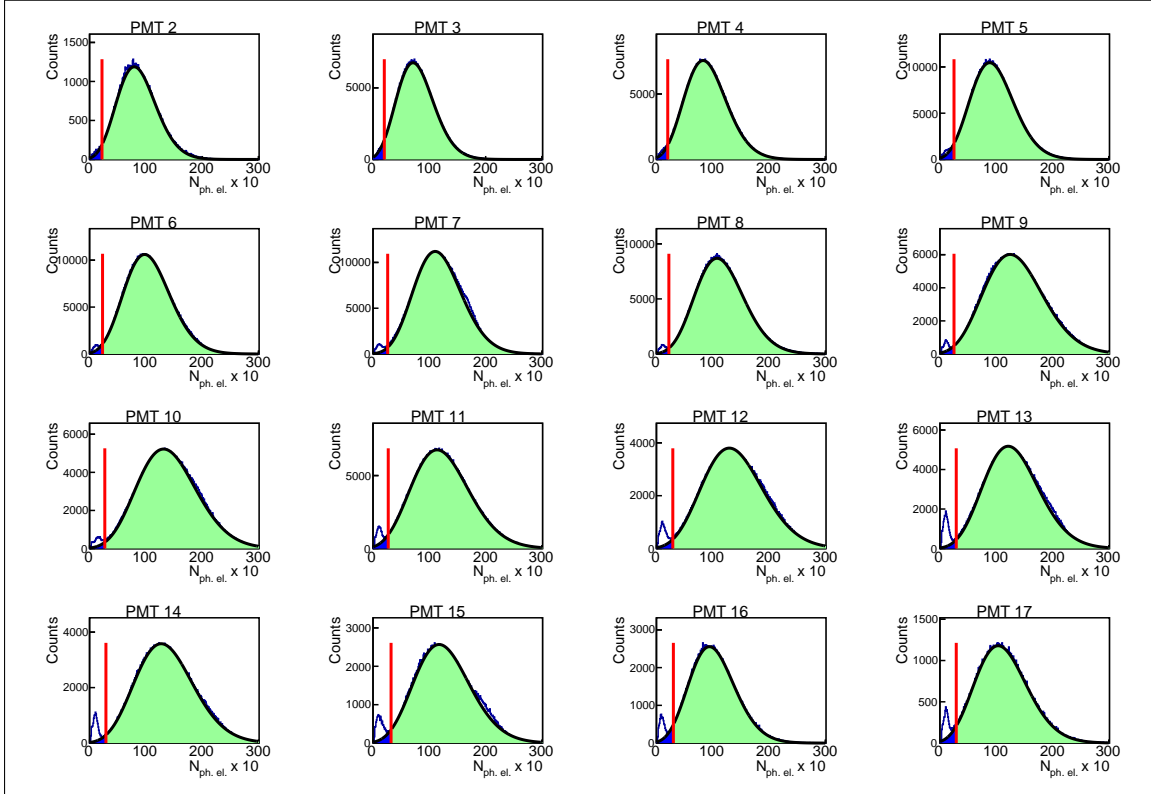
Figure 3.7: Distributions of number of photoelectrons multiplied by ten for the left side of sector one of the CC. Various plots correspond to various CC segments. Black curves show the fit by the function (3.1.11). Red vertical lines show the applied cut. Regions that are needed to calculate the correction ratio (3.1.12) are shown in blue and green.

The fitting function is then continued into the region on the left side of the red line. In this way the two regions, shown in blue and green in Fig. 3.7, are determined. Finally the correction factors are defined by (3.1.12) and applied as a weight for each event, which goes to the particular PMT. These correction factors depend on the PMT number and are typically on a level of a few percent.

$$F_{ph.\ el.} = \frac{\text{green area} + \text{blue area}}{\text{green area}} \qquad (3.1.12)$$

Note that segments #1 and #18 are removed from the analysis completely (both in data and Monte Carlo), since they are dominated by events from the single-photoelectron peak.

3.2 Hadron identification

Hadron are identified relying on the information provided by the TOF system [28, 29]. This information allows the velocity of the hadron candidates to be determined according to the following relation.

$$\beta_h = \frac{v_h}{c} = \frac{l_h}{t_h \cdot c}, \qquad (3.2.1)$$

where v_h is the hadron velocity, c the speed of light, l_h the hadron path length from the vertex to the SC-plane (variable *Path* in the SCPB bank), and t_h the time that it took the hadron to travel from the vertex to the SC-plane. This time can be calculated in the following way.

$$t_h = t_e + (t_h^{tof} - t_e^{tof}) = \frac{l_e}{c} + (t_h^{tof} - t_e^{tof}), \qquad (3.2.2)$$

where $t_e = \frac{l_e}{c}$ is the time that the electron spent on traveling from the vertex to the SC-plane and l_e the electron path length. The quantities t_e^{tof} and t_h^{tof} are the times, when the electron and hadron hit the SC-plane, respectively (the variable *Time* in the SCPB bank).

Equation (3.2.2) assumes that the hadron and electron departed from the vertex at the same time, but the electron traveling with the speed of light reached the SC-plane earlier than the hadron. The difference $t_h^{tof} - t_e^{tof}$ indicates the hadron delay time, which is the consequence of traveling with the velocity $v_h < c$. Thus Eq. (3.2.2) makes the hadron time related to that of electron for each event[4].

The charged hadron can be identified by comparing β_h determined from TOF according to Eqs. (3.2.1) and (3.2.2) with β_n given by

$$\beta_n = \frac{p_h}{\sqrt{p_h^2 + m_h^2}}. \tag{3.2.3}$$

In Eq. (3.2.3) β_n is a so-called nominal value that is calculated using the particle momentum (p_h) known from the DC and the exact particle mass assumption (m_h).

The usual way to develop hadron id cuts is to investigate β versus momentum distributions for different TOF paddles for each hadron type separately. This investigation reveals three types of problematic paddles, i.e.

A Paddles which signals are completely unreliable (bad paddles). These are paddles #16 in sector 2, #44 in sector 3, #17 in sector 5, and #48 in each sector. They are excluded from this analysis both for experimental data and reconstructed Monte Carlo events.

---

[4] It worth noting that usually one uses the value of β directly defined in the EVNT bank (variable *Betta*), but it turned out that this quantity shows noticeable inaccuracies in electron bunch determination, which were made during the cooking. The value of β calculated by Eqs. (3.2.1) and (3.2.2) do not show these inaccuracies because in this method the timing of the hadron is related to that of electron for each event.

B Paddles in which the distributions are shifted from their expected positions. The reason for this is most likely mistakes during data cooking/calibration. Typical examples of such paddles are shown in Fig. 3.8.

C Paddles for which the distributions for a given hadron have double band structure. This problem appears for most of the paddles with number ≥ 40 and originates from the fact that (along with the mistakes during cooking/calibration) for these paddles two scintillation bars were connected to one TDC [29]. Typical examples of such paddles are shown in Fig. 3.9.
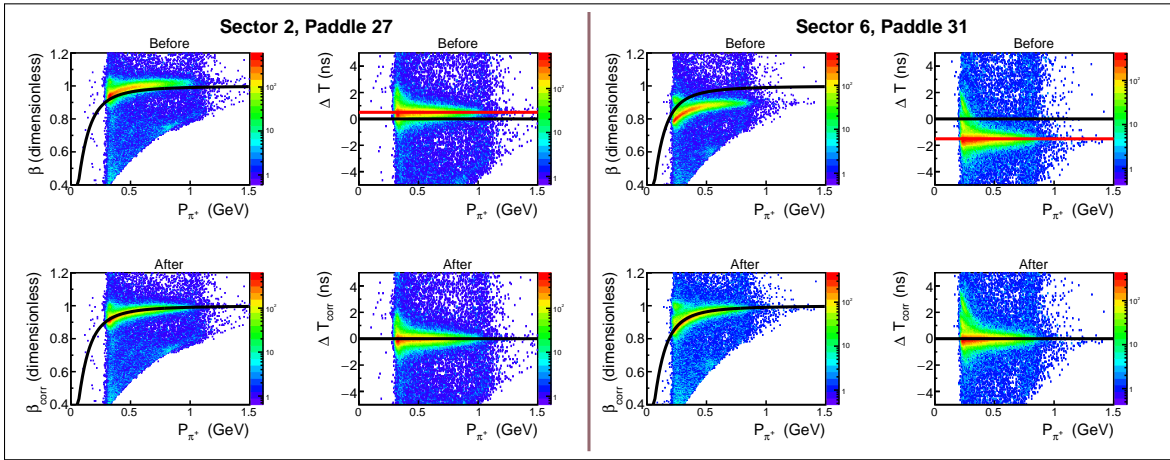
Figure 3.8: Timing correction for type B problematic paddles #27 in sector 2 (left side) and #31 in sector 6 (right side) for π^+ candidates. The first column in each side shows the β_h versus momentum distributions with the black curve corresponding to the nominal β_n defined by Eq. (3.2.3). The second column in each side corresponds to the ΔT versus momentum distributions, where the black horizontal line shows the position of zero and the red line shows the position of shifted ΔT-band. The uncorrected distributions are given in the first row, while the influence of the correction is shown in the second row.

To cure the latter two types of problems, a so-called timing correction is developed. To perform this correction, the quantity ΔT is calculated, which corresponds to the time difference between the real TOF signal and the expected one.

$$\Delta T = \frac{l_h}{c} \left(\frac{1}{\beta_n} - \frac{1}{\beta_h} \right). \tag{3.2.4}$$

29

Figure 3.8 illustrates the timing correction for type B problematic paddles #27 in sector 2 (left side) and #31 in sector 6 (right side) for π^+ candidates. The plots in the first row correspond to the β_h versus momentum and ΔT versus momentum distributions before the correction. It is seen that β_h versus momentum bands are shifted from their expected position shown by the black curve, which corresponds to the nominal β_n defined by Eq. (3.2.3). These shifts of β_h versus momentum bands are caused by the corresponding shifts of the ΔT versus momentum bands from zero position shown by the black horizontal lines. The idea of the timing correction is to move ΔT bands back to the position around zero, as shown in the corrected ΔT versus momentum plots in the second row. The corrected value of β is then calculated as

$$\beta_{corr} = \frac{1}{\frac{1}{\beta_n} - \frac{(\Delta T - t_{shift}) \cdot c}{l_h}}, \tag{3.2.5}$$

where t_{shift} is the position of shifted ΔT-band shown by the corresponding red horizontal line in Fig. 3.8.

The β_{corr} versus momentum distributions are shown in second row in Fig. 3.8. As seen in these plots, β_{corr} versus momentum bands demonstrate no shift from the black curves after the timing correction is applied.

Figure 3.9 illustrates the timing correction for type C problematic paddles #46 in sector 3 (left side) and #40 in sector 5 (right side) for π^+ candidates. The plots in the first row clearly show the double band structures in β_h versus momentum and ΔT versus momentum distributions. To perform timing correction for this type of paddles, one needs to determine the position t_{shift} of each incorrect ΔT-band (see horizontal red lines in Fig. 3.9) and then to move both of them to the correct position around zero, as demonstrated in the second row. The corrected value of β is again calculated according to Eq. (3.2.5) with the only distinction, that events from different ΔT-bands are treated separately and different t_{shift} values are used for them.
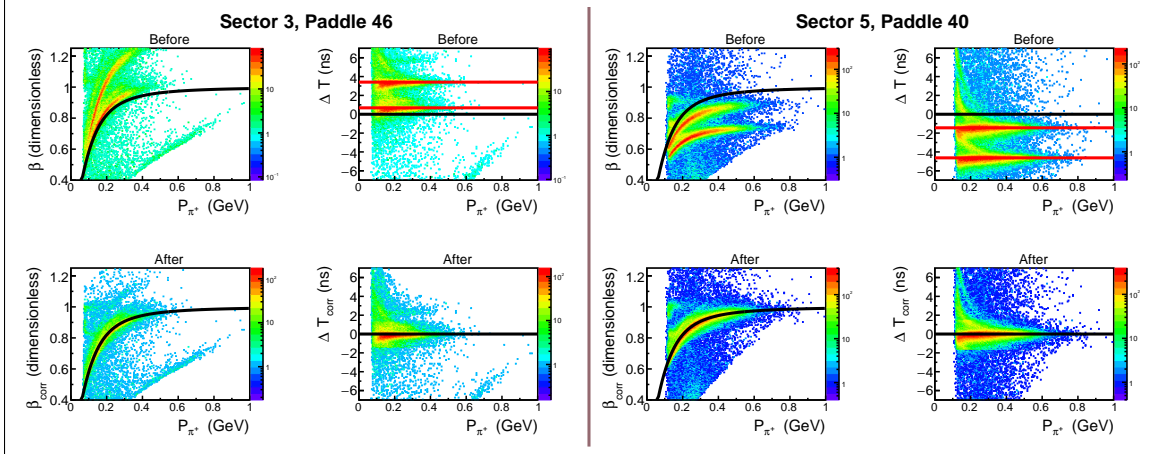
Figure 3.9: Timing correction for type C problematic paddles #46 in sector 3 (left side) and #40 in sector 5 (right side) for π^+ candidates. The first column in each side shows the β_h versus momentum distributions with the black curve corresponding to the nominal β_n defined by Eq. (3.2.3). The second column in each side corresponds to the ΔT versus momentum distributions, where the black horizontal line shows the position of zero and the red lines show the position of shifted ΔT-bands. The uncorrected distributions are given in the first row, while the influence of the correction is shown in the second row.

The β_{corr} versus momentum distributions are shown in the second row in Fig. 3.9. As seen in these plots, after the timing correction is applied β_{corr} versus momentum bands demonstrate neither double band structures nor shifts from the black curves.

Figures 3.8 and 3.9 give examples of the timing correction for π^+ candidates. Similar corrections have also been performed for proton and π^- candidates.

After the timing problems are eliminated in each TOF paddle, the hadron identification can be made. For the hadron identification, only events with good electron candidates that have been selected in the previous step are used. Figure 3.10 shows β_{corr} versus momentum distributions for each type of hadron candidate: protons (upper plot), positive pions (middle plot), and negative pions (bottom plot). These distributions include all sectors and all TOF paddles (with the exclusion of bad ones). The red curves show the corresponding hadron id cuts. These curves were obtained in the following way. Firstly, x-slices of the 2D histograms are fit by Gaussians. In this way points that correspond to the positions of the fit maxima $\pm 3\sigma$ are obtained.
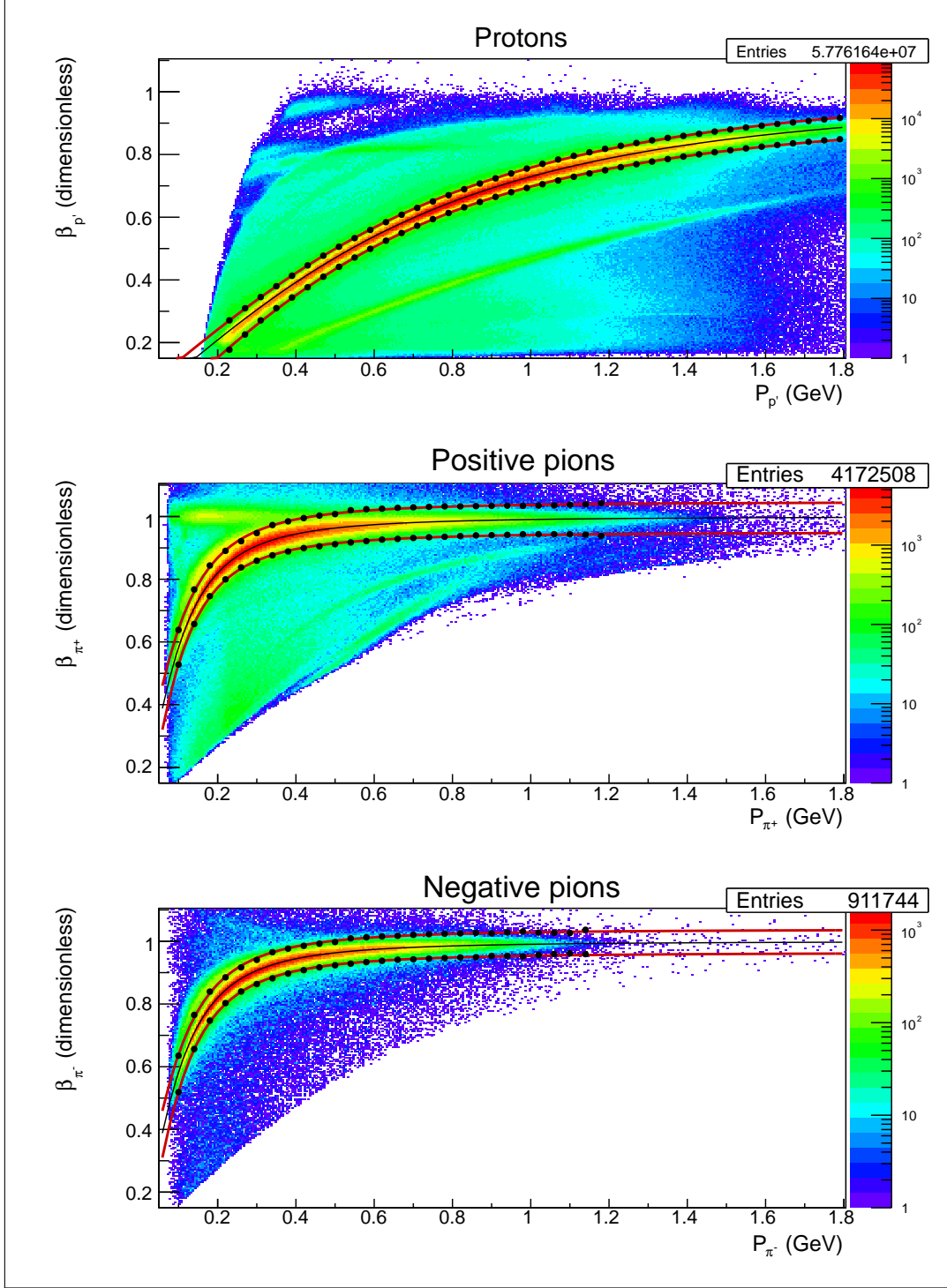
Figure 3.10: β_{corr} versus momentum distributions for proton (upper plot), positive pion (middle plot), and negative pion (bottom plot) candidates. Thin black solid curves in the middle of each band correspond to the nominal β_n given by Eq. (3.2.3). Black points correspond to the positions of Gaussian fit maxima $\pm 3\sigma$ for individual x-slices of the 2D histograms. These points are fit by the function Eq. (3.2.6), the resulting functions are shown by the red curves. Events between the red curves are selected for further analysis.

These points are shown by black bullets in Fig. 3.10. They determine the upper and lower boundaries for the cut[5]. Finally, to obtain smooth curves, all points are fit by the following function,

$$f(p_h) = \frac{a_0 \cdot p_h}{\sqrt{a_1 \cdot p_h^2 + m_h^2 + a_2}} + a_3, \qquad (3.2.6)$$

where p_h is the hadron momentum, m_h hadron mass, and a_0, a_1, a_2, a_3 fit parameters.

Events which are located between the red curves in Fig. 3.10 are selected for further analysis and treated as good corresponding hadron candidates. It also needs to be mentioned that the distribution for positive pions was plotted only for events that already have a good proton candidate, and the distribution for negative pions was plotted only for events with good proton and positive pion candidates. Furthermore, in order to simplify the analysis process, all hadrons were preselected on an initial analysis step. The consequence of this preselection is the fact that distributions shown in Fig. 3.10 contain areas that are not populated with events.

The hadron identification cuts established in this way are applied to the reconstructed Monte Carlo events as well.

3.3 Momentum corrections

3.3.1 Proton momentum correction (energy loss)

While traveling through the detector and the target, the final state particles lose a part of their energy due to the interactions with the medium. Therefore, the measured particle momentum appears to be lower than the actual value. GSIM simulation of the CLAS detector correctly propagates particles through the media and, therefore,

---

[5] Note that to establish the upper cut boundary for pions, the 3σ value was used only for $p_\pi > 0.54$ GeV. For $p_\pi < 0.54$ GeV different smaller values were used in order to better separate pions from the small upper band, which is thought to correspond to muons.

the effect of the energy loss is included into the efficiency and does not impact the extracted cross sections. However, in order to avoid shifts in the distributions of some kinematic quantities (e.g. missing masses) from their expected values, an energy loss correction is applied to the proton momentum magnitude, since the low-energy protons are affected the most by energy loss in the materials. This correction is based on the GSIM simulation of the CLAS detector and is performed for both experimental and reconstructed Monte Carlo events.
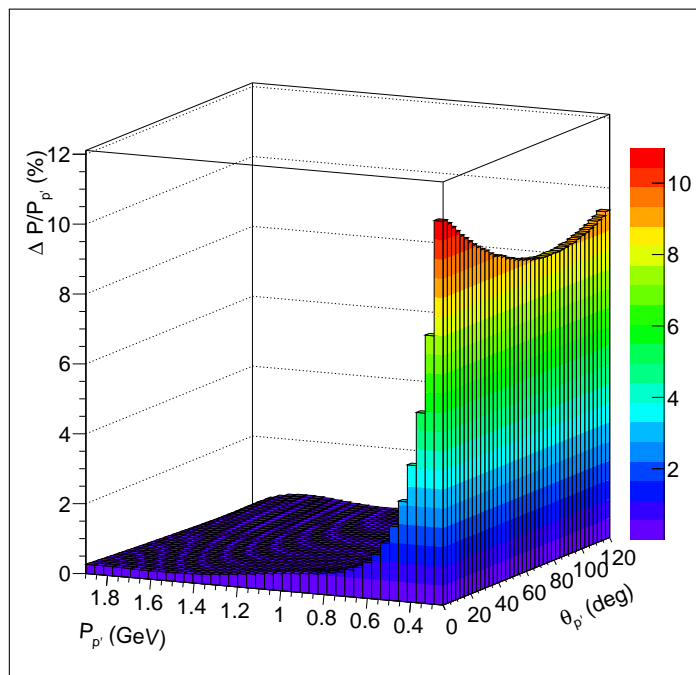
Figure 3.11: Percentage of momentum that protons lose when they move through the detector and target media as a function of the momentum $P_{p'}$ and scattered angle $\theta_{p'}$ of the final proton.

To obtain the correction function, the quantity ΔP that is the difference between the generated and reconstructed proton momenta was considered. This quantity was binned in the reconstructed proton momentum $P_{p'}$ and polar angle $\theta_{p'}$ and fit by a Gaussian in each ($P_{p'}$, $\theta_{p'}$) bin. The obtained mean values were further fit by a fifth order polynomial as a function of $P_{p'}$ in each $\theta_{p'}$ bin. Then the parameters of the resulting fit functions were fit as a function of $\theta_{p'}$ by a second order polynomial.

34

The resulting energy loss correction function is shown in Fig. 3.11. It gives the percentage of the momentum that protons lose when they move through the detector and target media.

Note that if one wants to isolate the pure effect of the energy loss, the difference between proton momenta for events reconstructed with and without detector and target materials must be considered. Since in the applied procedure the difference between generated and reconstructed proton momenta is analyzed, the correction function shown in Fig. 3.11 can also include other effects that lead to improper proton momentum reconstruction.

3.3.2 Electron momentum correction

Due to slight misalignments in the DC position, small inaccuracies in the description of the torus magnetic field, and other possible reasons the momentum and angle of particles may have some small systematic deviations from their real values. These effects being of undefined origin cannot be simulated in GSIM, therefore a special momentum correction procedure is needed for the experimental data. According to [37], the evidence of the need for such corrections is most directly seen in the dependence of the elastic peak position on the azimuthal angle of the scattered electrons. It is shown in [37] that the elastic peak position is shifted from the true value (0.938 GeV) and this shift is sector dependent.

The significance of this effect depends on the beam energy. In the analysis [22] it is shown that a beam energy of 2.039 GeV leads to the small shift ($\sim$ 3 MeV) in elastic peak position, while the study [37] demonstrates that in case of 5.754 GeV beam energy this shift reaches 20 MeV. Moreover, the study [37] also shows that this effect becomes discernible only if the particle momentum is sufficiently high (e.g. for pions the correction is needed only if their momentum is higher than 2 GeV). Thus, the small beam energy of this analyzed dataset and the fact that in double-

pion kinematics hadrons carry only a small portion of the total momentum allows us to come to the conclusion that the correction is needed only for electrons, while deviation in hadron momenta can be neglected.
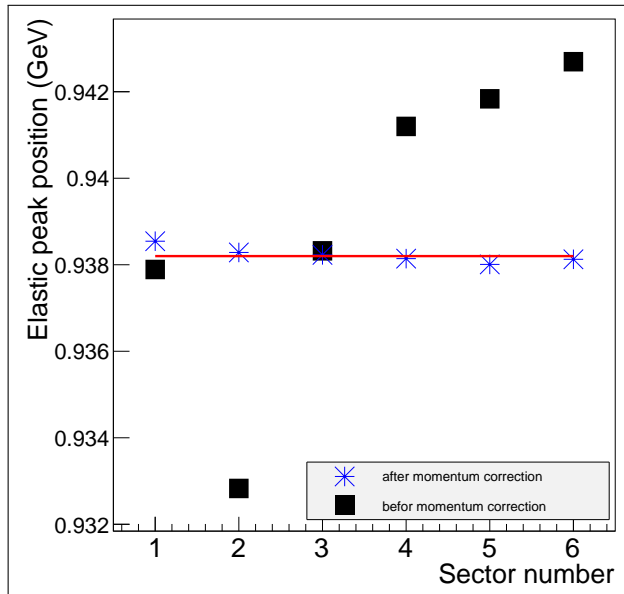
Figure 3.12: Elastic peak position for the six CLAS sectors before (black squares) and after (blue stars) electron momentum correction for the proton part of "e1e" dataset. The horizontal red line shows the proton mass. This figure is taken from the analysis [22].

Since this analysis suffers from additional complications as binding and motion of the target proton inside the deuteron, it was considered sensible to use the electron momentum corrections that have previously been developed and tested in the analysis of the free proton part of "e1e" dataset at the same beam energy [22]. To establish them, the approach [37], which is based on elastic kinematics, was used. These corrections include electron momentum magnitude correction as well as electron polar angle correction, which were developed for each CLAS sector individually.

Figure 3.12, which was taken from the analysis [22], demonstrates that after the electron momentum corrections the elastic peak position for all CLAS sectors gets closer to the proton mass, shown by the red horizontal line.
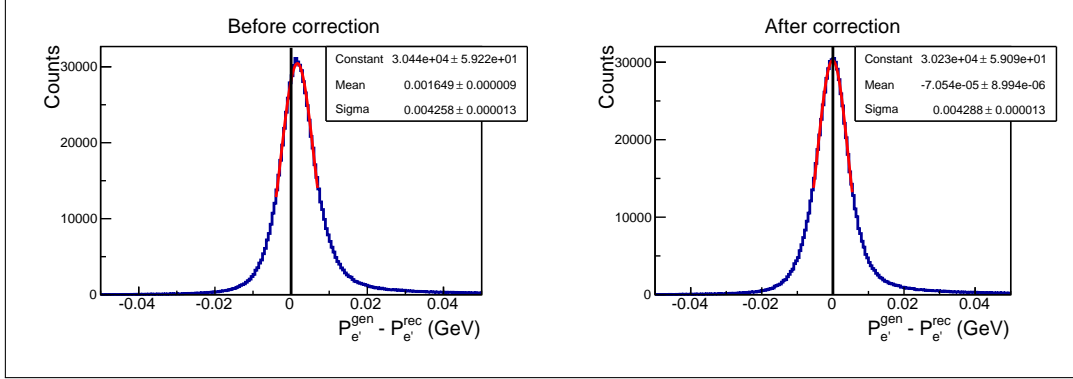
Figure 3.13: Difference between generated and reconstructed electron momenta before (left plot) and after (right plot) the correction of the momentum magnitude, which has been applied to the reconstructed electrons. The vertical black line shows the position of zero.

The correction discussed above is applied only for experimental data. As for the Monte Carlo simulation, it turns out that due to unknown reasons (most likely because electrons lose some energy when they travel through the detector and target media) the reconstructed electron momentum appears to be slightly lower than the generated one. This effect is demonstrated in the left plot of Fig. 3.13, where the event distribution of the quantity ΔP (which is the difference between generated and reconstructed electron momenta) is presented. Therefore, an adapted procedure of correcting the electron momentum magnitude is also applied to the reconstructed Monte Carlo events. This procedure is similar to that used for the proton energy loss (see Sect. 3.3.1). The correction depends only on the scattered electron momentum and polar angle, but not on the CLAS sector. The typical value of this correction is 0.2%. The right plot in Fig. 3.13 shows the result of the correction. As seen in this plot, the mean value of the quantity ΔP demonstrates no shift from zero when the momentum magnitude for reconstructed electron is corrected.

3.4 Other cuts

3.4.1 Fiducial cuts

The active detection solid angle of the CLAS detector is smaller than 4π [4]. This is in part due to the space filled with the torus field coils: the angles covered by the coils are not equipped with any detection system and therefore form a "dead" area for detection. Additionally, the detection area is also limited in polar angle from $8°$ up to $45°$ for electrons and up to $140°$ for other charged particles [4]. Moreover, different studies and analyses have shown that also the edges of the active area do not provide a safe region for the particle reconstruction, being affected by rescattering from the coil, field distortions, and similar effects. Therefore, it is now common practice to accept for the analysis only events inside specific fiducial cuts, i.e. cuts on the kinematic variables (momentum and angles) of each particle. This method guarantees that events accepted in the analysis include only particles detected in "safe" areas of the detector, where the acceptance is thought to be well understood. These cuts are applied to both real events and reconstructed Monte Carlo events.

Fiducial cuts for negatively charged particles

In CLAS experiments with normal direction of the torus magnetic field, like in the "e1e" experiment, negatively charged particles are inbending, which means that their trajectories are bent in the forward direction. For these particles sector independent, symmetrical, and momentum dependent cuts are applied.

For electron and negative pion candidates the analytical shapes of the fiducial cuts can be found in Ref. [32]. They were taken from the similar analysis [22] of the "e1e" dataset (but off proton target) and carefully adjusted to the data.
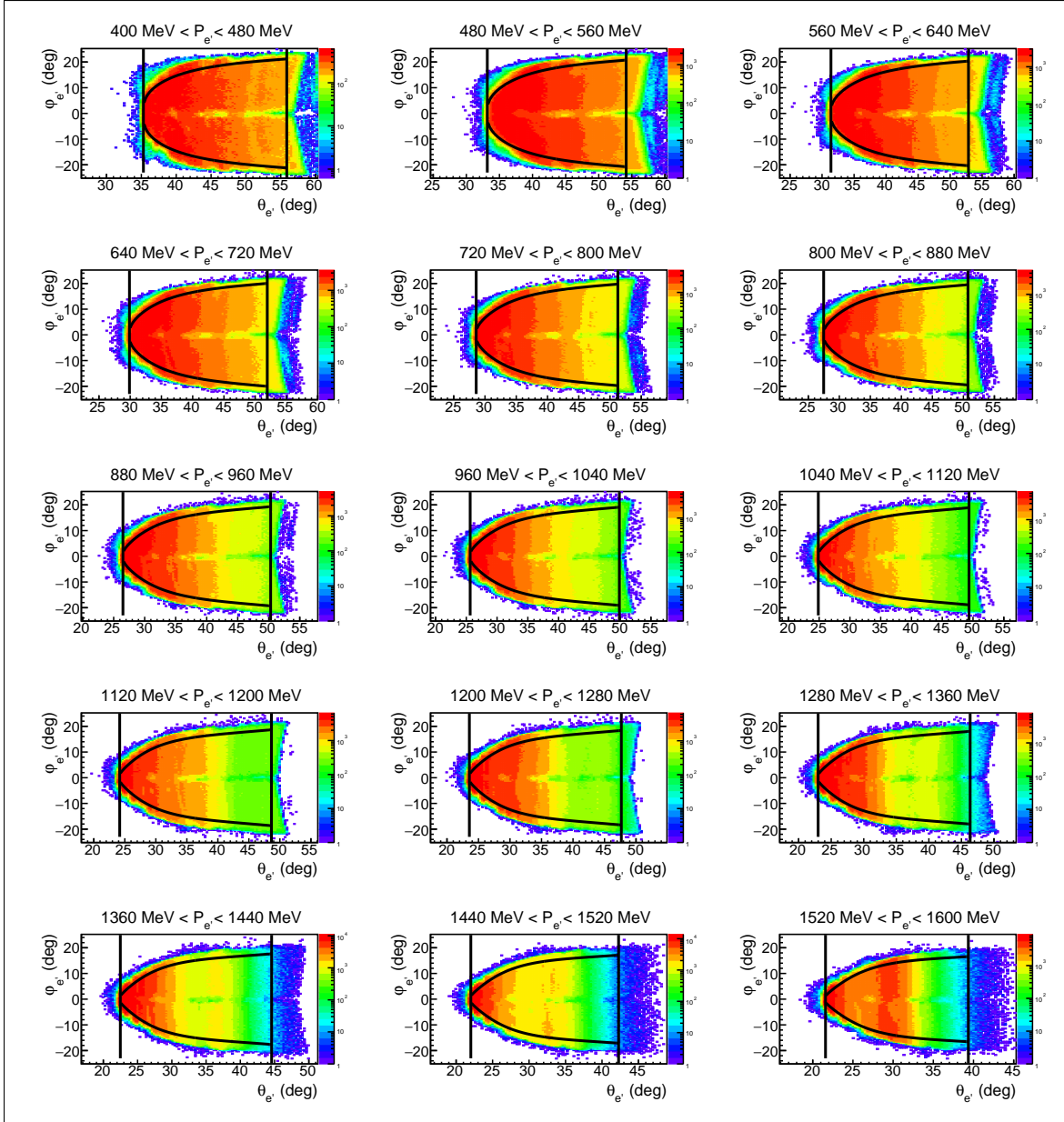
Figure 3.14: φ versus θ distributions for electron candidates for different 80-MeV-wide momentum slices plotted for events from all CLAS sectors. Curves show the applied fiducial cuts, vertical lines stand for $\theta_{e'}^{min}$ and $\theta_{e'}^{max}$. The angles are taken at the interaction vertex. For each momentum slice the shape of the fiducial cut was calculated for the value of the electron momentum taken in the center of the momentum bin.
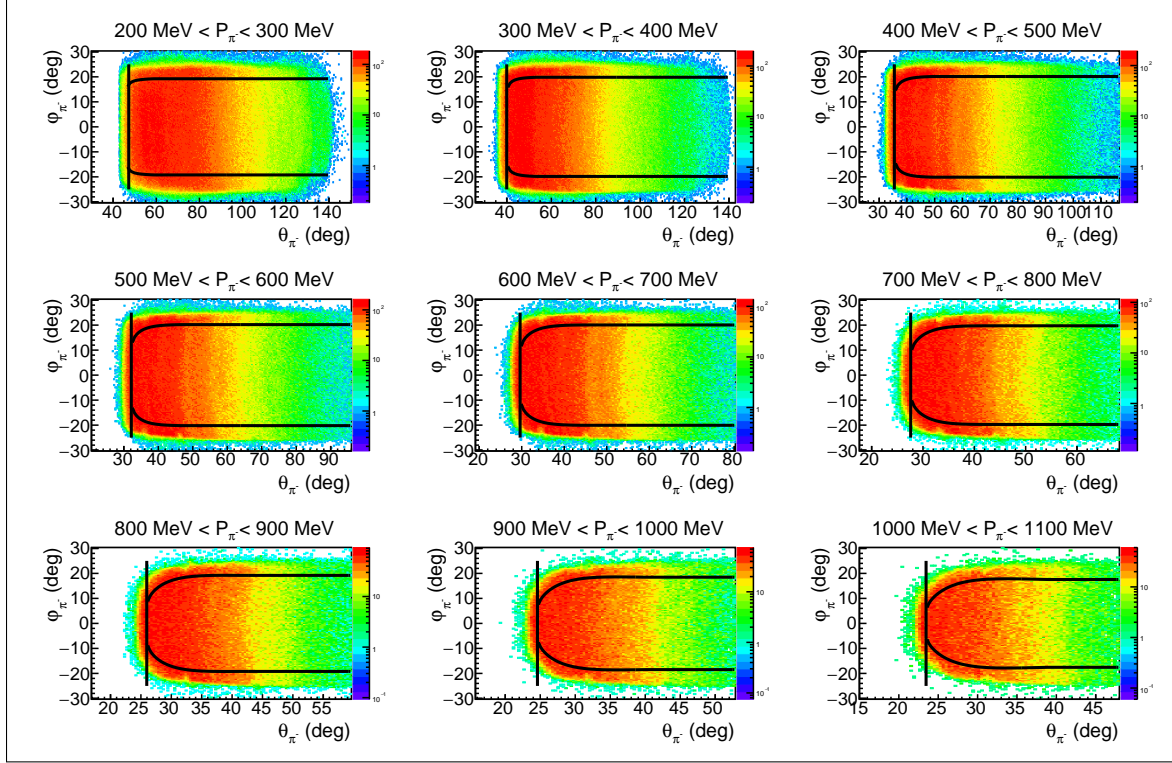
Figure 3.15: φ versus θ distributions for negative pion candidates for different 100-MeV-wide momentum slices plotted for events from all CLAS sectors. Curves show the applied fiducial cuts, vertical lines stand for θ_π^{min} and θ_π^{max}. The angles are taken at the interaction vertex. For each momentum slice the shape of the fiducial cut was calculated for the value of the pion momentum taken in the center of the momentum bin.

The fiducial cut for electron candidates is illustrated in Fig. 3.14, where the cut curves are superimposed on the φ versus θ distributions for different 80-MeV-wide momentum slices. Vertical lines correspond to $\theta_{e'}^{min}$ and $\theta_{e'}^{max}$. For each momentum slice the shape of the fiducial cut was calculated for the value of the electron momentum taken in the center of the momentum bin. The depleted area around $\varphi_{e'} = 0$ corresponds to the inefficient region in CC and was discussed above in Sect. 3.1.2.

The fiducial cut for negative pion candidates is illustrated in Fig. 3.15, where the cut curves are superimposed on the φ versus θ distributions for different 100-MeV-wide momentum slices. Vertical lines correspond to θ_π^{min} and θ_π^{max}. For

each momentum slice the shape of the fiducial cut was calculated for the value of the pion momentum taken in the center of the momentum bin.

The same fiducial cuts for negatively charged particles are also applied to the reconstructed Monte Carlo events.
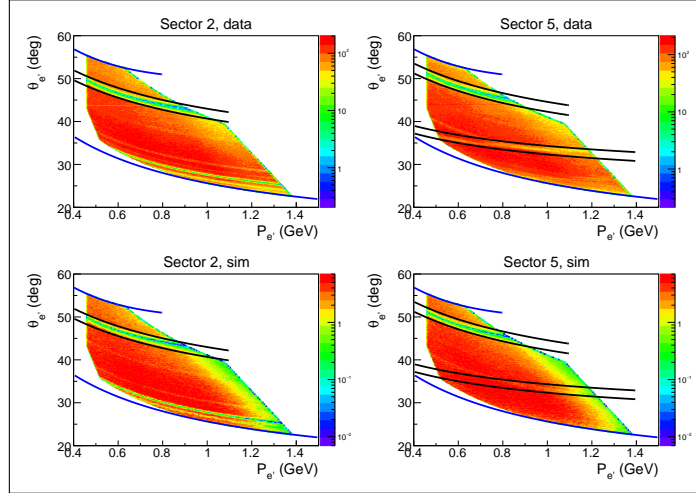
Figure 3.16: θ versus momentum distributions for electron candidates for CLAS sectors two (left side) and five (right side). The angle θ is taken at the interaction vertex. Top row corresponds to the data, bottom row corresponds to the reconstructed Monte Carlo events. Blue curves correspond to $\theta_{e'}^{min}$ and $\theta_{e'}^{max}$. Black curves correspond to additional fiducial θ versus momentum cuts. These distributions are plotted under the conditions 1.3 GeV $< W < 1.825$ GeV and 0.4 GeV$^2 < Q^2 < 1.0$ GeV^2 which account for the extra cuts of the distribution edges. Other small inefficiencies that are seen in these plots are due to the geometrical cut in the CC plane (see Sect. 3.1.2).

There are some additional dead areas in CLAS acceptance that are not related to the gaps between the sectors and limitations on the detection polar angle. They are typically caused by some inefficiencies in the Drift Chambers and Time-of-Flight system (dead wires or PMTs). Some of them are well reproduced in the Monte Carlo simulation, while others are not. To exclude the latter from the analysis and to eliminate events near the acceptance edges, additional fiducial cuts on θ versus momentum distributions are applied. These cuts are individual for each CLAS sector. They are shown by the black curves for real and Monte Carlo events in Fig. 3.16 for electron candidates and in Fig. 3.17 for negative pion candidates.
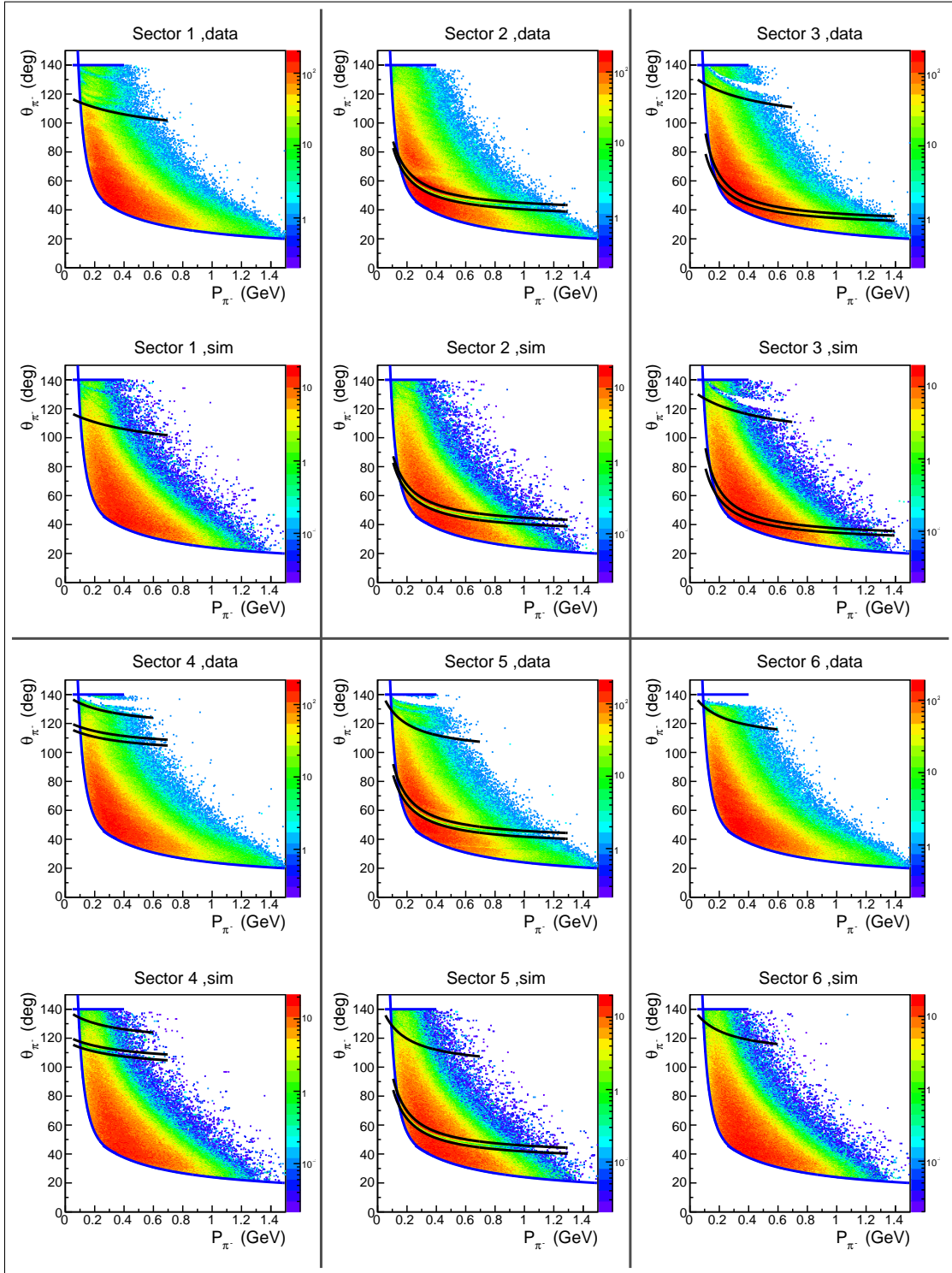
Figure 3.17: θ versus momentum distributions for negative pion candidates for different CLAS sectors. The angle θ is taken at the interaction vertex. Plots are given both for real data and reconstructed Monte Carlo events. Blue curves correspond to θ_π^{min} and θ_π^{max}. Black curves correspond to additional fiducial θ versus momentum cuts.

For the electron distributions shown in Fig. 3.16 inefficient areas in sectors two and five correspond to bad TOF paddles #16 and #17, respectively. Other small inefficiencies that are seen in these plots are due to the geometrical cut in the CC plane (see Sect. 3.1.2), they are almost identical for data and Monte Carlo events and, therefore, no additional fiducial cuts are needed for them. θ versus momentum distributions for electron candidates in other sectors do not show significant inefficiencies.

Fiducial cuts for positively charged particles

For positively charged particles, which are outbending in the "e1e" experiment, momentum independent and symmetrical fiducial cuts suit our purpose best. The analytical shapes of these cuts can be found in Ref. [32]. They were also taken from the analysis [22] and carefully adjusted to the data.

Fiducial cuts for positive hadron candidates are illustrated in Fig. 3.18, where the cut curves are superimposed on the φ versus θ distributions for protons (left) and pions (right). Vertical lines correspond to θ^{min} and θ^{max}. Additional fiducial cuts in θ versus momentum coordinates are shown in Fig. 3.19 for protons and in Fig. 3.20 for π^+. The same fiducial cuts for positively charged particles are also applied to the reconstructed Monte Carlo events.
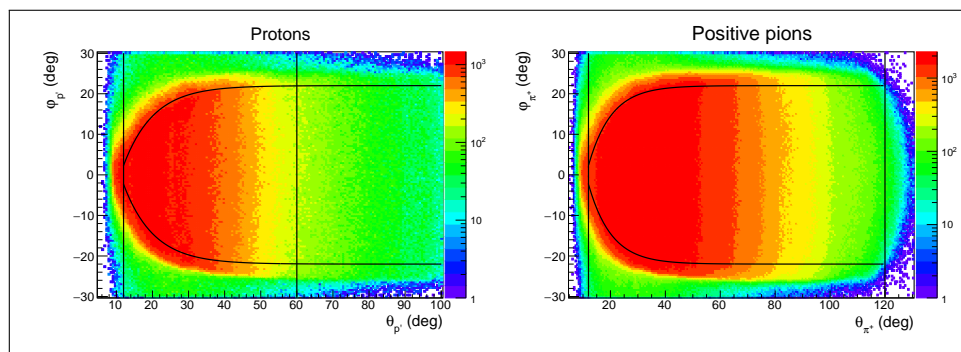
Figure 3.18: φ versus θ distributions for positive hadron candidates: left plot – for protons, right plot – for positive pions. The distributions are plotted for all CLAS sectors. Curves show the applied fiducial cuts, vertical lines stand for θ^{min} and θ^{max}. The angles are taken at the interaction vertex.
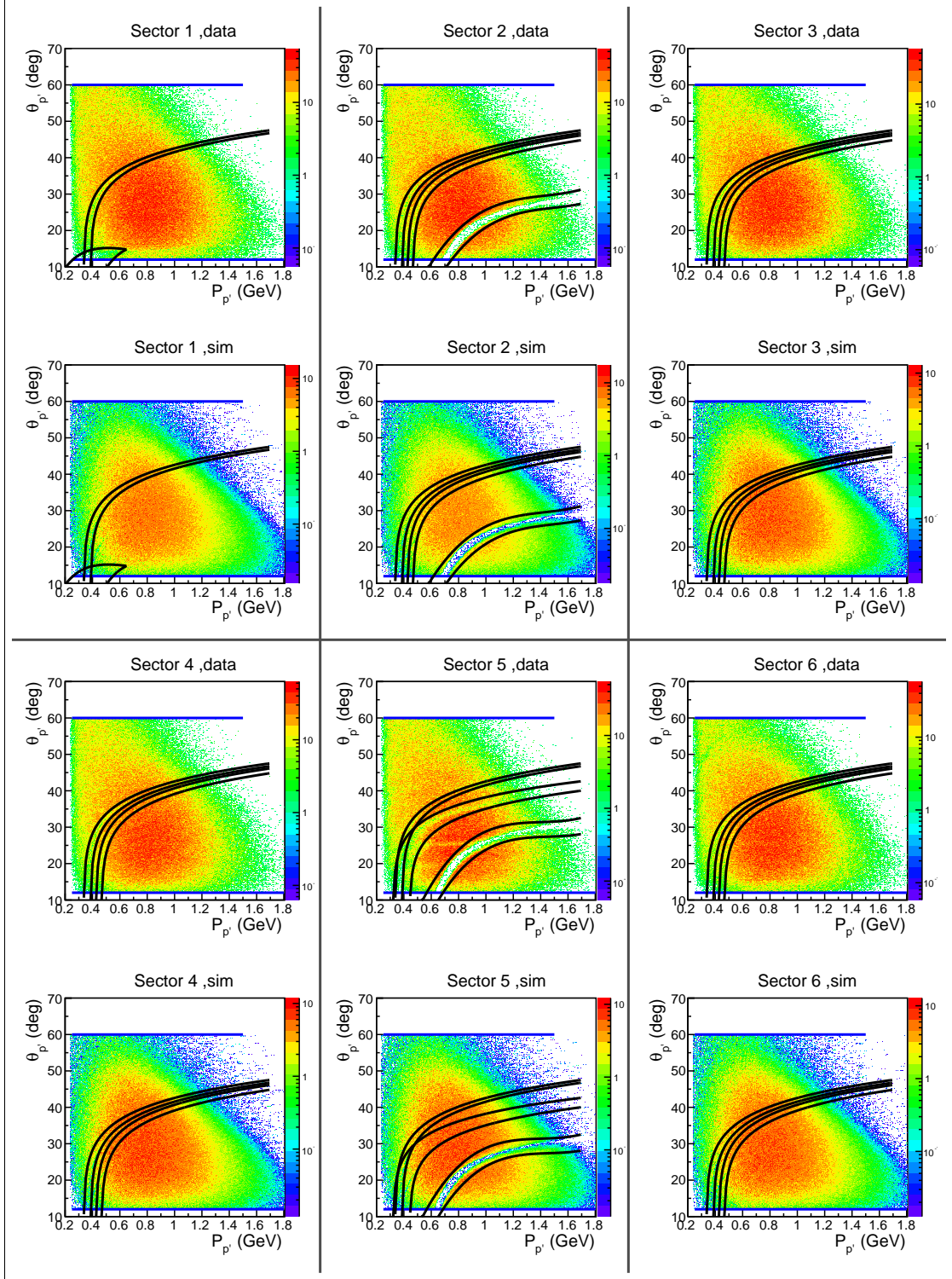
Figure 3.19: θ versus momentum distributions for proton candidates for different CLAS sectors. The angle θ is taken at the interaction vertex. Plots are given both for the real data and reconstructed Monte Carlo events. Blue lines correspond to θ^{min} and θ^{max}. Black curves correspond to additional fiducial θ versus momentum cuts.
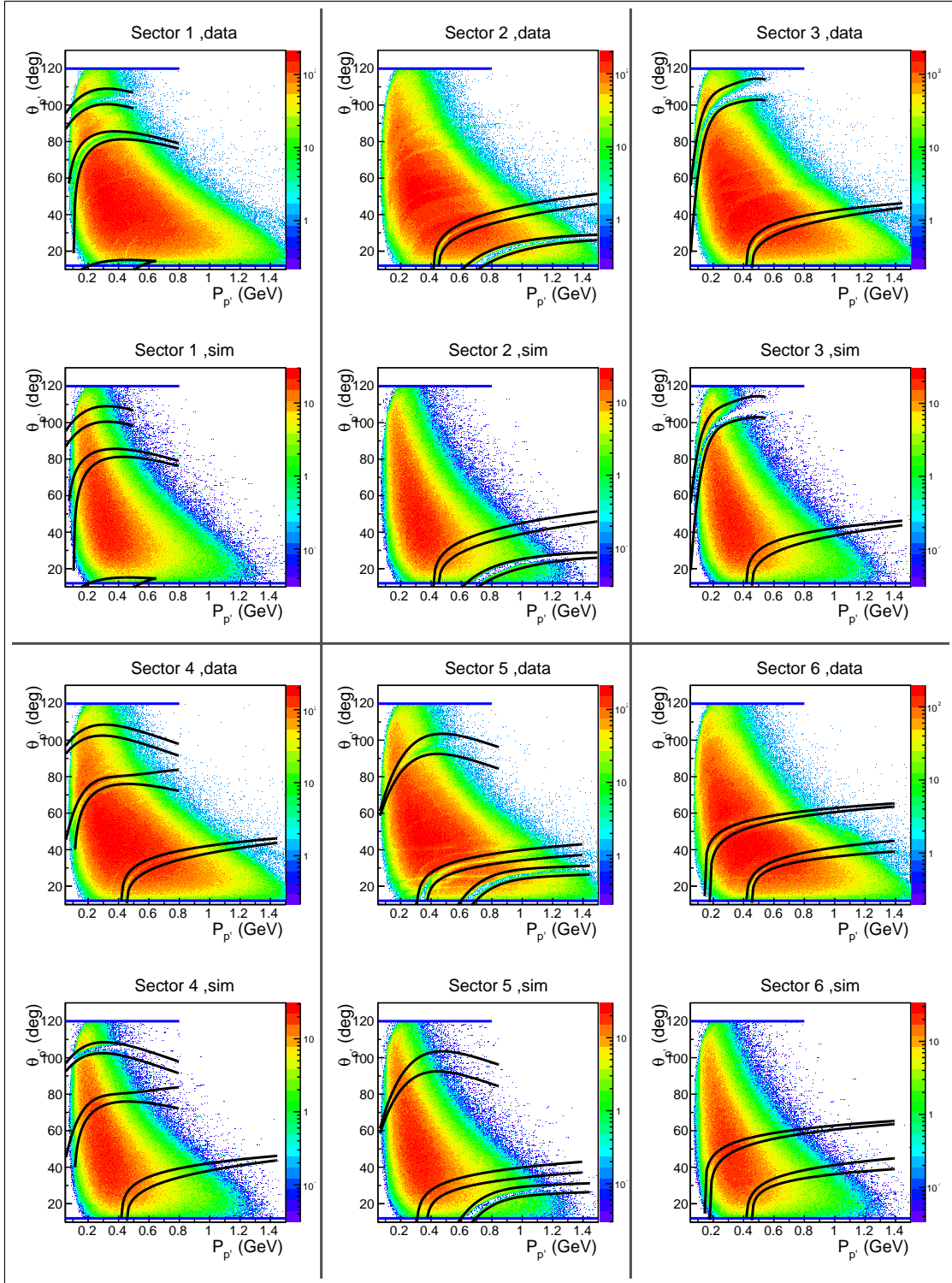
Figure 3.20: θ versus momentum distributions for positive pion candidates for different CLAS sectors. The angle θ is taken at the interaction vertex. Plots are given both for the real data and reconstructed Monte Carlo events. Blue lines correspond to θ^{min} and θ^{max}. Black curves correspond to additional fiducial θ versus momentum cuts.

3.4.2 Data quality check

During a long experimental run, variations of the experimental conditions, e.g. fluctuations in the target density, deviations of the beam current and position as well as changes in the response of parts of the detector, can lead to fluctuations in event yields. Only the parts of the run with relatively stable event rates are selected for the analysis. Therefore, cuts on Data Acquisition (DAQ) live time and number of events per Faraday cup (FC) charge need to be established.
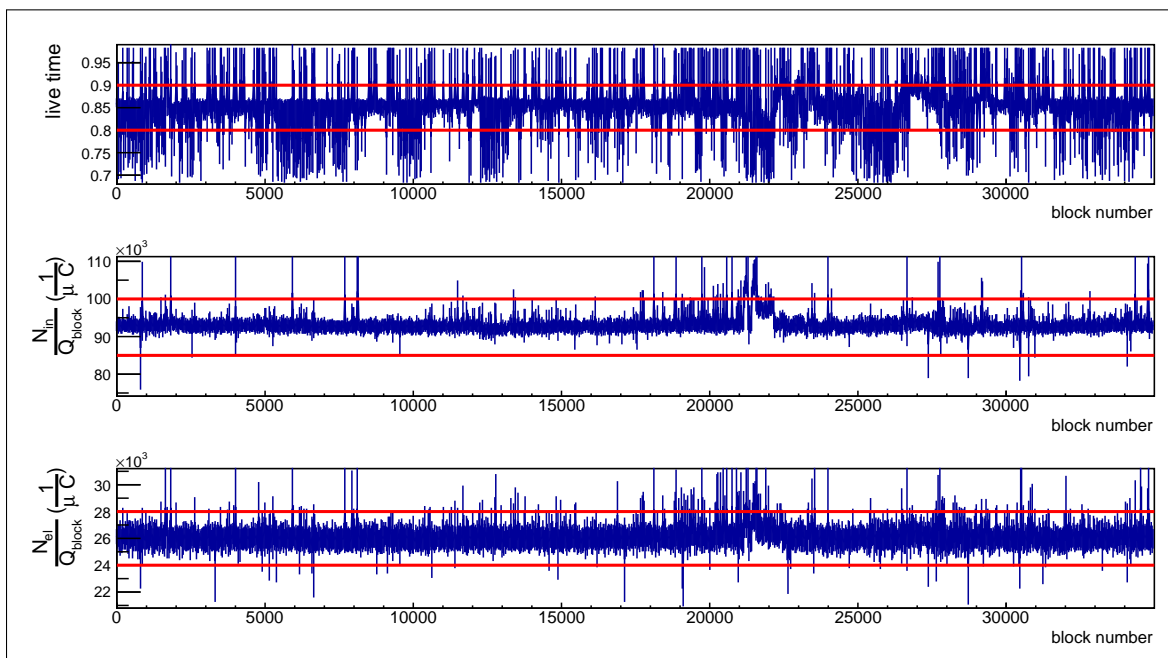
Figure 3.21: In the top plot DAQ live time is shown as a function of *block* number. Each *block* corresponds to the portion of events that is accumulated during a single Faraday cup charge reading cycle. *Block* numbers range from one to the maximum number and represent the run duration in the units of Faraday cup readouts. In the middle plot the number of inclusive events accumulated within each *block* divided by FC charge accumulated during the *block* is plotted versus *block* number. The bottom plot shows the number of elastic events accumulated within each *block* divided by FC charge accumulated during the *block* as a function of *block* number. Horizontal red lines show the applied cuts.

The FC charge updates with a given frequency, so the whole run time can be divided into so-called *blocks*. Each *block* corresponds to the portion of time between two FC charge readouts. FC charge readouts happen approximately once every ten

46

seconds. The *block* number ranges over the run time from one to a certain maximum number. The first and last *blocks* in each run file are excluded from the analysis, since FC readout is not synchronized in time with the start/stop of writing to the file.

The DAQ live time is the portion of time within the *block* during which the DAQ system is able to accumulate events. A significant deviation of the live time from the average value indicates event rate alteration. For instance, if the live time is close to one, then the event rate is too low and vice versa. In Fig. 3.21 the DAQ live time (top plot) as well as the yields of inclusive (middle plot) and elastic (bottom plot) events normalized to FC charge are shown as a function of *block* number. *Blocks* between the horizontal red lines in Fig. 3.21 are selected for the analysis. Due to the enormous amount of *blocks* all of them cannot be made visible in two-dimensional histograms, therefore, to have a general feeling of what amount of blocks are removed, the *y*-axis projections of the histograms in Fig. 3.21 are given in Fig. 3.22. The horizontal red cut lines in Fig. 3.21 correspond to the vertical red cut lines in Fig. 3.22.
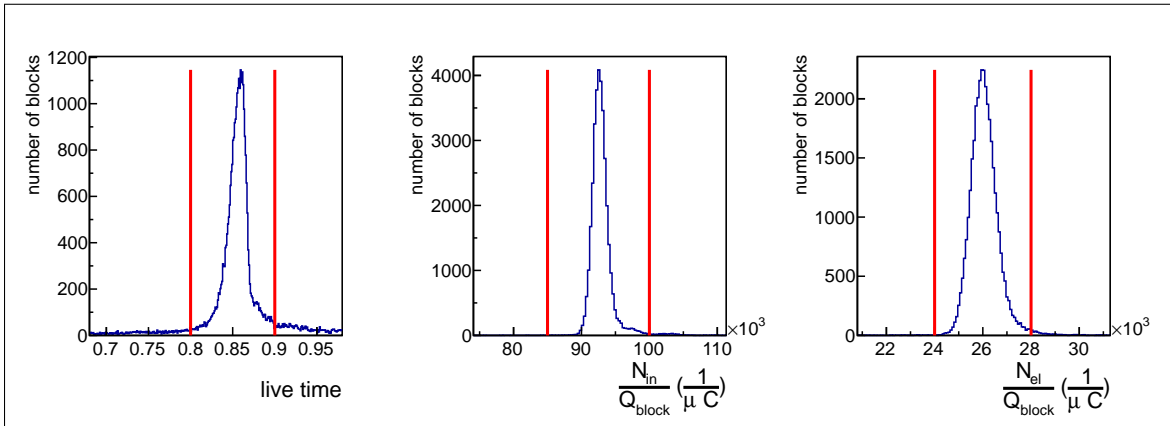
Figure 3.22: Number of *block* occurrences (see explanation in the text) as a function of DAQ live time (left plot), inclusive event yield normalized to FC charge (middle plot), and elastic event yield normalized to FC charge (right plot). The vertical red cut lines correspond to the horizontal red cut lines in Fig. 3.21.

3.4.3 Vertex cut

In Fig. 3.23 distributions of electron z-coordinate at the interaction vertex are shown for events from both empty and full target runs for all six CLAS sectors. The vertical red lines show the cut that is applied in addition to the empty target event subtraction. The vertical dashed line marks the position $z = -0.4$ cm, where the center of the target is expected to be. However, as seen in Fig. 3.23, the $z_{e'}$ distributions demonstrate small sector dependent deviations from their expected position. The source of these deviations is an offset of the beam position from the CLAS central line $(x, y) = (0, 0)$.
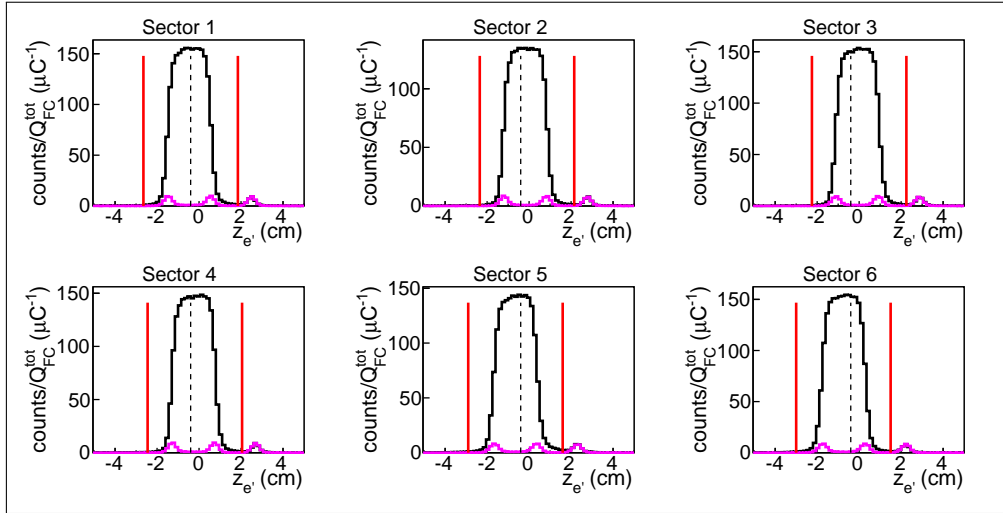
Figure 3.23: Distributions of the electron z-coordinate at the vertex for full (black curves) and empty (magenta curves) target runs for the six CLAS sectors. Vertical dashed lines mark the position $z = -0.4$ cm, where the center of the target is expected to be. Vertical red lines show the applied cuts. Both full and empty target distributions are normalized to the corresponding FC charge.

To estimate the beam offset, the $y_{e'}^{dc}$ versus $x_{e'}^{dc}$ distribution was investigated, where $x_{e'}^{dc}$ and $y_{e'}^{dc}$ are the corresponding coordinates of an electron at the point of interaction, which are taken from the DCPB bank (variables X_v and Y_v, respectively). This distribution is shown in Fig. 3.24, where the intersections of black dashed and solid red lines indicate the nominal and actual beam positions, respectively. The actual

beam position was found to be $(x, y) = (0.057 \text{ cm}, -0.182 \text{ cm})$. The generated Monte Carlo events were reconstructed taking into account the determined beam offset to improve resemblance to the real data[6].
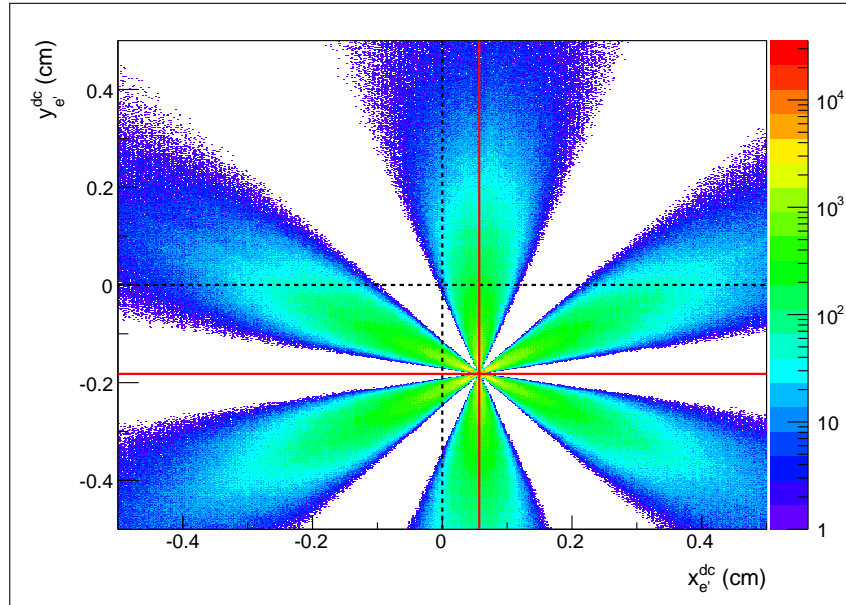
Figure 3.24: $y_{e'}^{dc}$ versus $x_{e'}^{dc}$ distribution that demonstrates the beam offset. Black dashed lines mark the position $(x, y) = (0, 0)$, where the beam is expected to be. Red lines demonstrate the actual beam position at $(x, y) = (0.057 \text{ cm}, -0.182 \text{ cm})$.

In Fig. 3.25 event distributions after the subtraction of the empty target contribution are shown in comparison with Monte Carlo events reconstructed taking into account the beam offset. As can be seen in this figure the simulation matches the data well enough and almost completely reproduces the sector dependent deviation of the distributions from the nominal position marked by the black dashed lines.

To reduce the number of events in which the final state particles came from different events and/or took part in final state interactions, the following two additional cuts on the particle z-coordinates at the vertex are applied. The first cut is $|z_h + 0.4| < 4.4 \text{ cm}$, where the index h corresponds to the final hadron type (proton, π^+, and π^-). The left side of Fig. 3.26 shows an example of this cut for the case

---

[6] The following option was used in the *ffread card*: POSBEAM 0.057 -0.182.

$h = \pi^+$. The second cut is $|z_i - z_j| < 5$ cm, where the indices i and j $(i \neq j)$ correspond to the final particle type (electron, proton, π^+, and π^-). The right side of Fig. 3.26 shows an example of this cut for the case $i = \pi^-$, $j = \pi^+$. These additional cuts are made rather loose in order to avoid unjustified loss of good events.
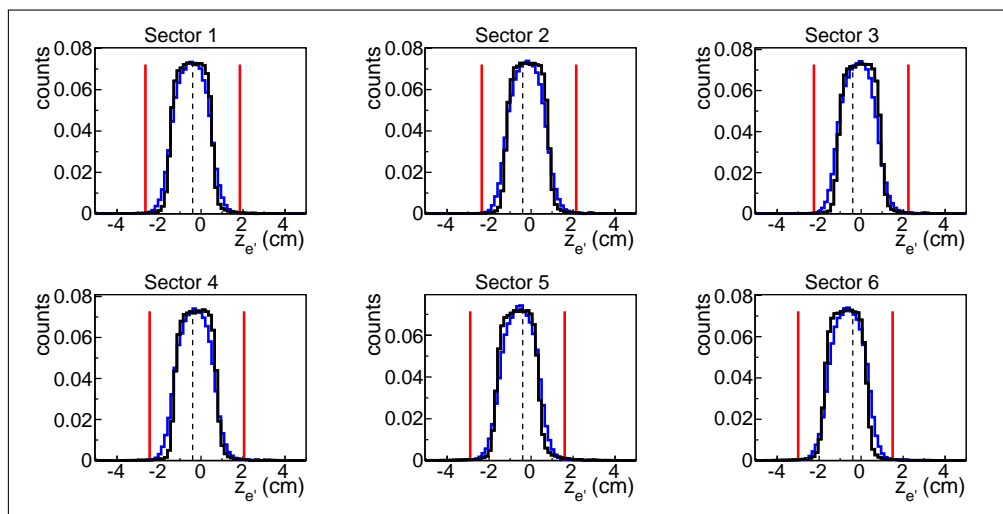
Figure 3.25: Distributions of the electron z-coordinate at the vertex for the experimental data (black curves) and the Monte Carlo events reconstructed taking into account the beam offset (blue curves) for the six CLAS sectors. For the data empty target contributions are subtracted. Vertical dashed lines mark the position $z = -0.4$ cm, where the center of the target is expected to be. Vertical red lines show the applied cuts. All distributions are normalized to the integral.
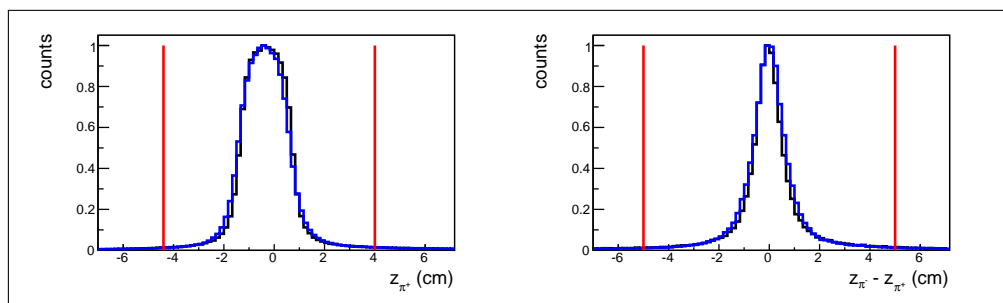
Figure 3.26: Left plot: an example of the cut on the hadron z-coordinate, $|z_{\pi^+} + 0.4| < 4.4$ cm. Right plot: an example of the cut on the difference of the vertex z-coordinates of the final particles, $|z_{\pi^-} - z_{\pi^+}| < 5$ cm. The black curves correspond to the data, while the blue ones correspond to the reconstructed Monte Carlo events. All histograms are normalized to their maxima.

50

3.5 Exclusivity cut in the presence of Fermi smearing and FSI

For picking out certain exclusive reactions one needs to register the scattered electron and either all final hadrons or all except one. In the latter case the four-momentum of the unregistered hadron can be restored using energy-momentum conservation (a so-called "missing mass technique"). Thus for the reaction $ep \to e'p'\pi^+\pi^-$ one can in general distinguish between four so-called "topologies" depending on the specific combination of registered final hadrons. In this particular analysis the following two topologies are analyzed,

- the fully exclusive topology (all final particles registered) $ep \to e'p'\pi^+\pi^- X$, and

- the π^- missing topology $ep \to e'p'\pi^+ X$.

Due to the experimental conditions the statistics of the fully exclusive topology is very limited. This happens mainly because CLAS does not cover the polar angle range $0° < \theta_{lab} < 8°$ [4]. The presence of this forward acceptance hole does not affect much the registration of the positive particles (p and π^+), since their trajectories are bent by the magnetic field away from the hole. Meanwhile, the negative particles (e and π^-) are inbending, which means that their trajectories are bent into the forward direction. Electrons being very light and rapid undergo small track curvature, and the presence of the forward hole leads for them only to a constraint on the minimum achievable Q^2. However, for negative pions the situation is dramatic: being heavier and slower they are bent dominantly into the forward detector hole and, therefore, most of them cannot be registered. This leads to the fact that the π^- missing topology contains the dominant part of the statistics. The contribution of the fully exclusive

topology to the total analyzed statistics[7] varies from $\sim$5% near the reaction threshold to $\sim$25% at $W \sim 1.7 - 1.8$ GeV.

For reactions with multi-particle final states the problem of limited acceptance is an essential issue. Specifically, in the case of the $p\pi^+\pi^-$ final state the cross section depends on five final hadron variables and hence is multi-dimensional, but the limited statistics only allows the extraction of a set of one-fold differential cross sections (see Sects. 4.3 and 4.5). This leads to the necessity to fill kinematic cells with zero acceptance (so-called "empty cells") based on some model assumptions, which leads to model dependent results (see Sect. 5.1). The fully exclusive topology suffers from the problem of limited acceptance (and therefore large amount of empty cells) that along with the problem of limited statistics does not allow any sensible cross section information to be obtained from this topology alone. The π^- missing topology, having significantly fewer empty cells, serves the purpose of the cross section extraction best. The use of both topologies combined allows the model dependence of the cross section (that originates from empty cells filling) to be reduced as well as slightly increasing the statistics.

The aforementioned features of the two topologies are caused by the experimental conditions and valid either for an experiment off the free proton or for one off the proton bound in the deuteron. Meanwhile, there are also some features that appear only in bound proton experiments. Those that are crucial for exclusive event selection are addressed later in this Section, while others are discussed later in the report.

Actually, two more topologies can be distinguished, i.e. the proton missing topology and the π^+ missing topology. Both require registration of the π^- in the final state and as a consequence suffer from the similar problems of suppressed statistics[8] and limited acceptance as in the case of the fully exclusive topology. Therefore, these two topologies are usually ignored in analyses of the reaction $ep \rightarrow e'p'\pi^+\pi^-$ [15–19].

---

[7] The combined statistics of both the π^- missing and the fully exclusive topologies.
[8] Each of them contains about 10% of the full statistics of all four topologies combined.

Nevertheless, as demonstrated in the sophisticated analysis of this reaction off the free proton target [22, 23], they can be used as complimentary topologies to the main π^- missing topology, that allows a slight increase in the statistics and a reduction in the amount of empty cells as much as possible, therefore minimizing the model dependence of the extracted cross sections. However, if the pion pair is produced off the proton bound in the deuteron, additional complications appear: these topologies turn out to be polluted with events from other reaction channels. In the proton missing topology the missing mass technique fails to distinguish whether the pion pair was produced off the proton or off the neutron, because their masses are almost identical. A similar situation occurs for the π^+ missing topology, where the same reason prevents distinguishing between the production of $\pi^+\pi^-$ pair off the proton and $\pi^0\pi^-$ pair off the neutron, if only the proton and the π^- in the final state are registered. Moreover, the event sample in the π^+ missing topology demonstrates strong admixture of events from the reaction $en(p) \to e'p'(p')\pi^-$, which was found to be not very easy to remove.

Taking into account all the above arguments, the following topology ranking takes place in this particular analysis: the π^- topology is the main one and the fully exclusive topology is treated as the complimentary one, which gives a slight increase in statistics as well as some reduction in the amount of empty cells, while the proton missing and the π^+ missing topologies are not used at all.

Meanwhile, an exclusive reaction that happens off bound nucleons has some specific features, which are extrinsic to reactions off free protons. Those of them that are related to the problem of the channel identification are listed below.

- The Fermi motion of the target proton.

- Complex effects of Final State Interactions (FSI) due to the presence of the neutron and the multi-particle final state.

The manifestations of these effects in the π^- missing and fully exclusive topologies differ.

Motion of the target proton within the deuterium nucleus is concealed from the observer and is not measured[9]. However, if all particles in the final state are registered, one can restore the information about the momentum distribution of the target proton via energy-momentum conservation (see Sect. 3.5.1 for details). This is not the case for the π^- missing topology, where incomplete knowledge about the final state leads to the fact that information about the motion of the initial proton turns out to be totally lost. Therefore, one is forced to work under a so-called "target-at-rest-assumption" that considers the target proton to have no motion and as a consequence inevitably leads to the smearing of various kinematic quantities, such as missing mass, reaction invariant mass (W), etc [38]. Although the fully exclusive topology has the advantage of the possibility of avoiding the smearing[10], all kinematic quantities are nevertheless calculated under the target-at-rest-assumption in order to treat this complimentary topology in the same way as the main one.

In order to reliably identify the exclusive channel and correctly calculate the detector efficiency, the distributions of the reconstructed Monte Carlo events must match experimental ones as well as possible. As mentioned above, the necessity to work under the target-at-rest-assumption smears the experimental distributions, which in turn demands the simulated distributions reproduce this smearing. Therefore, the effects of the target motion should be properly included in the Monte Carlo simulation.

That is why the event generator TWOPEG-D [24] was used to perform the Monte Carlo simulation. It is a version of the TWOPEG (event generator for double-pion electroproduction off the free proton [39]) that was developed for this analysis in

---

[9] In general it can be measured by detecting the recoil nucleon (neutron in this case), but it was not an option in this experiment.

[10] For example, in the fully exclusive topology the value of W, being calculated using the four-momenta of the registered final hadrons, turns out to be determined within the detector resolution and not affected by the effects of the target motion.

order to simulate the effects of the target motion. In this version of the event generator the Fermi motion of the initial proton is generated according to the Bonn potential [40] and then naturally merged into the specific kinematics of double-pion electroproduction.

The second intrinsic feature of an exclusive reaction off bound nucleons is complex effects of FSI. This phenomenon is driven by the strong interaction and consists in the fact that after the production of the final state hadrons and before their registration they manage to interact with each other and/or the recoil nucleon.

Final hadrons produced off free protons are subject to FSI as well, but they are limited to interactions of the hadrons with each other, which are not substantial. Meanwhile, for reactions off protons in deuterium, the presence of spectator neutrons changes the situation drastically as the final hadrons can impact the neutron. As a result, FSI effects in such reactions are rather strong.

Events, in which all final hadrons manage to avoid FSI, belong to a so-called "quasi-free regime". Meanwhile, events with FSI-affected hadrons are attributed to so-called "FSI-disturbed kinematics" because FSI alter the final hadron momenta. Events in FSI-disturbed kinematics introduce distortions into distributions of various kinematic quantities, such as missing masses, thus complicating the identification of a desired exclusive channel.

The main goal of this study is to extract the double-pion cross sections in the quasi-free regime, which implies the need to select for the analysis only events in quasi-free kinematics and to get rid of events with FSI. The latter, however, also deserve attention as FSI effects represent an essential issue in studies of any exclusive reaction, especially off nuclei. Therefore, to balance the analysis, Chapter 9 of the thesis is fully devoted to the examination of features and manifestations of FSI-affected events.

In contrast to the effects of the target motion, which can be simulated fairly easy, the effects of FSI can hardly be taken into account in the simulation because they

are of very complex nature and hence not yet fully understood. Therefore, the Monte Carlo simulation is not able to reproduce the distortions due to FSI that occur in some experimental distributions, but this is not a problem if events in quasi-free kinematics are properly separated from those in FSI-disturbed kinematics. This leads to the necessity to develop special procedures of selecting quasi-free events as well as correcting for the remaining admixture of undesired events, if they cannot be fully eliminated.

The yield of events in FSI-disturbed kinematics turned out to strongly depend on (i) the reaction invariant mass (W) and (ii) on the hadron scattering angles. The latter issue causes FSI effects to manifest themselves differently depending on the reaction topology, since the topologies have non-identical geometrical acceptance.

As follows from the above, the two analyzed topologies differ from each other both in treating of the Fermi motion of the initial proton and in FSI manifestations. Therefore, the channel identification is performed in each topology individually (see subsequent subsections).

The problem of background channels is also an issue that deserves special attention. For the reaction of double-pion production off free protons, the main background channel is $ep \rightarrow e'p'\pi^+\pi^-\pi^0$. In the analysis [22] that was carried out for the same beam energy $E_{beam} = 2.039$ GeV, it is shown that although the admixture of the events from this background channel becomes discernible at $W \gtrsim 1.6$ GeV, it remains negligible and well separated from the double-pion events via the exclusivity cuts. For the experiments with the deuteron target, the reaction $en(p) \rightarrow e'p'(p')\pi^+\pi^-\pi^-$ can also act as a background channel for the investigated $ep(n) \rightarrow e'p'(n')\pi^+\pi^-$ reaction, however it is also expected to give an insignificant and well separated admixture. Here and hereinafter the term "background channel" is used to denote the reaction that happened in electron scattering off the target nucleon along with the investigated double-pion reaction. Any reaction that might occur during the FSI is not treated as the contribution from "background channels", but is attributed to the FSI-background.

3.5.1 Fully exclusive topology

In the fully exclusive topology for the selection of double-pion events in quasi-free kinematics the distributions of the following quantities were investigated: the missing momentum P_X and the missing mass squared $M^2_{X[0]}$ for the reaction $ep(n) \to e'p'(n')\pi^+\pi^-X$ as well as the missing mass squared $M^2_{X[\pi^-]}$ for the reaction $ep(n) \to e'p'(n')\pi^+X$. These quantities are defined by

$$
\begin{aligned}
P_X \quad &= |\vec{P}_e - \vec{P}_{e'} - \vec{P}_{p'} - \vec{P}_{\pi^+} - \vec{P}_{\pi^-}|, \\
M^2_{X[0]} \quad &= [P^\mu_e + P^\mu_p - P^\mu_{e'} - P^\mu_{p'} - P^\mu_{\pi^+} - P^\mu_{\pi^-}]^2, \\
M^2_{X[\pi^-]} \quad &= [P^\mu_{\pi^- \; miss}]^2 = [P^\mu_e + P^\mu_p - P^\mu_{e'} - P^\mu_{p'} - P^\mu_{\pi^+}]^2,
\end{aligned}
\tag{3.5.1}
$$

where P^μ_i are the four-momenta and $\vec{P}_i$ the three-momenta of the particle i. All three quantities are calculated under the target-at-rest-assumption, i.e. considering $P^\mu_p = (0, \ 0, \ 0, \ m_p)$, where m_p is the proton mass.

The quantities P_X and $M^2_{X[0]}$ are unique for the fully exclusive topology as they can be calculated only if all final hadrons are registered. Although adding the quantity $M^2_{X[\pi^-]}$ to this set does not seem to provide any additional information, it is examined in order to observe consistency with the π^- missing topology, where the distributions of $M^2_{X[\pi^-]}$ is the only source for developing a criterion for the channel identification. See Ref. [41] for details on features of missing mass distributions.

Distributions of the quantities P_X (first column), $M^2_{X[0]}$ (second column), and $M^2_{X[\pi^-]}$ (third column) for five 100-MeV-wide bins[11] in W are shown in Fig. 3.27 for the experimental data (black curves) and reconstructed Monte Carlo events (blue curves).

The quantity P_X (first column in Fig. 3.27) is the missing momentum of the initial proton calculated under the target-at-rest-assumption, therefore the blue curves stand for the Fermi momentum (simulated according to Bonn potential [40]) convoluted with the detector resolution, whereas the black ones correspond to

---

[11] The value of W is calculated for the initial state under the target-at-rest-assumption.
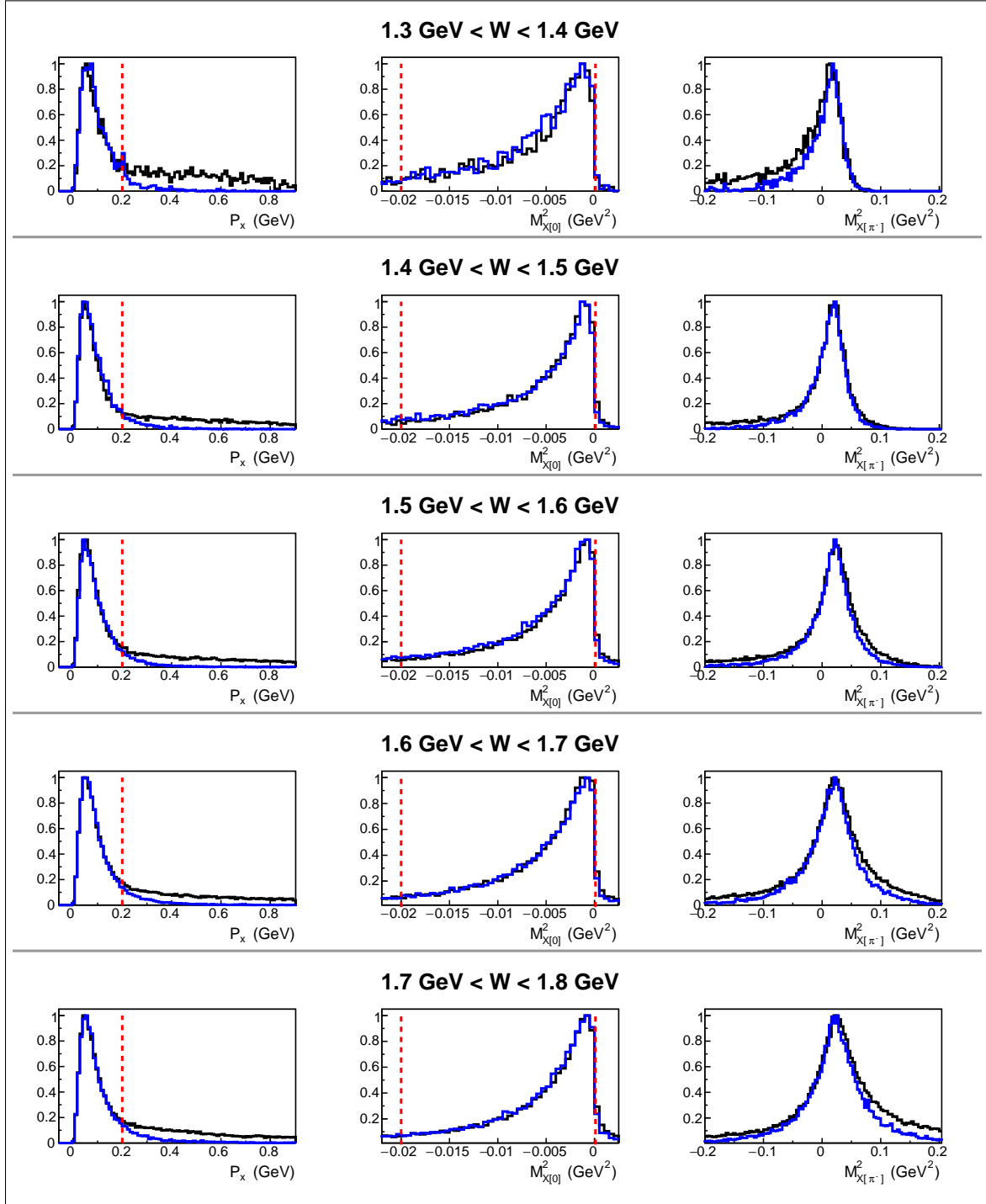
Figure 3.27: Distributions of the quantities P_X (left column), $M^2_{X[0]}$ (middle column), and $M^2_{X[\pi^-]}$ (right column) defined in Eq. (3.5.1) for experimental data (black curves) and Monte Carlo simulation (blue curves) for different 100-MeV-wide W bins. Vertical red lines indicate the cuts applied for the selection of exclusive quasi-free events. All plotted quantities as well as the values of W are calculated under the target-at-rest-assumption. All distributions are normalized to their maxima.

the experimental momentum of the initial proton, mixed with the FSI effects, contributions from background channels, and the detector resolution. As seen in the left column of Fig. 3.27, the simulated distributions perfectly match the experimental ones for $P_x < 0.2$ GeV, while for $P_x > 0.2$ GeV the simulation underestimates data. Such behavior is mostly related to the fact that relative contributions from FSI, which were not included into the Monte Carlo simulation, turn out to be the most significant outside of the peak region. The background channels, being not included into the Monte Carlo as well, also contribute to this mismatch, but as mentioned above their contribution is minor. The value $P_x = 0.2$ GeV (marked by the red dashed lines in each plot in the left column) was chosen as a criterion for the selection of events in quasi-free kinematics. Thus, experimental events located at the left side of this line correspond to the reaction in the quasi-free regime, while events at the right side correspond mostly to "disturbed" kinematics with great impact of FSI.

The distributions of the quantity $M^2_{X[0]}$ shown in the middle column in Fig. 3.27 deserve more attention. As demonstrated in Refs. [22, 23, 41], in free proton experiments this quantity forms a very narrow peak at zero position barely affected either by radiative effects or by detector resolution. An admixture from the three-pion background, if present in the analyzed event sample, forms then an additional peaked structure at m^2_π well-separated from the main distribution peak. Meanwhile, in this analysis, $M^2_{X[0]}$, being calculated under the target-at-rest-assumption, loses its thinness and acquires the smearing (mostly left-sided), which is well-reproduced by the Monte Carlo simulation.

In order to clean up the sample of exclusive events, the cut on the missing mass squared $M^2_{X[0]}$ was also applied as a complementary to the cut on the missing momentum. This cut is shown in Fig. 3.27 (middle column) by the vertical red dashed lines. The plots in the middle column are zoomed near the peak to demonstrate good agreement between the data and the simulation within the cut limits. The behavior

of $M_{X[0]}^2$ in a wider range is shown in Fig. 3.28, where the distributions are zoomed in on small y. As seen, outside the cut boundaries there is a mismatch between the data and simulation, which originates from FSI effects at the left and the contribution from the three-pion background at the right. The latter forms a peaked structure around m_π^2 ($\sim$0.02 GeV^2), which is more smeared compared to the free proton case due to the target-at-rest-assumption and FSI disturbances. The example is given for high W to observe the greatest background admixture over the investigated W range.
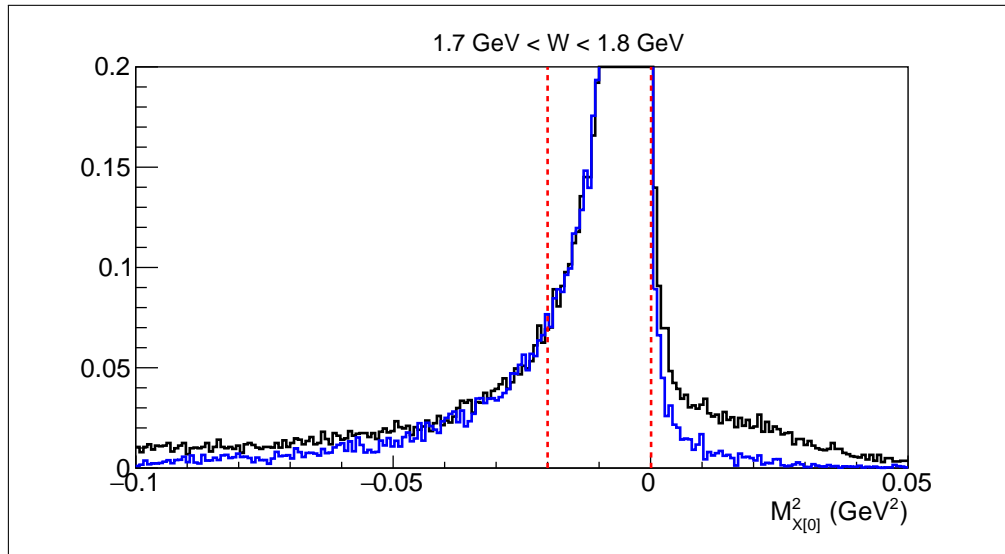
Figure 3.28: Distributions of the quantity $M_{X[0]}^2$ for experimental data (black curves) and Monte Carlo simulation (blue curves) zoomed in on small y. Vertical red lines indicate the applied cut. The mismatch between data and simulation originates from FSI effects at the left and three-pion background at the right. The example is given for 1.7 GeV $< W <$ 1.8 GeV, where the latter is greatest over the whole W range. The agreement between data and simulation within the cut boundaries is better shown in Fig. 3.27 (middle column).

The three-pion background in this topology is thus considered to be fully eliminated by the described above cuts on the quantities P_X and $M_{X[0]}^2$.

Meanwhile, the right column in Fig. 3.27 stands for the missing mass squared $M_{X[\pi^-]}^2$ defined by Eq. (3.5.1) under the target-at-rest-assumption, thus being Fermi smeared. The observed mismatch between the measured and simulated distributions is W-dependent and caused mostly by the FSI effects.
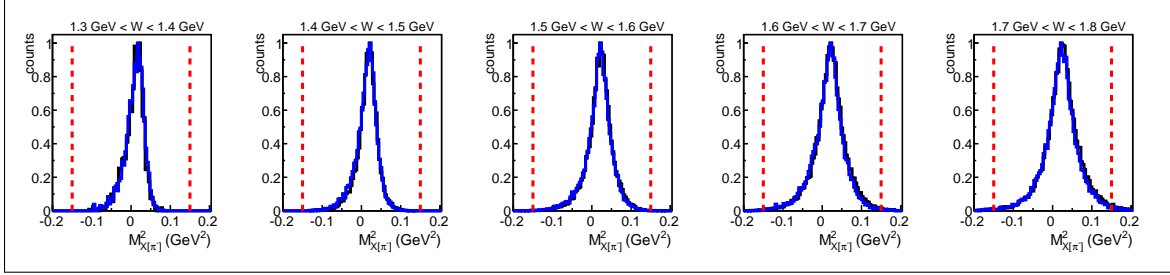
Figure 3.29: Distributions of the missing mass squared $M^2_{X[\pi^-]}$ defined in Eq. (3.5.1) for the fully exclusive topology plotted for selected quasi-free exclusive events for experimental data (black curves) and Monte Carlo simulation (blue curves). The comparison is shown for different 100-MeV-wide W bins. The quantity $M^2_{X[\pi^-]}$ as well as the values of W are calculated under the target-at-rest-assumption. The vertical red lines show the applied cuts. All distributions are normalized to their maxima. See text for details.

Figure 3.29 shows the distributions of the quantity $M^2_{X[\pi^-]}$ plotted for quasi-free exclusive events selected by the cuts on P_x and $M^2_{X[0]}$. The distributions for the experimental (black curves) and reconstructed Monte Carlo (blue curves) events perfectly match each other in all W subranges, which demonstrates the reliability of quasi-free exclusive event selection as well as the fact that effects of the target motion are correctly implemented into the simulation. The vertical red lines in Fig. 3.29 correspond to the additional cut that was applied on the missing mass squared $M^2_{X[\pi^-]}$.

Although in the fully exclusive topology the four-momentum of the π^- is measured precisely within the detector resolution, it is not used in the subsequent calculation of kinematic variables for the cross section extraction. The measured four-momentum is instead replaced by the one that is calculated as missing ($P^\mu_{\pi^-\ miss}$ in Eq. (3.5.1)) and thus is Fermi smeared. This is done to imitate the event selection in the main π^- missing topology in order to treat events in both topologies identically.

3.5.2 π^- missing topology

In the π^- missing topology the quantities P_X and $M^2_{X[0]}$ defined in Eq. (3.5.1) are not available due to the incomplete knowledge about the final state, and $M^2_{X[\pi^-]}$ is the only remaining quantity suitable for the selection of exclusive events in quasi-free kinematics. The distributions of this quantity are shown in Fig. 3.30 for five 100-MeV-wide bins in W for the experimental data (black curves) and the Monte Carlo simulation (blue curves). The comparison shown in this figure demonstrates again the W-dependent mismatch between data and simulation, which is different from that seen in the fully exclusive topology. The mismatch is mostly observed at the right side of the distribution peak and becomes discernible only for $W \gtrsim 1.5$ GeV.
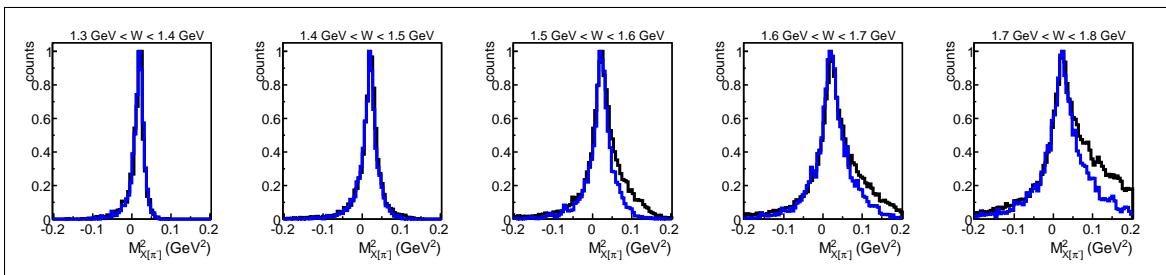
Figure 3.30: Distributions of the missing mass squared $M^2_{X[\pi^-]}$ defined in Eq. (3.5.1) for the π^- missing topology plotted before the selection of quasi-free exclusive events for experimental data (black curves) and Monte Carlo simulation (blue curves). The comparison is shown for different 100-MeV-wide W bins. The quantity $M^2_{X[\pi^-]}$ as well as the values of W are calculated under the target-at-rest-assumption. All distributions are normalized to their maxima. See text for details.

The similar analysis [22] carried out for the same beam energy but off a free proton target did not reveal any substantial discrepancies between the experimental and simulated distributions of the quantity $M^2_{X[\pi^-]}$; they are shown to be in a very good agreement for all W values. Figure 3.29 plotted for selected exclusive quasi-free events in the fully exclusive topology in turn proves that the Monte Carlo simulation incorporates effects of the target motion correctly. Therefore, the discrepancy between

data and simulation observed in Fig. 3.30 is attributed mainly to the FSI effects, which are not included into the simulation.

This mismatch between data and simulation together with the fact that in the π^- missing topology the quantity $M^2_{X[\pi^-]}$ is the only one available for the channel identification makes the task of selecting events in quasi-free kinematic rather challenging. To accomplish this goal, a special procedure was developed. This procedure is described below.

In order to isolate events in quasi-free kinematics, the following quantity is subjected to examination,

$$M_{X[\pi^-]} = \sqrt{|M^2_{X[\pi^-]}|} = \sqrt{|[P^\mu_{\pi^-\ miss}]^2|} = \sqrt{|[P^\mu_e + P^\mu_p - P^\mu_{e'} - P^\mu_{p'} - P^\mu_{\pi^+}]^2|}. \quad (3.5.2)$$

The distributions of the quantity $M_{X[\pi^-]}$ in different 25-MeV-wide W bins are shown in Fig. 3.31 for experimental data (black histograms) and for Monte Carlo simulation (blue histograms). Both are normalized to their maxima. The mismatch between data and simulation becomes discernible at $W \approx 1.5$ GeV, increases as W grows and becomes large at $W \approx 1.8$ GeV. The magenta histogram stands for the difference between the black and blue histograms and thus represents the distribution of background events originated mainly from FSI effects. The green vertical lines correspond to the position of the cut that is intended to select quasi-free events. This cut is applied to the reconstructed Monte Carlo events as well. However, as seen in Fig. 3.31, one can hardly completely separate the quasi-free event sample from the FSI-background by tightening the cut: in this way the statistics of quasi-free events will be subject to significant reduction, while the background admixture will still not be completely eliminated. Therefore, it was decided to perform a so-called "effective correction" of the FSI-background admixture, which includes the following steps.
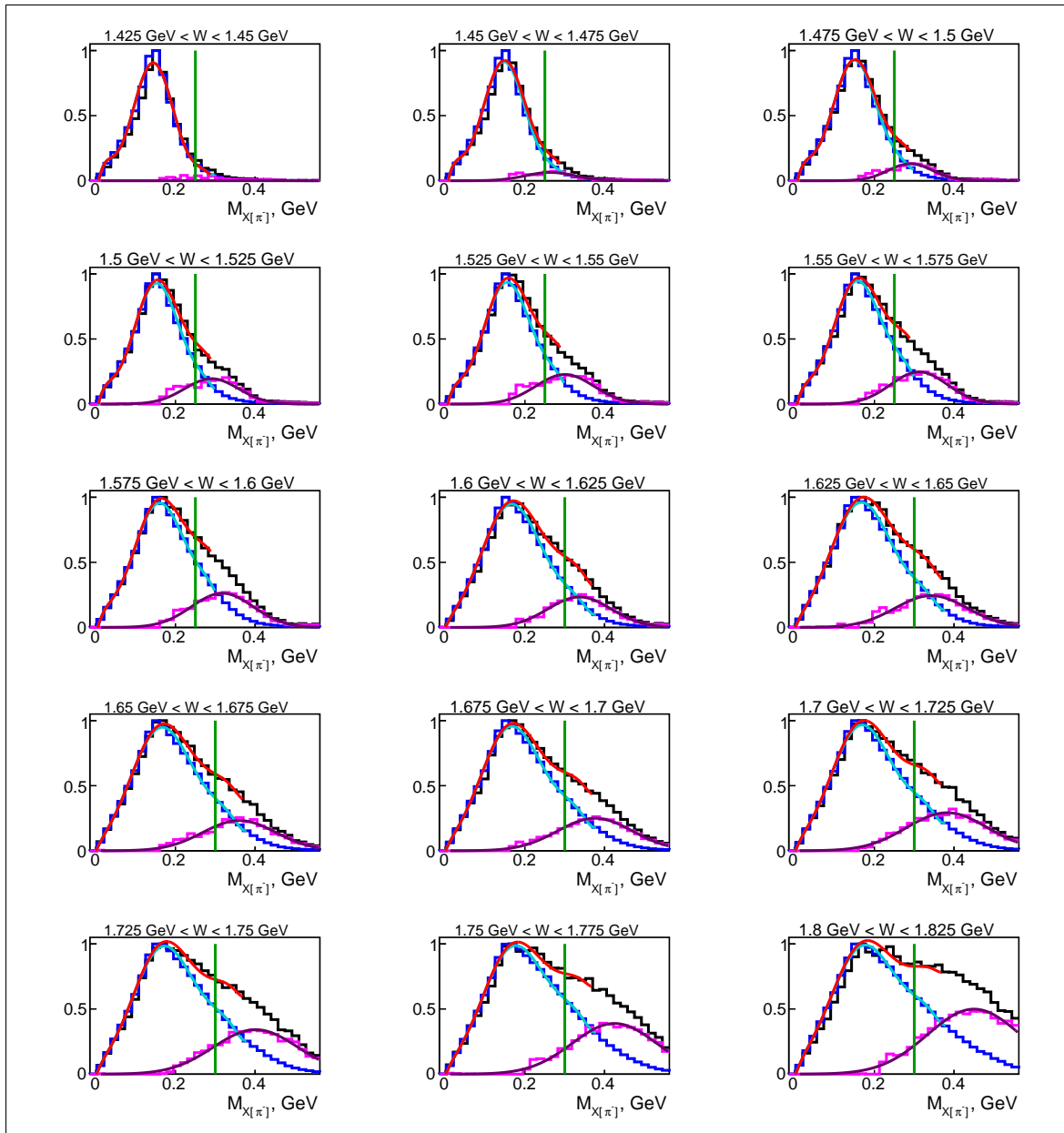
Figure 3.31: Distributions of the quantity $M_{X[\pi^-]}$ (defined by Eq. (3.5.2)) in different 25-MeV-wide W bins for the experimental data (black histograms), Monte Carlo simulation (blue histograms), and their difference (magenta histograms). The explanation of the fit curves is given in the text. Green vertical lines correspond to the position of the cut that is intended to select quasi-free events. The cut is applied to the reconstructed Monte Carlo events as well.

- The distributions of $M_{X[\pi^-]}$ for the reconstructed Monte Carlo events (blue histograms) were fit by a ninth order polynomial in a slightly wider range than marked by the green cut lines. The results of the fit are shown in Fig. 3.31 by the cyan curves.

- The magenta background distributions were fit by Gaussians. The results of the fit are shown by the dark-magenta curves.

- The cyan and dark-magenta curves were summed up to produce the red curve, which perfectly matches the black experimental histogram in each W bin.

- The correction factor F_{fsi} was determined in the left side of the green cut line,

$$F_{fsi}(W) = \frac{area\ under\ the\ cyan\ curve}{area\ under\ the\ red\ curve} \leq 1. \qquad (3.5.3)$$

- In each W bin the experimental event yield in the π^--missing topology is multiplied by the factor F_{fsi}, which serves as an effective correction due to the remaining admixture of the FSI-background events.

The factor F_{fsi} is assumed to be only W dependent as it was found that it does not demonstrate any Q^2 dependence, and the dependence on the final hadron variables is neglected due to the statistics limitation. The value of F_{fsi} varies from $\sim$0.97 to $\sim$0.93 in the W range from 1.4625 GeV to 1.8125 GeV, while for $W < 1.4625$ GeV $F_{fsi} = 1$ as the correction there is not needed.

Note that the exclusivity cut shown in Fig. 3.31 accompanied by the corresponding correction cares for all other possible effects that along with the FSI effects may contribute to the mismatch between the data and the simulation in this topology (including the three-pion background).

Chapter 4
Cross section calculation

4.1 W-smearing and blurring of the Q^2 versus W distribution boundaries

The smearing of the invariant mass W has the same origin as the smearing of the missing mass, which is already discussed in Sect. 3.5, but since W is the variable needed to describe the reaction (and the extracted cross section is binned in W), the issue of W-smearing requires special attention and, therefore, is separately addressed here.

For the process of double-pion electroproduction off the proton (as for any other exclusive process) the reaction's invariant mass can in general be determined in two ways, i.e. either from the initial particle four-momenta[1] (W_i) or from the final particle four-momenta (W_f) as Eqs. (4.1.1) and (4.1.2) demonstrate.

$$W_i = \sqrt{(P_p^\mu + P_{\gamma_v}^\mu)^2} \tag{4.1.1}$$

$$W_f = \sqrt{(P_{\pi+}^\mu + P_{\pi-}^\mu + P_{p'}^\mu)^2} \tag{4.1.2}$$

Here $P_{\pi+}^\mu$, $P_{\pi-}^\mu$, and $P_{p'}^\mu$ are the four-momenta of the final state hadrons, P_p^μ is the four-momentum of the initial proton and $P_{\gamma_v}^\mu = P_e^\mu - P_{e'}^\mu$ the four-momentum of the virtual photon with P_e^μ and $P_{e'}^\mu$ the four-momenta of the incoming and scattered electrons, respectively.

---

[1] Although the scattered electron is treated as a final particle, here it is classified as "initial", since it defines the virtual photon, which in turn is attributed to the initial state.

To determine W_f, all final hadrons should be registered, while for the calculation of W_i it is sufficient to register the scattered electron. The latter opportunity allows event samples with one unregistered final hadron, whose four-momentum is recovered via the missing mass technique, to be used. This approach allows for a significant increase of the analyzed statistics (see Sect. 3.5).

In experiments off protons at rest W_f and W_i may differ due to the detector resolution and the radiative effects, which electrons undergo. In moving proton experiments one more aspect takes effect, i.e. in order to calculate W_i, one needs information about the target proton momentum (P_p^μ), which is accessible only in the fully exclusive topology[2]. Therefore, the value of W_i given by Eq. (4.1.1) turns out to be ill-defined, if one of the final hadrons is not registered. This brings us to the choice to either demand the registration of all final hadrons to determine W_f (that reduces the flexibility of the analysis) or to work under a so-called "target-at-rest-assumption", which assumes the initial proton to be at rest. In the last approach the value of W_i appears to be smeared. This smeared value of the invariant mass is hereinafter denoted as W_{sm}. Meanwhile, the value W_f corresponds to the true reaction invariant mass and, therefore, is denoted as W_{true}. It can be calculated only in the fully exclusive topology.

If a smeared value W_{sm} is used to describe the reaction, the extracted cross sections turned out to be convoluted with a function that is determined by the Fermi motion of the initial proton [24, 38]. To retrieve the non-smeared observable, a correction that unfolds this effect should be applied to the cross sections.

Besides the W-smearing, the Fermi motion of the target proton is also responsible for the boundary blurring of the Q^2 versus W distribution[3]. This happens because the experiment off the moving proton with fixed laboratory beam energy is equivalent

---

[2] If the spectator nucleon momentum is not directly measured in the experiment. This was not an option in the analyzed "e1e" experiment.

[3] This issue is addressed in more details in Ref. [24].

to that off the proton at rest performed with altered effective beam energy [24]. The boundaries of the Q^2 versus W distribution, however, are beam energy dependent. Therefore, the distribution edges, being sharp and distinct in the proton at rest experiment, become blurred in the experiment off a moving proton.

The blurring, however, affects only the edges of Q^2 versus W_{true} distribution, where W_{true} is the true reaction invariant mass given by Eq. (4.1.2), since W_{true} accounts for the target motion and, therefore, for the alteration of the effective beam energy. If the smeared value W_{sm}, calculated by Eq. (4.1.1) under the target-at-rest-assumption, is used instead, the distribution edges are not subject to the blurring because the fixed value of the laboratory beam energy is used in calculations.
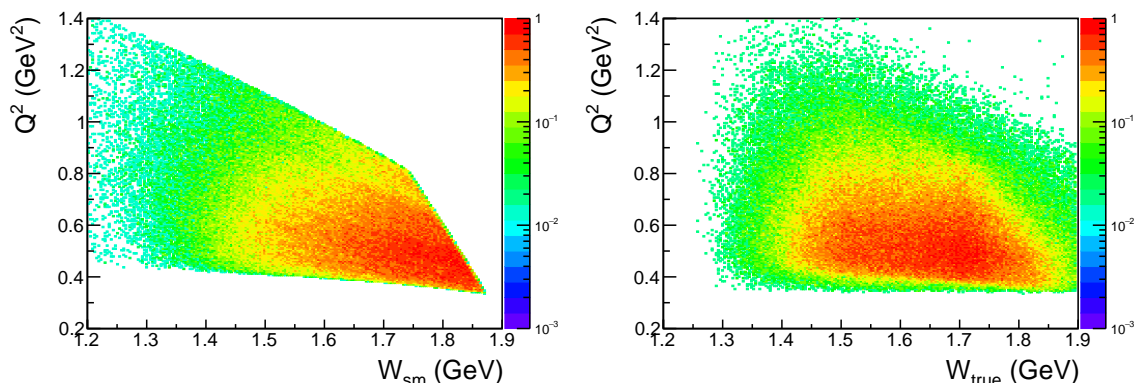
Figure 4.1: Experimental Q^2 versus W distributions for W_{sm} (left) and W_{true} (right) plotted for the fully exclusive topology. The boundaries of the left distribution are sharp, since the W_{sm} is calculated under the target-at-rest-assumption and the fixed value of the laboratory beam energy is used in calculations. The boundaries of the right distribution are blurred, since the calculation of W_{true} accounts for the target proton motion and therefore for the alteration of the effective beam energy of the experiment.

This situation is illustrated in Fig. 4.1, where the Q^2 versus W distributions are shown for W_{sm} (left) and W_{true} (right). These distributions are plotted for the fully exclusive topology only, since it allows for the determination of both W_{sm} and W_{true}. The distributions, therefore, contain only a small portion of the total analyzed statistics. The boundaries of the left distribution are sharp, since the W_{sm} is calculated assuming the fixed laboratory beam energy and the target at rest. The boundaries

of the right distribution are blurred, since the calculation of W_{true} accounts for the target proton motion and, therefore, for the alteration of the effective beam energy of the experiment.

The event yield in the blurred region suffers from depletion of events (compared to that for the case of fixed beam energy and sharp distribution edges). To estimate this effect, one should know the function that describes the alteration of the effective beam energy. This function is in turn determined by the target proton momentum distribution. The cross sections extracted in the blurred region need a special correction, otherwise they will suffer from the underestimation.

The situation described above offers two options, i.e. to use either W_{sm} or W_{true} to describe the reaction. The former opportunity leads to the need to apply a correction that unfolds the cross section smearing, while the latter requires the correction due to the blurring effect. The first option was chosen in this analysis because it has the advantage of using the π^- missing topology that accumulates the majority of the experimentally available statistics.

Thus, to calculate the cross section in this analysis, events are binned in W_{sm}. Note, however, that the corresponding W points on the chosen W_{sm} grid (see Sect. 4.4) are then treated as actual W-values where the cross section is eventually reported. However, the cross section values assigned to these W points is treated as distorted. The necessary correction to the cross section is based on the TWOPEG-D event generator [24], which offers a proper Monte Carlo simulation of the double-pion electroproduction off moving protons. This correction is described in Sect. 5.3.

4.2   Lab to CMS transformation

Once the quasi-free double-pion events are selected as described in Chapter 3, the laboratory four-momenta of all final particles are known: they are either registered

or calculated as missing. These four-momenta are then used for the calculation of the kinematic variables, which are introduced in Sect. 4.3. The cross sections meanwhile are extracted in the center-of-mass frame of the *virtual photon – initial proton* system (CMS). Therefore, to calculate the kinematic variables, the four-momenta of all particles need to be transformed from the laboratory system (Lab) to the CMS.

The CMS is uniquely defined as the system, where the initial proton and the photon move towards each other with the z_{CMS}-axis along the photon and the net momentum equal to zero. However, the procedure of the Lab to CMS transformation differs depending on the specificity of the reaction initial state (real or virtual photons, at rest or moving target). Figure 4.2 illustrates three options[4] for the experimental specification of the reaction initial state.

The correct procedure of the Lab to CMS transformation for an electroproduction experiment off a moving target (bottom right illustration in Fig. 4.2) can be subdivided into two major steps.

A. First, one needs to perform the transition to the auxiliary system, where the target proton is at rest, while the incoming electron moves along the z-axis. This system is called "quasi-Lab", since the initial conditions of the reaction in this frame imitate those existing in the Lab system in the case of the free proton experiment. The recipe of the Lab to quasi-Lab transformations is given in detail in Ref. [24].

B. Then, the quasi-Lab to CMS transformation should be performed by the standard method used for an electroproduction experiment off a proton at rest [22] (bottom left illustration in Fig. 4.2). Further details are given in App. A.

To perform the first step of this procedure (Lab to quasi-Lab transformation), one should be aware of the initial proton momentum for each reaction event [24]. In this

---

[4] The fourth option of the reaction off the moving proton induced by real photons is not shown.

Photoproduction on the free proton

y_{lab}

x_{lab}

z_{lab}

γ p

$$\vec{\beta} = \left(0, 0, \frac{|\vec{q_\gamma}|}{E_\gamma + m_p}\right)$$

Electroproduction on the free proton

y_{lab}

x_{lab}

z_{lab}

$$\vec{\beta} = \frac{\vec{q_\gamma}}{E_\gamma + m_p}$$

e'

e

γ_v

p

Electroproduction on the moving proton

y_{lab}

x_{lab}

z_{lab}

$$\vec{\beta} = \frac{\vec{q_\gamma} + \vec{p_f}}{E_\gamma + E_p}$$

e'

e

γ_v

p

p_f

y_{cms}

x_{cms}

z_{cms}

γ p

CMS
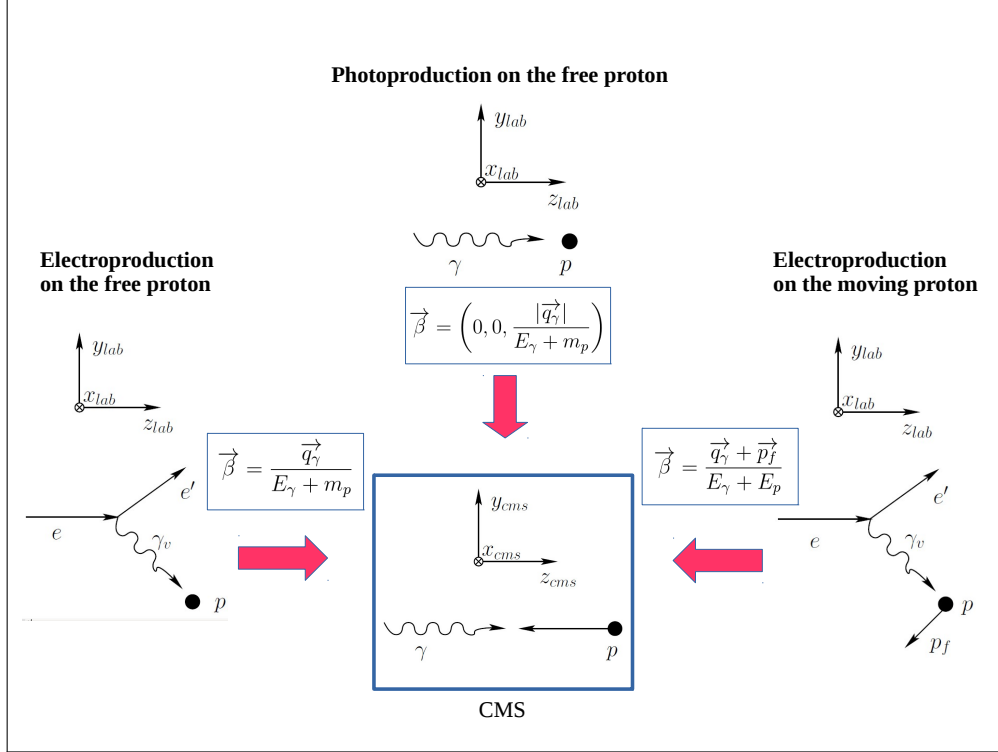
Figure 4.2: Illustration of three options for the experimental specification of the reaction initial state. Here m_p is the proton mass, $\vec{q_\gamma}$ and E_γ are the three-momentum and the energy of the interacting photon, respectively, while p_f is the Fermi momentum of the target proton.

analysis, however, this information is available only in the fully exclusive topology, while the main π^- missing topology lacks this information. This situation brings us to the impossibility to perform the correct Lab to CMS transformation for the majority of events. Therefore, in this analysis the procedure of Lab to CMS transformation for an electroproduction experiment off a proton at rest [22] is used (bottom left illustration in Fig. 4.2). The procedure is described in App. A. This is done for both fully exclusive and main π^- missing topologies for consistency.

This approximation in the Lab to CMS transformation introduces a systematic inaccuracy to the extracted cross sections. A correction for this effect is included into the procedure of unfolding the effects of the target motion (see Sect. 5.3).

4.3 Kinematic variables

When the four-momenta of all particles are defined and transformed to the CMS, one can calculate the kinematic variables that describe the reaction $ep(n) \rightarrow e'p'(n')\pi^+\pi^-$. For the description of the reaction initial state two variables are needed. In this study they are chosen in the following way: the invariant mass W, which is calculated according to Eq. (4.1.1), and the photon virtuality Q^2, which is defined as

$$Q^2 = -(P_{\gamma_v}^\mu)^2 = -(P_e^\mu - P_{e'}^\mu)^2, \qquad (4.3.1)$$

where $P_{\gamma_v}^\mu$ is the four-momentum of the virtual photon, while P_e^μ and $P_{e'}^\mu$ the four-momenta of the incoming and scattered electrons, respectively.

The three-body final hadron state is unambiguously determined by five kinematic variables [22], and there are several options for their choice. The following generalized set of variables is used in this analysis[5]:

- invariant mass of the first pair of the hadrons $M_{h_1h_2}$,

- invariant mass of the second pair of the hadrons $M_{h_2h_3}$,

- the first particle solid angle $\Omega_{h_1} = (\theta_{h_1}, \varphi_{h_1})$, and

- the angle α_{h_1} between the two planes (i) defined by the three-momenta of the virtual photon (or initial proton) and the first final hadron and (ii) defined by the three-momenta of all final hadrons[6].

The cross sections in this analysis are obtained in three sets of variables depending on various assignments for the first, second, and third final hadrons:

1. $[p', \pi^+, \pi^-]$ $M_{p'\pi^+}$, $M_{\pi^+\pi^-}$, $\theta_{p'}$, $\varphi_{p'}$, $\alpha_{p'}$ (or $\alpha_{[pp'][\pi^+\pi^-]}$),

2. $[\pi^-, \pi^+, p']$ $M_{\pi^-\pi^+}$, $M_{\pi^+p'}$, θ_{π^-}, φ_{π^-}, α_{π^-} (or $\alpha_{[p\pi^-][p'\pi^+]}$),

3. $[\pi^+, \pi^-, p']$ $M_{\pi^+\pi^-}$, $M_{\pi^-p'}$, θ_{π^+}, φ_{π^+}, α_{π^+} (or $\alpha_{[p\pi^+][p'\pi^-]}$).

---

[5] More details on the organization of the reaction phase-space can be found in App. B.

[6] Note that the three-momenta of the π^+, π^-, p' are in the same plane, since in the CMS their total three-momentum has to be equal to zero.

Let's explain in more detail the calculation of the kinematic variables for the case of the set number two. The invariant masses $M_{\pi^+\pi^-}$ and $M_{\pi^+p'}$ are calculated from the four-momenta of the final particles $P^{\mu}_{\pi^-}$, $P^{\mu}_{\pi^+}$, $P^{\mu}_{p'}$ in the following way:

$$M_{\pi^+\pi^-} = \sqrt{(P^{\mu}_{\pi^+} + P^{\mu}_{\pi^-})^2} \quad \text{and}$$
$$M_{\pi^+p'} = \sqrt{(P^{\mu}_{\pi^+} + P^{\mu}_{p'})^2}.$$

(4.3.2)

The polar (θ_{π^-}) and azimuthal (φ_{π^-}) angles of the π^- in the CMS are shown in Fig. 4.3. In this figure the z-axis is directed along the virtual photon (with the unit vector $\vec{n}_z$), while the x-axis is located in the electron scattering plane and follows the direction of the scattered electron (see App. A for details). The plane A in Fig. 4.3 is defined by the three-momenta of the π^- and initial proton.

The angle θ_{π^-} varies in the range $[0, \pi]$ and is calculated as:

$$\theta_{\pi^-} = \arccos\left(\frac{(\vec{P}_{\pi^-} \cdot \vec{P}_{\gamma})}{|\vec{P}_{\pi^-}||\vec{P}_{\gamma}|}\right),$$

(4.3.3)

where $\vec{P}_{\gamma}$ is the three-momentum of the virtual photon and $\vec{P}_{\pi^-}$ is the three-momentum of the π^- (both are situated in the plane A).

The angle φ_{π^-} varies in the range $[0, \ 2\pi]$ and is determined as:

$$\varphi_{\pi^-} = \arctan\left(\frac{P_y}{P_x}\right), \qquad \text{if } P_x > 0 \ \text{and} \ P_y > 0,$$
$$\varphi_{\pi^-} = \arctan\left(\frac{P_y}{P_x}\right) + 2\pi, \quad \text{if } P_x > 0 \ \text{and} \ P_y < 0,$$
$$\varphi_{\pi^-} = \arctan\left(\frac{P_y}{P_x}\right) + \pi, \quad \text{if } P_x < 0 \ \text{and} \ P_y < 0,$$
$$\varphi_{\pi^-} = \arctan\left(\frac{P_y}{P_x}\right) + \pi, \quad \text{if } P_x < 0 \ \text{and} \ P_y > 0,$$

(4.3.4)

where P_i is the i-component of the π^- three-momentum in the CMS ($i = x, y, z$).

The calculation of the angle α_{π^-}, which is shown in Fig. 4.4, is more complicated. This is the angle between the two planes A and B, which varies in a range $[0, \ 2\pi]$.

The plane A is defined by the three-momentum of the initial proton and the three-momentum of the π^-. The plane B is defined by the three-momenta of all final hadrons. For the calculation of the α_{π^-}, one determines first three auxiliary vectors $\vec{\gamma}$, $\vec{\beta}$, and $\vec{\delta}$, which are also shown in Fig. 4.4.

The auxiliary unit vector $\vec{\gamma}$ is situated in the plane A. This vector is perpendicular to the three-momentum of the π^- and directed toward the vector $[-\vec{n}_z]$, where $\vec{n}_z$ is the unit vector directed along the z-axis. The vector $\vec{\gamma}$ can be expressed as

$$\vec{\gamma} = a_\alpha \cdot [-\vec{n}_z] \ + \ b_\alpha \cdot \vec{n}_{\pi^-}$$

$$\text{with} \quad a_\alpha = \sqrt{\frac{1}{1 - (\vec{n}_{\pi^-} \cdot [-\vec{n}_z])^2}} \quad \text{and} \quad b_\alpha = -a_\alpha \cdot (\vec{n}_{\pi^-} \cdot [-\vec{n}_z]) \ ,$$

where $\vec{n}_{\pi^-}$ is the unit vector directed along the three-momentum of the π^-.

The auxiliary unit vector $\vec{\beta}$ is situated in the plane B. This vector is perpendicular to the three-momentum of the π^- and directed toward the three-momentum of the π^+. The vector $\vec{\beta}$ can be expressed as

$$\vec{\beta} = a_\beta \cdot \vec{n}_{\pi^+} \ + \ b_\beta \cdot \vec{n}_{\pi^-}$$

$$\text{with} \quad a_\beta = \sqrt{\frac{1}{1 - (\vec{n}_{\pi^+} \cdot \vec{n}_{\pi^-})^2}} \quad \text{and} \quad b_\beta = -a_\beta \cdot (\vec{n}_{\pi^+} \cdot \vec{n}_{\pi^-}) \ ,$$

where $\vec{n}_{\pi^+}$ is the unit vector directed along the three-momentum of the π^+.

Taking the scalar products $(\vec{\gamma} \cdot \vec{\gamma})$, $(\vec{\beta} \cdot \vec{\beta})$, $(\vec{\gamma} \cdot \vec{n}_{\pi^-})$, and $(\vec{\beta} \cdot \vec{n}_{\pi^-})$, it is straightforward to verify that $\vec{\gamma}$ and $\vec{\beta}$ are the unit vectors perpendicular to the three-momentum of the π^-.

The auxiliary unit vector $\vec{\delta}$ is the vector product of the auxiliary vectors $\vec{\gamma}$ and $\vec{\beta}$,

$$\vec{\delta} = [\vec{\gamma} \times \vec{\beta}]. \tag{4.3.5}$$
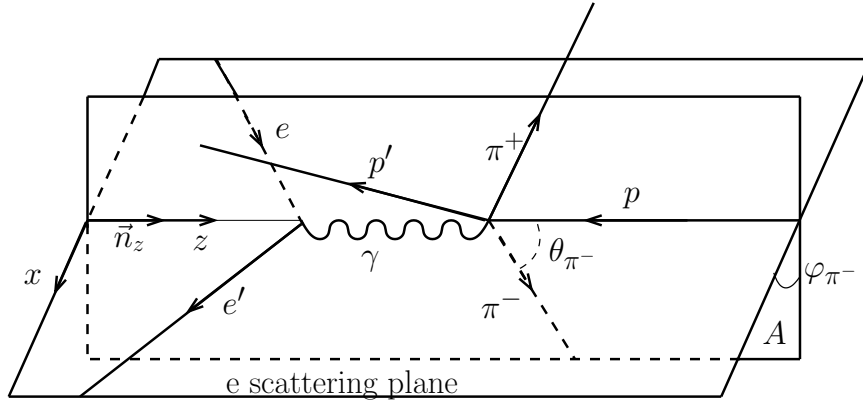
Figure 4.3: Polar (θ_{π^-}) and azimuthal (φ_{π^-}) angles of the π^- in the CMS. The z-axis is directed along the virtual photon (with the unit vector $\vec{n}_z$), while the x-axis is located in the electron scattering plane and follows the direction of the scattered electron. The plane A is defined by the three-momenta of the π^- and initial proton.
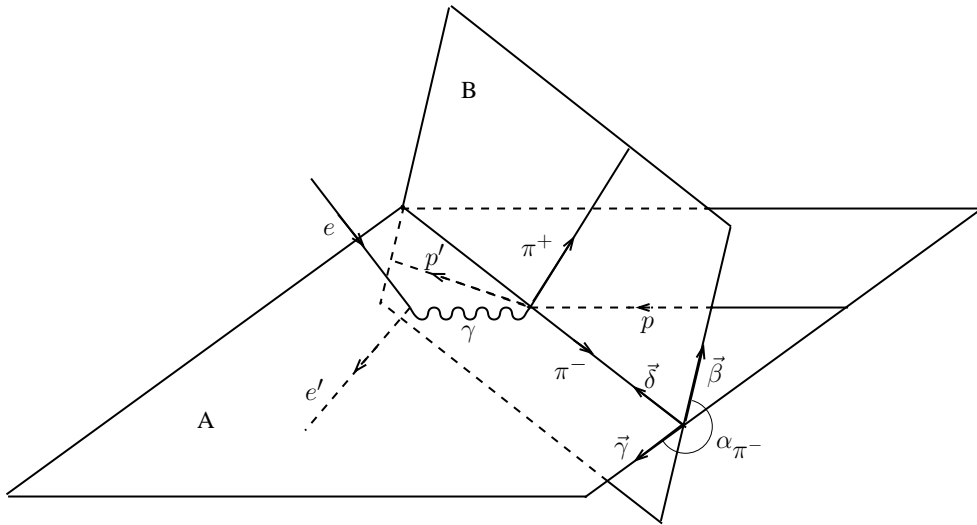
Figure 4.4: Definition of the angle α_{π^-} between the two planes: the plane A is defined by the three-momenta of the π^- and initial proton, while the plane B is defined by the three-momenta of all final hadrons. The definitions of auxiliary vectors $\vec{\beta}$, $\vec{\gamma}$, and $\vec{\delta}$ are given in the text.

Then the angle α_{π^-} is determined as:

$$\alpha_{\pi^-} = \arccos(\vec{\gamma} \cdot \vec{\beta}), \qquad \text{if} \quad \vec{\delta} \uparrow\uparrow \vec{n}_{\pi^-},$$
$$\alpha_{\pi^-} = 2\pi - \arccos(\vec{\gamma} \cdot \vec{\beta}), \quad \text{if} \quad \vec{\delta} \uparrow\downarrow \vec{n}_{\pi^-}. \tag{4.3.6}$$

The kinematic variables for the first and third sets are calculated in a similar way (see Refs. [22, 32] for details). Further information on the kinematic of reactions with multi-particle final states can be found in Ref. [42].

4.4 Binning and kinematic coverage

The available kinematic coverage in the initial state variables is shown by the Q^2 versus W distribution[7] in Fig. 4.5. This distribution is filled with the double-pion events survived after the event selection described above. The blue boundary limits the analyzed kinematic area, where the double-pion cross sections are extracted. The black grid demonstrates the chosen binning in the initial state variables (25 MeV in W and 0.05 GeV^2 in Q^2).

The kinematic coverage in the final state variables has the following reaction related features. The angular variables θ_{h_1}, φ_{h_1}, and α_{h_1} vary in the fixed ranges of $[0, \pi]$, $[0, 2\pi]$, and $[0, 2\pi]$, respectively. Meanwhile, the ranges of the invariant masses $M_{h_1 h_2}$ and $M_{h_2 h_3}$ are W dependent and broaden as W grows. More details on the specificity of the double-pion production phase-space are given in App. B.

The binning in the final hadron variables used in this study is listed in Tab. 4.1. In each W and Q^2 bin the range of each final hadron variable is divided into bins of equal size. However, the number of bins differs in various W subranges, in order to take into account (i) the statistics drop near the reaction threshold, which is at ≈ 1.22 GeV and (ii) the aforementioned broadening of the reaction phase-space with

---

[7] Note that W here is W_{sm}, and therefore, the distribution boundaries are not subject to the blurring. See Sect. 4.1 for details.

increasing W. The chosen amount of bins in each considered W subrange reflects the intention to maintain reasonable statistical uncertainties of the single-differential cross sections for all W and Q^2 bins.
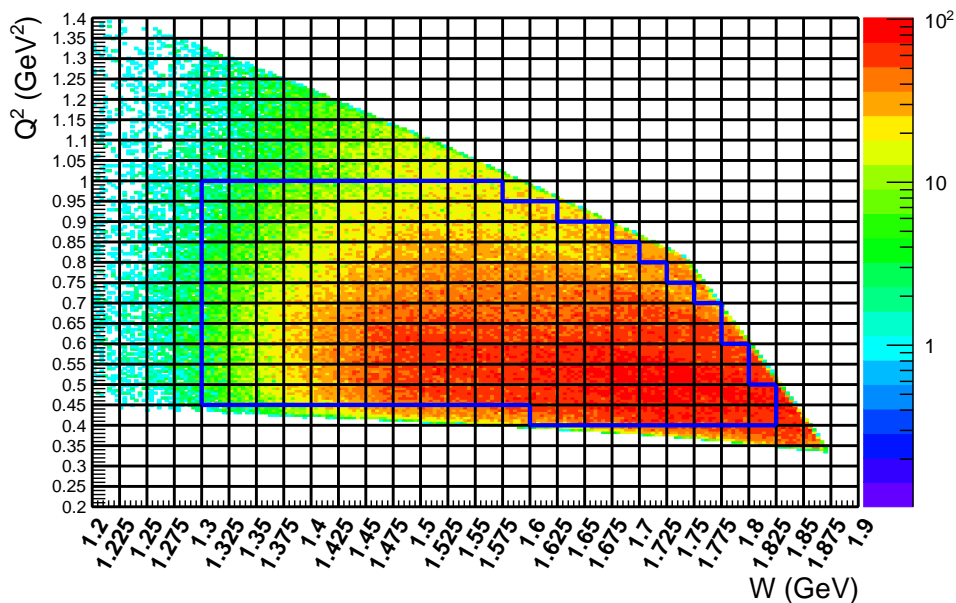
Figure 4.5: Q^2 versus W distribution populated with the selected double-pion events. The cross section is calculated in 2D cells within the blue boundaries.

For the binning in the polar angle note the following. The cross section, although being differential in $[-\cos\theta]$, is binned in θ. These $\Delta\theta$ bins are of equal size in the corresponding W subrange. See also Sect. 4.5 on this matter.

Table 4.1: Number of bins for hadronic variables.

		W subrange (GeV)			
	Hadronic variable	$[1.3, 1.35]$	$[1.35, 1.4]$	$[1.4, 1.475]$	$[1.475, 1.825]$
$M_{h_1 h_2}$	Invariant mass	8	10	12	12
$M_{h_2 h_3}$	Invariant mass	8	10	12	12
θ_{h_1}	Polar angle	6	8	10	10
φ_{h_1}	Azimuthal angle	5	5	5	6
α_{h_1}	Angle between planes	5	6	8	8
	Total number of bins in hadronic variables	9600	24000	57600	69120

The total numbers of multi-dimensional bins for the corresponding W ranges are listed in the last row of Tab. 4.1 and require some clarification. In fact the invariant masses border of the double-pion production phase-space is W-dependent and determined by the Byckling function (see App. B). Therefore, the bins located outside this border contain no double-pion events and hence do not contribute to the cross section. For a given W value, the border is distinct, however for a W bin, which corresponds to a range of W values, it is somewhat diffused. If events are binned in W_{true} (like in a free proton experiment) and the bin is small, e.g. 25 MeV, this diffusion is marginal. Then the quantity of bins involved in the cross section calculation (including both non-empty and empty cells) varies from 90% to 70% of the total numbers given in the last row of Tab. 4.1 as W increases from the threshold. However, if events are binned in W_{sm} (like in this analysis), each W_{sm} value in a bin corresponds to a sequence of W_{true} spread over 50-100 MeV. In this case a very pronounced boundary diffusion takes place, increasing the quantity of bins filled with events, i.e. the fraction of bins involved in the cross section calculation turn out to vary from 100% to 80% as W increases[8].

The specific organization of the double-pion production phase-space in the invariant masses $(M_{h_1 h_2}, M_{h_2 h_3})$ causes the need to pay special attention to the binning in these variables. Equation (4.4.1) gives the expressions for the lower and upper boundaries of the $M_{h_1 h_2}$ distribution and demonstrates that the upper boundary depends on the value of W, while the lower does not (see also App. B on this matter).

$$M_{lower} = m_{h_1} + m_{h_2}$$

$$M_{upper}(W) = W - m_{h_3}. \tag{4.4.1}$$

Here m_{h_1}, m_{h_2}, and m_{h_3} are the masses of the final hadrons.

---

[8] This estimation is based on the Monte Carlo simulation performed with TWOPEG [39] and TWOPEG-D [24] for the reactions off the proton at rest and off the moving proton, respectively.

Since the cross section is calculated in a bin $W_{left} < W < W_{right}$, the boundary of M_{upper} is not distinct. For the purpose of binning in mass, the value of M_{upper} is calculated using W_{center}, at the center of the W bin. As a result, some events with $W > W_{center}$ turned out to be located beyond M_{upper}. Hence it was decided to use a specific arrangement of mass bins with the bin width ΔM determined by

$$\Delta M = \frac{M_{upper} - M_{lower}}{N_{bins} - 1}, \tag{4.4.2}$$

where N_{bins} is the number of bins specified in the first row of Tab. 4.1. The left boundary of the first bin is set to M_{lower}.

The chosen arrangement of bins forces the last bin to be situated completely out of the boundaries[9] given by Eq. (4.4.1) using W_{center}. Therefore, the cross section in this extra bin finally is not reported. However, this bin is kept in the analysis since its content (though being very small) contributes to all cross sections that are obtained by integrating over the corresponding invariant mass distribution.

Note that the cross section in the next to last bin in invariant mass needs a special correction. This correction is described in Sect. 5.4.

4.5   Cross section formulae

4.5.1   Electron scattering cross section

The experimental electron scattering cross section σ_e for the reaction $ep(n) \rightarrow e'p'(n')\pi^+\pi^-$ is seven-fold differential and calculated as[10]

$$\frac{\mathrm{d}^7\sigma_e}{\mathrm{d}W\mathrm{d}Q^2\mathrm{d}^5\tau} = \frac{1}{R\cdot\mathcal{F}} \cdot \frac{\left(\frac{N_{full}}{Q_{full}} - \frac{N_{empty}}{Q_{empty}}\right)}{\Delta W\cdot\Delta Q^2\cdot\Delta^5\tau\cdot\left[\frac{l\cdot\rho\cdot N_A}{q_e\cdot\mu_d}\right]\cdot\mathcal{E}} \text{ , where} \tag{4.5.1}$$

---

[9] Note that for each W bin and for each invariant mass, ΔM given by Eq. (4.4.2) is greater than 12.5 MeV, which is the half of the W bin width.

[10] To deal with the multi-differential cross section, THnSparse multi-dimensional root histograms are used.

- $d^5\tau = dM_{h_1 h_2} dM_{h_2 h_3} d\Omega_{h_1} d\alpha_{h_1}$ is the differential of the five independent variables of the $\pi^+\pi^- p$ final state, which are described in Sect. 4.3;

- N_{full} and N_{empty} are the numbers of selected double-pion events inside the seven-dimensional bin for runs with deuterium and empty target, respectively;

- the quantity in the square brackets in the denominator corresponds to the luminosity of the experiment $\mathcal{L}$ in the units cm^{-2}·C^{-1} and its components are

  $l = 2$ cm the length of the target,

  $\rho = 0.169$ g·cm^{-3} the density of liquid deuterium,

  $N_A = 6.022\cdot10^{-19}$ mol^{-1} Avogadro's number,

  $q_e = 1.602\cdot10^{-19}$ C the elementary charge, and

  $\mu_d = 2.014$ g·mol^{-1} the molar mass of deuterium,

  which results in the luminosity value of $\mathcal{L} = 0.63\cdot10^{42}$ cm^{-2}·C^{-1} = $0.63\cdot10^{12}$ μb^{-1}·C^{-1};

- $Q_{full} = 3734.69$ μC and $Q_{empty} = 464.797$ μC are the values of the charge accumulated in the Faraday Cup for deuterium and empty target runs, respectively[11], which results in the corresponding values of the integrated luminosity $L = \mathcal{L} \cdot Q$ of $2.35\cdot10^9$ μb^{-1} and $0.29\cdot10^9$ μb^{-1};

- $\mathcal{E} = \mathcal{E}(\Delta W, \Delta Q^2, \Delta^5\tau)$ is the detector efficiency (which includes the detector acceptance) for each seven-dimensional bin as determined by the Monte Carlo simulation (see Sect. 4.6);

- $R = R(\Delta W, \Delta Q^2)$ is the radiative correction factor described in Sect. 5.2;

- $\mathcal{F} = \mathcal{F}(\Delta W, \Delta Q^2, \Delta^5\tau)$ is the correction factor that aims at unfolding the effects of the target motion (see Sect. 5.3).

---

[11] They are calculated by summing up the charges of all analyzed *blocks* (see Sect. 3.4.2 for details).

The electron scattering cross section σ_e in the left hand side of Eq. (4.5.1) is assumed to be obtained in the center of the finite seven-dimensional kinematic bin $\Delta W \Delta Q^2 \Delta^5 \tau$.

4.5.2 Virtual photoproduction cross section

The goal of the analysis is to extract the virtual photoproduction cross section σ_v of the reaction $\gamma_v p(n) \rightarrow p'(n')\pi^+\pi^-$. This virtual photoproduction cross section σ_v is five-fold differential and in the single-photon exchange approximation connected with the seven-fold differential electron scattering cross section[12] σ_e via

$$\frac{\mathrm{d}^5\sigma_v}{\mathrm{d}^5\tau} = \frac{1}{\Gamma_v}\frac{\mathrm{d}^7\sigma_e}{\mathrm{d}W\,\mathrm{d}Q^2\mathrm{d}^5\tau} \; , \tag{4.5.2}$$

where Γ_v is the virtual photon flux given by

$$\Gamma_v(W, Q^2) = \frac{\alpha}{4\pi}\frac{1}{E_{beam}^2 m_p^2}\frac{W(W^2 - m_p^2)}{(1 - \varepsilon_T)Q^2} \; . \tag{4.5.3}$$

Here α is the fine structure constant $(1/137)$, m_p the proton mass, $E_{beam} = 2.039$ GeV the laboratory energy of the incoming electron beam, and ε_T the virtual photon transverse polarization given by

$$\varepsilon_T = \left(1 + 2\left(1 + \frac{\nu^2}{Q^2}\right)\tan^2\left(\frac{\theta_{e'}}{2}\right)\right)^{-1} \; , \tag{4.5.4}$$

where $\nu = E_{beam} - E_{e'}$ is the virtual photon energy, while $E_{e'}$ and $\theta_{e'}$ are the energy and the polar angle of the scattered electron in the lab frame, respectively.

The value of the virtual photon flux given by Eq. (4.5.3) is calculated for the central point of the $\Delta W \Delta Q^2$ bin.

---

[12] Note that after the corrections introduced in Eq. (4.5.1) by the factors R and $\mathcal{F}$, the cross section σ_e is the true electron scattering cross section attributed to the central values of the corresponding $\Delta W \Delta Q^2 \Delta^5 \tau$ bin and the distinct value of the beam energy $E_{beam} = 2.039$ GeV.

The limited statistics of the experiment does not allow for estimates of the five-fold differential cross section σ_v with a reasonable accuracy. Therefore, the cross section σ_v is first obtained on the multi-dimensional grid and then is integrated over at least four hadron variables. Hence, only the sets of the single-differential and fully-integrated cross sections are obtained.

For each W and Q^2 bin, the following cross sections are extracted for each set of variables,

$$\frac{\mathrm{d}\sigma_v}{\mathrm{d}M_{h_1 h_2}} = \int \frac{\mathrm{d}^5 \sigma_v}{\mathrm{d}^5 \tau} \mathrm{d}M_{h_2 h_3} \mathrm{d}\Omega_{h_1} \mathrm{d}\alpha_{h_1},$$

$$\frac{\mathrm{d}\sigma_v}{\mathrm{d}M_{h_2 h_3}} = \int \frac{\mathrm{d}^5 \sigma_v}{\mathrm{d}^5 \tau} \mathrm{d}M_{h_1 h_2} \mathrm{d}\Omega_{h_1} \mathrm{d}\alpha_{h_1},$$

$$\frac{\mathrm{d}\sigma_v}{\mathrm{d}[-\cos\theta_{h_1}]} = \int \frac{\mathrm{d}^5 \sigma_v}{\mathrm{d}^5 \tau} \mathrm{d}M_{h_1 h_2} \mathrm{d}M_{h_2 h_3} \mathrm{d}\varphi_{h_1} \mathrm{d}\alpha_{h_1}, \qquad (4.5.5)$$

$$\frac{\mathrm{d}\sigma_v}{\mathrm{d}\alpha_{h_1}} = \int \frac{\mathrm{d}^5 \sigma_v}{\mathrm{d}^5 \tau} \mathrm{d}M_{h_1 h_2} \mathrm{d}M_{h_2 h_3} \mathrm{d}\Omega_{h_1}, \quad \text{and}$$

$$\sigma_v^{int}(W, Q^2) = \int \frac{\mathrm{d}^5 \sigma_v}{\mathrm{d}^5 \tau} \mathrm{d}M_{h_1 h_2} \mathrm{d}M_{h_2 h_3} \mathrm{d}\Omega_{h_1} \mathrm{d}\alpha_{h_1}.$$

As a final result for each W and Q^2 bin, the integral cross section σ_v^{int}, averaged over the three variable sets, is reported together with the nine single-differential cross sections given in (4.5.6), where each column is taken from the corresponding variable set.

$$\begin{array}{ccc} \dfrac{\mathrm{d}\sigma_v}{\mathrm{d}M_{p'\pi^+}} & \dfrac{\mathrm{d}\sigma_v}{\mathrm{d}M_{\pi^-\pi^+}} & \dfrac{\mathrm{d}\sigma_v}{\mathrm{d}M_{\pi^-p'}} \\[3ex] \dfrac{\mathrm{d}\sigma_v}{\mathrm{d}[-\cos\theta_{p'}]} & \dfrac{\mathrm{d}\sigma_v}{\mathrm{d}[-\cos\theta_{\pi^-}]} & \dfrac{\mathrm{d}\sigma_v}{\mathrm{d}[-\cos\theta_{\pi^+}]} \\[3ex] \dfrac{\mathrm{d}\sigma_v}{\mathrm{d}\alpha_{p'}} & \dfrac{\mathrm{d}\sigma_v}{\mathrm{d}\alpha_{\pi^-}} & \dfrac{\mathrm{d}\sigma_v}{\mathrm{d}\alpha_{\pi^+}} \end{array} \qquad (4.5.6)$$

Regarding the middle row in (4.5.6) note the following. Although being differential in $[-\cos\theta]$, the cross sections are calculated in $\Delta\theta$ bins, which are of equal size in the corresponding W subrange (see Sect. 4.4 for details). This is a conventional way of presenting the θ-distributions in the studies of double-pion cross sections [15–19, 21–23].

4.6   Efficiency evaluation

For the Monte Carlo simulation the TWOPEG-D event generator was used [24]. This is the version of TWOPEG (an event generator for double-pion electroproduction off the free proton [39]), which is able to simulate the effects of the initial proton motion. In this version of the event generator the Fermi motion of the initial proton is generated according to the Bonn potential [40] and then naturally merged into the specific kinematics of double-pion electroproduction. TWOPEG-D accounts for radiative effects according to the approach described in Refs. [39, 43].

The generated events are passed through the standard detector simulation (GSIM, GPP) and reconstruction procedures (recsis) with the majority of parameters kept the same as in the studies [22, 44], which were also devoted to the "e1e" run period[13].

In the studies of double-pion production cross section it is especially important to generate enough Monte Carlo statistics in order to saturate each multi-dimensional bin of the reaction phase-space with events (see Tab. 4.1). Insufficient Monte Carlo statistics leads to an improper efficiency evaluation and an unnecessary rise in the empty cells contribution (see Sect. 5.1), thus systematically affecting the accuracy of the extracted cross sections. For this study the total of about $4 \cdot 10^{10}$ double-pion events were generated in the investigated kinematic region, which is considered adequate.

The TWOPEG-D event generator performs a weighted event generation [39], i.e. all kinematic variables are generated randomly according to the double-pion production phase-space, while each event generated at a particular kinematic point acquires an individual weight, which corresponds to the cross section at this point. Therefore, the efficiency factor $\mathcal{E}$ from Eq. (4.5.1) is calculated in each $\Delta W \Delta Q^2 \Delta^5 \tau$ bin as

---

[13] See Sect. 2.4 and also Ref. [32] for more details on the simulation/reconstruction procedure and for the information on the corresponding parameters used in this analysis.

$$\mathcal{E}(\Delta W, \Delta Q^2, \Delta^5 \tau) = \frac{\mathbb{N}_{rec}}{\mathbb{N}_{gen}} = \frac{\sum\limits_{i=1}^{N_{rec}} w_i}{\sum\limits_{j=1}^{N_{gen}} w_j}, \qquad (4.6.1)$$

where N_{gen} is the number of generated double-pion events (without any cuts) inside the multi-dimensional bin, N_{rec} is the number of reconstructed double-pion events that survived in the bin after the event selection, while $\mathbb{N}_{gen}$ and $\mathbb{N}_{rec}$ are the weighted numbers of the corresponding events and w is a weight of an individual event.

The efficiency in some kinematic bins could not be reliably determined due to boundary effects, bin to bin event migration, and limited Monte Carlo statistics. Such cells were excluded from consideration. They can be differentiated from the cells with reliable efficiency by a larger relative efficiency uncertainty $\delta\mathcal{E}/\mathcal{E}$.

Meanwhile, the calculation of the efficiency uncertainty $\delta\mathcal{E}$ is not straightforward and needs special attention, since (i) N_{gen} and N_{rec} in Eq. (4.6.1) are not independent and (ii) Monte Carlo events in this equation are subject to weighting. Therefore, the special approach described in Ref. [45] was used to calculate $\delta\mathcal{E}$. Neglecting the event migration between the bins, this approach gives the following expression for the absolute statistical uncertainty of the efficiency in a bin for the case of weighted Monte Carlo simulation,

$$\delta\mathcal{E} = \sqrt{\frac{\mathbb{N}_{gen} - 2\mathbb{N}_{rec}}{\mathbb{N}_{gen}^3} \sum\limits_{i=1}^{N_{rec}} w_i^2 + \frac{\mathbb{N}_{rec}^2}{\mathbb{N}_{gen}^4} \sum\limits_{j=1}^{N_{gen}} w_j^2}. \qquad (4.6.2)$$

Meanwhile, according to Ref. [45], in the case of unweighted Monte Carlo simulation, the formula in Eq. (7.1.3) reduces to

$$\delta\widetilde{\mathcal{E}} = \sqrt{\frac{N_{rec}(N_{gen} - N_{rec})}{N_{gen}^3}}, \quad \text{where } \widetilde{\mathcal{E}} = \frac{N_{rec}}{N_{gen}}. \qquad (4.6.3)$$

Figure 4.6 (a) shows the distribution of the relative efficiency uncertainty $\delta\mathcal{E}/\mathcal{E}$ versus efficiency $\mathcal{E}$ plotted taking the weights (see Eq. (7.1.3)) into account. In this plot the statistical effects turn out to be convoluted with the distribution of weights thus complicating the revealing of cells with unreliable efficiency. To isolate only the statistical effects, the distribution $\delta\widetilde{\mathcal{E}}/\widetilde{\mathcal{E}}$ versus $\widetilde{\mathcal{E}}$, which is produced ignoring the weights (see Eq. (4.6.3)), is plotted in the panel (b). As seen in this plot, the cells with high relative efficiency uncertainty are clustered along the horizontal stripes. This clustering originates from the fact that (if the weights are ignored) the efficiency is obtained by the division of two integer numbers, which reveals the bins with small statistics of the reconstructed events. These horizontal stripes, furthermore, contain many cells with unreliable extremely small efficiency. Therefore, the following criterion for the selection of cells with reliable efficiency is used $\delta\widetilde{\mathcal{E}}/\widetilde{\mathcal{E}} < 0.3$. This cut is shown in Fig. 4.6 (b) by the red horizontal line. All cells above this line were excluded from the analysis. The influence of this cut on the distribution $\delta\mathcal{E}/\mathcal{E}$ (with the weights taken into account) is shown in Fig. 4.6 (c).
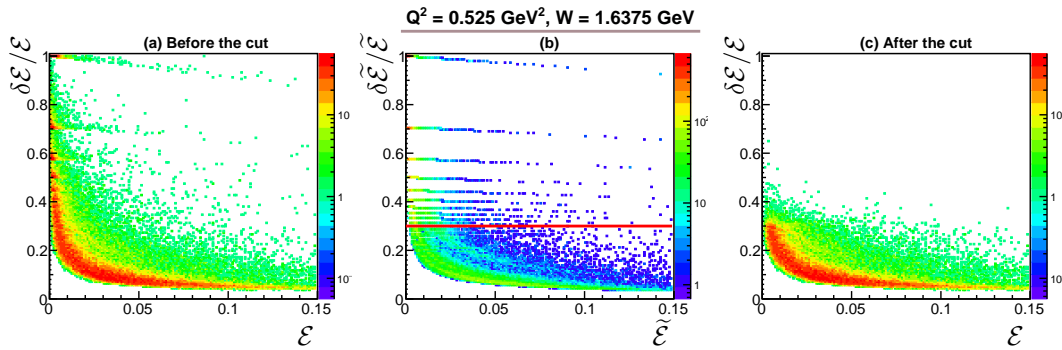
Figure 4.6: Distributions of the relative efficiency uncertainty versus efficiency (a) taking into account the weights (see Eq. (7.1.3)) and (b) ignoring them (see Eq. (4.6.3)). The cut that aims to select the cells with reliable efficiency is shown by the red horizontal line in panel (b). Panel (c) shows the influence of this cut on the distribution $\delta\mathcal{E}/\mathcal{E}$ (with the weights taken into account). The distributions are provided for one particular $\Delta W \Delta Q^2$ bin (with the central values specified in figure), and the color code represents the number of multi-dimensional cells within this bin. Note that the z-axis maximum for the plot (a) is set the same as for the plot (c).

The number of reconstructed events in the revealed cells with unreliable efficiency is set to zero ($N_{rec} = 0$). Then such a cell is ranked as an "empty cell" and, along with other empty cells, is subject to the filling procedure, which is described in Sect. 5.1.

The described above cut on the relative efficiency uncertainty directly impacts the cross section's uncertainties. On the one hand, it eliminates the $\Delta^5\tau$ bins with high relative efficiency uncertainty, thus reducing the total statistical uncertainty of the extracted cross sections (see Sect. 7.1). On the other hand, this cut increases the amount of empty cells, thus increasing the cross section's model dependence and the uncertainty associated with it (see Sect. 7.2). The cut value is therefore chosen as a compromise between these two effects.

The idea of this cut is taken from the study [22, 23], which uses unweighted Monte Carlo simulation and therefore employs Eq. (4.6.3) to calculate the efficiency uncertainty. The study [22, 23] observed the similar cell clustering along horizontal stripes as that revealed in this analysis in the distributions of $\delta\widetilde{\mathcal{E}}/\widetilde{\mathcal{E}}$ versus $\widetilde{\mathcal{E}}$ (produced ignoring the weights) and also set the cut at the position of 0.3.

Note that in this particular analysis the formula (4.6.3) for the unweighted Monte Carlo is used only for selecting the bins with reliable efficiency, since it allows the pure statistical behavior of the efficiency uncertainty to be determined. For the estimation of the cross section's statistical uncertainty the weights are taken into account and the formula (7.1.3) is applied (see Sect. 7.1).

Chapter 5

Corrections to the cross sections

This chapter gives the description of the corrections to the extracted cross sections in the order they were applied.

5.1   Filling kinematic cells with zero acceptance

Due to blind areas in the geometrical coverage of the CLAS detector, some kinematic bins of the double-pion production phase-space turned out to have zero acceptance. In such bins, which are usually called empty cells, the cross section cannot be experimentally defined. For the studies, which aim at extracting fully-differential cross sections (i.e. single-pion production analyses), this is not a problem of great importance, since the cross section in blind areas is just not reported. However, in the studies of double-pion production, where the limited experimental statistics allows only single-differential cross sections to be extracted, this issue becomes a point of special attention [17–19, 21–23]. The empty cells contribute to the integrals in Eqs. (4.5.5) along with the other kinematic bins. Ignoring the contribution from the empty cells leads to a systematic cross section underestimation and, therefore, some assumptions for the empty cells' content are needed. This situation causes some model dependence of the final result.

The map of the empty cells is determined using the Monte Carlo simulation. A cell is treated as empty, if it contains generated events ($N_{gen} > 0$), but does not contain any reconstructed events ($N_{rec} = 0$). The cells with unreliable efficiencies, revealed

based on the cut on the efficiency uncertainty (see Sect. 4.6), are also treated as empty. Empty cells should not be confused with the cells that contain both generated and reconstructed events, but do not contain experimental data, i.e. they appear due to the limited experiment duration, which is taken into account via the normalization on the Faraday Cup charge, and therefore, no model assumptions for them are needed.

It is conventional practice in the studies of the double-pion production to fill the empty cells by means of the Monte Carlo event generator (usually the one that is used to evaluate the efficiency). The studies [15–19, 21] used GENEV [46] (the double-pion event generator based on the JM05 reaction model) for this purpose. The empty cells in these studies were filled with the generated events, which were subject to a special scaling procedure in order to match the experimental data in the regular (non-empty) cells. Meanwhile, the study [22, 23] used TWOPEG [39] for the empty cells filling. TWOPEG is the new double-pion event generator, which is based on the JM15 model and up to now provides the best cross section estimation in the kinematic region $W <$ $2\,\mathrm{GeV}$ and $Q^2 < 1.3\,\mathrm{GeV}^2$. Since TWOPEG is capable of providing the absolute cross section value for a given kinematic point, the study [22, 23] used the cross section estimated by TWOPEG as an assumption for the empty cells content.

In this particular study the empty cells are filled by means of the TWOPEG-D event generator [24], which is the version of TWOPEG for moving protons. Although TWOPEG-D is also capable of providing the absolute cross section value, the empty cells in this study were nevertheless filled with the scaled generated events (as in Refs. [15–19, 21]). This method was chosen because TWOPEG-D assumes all events to be produced in the quasi-free regime (ignoring FSI) and therefore somewhat overestimates the quasi-free cross section.

Thus, in this study empty multi-dimensional cells are filled with the Monte Carlo events generated by TWOPEG-D (following Refs. [15–19, 21]), relying on the cross section shape implemented in the generator. These generated events are subject to

the scaling, which leaving the shape unchanged adjusts the empty cells content to the experimental yield in the regular (non-empty) cells. The scaling is performed individually in each $\Delta W \Delta Q^2$ bin according to the integral yields of the experimental and simulated events in the non-empty cells within this bin. The number of events N_{model} that is assigned as a content for the empty $\Delta^5 \tau$ cell located in the corresponding $\Delta W \Delta Q^2$ bin is then estimated as

$$N_{model}(\Delta W, \Delta Q^2, \Delta^5 \tau) = \frac{\mathcal{N}_{data}^{int}}{\mathcal{N}_{rec}^{int}} \cdot \mathbb{N}_{gen}(\Delta W, \Delta Q^2, \Delta^5 \tau), \qquad (5.1.1)$$

where $\mathbb{N}_{gen}$ is the weighted number of generated events in the corresponding multi-dimensional bin, while the fraction represents the integral scaling factor with $\mathcal{N}_{data}^{int}$ and $\mathcal{N}_{rec}^{int}$ being the total number of experimental events (normalized by the FC charge) and the total number of reconstructed events in all non-empty $\Delta^5 \tau$ bins within the considered $\Delta W \Delta Q^2$ bin, respectively. These quantities are given by

$$\mathcal{N}_{data}^{int}(\Delta W, \Delta Q^2) = \sum_{\substack{All\ \Delta^5\tau \\ with\ N_{rec}>0}} \left[\frac{N_{full}}{Q_{full}} - \frac{N_{empty}}{Q_{empty}} \right] , \text{ and}$$

$$\mathcal{N}_{rec}^{int}(\Delta W, \Delta Q^2) = \sum_{\substack{All\ \Delta^5\tau \\ with\ N_{rec}>0}} \mathbb{N}_{rec}, \qquad (5.1.2)$$

where $\mathbb{N}_{rec}$ is the weighted number of reconstructed events in the $\Delta^5 \tau$ bin.

For each empty $\Delta W \Delta Q^2 \Delta^5 \tau$ bin, the quantity given by Eq. (5.1.1) imitates the yield of experimental events normalized by the FC charge and corrected by the detector efficiency (see Eq. (4.5.1)). The cross section in the empty cells is then calculated as the following,

$$\frac{d^7 \sigma_e}{dW dQ^2 d^5 \tau} = \frac{N_{model}}{\Delta W \cdot \Delta Q^2 \cdot \Delta^5 \tau \cdot [\mathcal{L}]} , \qquad (5.1.3)$$

with N_{model} given by Eq. (5.1.1), and all other variables explained after Eq. (4.5.1). Note that the empty cells are filled before applying the correction factors R and $\mathcal{F}$.

Figure 5.1 introduces the single-differential cross sections given by Eqs. (4.5.5) and $(4.5.6)$[1]. The empty squares correspond to the case when the contribution from the empty cells was ignored, and the black circles are for the case when that was taken into account in the way described above. The figure demonstrates a satisfactory small contribution from the empty cells (and therefore a small model dependence of the results). Only the edge points in the θ distributions (middle row) reveal pronounced empty cell contributions due to the negligible/zero CLAS acceptance in the corresponding directions.

Table 5.1 demonstrates the relative empty cell contribution to the integral cross sections for all reported $(W,\ Q^2)$-points[1]. Different shades of red correspond to different percentage ranges, i.e. the lightest shade corresponds to the contribution $\leq 20\%$, darker shade – from 21% to 30%, and the darkest one shows the contribution $> 30\%$. As seen from the table, for most of the $(W,\ Q^2)$-points the contribution from the empty cells is kept on a low level of $\sim 15\%$, having a small rise at the low Q^2 and high W boundaries, which originates from the momentum-dependent restrictions on the minimal and maximal polar angles of the scattered electron, respectively (see Sect. 3.4.1). Additionally, the rise of the empty cells contribution for small $W \sim 1.3$ GeV is thought to be related to the fact that near the production threshold the hadrons carry small momentum and hence failed to be registered since (i) they are more likely bent to the detector holes, (ii) CLAS is not designed to register hadrons with a momentum less than a certain value (see e.g. Fig. 3.10), and (iii) the smaller the hadron velocity is, the more energy it loses in materials (Bragg peak). A similar rise of the empty cells contribution near the threshold was also observed in Refs. [17, 18, 22, 23], which are devoted to the double-pion electroproduction off the free proton.

---

[1] Both Figure 5.1 and Table 5.1 are given for the cross sections, which (although being divided by the virtual photon flux) are neither corrected for the radiative effects (see Sect. 5.2) nor for the effects of the target motion (see Sect. 5.3).

To account for the model dependence, the approach established for the previous studies of double-pion production cross sections is followed [19, 20, 22], i.e. the part of the single-differential cross section that came from the empty cells is assigned a 50% relative uncertainty. The corresponding absolute uncertainty δ_{model} is then combined with the total statistical uncertainty, as was done in Refs. [19, 20, 22] (more details are in Sect. 7.1).
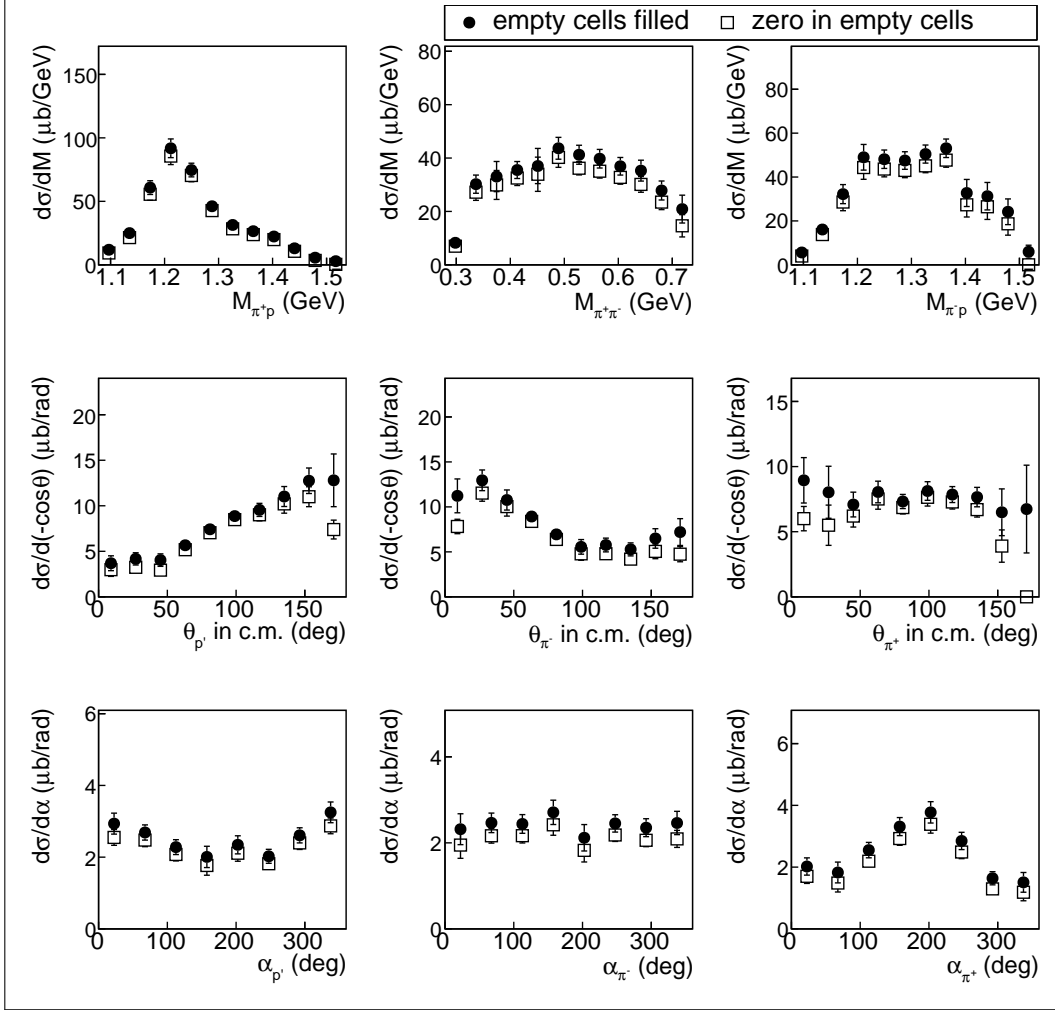
Figure 5.1: Extracted single-differential cross sections for the cases when the contribution from the empty cells was ignored (empty squares) and when it was taken into account (black circles). The former are reported with the uncertainty $\delta_{\mathrm{stat}}^{\mathrm{tot}}$ given by Eq. (7.1.4), while the latter are with the uncertainty $\delta_{\mathrm{stat,mod}}^{\mathrm{tot}}$ given by Eq. (7.4.1). All distributions are given for one particular bin in W and Q^2 (W =1.6375 GeV, Q^2 =0.625 GeV^2).

Table 5.1: Relative empty cell contribution to the integral cross sections for all reported (W, Q^2)-points. The columns correspond to the Q^2 values in GeV^2 and the rows to the W values in GeV. Different shades of red correspond to different percentage range, i.e. the lightest shade corresponds to the contribution $\leq 20\%$, darker shade – from 21% to 30%, and the darkest one shows the contribution $> 30\%$.

	0.425	0.475	0.525	0.575	0.625	0.675	0.725	0.775	0.825	0.875	0.925	0.975
1.3125	–	41	34	32	35	37	41	33	33	45	35	48
1.3375	–	28	28	27	26	28	31	32	33	35	33	35
1.3625	–	28	26	23	24	25	25	25	27	27	28	27
1.3875	–	21	19	18	17	19	19	18	18	21	23	21
1.4125	–	27	20	18	17	17	18	20	19	20	20	20
1.4375	–	23	17	17	14	14	14	17	15	15	16	18
1.4625	–	21	16	14	13	13	12	13	13	13	14	16
1.4875	–	24	18	15	14	14	13	13	15	15	15	16
1.5125	–	23	18	16	15	14	14	13	14	15	16	16
1.5375	–	23	19	16	16	14	14	14	14	17	18	15
1.5625	–	22	19	16	16	15	15	15	15	17	17	17
1.5875	–	23	18	17	20	15	15	17	16	18	17	–
1.6125	26	20	17	16	15	15	15	15	17	16	15	–
1.6375	26	19	17	16	14	16	14	16	17	16	–	–
1.6625	25	19	17	15	15	15	15	17	18	17	–	–
1.6875	24	20	17	16	15	15	16	19	18	–	–	–
1.7125	23	19	17	17	16	17	19	18	–	–	–	–
1.7375	23	20	17	17	17	18	19	–	–	–	–	–
1.7625	22	20	18	18	18	19	–	–	–	–	–	–
1.7875	21	19	18	18	–	–	–	–	–	–	–	–
1.8125	21	17	–	–	–	–	–	–	–	–	–	–

5.2 Radiative correction

The incoming and scattered electrons are subject to radiative effects, which means that they can emit photons thus reducing their energy. However, in the experiment the information on these emissions is not accessible, and one has to assume the electron energy to be unchanged. Therefore, when extracting the cross sections, one assumes the energy of the incoming/scattered electron to be greater/smaller than it actually was in the reaction. This, in turn, leads to the systematic overestimation of the virtual photon energy with the consequent overestimation[2] of W. As a result, the extracted cross section is assigned to the W value higher than the actual one. This distorts the measured W spectrum and leads to its agglomeration in the high-lying region.

The common way of handling this problem is to apply the radiative correction to the extracted cross sections. In this study the radiative correction is performed using TWOPEG-D [24], which is the event generator for the double-pion electroproduction that simulates effects of the target motion. TWOPEG-D accounts for the radiative effects by means of the well-known approach of Ref. [43], which is traditionally used for the radiative corrections in the studies of double-pion electroproduction [15–19, 21–23]. In Ref. [43] the approach is applied to the inclusive case, while in TWOPEG-D, the double-pion integrated cross sections are used instead [24, 39].

In the approach [24, 39, 43] the radiative photons are supposed to be emitted collinearly either to the direction of the incoming or scattered electron (the so-called "peaking approximation"). The calculation of the radiative cross section is split into two parts. The "soft" part assumes the energy of the emitted radiative photon to be less than a certain minimal value (10 MeV), while the "hard" part is for the photons with an energy greater than that value. The "soft" part is evaluated explicitly, while

---

[2] The Q^2 value is overestimated if the incoming electron emits and underestimated if the scattered electron emits. That is why the radiative effects do not significantly impact the Q^2 dependence of the cross section.

for the calculation of the "hard" part, an inclusive hadronic tensor is assumed. The latter assumption is however considered adequate, especially taking into account that approaches that are capable of describing radiative processes in exclusive double-pion electroproduction are not yet available.

The radiative correction factor R in Eq. (4.5.1) is determined in the following way. The double-pion events either with or without radiative effects are generated with TWOPEG-D. Both radiated and non-radiated events are subjected to the smearing due to the Fermi motion of the target. Then the ratio given by Eq. (5.2.1) is taken in each $\Delta W \Delta Q^2$ bin.

$$R(\Delta W, \Delta Q^2) = \frac{\mathbb{N}_{rad}}{\mathbb{N}_{norad}}, \qquad (5.2.1)$$

where $\mathbb{N}_{rad}$ and $\mathbb{N}_{norad}$ are the weighted numbers of generated events in each $\Delta W \Delta Q^2$ bin with and without radiative effects, respectively. Note that neither $\mathbb{N}_{rad}$ nor $\mathbb{N}_{norad}$ are subject to any cuts.
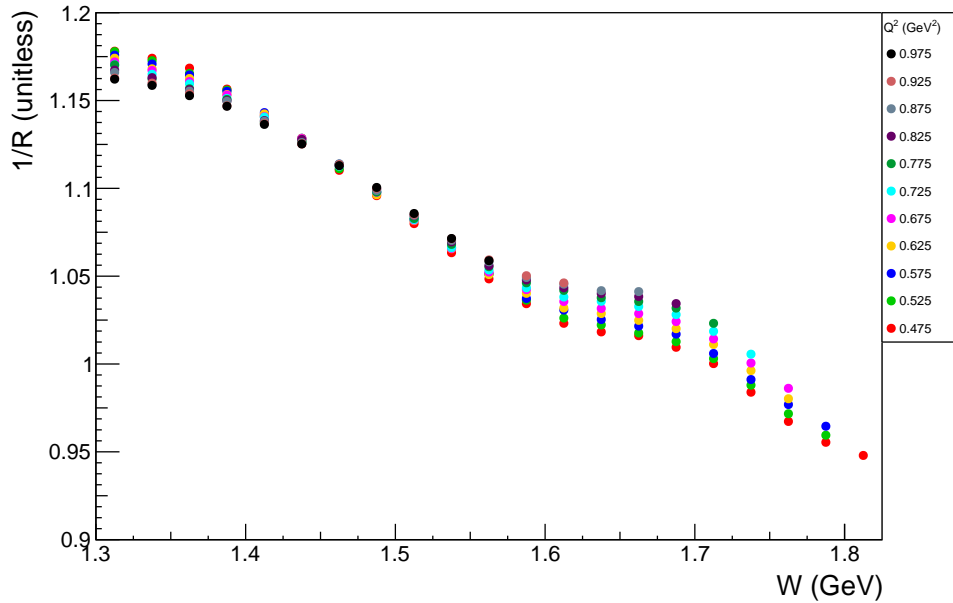
Figure 5.2: Reciprocal of the radiative correction factor $(1/R)$ as a function of W for different Q^2 bins (see Eq. (5.2.1)).

This approach gives the correction factor R only as a function of W and Q^2, disregarding its dependence on the hadronic variables. However, the need to integrate the cross section at least over four hadronic variables (see Eq. (4.5.5)) considerably reduces the influence of the final state hadron kinematics on the radiative correction factor, thus justifying the applicability of the procedure [24, 39, 43].

The quantity $1/R$ is plotted in Fig. 5.2 as a function of W for different Q^2 bins. The uncertainties associated with the statistics of generated events are very small and therefore not seen in the plot[3]. Note that the correction factor introduced in Fig. 5.2 is slightly different from that given in Ref. [22] for the same beam energy of the free proton experiment ($E_{beam} = 2.039$ GeV). This difference comes from the fact that generated events in Eq. (5.2.1) are subjected to the smearing due to the Fermi motion of the target proton.

Once this correction is applied, the extracted cross sections are treated as non-radiated, but Fermi-smeared.

5.3   Unfolding the effects of the target motion

The motion of the target proton in a deuterium nucleus introduces into this analysis some specific issues that are not inherent for the previously conducted studies of the double-pion cross sections [15–19, 21–23]. As was described in Sects. 3.5 and 4.1, the intention to use in the analysis the π^- missing topology (that serves the purpose of the cross section extraction best) leads inevitably to working under the target-at-rest-assumption. The latter, however, not only complicates the selection of exclusive events (see Sect. 3.5), but also impacts the extracted cross sections due to the following reasons.

---

[3] The total of about $2.5 \cdot 10^9$ either radiated or non-radiated events were generated in the investigated kinematic region for the calculation of the radiative correction factor.

- One has to use the smeared reaction invariant mass W_{sm} for the cross section binning (see Sect. 4.1). As a result, the extracted cross section is assigned to the W value different from the actual one. This makes both integral and single-differential cross sections to be distorted.

- One has to use an approximate Lab to CMS transformation that ignores the target motion (see Sect. 4.2). This approximation introduces some inaccuracy to the measured angular (θ, φ, and α) distributions without having an impact on the invariant mass distributions and W and Q^2 cross section dependencies due to their Lorentz invariance.

The former effect is thought to have a much greater impact on the cross section than the latter. Thus, being folded with the aforementioned effects of the target motion, the extracted cross sections are seeking the corresponding unfolding correction. This correction is performed by means of two Monte Carlo event generators TWOPEG [39] and TWOPEG-D [24]. TWOPEG is the event generator for the double-pion electroproduction off the free proton that currently provides the best cross section estimation in the investigated kinematic region. TWOPEG-D is the event generator for the same exclusive reaction but off the proton that moves in the deuterium nucleus. This event generator was especially developed to be used in the studies, where the experimental information of the target proton momentum is inaccessible, and one is forced to work under the target-at-rest-assumption. TWOPEG-D convolutes the double-pion cross section with effects of the target motion and thus imitates the conditions of the experimental cross section extraction.

To calculate the correction factor, two samples of double-pion events produced either off the proton at rest and off the moving proton were generated (with TWOPEG and TWOPEG-D, respectively). Both event generators provide the particle's four-momenta written in the Lab system and distribute events according to the corresponding electron-scattering cross section. As the reaction invariant mass both samples use

96

the value calculated from the initial particles (see Eq. (4.1.1)), which for the "moving proton" events is calculated under the target-at-rest-assumption (as was done for the cross section calculation). The generated four-momenta are then subject to the transformation to the CMS. For both samples the transformation is performed according to the procedure given in App. A for the case of the proton at rest. For the "moving proton" sample, this approximation introduces in the event distributions the same inaccuracy as appears in the extracted cross sections. Then the kinematic variables are calculated and the generated events of both samples are binned in the same way as the extracted cross sections (see Sect. 4.4).

Therefore, the distributions of events generated with TWOPEG-D acquire the same inaccuracies as the extracted cross sections, i.e. the value W_{sm} is used for the binning and the approximate Lab to CMS transformations are applied. The manifestation of these inaccuracies differs depending on various final state variables and has a strong W dependence as Figs. 5.3 and 5.4 demonstrate. These figures show the single-differential distributions of $\mathbb{N}_{nofermi}$ (blue symbols) and $\mathbb{N}_{fermi}$ (black symbols), which are the weighted numbers of events generated with TWOPEG and TWOPEG-D, respectively. In Fig. 5.3 these distributions are shown for a low $W =$ 1.3375 GeV, while in Fig. 5.4 they are shown for a higher $W = 1.5625$ GeV. The uncertainties associated with the statistics of generated events are very small and therefore not seen in the plots[4].

As seen from Figs. 5.3 and 5.4, the target motion considered under the itemized conditions listed above affects mostly the cross section near the threshold, while for higher W their impact is significantly less pronounced. This happens due to the following. Let's consider a particular W_{true} bin. As shown in Ref. [24], each value of W_{true} corresponds to a sequence of W_{sm} values, which are symmetrically scattered in the vicinity of W_{true} with a spread of 50-100 MeV. This leads to the fact that

---

[4] For each event sample the total of about $2.5 \cdot 10^{10}$ events were generated in the investigated kinematic region for the calculation of the correction factor.
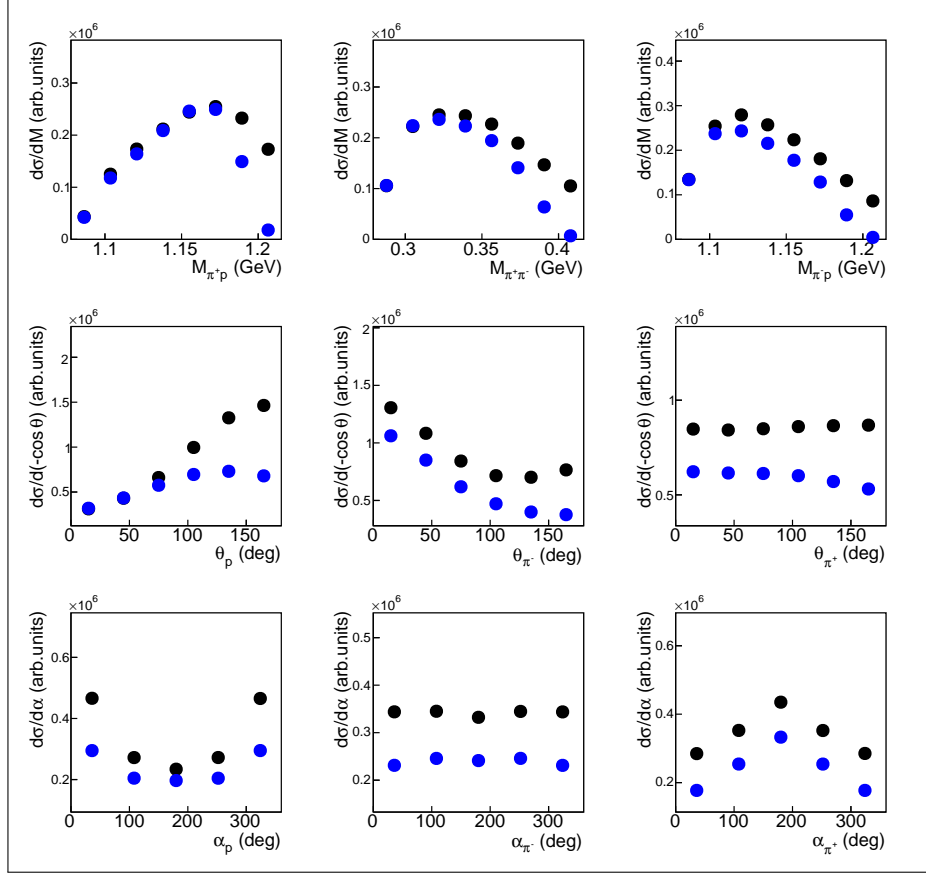
Figure 5.3: Single-differential distributions of generated double-pion events produced off the proton at rest (blue symbols) and off the moving proton (black symbols). The former were generated with TWOPEG [39] and the latter with TWOPEG-D [24]. The example is given for the particular $\Delta W \Delta Q^2$ bin with the central point at $W = 1.3375$ GeV and $Q^2 = 0.475\,\text{GeV}^2$. As this bin is located near the threshold, the moving proton distributions (black symbols) have a high relative event excess comparing with the free proton distributions (blue symbols). See text for details.
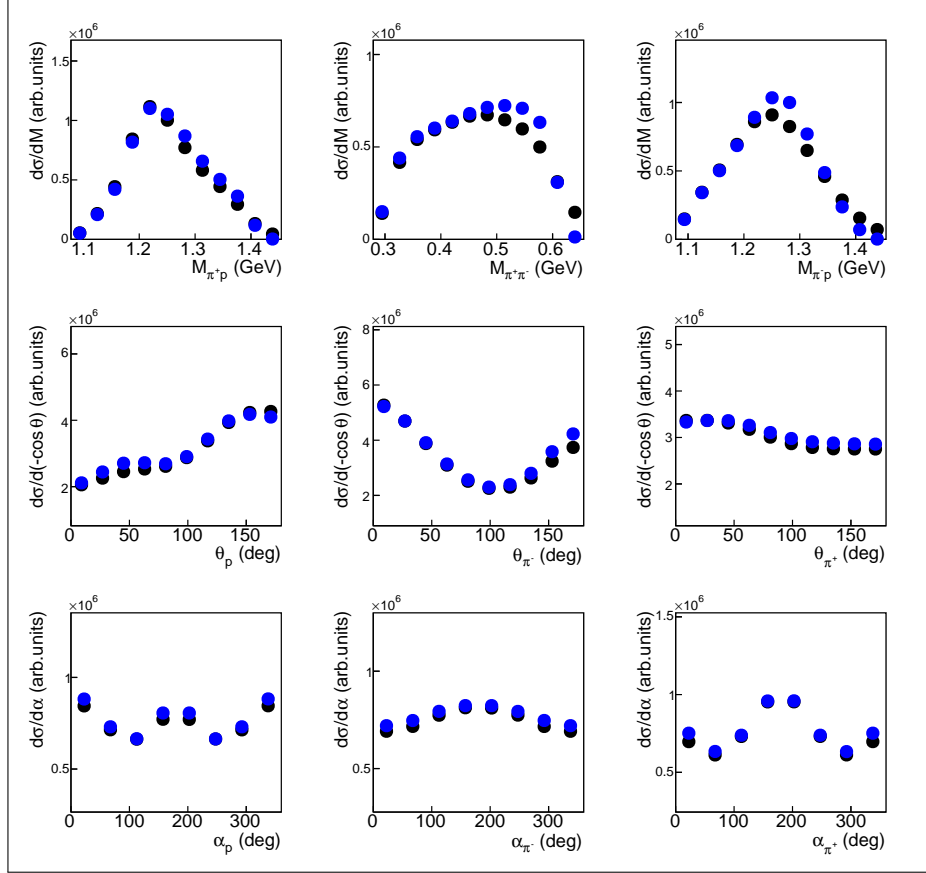
Figure 5.4: Single-differential distributions of generated double-pion events produced off the proton at rest (blue symbols) and off the moving proton (black symbols). The former were generated with TWOPEG [39] and the latter with TWOPEG-D [24]. The example is given for the particular $\Delta W \Delta Q^2$ bin with the central point at $W = 1.5625$ GeV and $Q^2 = 0.475$ GeV^2. As the bin is located in the peak region, the moving proton distributions (black symbols) have a small relative event deficit comparing with the free proton distributions (blue symbols). See text for details.

the same bin in W_{sm} has a different number of events compared to the W_{true} bin. This difference depends on the cross section behavior in the vicinity of 50-100 MeV of this bin. The cross section abruptly rises from the threshold with a strong convex nonlinearity, which smooths as W grows up to 1.4 GeV, and then turns to a concave nonlinearity forming the left slope of the resonance peak at 1.5 GeV. Then the cross section modestly increases and decreases several times changing its nonlinearity type. In any W_{true} subrange the cross section can be written as $a + f(W)$, where $a = const$, while $f(W)$ evolves from zero and determines the cross section nonlinearity within the subrange. Then the absolute variation in the event number in W_{sm} bin is determined solely by the nonlinearity of the function $f(W)$, i.e. convex nonlinearity leads to an event excess in the bin, while concave nonlinearity – to an event deficit. Hence, in the resonance peaks an event deficit is observed, while the region close to the threshold and the dip between the peaks have an event excess. However, the relative event variation depends on a and is higher for smaller a. The smallest value of a is reached at the threshold ($a = 0$), therefore the near-to-threshold subrange has the greatest relative variation of event number.

Indeed, in Fig. 5.3, which is plotted for the W bin located close to the threshold, the moving proton distributions (black symbols) have a high relative event excess compared to the free proton distributions (blue symbols). Meanwhile, in Fig. 5.4, which is plotted for the W bin located at the peak region, the moving proton distributions (black symbols) have small relative event deficit comparing with the free proton distributions (blue symbols).

For the low W region (as in Fig. 5.3) it is noteworthy that a very large relative difference between the free proton and the moving proton cross sections is observed for the right part of the invariant mass distributions. This happens due to the phase space broadening with W that takes place for invariant masses (see App. B). The invariant mass distribution typically has a maximum in the middle and gradually goes to zero

on both edges. The lower the W value is, the narrower is the distribution width. As W grows, the distribution widens to the right and goes to zero farther away. Meanwhile, each bin in W_{sm} contains a mixture of events with the values of W_{true} spread within 50-100 MeV near this bin. For low W this spread is comparable with the total width of the invariant mass distribution. Therefore, the right distribution side acquired the event excess that comes from the same bins in invariant mass but located at higher W_{true} and hence having high cross sections.

The unfolding correction is performed in each multi-dimensional bin of the double-pion production phase-space (see Sect. 4.3 as well as App. B), i.e. in each $\Delta W \Delta Q^2 \Delta^5 \tau$ bin the cross section is divided by the correction factor $\mathcal{F}$ (see Eq. (4.5.1)) that is calculated as

$$\mathcal{F}(\Delta W, \Delta Q^2, \Delta^5 \tau) = \frac{\mathbb{N}_{fermi}}{\mathbb{N}_{nofermi}}, \tag{5.3.1}$$

where $\mathbb{N}_{nofermi}$ and $\mathbb{N}_{fermi}$ are the weighted numbers of generated double-pion events in the $\Delta W \Delta Q^2 \Delta^5 \tau$ bin produced off the proton at rest and off the moving proton, respectively. Both event samples were generated without radiative effects, since the correction factor $\mathcal{F}$ is applied to the cross sections that are already corrected for the radiative effects (see Sect. 5.2).

The impact of the unfolding correction on the extracted integral cross sections is illustrated in Fig. 5.5, where the distributions before the correction are plotted in orange, while the distributions after the correction are plotted in dark blue. The comparison is given for two Q^2 bins. As was expected, the correction causes a slight cross section increase in the resonance peaks and a decrease near the threshold and in the dip between the peaks.

The value of the correction factor in Eq. (5.3.1) depends on both the free proton cross sections and the model of the deuteron wave function that were employed in the event generators. The former relies strongly on the JM model fit of the available data on double-pion cross sections, while for the latter the Bonn model was used (see
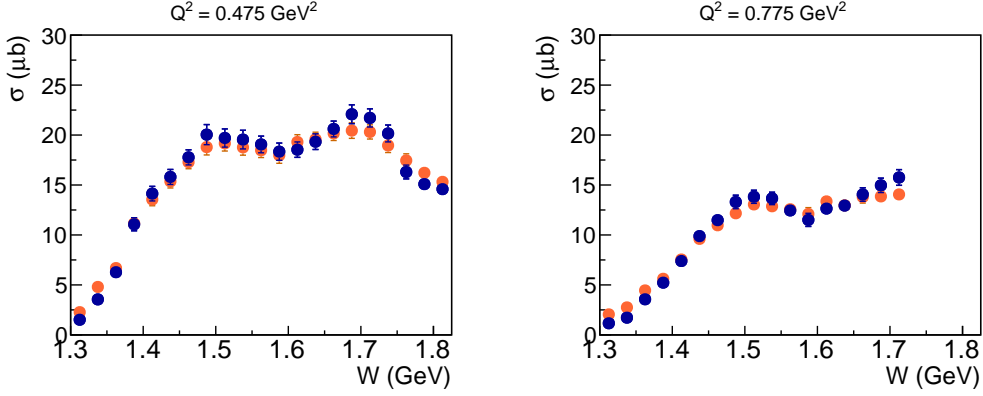
Figure 5.5: Impact of the unfolding correction on the extracted integral cross sections. The cross section before the correction is plotted in orange, while the cross section after the correction is plotted in dark blue (both are divided by the virtual photon flux). The comparison is given for two Q^2 bins as specified above the plots.

Refs. [24, 39] for more detail). Therefore, the uncertainty of the extracted cross sections that comes from this unfolding correction is attributed to the model dependence uncertainty and is discussed in Sect. 7.2.

Once corrected for the effects of the target motion and then divided by the virtual photon flux, the cross section is treated as the true virtual photoproduction cross section and is attributed to the central point of the corresponding $\Delta W \Delta Q^2 \Delta^5 \tau$ bin.

5.4   Correction for binning effects

The cross section, extracted in bins of a finite size, is assigned to the central point of a bin. On this way the cross sections acquire binning caused distortions and, therefore, are seeking the corresponding corrections. In this section, which is devoted to the binning effects, two separate binning issues are distinguished, i.e. (i) the specific issue of affecting the cross section value in the next to last point of the invariant mass distributions and (ii) the common binning issue that impacts the cross section value in any bin of finite size.

Let's address the specific binning issue in the invariant mass distributions first. As shown in Sect. 4.4, the binning in invariant mass requires special attention due to the broadening of the reaction phase-space with W (see App. B) and the corresponding W dependence of the upper boundary of the invariant mass distributions (see Eq. (4.4.1)). This effect makes the upper boundary M_{upper} to be indistinct, since the cross section is calculated in a bin $W_{left} < W < W_{right}$. To deal with this difficulty, the value of M_{upper} is calculated using W_{center}, the center of the W bin. Then a specific arrangement of mass bins is used, which forces the last bin to be situated completely out of the boundaries given by Eq. (4.4.1) using W_{center}. When integrating the cross section over the mass distribution, the events in the extra bin are included, but a cross section for this bin is not reported.

Meanwhile, the cross section in the next to last bin (labeled as bin number $N_{bins} - 1$) should be treated carefully. This is best illustrated in Fig. 5.6, which shows schematically the event distribution in mass, ending in M_{upper} for three choices of W at W_{left} (dot-dashed), W_{center} (solid) and W_{right} (dashed). The black points at $M_{left}^{N_{bins}-1}$ and $M_{right}^{N_{bins}-1}$ show the left and right boundaries of the next to last bin, respectively. In the next to last bin events with $W < W_{center}$ are distributed over a range, which is less than ΔM defined by Eq. (4.4.2). However, when extracting the cross sections, the event yield was divided by the full bin width ΔM, thus leading to an underestimation of the cross section.

The correction for this effect was taken from Ref. [22, 23]. It was made using the TWOPEG double-pion event generator [39]. The correction factor to the cross section in the next to last bin is the ratio of the simulated cross sections calculated with fixed ΔM defined by Eq. (4.4.2) and with $\widetilde{\Delta M} = W - m_{h_3} - M_{left}^{N_{bins}-1}$, which was different for each generated event. This factor provides the correction to the cross section in the next to last bin that varied from $\sim 5\%$ to $\sim 10\%$.
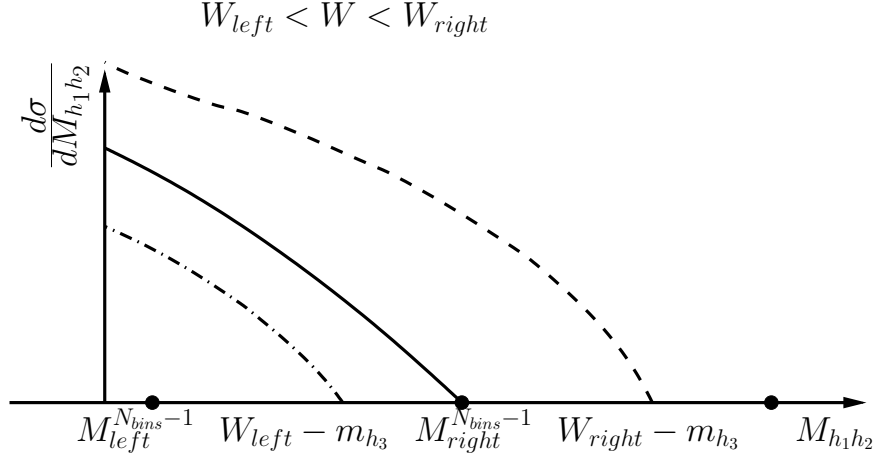
Figure 5.6: Schematic representation of the invariant mass distributions ending in M_{upper} calculated according to Eq. (4.4.1) for three choices of W at W_{left} (dot-dashed), W_{center} (solid) and W_{right} (dashed). The black points at $M_{left}^{N_{bins}-1}$ and $M_{right}^{N_{bins}-1}$ show the left and right boundaries of the next to last bin, respectively, while the remaining point marks the right boundary of the last mass bin.

Let's now address the common binning issue that impacts the cross section value in any bin of a finite size. Extracted in a finite bin, the cross section is subject to averaging within this bin. For instance, if there is a sharp peak in the middle of a bin, then the average value of the cross section in that bin will always be smaller than the peak value. Any non-linear behavior of the cross section will likely result in an offset of the obtained value. There are two methods of correcting this offset, i.e. (i) to correct the kinematic quantities associated with the bin and use the corrected values instead of the central values or (ii) to correct the cross section value in the center of the bin. Both these methods are widely used for the binning corrections. In the studies of double-pion cross sections, however, the second method has become conventional [17, 18, 22, 23]. Therefore, in this study the second method is chosen, in order to keep the initial binning over the kinematic variables and to facilitate the cross section comparison with the results obtained off the proton at rest [22, 23].

In this study one-dimensional binning corrections are performed, i.e., the cross section dependence on each kinematic variable x is corrected individually (where x

corresponds to W, Q^2, and hadron variables). In any one-dimensional bin $[x_{min}, x_{max}]$ the cross section value is multiplied by the correction factor C_{bin}. To estimate this factor some assumptions about the cross section behavior within the bin are needed, and hence, the cross section shape should be described by a continuous function $f(x)$. The multiplicative correction factor C_{bin} is then calculated in each bin $[x_{min}, x_{max}]$ as

$$C_{bin} = \frac{f(x_{center})}{\int\limits_{x_{min}}^{x_{max}} f(x)dx} \ , \tag{5.4.1}$$

where x_{center} is the central point of the $[x_{min}, x_{max}]$ bin.

For the single-differential distributions a cubic spline approximation is chosen to continuously describe the cross section shape, as shown in Fig. 5.7. The black and red points in this figure are the cross sections before and after binning corrections, respectively, and the curves correspond to the spline approximation. For the invariant mass and θ angular distributions the splines are forced to pass through the intermediate points that are obtained by averaging over two neighboring cross section points. This method reduces the splines sensitivity to accidental cross section fluctuations. Besides this, for the invariant mass distributions the splines are required to give zero at the distribution edges. For the α angular distributions the splines are forced to pass through the points that are obtained by averaging over two cross section points symmetrical with respect to $\alpha = 180°$. This approach reflects the fact that after the integration over φ, the cross section must be symmetrical in the α angle (meanwhile, the extracted experimental distributions are slightly asymmetrical)[5].

The integral cross sections are subjected to individual corrections of the Q^2 dependence inside the W bins and the W dependence inside the Q^2 bins, as shown on the left and right plots of Fig. 5.8, respectively. In this figure black and red points represent

_____

[5] Although the φ distributions are not reported here, they were nevertheless extracted and added to the CLAS physics database [5]. The φ distributions were thus subjected to the binning correction with the same approach used for the θ distributions.
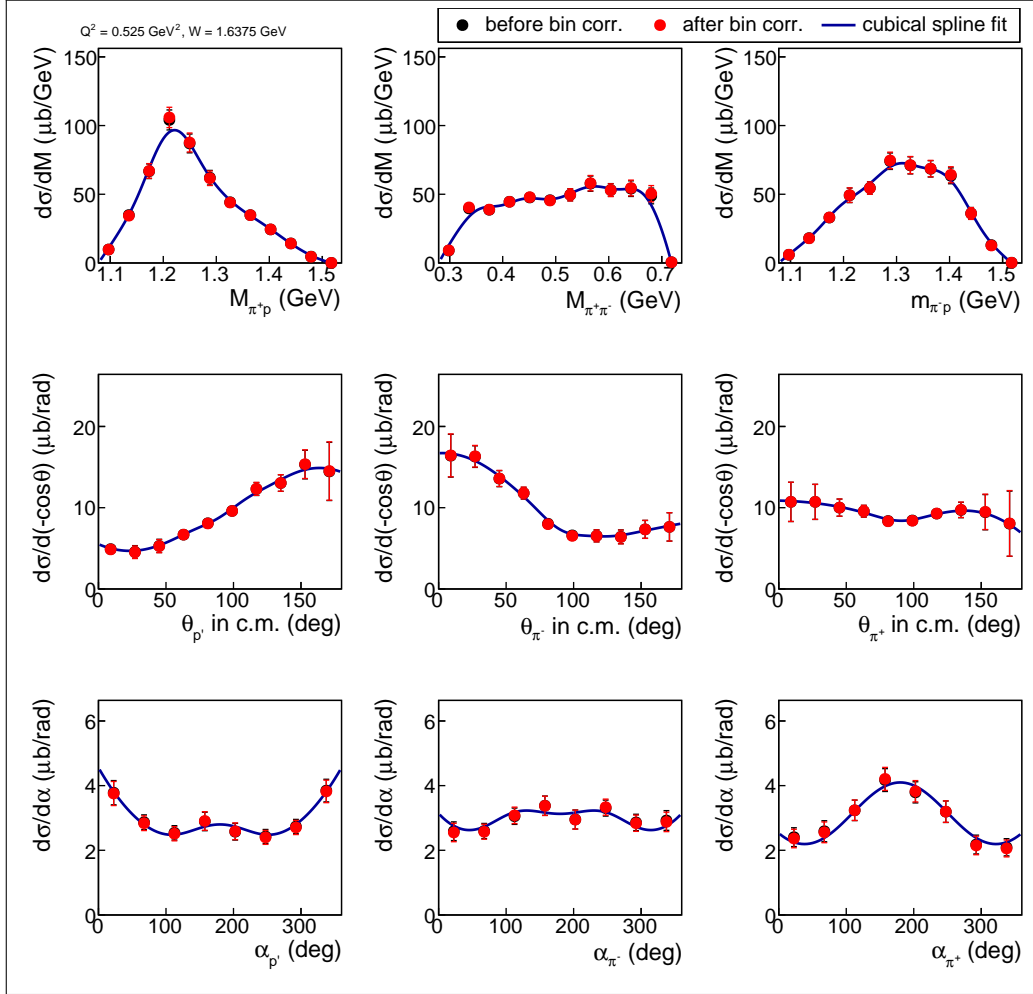
Figure 5.7: Single-differential cross sections as functions of the final hadron variables before (black points) and after (red points) the binning corrections. Curves represent a cubic spline approximation. The example is given for a particular $\Delta W \Delta Q^2$ bin with the central point $W = 1.6375$ GeV and $Q^2 = 0.525$ GeV^2.

the cross section values before and after binning corrections, respectively, while the curves correspond to the continuous cross section approximation. The latter are based on a second order polynomial fit of the Q^2 distributions (left plot) and on a cubic spline approximation for the W distributions (right plot). The splines are forced to pass through the intermediate points that are obtained by averaging over two neighboring cross section points. In this way, the integral cross section value in each $\Delta W \Delta Q^2$ bin acquires two multiplicative correction factors. The corrections obtained for the integral distributions are then propagated to the single-differential cross sections.
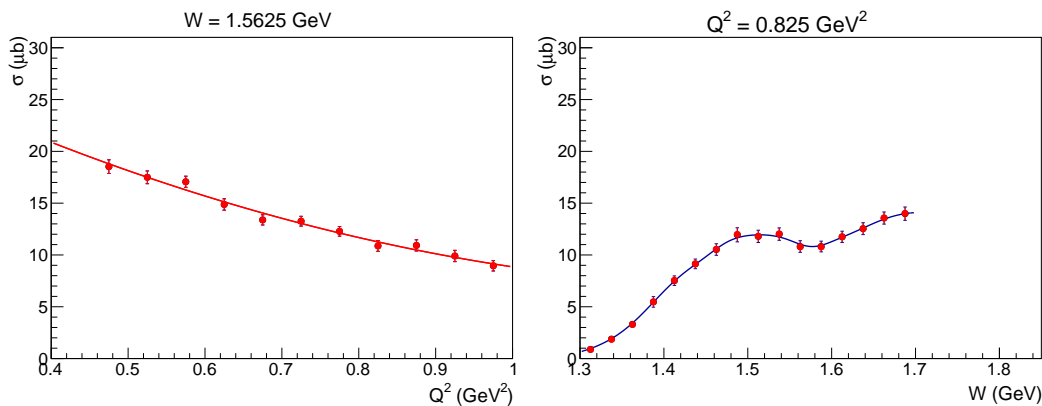
Figure 5.8: Q^2 dependence (left plot) and the W dependence (right plot) of the integral cross sections before (black points) and after (red points) the binning corrections. The curves correspond to a second order polynomial fit for the left plot and a cubic spline approximation for the right one. Each distribution is plotted for one particular bin as specified above the plots.

Since in this analysis a relatively fine binning in all kinematic variables is chosen (see Sect. 4.4), the effect of the binning corrections is almost insignificant. This is why in Figs. 5.7 and 5.8 the black points (before the correction) are almost completely covered by the red ones (after the correction). For the Q^2 dependences the correction factors are less than 1% in all bins, and for the W dependences they are $\sim$2%-3% for the first two low W bins and less than 1% in all other bins. For the single-differential distributions, the corrections are on the level of 1%-2% for the majority of bins, but rise for some points (mostly at low W) up to 5%-6%.

Chapter 6

Normalization verification

To prove the credibility of an extracted observable, some well-established quantity is commonly used as a reference point. For this purpose one can use already published measurements of this observable, if they exist in the desired kinematic region, but this usually is not the case. Alternatively, one can focus on some quantity, which can be reliably approximated in this kinematic region by a theoretical model or parameterization. This auxiliary quantity is then extracted from the analyzed dataset, and the comparison of the measured value with the approximated one allows the reliability of the main result to be judged.

For experiments off free protons, the elastic cross section usually serves as such a reference quantity as it can be approximated in a wide kinematic region by P. Bosted parameterization with an excellent accuracy of a few percent, as Ref. [47] demonstrates (see App. B there). Thus, an agreement between the auxiliary measured elastic cross section with the parameterized one, if achieved, indicates both the correct normalization of the main result and the trustworthy quality of the electron selection.

Meanwhile, for experiments off a deuterium target, the quasi-elastic cross section off nucleons can serve as the corresponding reference quantity. However, this observable, if compared with the elastic free proton cross section, is less understood and lacking the same quality of theoretical description [47]. Nonetheless, several techniques have been developed in this matter with the Bosted parameterization of the deuteron quasi-elastic peak being the most commonly used tool.

Ref. [47] gives some details on the performance of the Bosted parameterization of the deuteron quasi-elastic peak [48, 49] and tests its ability to describe experimental data by comparing the parameterized cross sections with published measurements [50–52]. This testing, being performed in the Q^2 range from ~ 0.3 GeV^2 to ~ 4 GeV^2, is of great importance for the current analysis as its Q^2 coverage falls within this range.

As follows from Ref. [47], the Bosted parameterization in its default implementation systematically overestimates the measured integrals under the quasi-elastic peak and the overall description quality gradually decreases from several percent to almost 20% as Q^2 grows from 0.3 GeV^2 to 4 GeV^2. The default implementation corresponds to the case when the nuclear scaling function is estimated using a PWIA calculation and the Paris deuteron wave function (see Refs. [48, 49] for details).

Meanwhile, as also shown in Ref. [47], the Bosted parameterization in its alternative implementation systematically underestimates the corresponding integrals with the description quality gradually increasing from ~ 15% to a few percent as Q^2 grows from 0.3 GeV^2 to 4 GeV^2. The alternative implementation corresponds to the case when the nuclear scaling function is estimated according to the parameterization from Ref. [53] and is available with some minor modifications of the source code.

Besides this, Ref. [47] describes a useful approximation formula for the cross section at the quasi-elastic peak, which came from Durand's theory [54]. This formula is of particular interest for this analysis, since it describes very nicely the experimental peak values in the Q^2 range from ~ 0.3 GeV^2 to ~ 1.8 GeV^2. As shown in Ref. [47], the normalization of the cross section distributions of the Bosted parameterization to the values provided by this formula improves the data description quality in this Q^2 range.

Once we have acquired an impression of the performance and reliability of the parameterizations currently available for the deuteron quasi-elastic peak, let's now estimate the quasi-elastic cross section from the analyzed dataset and then perform its comparison with the cross section approximated by various implementations of

the Bosted parameterization. This investigation is carried out in the framework established in Ref. [47] and therefore, uses the same notations and color codes.

To extract the cross section in the region of the quasi-elastic peak, the only particle that should be registered is the scattered electron. With the electron selection being exactly the same as for the double-pion cross section extraction, the quasi-elastic cross section is defined in each $\Delta E' \Delta \theta_{e'}$ bin by

$$\frac{d\sigma_{exp}}{d\Omega dE'} = \frac{1}{2\pi} \cdot \frac{\left(\frac{N_{full}}{Q_{full}} - \frac{N_{empty}}{Q_{empty}}\right)}{\Delta E' \Delta (-\cos\theta_{e'})[\mathcal{L}]} \cdot \frac{N_{gen}}{N_{rec}}, \qquad (6.1)$$

where N_{full} and N_{empty} are the numbers of selected events inside the $\Delta E' \Delta \theta_{e'}$ bin for runs with deuterium and empty target, respectively. N_{gen} and N_{rec} come from the Monte Carlo simulation and correspond to the numbers of generated and reconstructed quasi-elastic events inside the $\Delta E' \Delta \theta_{e'}$ bin, respectively. The latter were subject to the same electron selection cuts as the experimental events. For the Monte Carlo simulation an event generator based on the measurements from Ref. [10] was used. The other variables are defined in the context of Eq. (4.5.1).

The cross section calculated according to Eq. (6.1) is shown by the black symbols in Fig. 6.1 (note that it is the radiated cross section). The blue and green histograms in this figure correspond to the Bosted parameterization with the default and alternative methods of calculating the nuclear scaling function, respectively. The green horizontal lines correspond to the prediction of the peak value given by the aforementioned approximation formula.

Since the experimental cross section is radiated, while the parameterized cross section is not, their visual comparison looses informativeness. To judge more definitely the agreement of the measurement with the parameterization, the corresponding integrals under the quasi-elastic peak were compared. The distributions were integrated within the limits shown by the vertical lines in Fig. 6.1. To determine the positions of these limits, the procedure suggested in Ref. [47] was used. First,

110
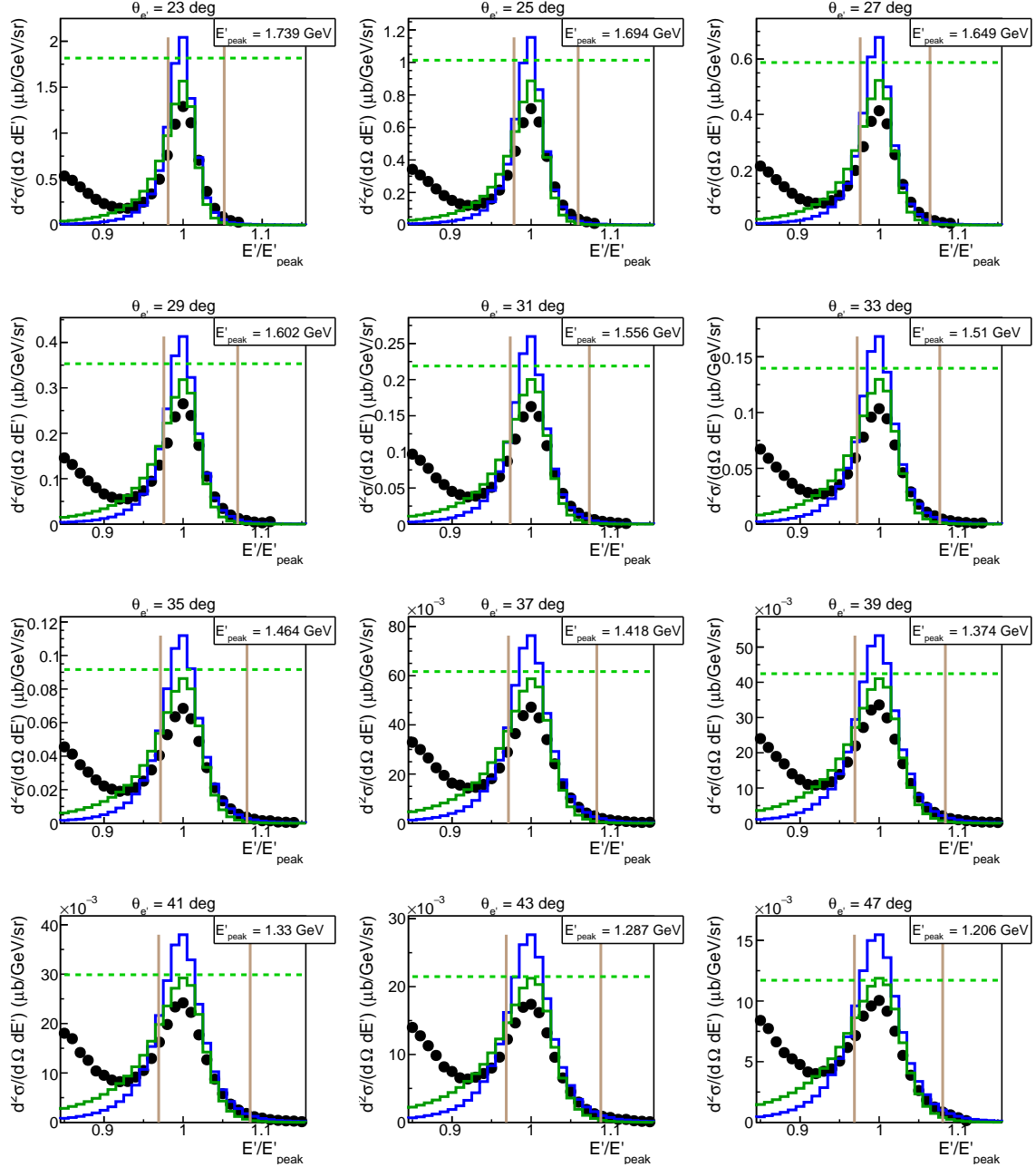
Figure 6.1: Black symbols correspond to the (radiated) cross section in the region of the quasi-elastic peak extracted from the analyzed dataset according to Eq. (6.1). The results of the Bosted parameterization [48, 49] are shown by the histograms. The blue histograms correspond to the default method to calculate the nuclear scaling function, while the green histograms to the alternative method. The green horizontal lines correspond to the peak values approximated by the formula described in Ref. [47]. The vertical lines correspond to the integration limits.

the quasi-elastic peaks in the experimental spectra were fit by Gaussians with polynomial background. Then the values $\mu - \sigma$ and $\mu + 3\sigma$ were set as the left and right integration limits, respectively, with μ and σ being the mean value and the standard deviation of the corresponding Gaussian function. The integration limits were chosen to be asymmetrical in order to minimize the inelastic background under the quasi-elastic peak. This procedure of obtaining the integration limits allows to achieve consistency among all plots, since the width of the quasi-elastic peak and its proximity to the inelastic part of the spectrum depend on the kinematics.

The experimental integrated cross sections were divided by the radiative correction factors (R), which were calculated in each $\theta_{e'}$ bin according to the Mo&Tsai approach [43]. These correction factors are listed in Tab. 6.1 together with the positions of the corresponding left integration limits. The peak cross section values given by the approximation formula are also given there. The last four columns contain the values of the ratio of the experimental integral under the quasi-elastic peak (σ_{exp}) to that obtained from the Bosted parameterization with the nuclear scaling function calculated by the default (σ_{par}^1) and alternative (σ_{par}^2) methods. The index *norm* indicates that the parameterization histogram was scaled in a way that its maximum is equal to the prediction of the considered approximation formula. The cells' coloring is the same as for Tab. 1 in Ref. [47], i.e. the dark-green shade stands for deviations $\leq 5\%$, light-green for 5%-10%, and light-red for more than 10%.

The ratios of the experimental integrals to the parameterized ones are also shown in Fig. 6.2 as a function of the polar angle of the scattered electron ($\theta_{e'}$). The left side corresponds to the case, when the nuclear scaling function was calculated by the default method (blue symbols), while for the right side it was calculated by the alternative method (green symbols). The top row stands for the unscaled parameterization histograms, while for the bottom row they were scaled to the peak value given by the approximation formula.

Table 6.1: Ratios of the experimental integrals under the quasi-elastic peak (σ_{exp}) obtained from the analyzed dataset to those obtained from the Bosted parameterization [48, 49] with the nuclear scaling function calculated by the default (σ_{par}^1) and alternative (σ_{par}^2) methods. The index *norm* means that the parameterization histogram was scaled in a way that its maximum was equal to the prediction of the formula described in Ref. [47]. The dark-green shade stands for deviations $\leq 5\%$, light-green for 5%-10%, and light-red for more than 10%.

$\theta_{e'}$, deg	Q^2, GeV^2	E'_{peak}, GeV	Left cut	R	σ^{peak}, μb	$\sigma_{exp}/\sigma_{par}^1$	$\sigma_{exp}/\sigma_{par,\ norm}^1$	$\sigma_{exp}/\sigma_{par}^2$	$\sigma_{exp}/\sigma_{par,\ norm}^2$
23	0.56	1.739	0.9811	0.8222	1.817E0	0.91	1.03	1.13	0.98
25	0.65	1.694	0.9784	0.8280	1.014E0	0.89	1.02	1.10	0.96
27	0.73	1.649	0.9761	0.8325	5.876E-1	0.87	1.00	1.07	0.95
29	0.82	1.602	0.9757	0.8324	3.531E-1	0.89	1.04	1.10	0.99
31	0.91	1.556	0.9736	0.8362	2.188E-1	0.87	1.03	1.07	0.98
33	0.99	1.51	0.9722	0.8384	1.397E-1	0.85	1.02	1.05	0.97
35	1.08	1.464	0.9715	0.8394	9.162E-2	0.84	1.02	1.04	0.98
37	1.17	1.418	0.9714	0.8390	6.167E-2	0.83	1.03	1.04	0.99
39	1.25	1.374	0.9694	0.8427	4.244E-2	0.83	1.04	1.04	1.00
41	1.33	1.33	0.9691	0.8428	2.988E-2	0.84	1.07	1.05	1.03
43	1.41	1.287	0.9686	0.8436	2.147E-2	0.83	1.07	1.04	1.03
45	1.49	1.246	0.9680	0.8444	1.571E-2	0.83	1.09	1.04	1.04
47	1.56	1.206	0.9688	0.8427	1.171E-2	0.83	1.10	1.04	1.05
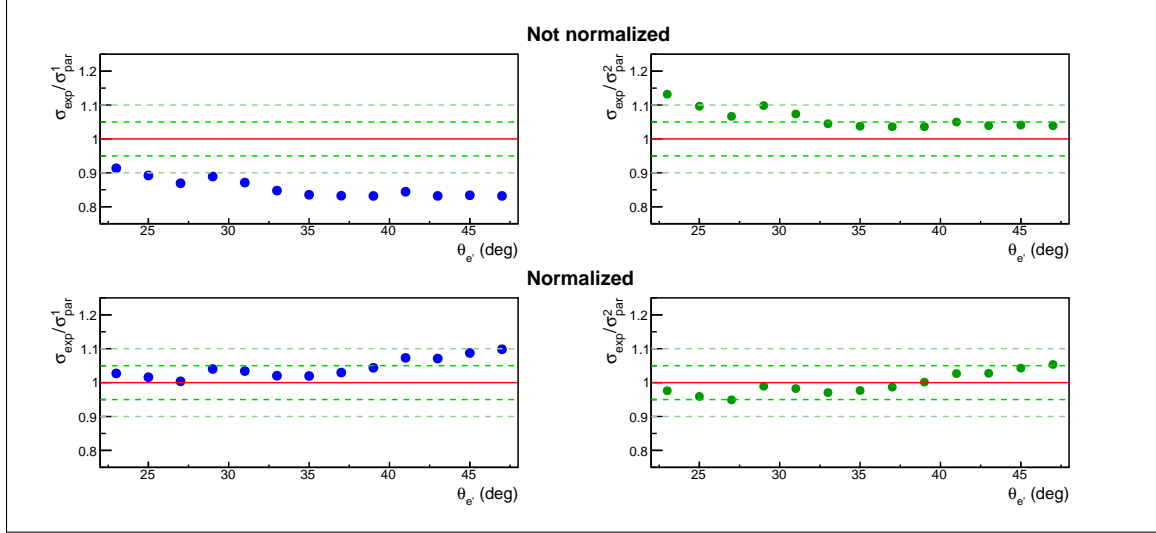
Figure 6.2: Ratios of the experimental integral under the quasi-elastic peak to the parameterized one as a function of the angle $\theta_{e'}$. The left side corresponds to the case, when the nuclear scaling function was calculated by the default method (blue symbols), while for the right side it was calculated by the alternative method (green symbols). The top row stands for the unscaled parameterized histograms, while for the bottom row, they were scaled to the peak value approximated by the formula described in Ref. [47]. The red solid line marks the position of unity. The dark-green dashed lines mark the deviation of 5%, while the light-green ones show the deviation of 10%.

As seen from both Tab. 6.1 and Fig. 6.2, the measured integrals under the quasi-elastic peak were found to be lower than the values given by the Bosted parameterization in its default implementation and their difference increases from $\sim 10\%$ to $\sim 15\%$ as Q^2 grows. The measured integrals were also found to be higher than the values given by the Bosted parameterization in its alternative implementation with the difference decreasing with Q^2 from $\sim 10\%$ to $\sim 5\%$. Meanwhile, if the parameterization histograms are scaled to the peak values predicted by the formula described in Ref. [47], the corresponding ratio stays in the vicinity of unity with a reasonable deviation for both options of scaling function calculation.

This result is fully consistent with the conclusion made in Ref. [47] regarding the ability of the Bosted parameterization to describe experimental measurements in this kinematic region. The deviations of the measured integrals from their parameterized

114

values revealed in this analysis and the Q^2 behavior of those deviations are almost exactly the same as those found in Ref. [47] for already established measurements.

Thus, one can conclude that the quality of agreement between the quasi-elastic cross section estimated in this analysis with the Bosted parameterization [48, 49] is the same as was observed for other published measurements. This, in turn, indicates that in this particular analysis, both the electron selection and overall cross section normalization are under control.

The value of the uncertainty due to normalization and electron identification is then estimated considering the following arguments.

- as shown in this chapter, the quasi-elastic cross section extracted from the current dataset have the same quality of agreement with the Bosted parameterization as other published measurements demonstrate [47];

- as follows from Tab. 6.1 and Fig. 6.2, one can achieve a good ∼5% agreement between the measured and parameterized values of the quasi-elastic cross sections when the parameterized distributions are normalized to the peak values approximated by the formula that was proven to describe well the experimental peak cross sections in this kinematic region [47];

- as shown in [22, 23], the elastic cross section off protons estimated from the same "e1e" run period (as it included both hydrogen and deuterium target runs in the same experimental configuration) agrees within ∼3% with the corresponding Bosted parameterization. The latter, meanwhile, employs the same empirical fit of the nucleon electromagnetic form factors as the Bosted parameterization of the quasi-elastic cross section off deuteron used in the current study [55].

Taking these facts into account, a 5% global uncertainty is assigned to the extracted double-pion cross sections due to potential inaccuracies in the normalization and electron selection.

Chapter 7
Cross section uncertainties

In this study (like in other studies of the double-pion cross sections [15–19, 21–23]) three separate types of the cross section uncertainties are considered, i.e. statistical uncertainty, uncertainty due to the model dependence, and systematic uncertainty. The recipe for estimating the uncertainty of each type is given below.

7.1   Statistical uncertainties

The limited statistics of both the experimental data and the Monte Carlo simulation are the two sources of statistical fluctuations of the extracted cross sections. The cut on the efficiency uncertainty described in Sect. 4.6 was chosen in a way that the latter source gives a minor contribution to the total statistical uncertainty.

The statistical uncertainty to the five-fold differential virtual photoproduction cross section is calculated individually in each non-empty multi-dimensional $\Delta^5\tau$ bin as described below.

The absolute statistical uncertainty due to the limited statistics of the experimental data is calculated in the non-empty bins as (see Eq. (C.1) in App. C).

$$\delta_{\text{stat}}^{\text{exp}}(\Delta^5\tau) = \frac{1}{\mathcal{E}\cdot R\cdot \mathcal{F}\cdot \Gamma_v} \cdot \frac{\sqrt{\left(\frac{N_{\text{full}}}{Q_{\text{full}}^2} + \frac{N_{\text{empty}}}{Q_{\text{empty}}^2}\right)}}{\Delta W\cdot \Delta Q^2\cdot \Delta^5\tau\cdot \mathcal{L}}, \tag{7.1.1}$$

where Γ_v is the virtual photon flux given by Eq. (4.5.3), while the other ingredients are explained after Eq. (4.5.1).

The absolute uncertainty due to the limited Monte Carlo statistics is estimated in the non-empty bins as (see Eq. (C.2) in App. C).

$$\delta_{\text{stat}}^{\text{MC}}(\Delta^5 \tau) = \frac{\mathrm{d}^5 \sigma_v}{\mathrm{d}^5 \tau} \left(\frac{\delta \mathcal{E}}{\mathcal{E}} \right), \tag{7.1.2}$$

where $\frac{\mathrm{d}^5 \sigma_v}{\mathrm{d}^5 \tau}$ is the virtual photoproduction cross section given by Eq. (4.5.2), $\mathcal{E}$ is the efficiency inside the multi-dimensional bin defined by Eq. (4.6.1), while $\delta \mathcal{E}$ is its absolute statistical uncertainty.

Meanwhile, the calculation of the efficiency uncertainty $\delta \mathcal{E}$ is not straightforward and needs special attention, since (i) N_{gen} and N_{rec} in Eq. (4.6.1) are not independent and (ii) Monte Carlo events in this equation are subject to weighting. Therefore, the special approach described in Ref. [45] was used for this purpose. Neglecting the event migration between the bins, this approach gives the following expression for the absolute statistical uncertainty of the efficiency in a bin for the case of weighted Monte Carlo simulation,

$$\delta \mathcal{E}(\Delta^5 \tau) = \sqrt{ \frac{\mathbb{N}_{gen} - 2\mathbb{N}_{rec}}{\mathbb{N}_{gen}^3} \sum_{i=1}^{N_{rec}} w_i^2 + \frac{\mathbb{N}_{rec}^2}{\mathbb{N}_{gen}^4} \sum_{j=1}^{N_{gen}} w_j^2 }, \tag{7.1.3}$$

where N_{gen} and N_{rec} are the numbers of the generated and reconstructed Monte Carlo events inside the multi-dimensional bin, respectively, $\mathbb{N}_{gen}$ and $\mathbb{N}_{rec}$ are the corresponding weighted event numbers, while w is a weight of an individual event.

The two parts of the statistical uncertainty given by Eqs. (7.1.1) and (7.1.2) are combined quadratically into the total absolute statistical uncertainty in each non-empty $\Delta^5 \tau$ bin,

$$\delta_{\text{stat}}^{\text{tot}}(\Delta^5 \tau) = \sqrt{ \left(\delta_{\text{stat}}^{\text{exp}} \right)^2 + \left(\delta_{\text{stat}}^{\text{MC}} \right)^2 }. \tag{7.1.4}$$

The cross section assigned to the empty $\Delta^5\tau$ cells (see Eq. (5.1.3)) acquires zero statistical uncertainty.

For the extracted single-differential cross sections the statistical uncertainty $\delta_{\text{stat}}^{\text{tot}}(\Delta X)$ (where X is one of the final state variables, i.e. $M_{h_1 h_2}$, $M_{h_2 h_3}$, θ_{h_1}, α_{h_1}) is obtained from the uncertainties $\delta_{\text{stat}}^{\text{tot}}(\Delta^5\tau)$ of the five-fold differential cross sections according to the standard error propagation rules[1].

7.2   Model dependent uncertainties

In the studies of the double-pion cross sections off the free proton [15–19, 21–23], the uncertainty of the model dependence is commonly treated as a unique uncertainty type and is associated with the filling of the empty cells. In this analysis one more source of the cross section model dependence had to be considered, which is unfolding the effects of the target motion. These two sources give comparable uncertainties only for the two lowest W bins, while for the other bins the dominant part of the model dependent uncertainty comes from the filling of the empty cells.

Both the contribution from the empty cells and the value of the unfolding correction vary greatly (from completely insignificant to considerable) for different final state variable bins. Therefore, it is convenient to estimate the model dependent uncertainties in each ΔX bin of the single-differential cross sections (where X is one of the final state variables introduced in Sect. 4.3).

---

[1] The THnSparse root histograms offer an easy way of dealing with the uncertainties. Each multidimensional bin of the histograms with the experimental data acquires the absolute uncertainty $\sqrt{N_{full}}$ and $\sqrt{N_{empty}}$ for full and empty target runs, respectively. The efficiency histograms get the uncertainty $\delta\mathcal{E}(\Delta^5\tau)$ given by Eq. (7.1.3). Then the uncertainty automatically propagates upon all manipulations with these histograms (addition, division, scaling).

7.2.1   Uncertainty of the empty cells filling

During the empty cell filling the extracted cross sections acquire a moderate model dependence (see Sect. 5.1). Once the empty cells are filled, the part of the single-differential cross section that came from the empty cells is assigned a 50% relative uncertainty[2] (see Sect. 5.1). The absolute cross section uncertainty $\widetilde{\delta}_{model}^{cells}(\Delta X)$ is hence given by

$$\widetilde{\delta}_{model}^{cells}(\Delta X) = \frac{1}{2}\left(\left[\frac{d\sigma}{dX}\right]_{filled} - \left[\frac{d\sigma}{dX}\right]_{not\ filled}\right), \qquad (7.2.1)$$

where the parentheses contain the difference between the cross section values calculated with the empty cell contributions ("filled") and without them ("not filled").

The corresponding relative uncertainty $\varepsilon_{model}^{cells}(\Delta X)$ is in turn given by

$$\varepsilon_{model}^{cells}(\Delta X) = \frac{\widetilde{\delta}_{model}^{cells}}{\left[\frac{d\sigma}{dX}\right]_{filled}}. \qquad (7.2.2)$$

After the filling of the empty cells the cross section is subject to several subsequent manipulations, i.e. virtual photon flux normalization, radiative correction, and unfolding the effects of initial proton motion. Along this path the absolute uncertainty $\widetilde{\delta}_{model}^{cells}(\Delta X)$ is propagated in such a way as to keep the relative uncertainty $\varepsilon_{model}^{cells}(\Delta X)$ in each ΔX bin of the single-differential distribution unchanged.

Therefore, the absolute uncertainty $\delta_{model}^{cells}(\Delta X)$ for the final single-differential distributions is obtained by

$$\delta_{model}^{cells}(\Delta X) = \left[\frac{d\sigma_{v}}{dX}\right]_{final} \cdot \varepsilon_{model}^{cells}, \qquad (7.2.3)$$

with the relative uncertainty $\varepsilon_{model}^{cells}$ given by Eq. (7.2.2) and the single-differential cross section determined according to Eq. (4.5.5).

---

[2] This conservative way to estimate this uncertainty has become conventional for the studies of double-pion production cross sections [19, 20, 22].

7.2.2 Uncertainty of unfolding the effects of target motion

In this study the cross sections are subjected to one extra correction compared to the cross sections extracted off the free proton [15–19, 21–23], i.e. unfolding the effects of initial proton motion. The potential inaccuracies due to this procedure are also attributed to the model dependent uncertainty, since the procedure is based on (i) the free proton cross sections taken from the model JM and (ii) the model of the deuteron wave function, which was the Bonn model (see Sect. 5.3 for more detail).

For each ΔX bin of the single-differential distributions the relative uncertainty due to the unfolding procedure was estimated by[3]

$$\varepsilon_{\mathrm{model}}^{\mathrm{unfold}}(\Delta X) = \left| \frac{\left[\frac{\mathrm{d}\sigma}{\mathrm{d}X}\right]_{folded} - \left[\frac{\mathrm{d}\sigma}{\mathrm{d}X}\right]_{unfolded}}{\left[\frac{\mathrm{d}\sigma}{\mathrm{d}X}\right]_{folded} + \left[\frac{\mathrm{d}\sigma}{\mathrm{d}X}\right]_{unfolded}} \right|. \tag{7.2.4}$$

The corresponding absolute uncertainty is then given by

$$\delta_{\mathrm{model}}^{\mathrm{unfold}}(\Delta X) = \left[\frac{\mathrm{d}\sigma_{\mathrm{v}}}{\mathrm{d}X}\right]_{final} \cdot \varepsilon_{\mathrm{model}}^{\mathrm{unfold}}. \tag{7.2.5}$$

7.3 Systematic uncertainties

The systematic uncertainty of the extracted cross sections is estimated in each bin in W and Q^2. As in the previous studies of the double-pion production cross sections [15–19, 21–23], the dependence of the systematic uncertainty on the hadronic variables is not investigated.

The following sources are considered to contribute to the total systematic uncertainty of the extracted cross sections.

---

[3] Although the relative uncertainty due to empty cell filling can also be estimated in this way, it was decided to calculate it according to Eq. (7.2.2) to observe consistency with the free proton study [22].

7.3.1 Normalization and electron identification

The presence of quasi-elastic events in the dataset advantages the verification of both the overall cross section normalization and the quality of the electron selection. The former may lack accuracy due to potential miscalibrations of the Faraday cup, fluctuations in the target density, deviations of the beam current and position, inaccuracies in determining the DAQ live-time as well as imprecise knowledge of other "luminosity ingredients" such as target length or the density of liquid deuterium (see Eq. (4.5.1)). Meanwhile, the quality of the electron selection may suffer from potential miscalibrations of different detector parts, inaccuracies in the electron tracking and identification as well as uncertainties of the cuts and corrections involved in the electron selection.

To verify the correct cross section normalization and the quality of the electron selection, the study [22, 23] (which is the study of double-pion cross sections off the free proton in the same kinematic region) estimates the elastic cross section and then compares it with the Bosted parameterization [55]. This comparison revealed a 3% agreement between the experimental and parameterized cross sections that allowed to assign a 3% global uncertainty to the extracted double-pion cross sections due to inaccuracies in the normalization and electron selection.

To achieve the same goals in the current analysis, the quasi-elastic cross section was estimated and then compared with the Bosted parameterization of the quasi-elastic cross section off the deuteron [48, 49] (see Sect. 6 for details). This comparison allows to claim a 5% agreement between the experimental and parameterized cross sections and, therefore, to assign a 5% global uncertainty to the extracted double-pion cross sections due to inaccuracies in the normalization and electron selection.

7.3.2 Integration over three sets of final hadron variables

According to Sect. 4.3, the cross sections are extracted in three sets of the kinematic variables. The integral cross sections are found to slightly differ among the sets due to the different data and efficiency propagation to various kinematic grids. As a final result, the integral cross sections averaged (as an arithmetic mean) over these three grids are reported. The standard error of the mean is interpreted as a systematic uncertainty (which is calculated according to Eq. (C.4) in App. C). The single-differential cross sections and the uncertainty $\delta_{\mathrm{stat,mod}}^{\mathrm{tot}}$ are scaled to the mean integral value.

Since different variable sets correspond to different registered final hadrons (and, therefore, to different combinations of the hadron cuts), this systematic error includes the error due to the shapes of the hadron cuts that are used in the analysis. The average value of this uncertainty among all W and Q^2 bins is 1.6%. However, the error is larger in the first two W bins (with the maximum of 9.5% achieved in the first W bin at $Q^2 = 0.675$ GeV^2), which being located near the reaction threshold, correspond to low momenta of the final hadrons.

7.3.3 Relative efficiency uncertainty cut

The cut on the relative efficiency uncertainty directly impacts both the cross section value and the cross section uncertainties, since it excludes entire kinematic cells from further consideration (see Sect. 4.6). This cut, therefore, reduces the total statistical uncertainty and increases the model dependent uncertainty, and a cut value $\delta\widetilde{\mathcal{E}}/\widetilde{\mathcal{E}} = 0.3$ is chosen as a compromise between these two effects. To estimate the systematic effect of the cut, the integral cross sections were also calculated for the cut values 0.25 and 0.35. As a final result, the arithmetic mean of the integral cross sections for these three cut values is reported, and the standard error of the mean is interpreted

as a systematic uncertainty (which is calculated according to Eq. (C.4) in App. C). The single-differential cross sections and the uncertainty $\delta_{\text{stat,mod}}^{\text{tot}}$ are reported for the cut value 0.3, being scaled to the mean integral value.

The systematic effect of the relative efficiency uncertainty cut is estimated for each bin in W and Q^2 individually and is found to be minor, i.e. the average uncertainty value is 0.8%. Taking into account that the cut on the relative efficiency uncertainty impacts directly the amount of empty cells, the revealed small uncertainty associated with this cut indicates that the procedure of the empty cell filling is well under control and that the cross section inaccuracy caused by the corresponding model dependence is not significant.

7.3.4 Correction due to FSI-background admixture

One more part of the systematic uncertainties comes from the effective correction due to FSI-background admixture. This correction is performed for the experimental events in the π^- missing topology and described in Sect. 3.5.2. The fit shown in Fig. 3.31 (as well as the corresponding correction factor given by Eq. (3.5.2)) turned out to be slightly dependent on the histogram binning. To account for this uncertainty, the correction factor is estimated for five different histogram bin sizes, and the arithmetic mean of these five individual values is used for the correction (for each bin in W). The absolute uncertainty of the resulting correction factor is estimated as a standard error of the mean (which is calculated according to Eq. (C.4) in App. C). The corresponding cross section uncertainty is estimated by Eq. (C.3), where the quantity a includes the number of events from the π^- missing topology, while c in the denominator includes the efficiency estimated for both topologies.

The systematic effect of the FSI-background correction is estimated for each bin in W and Q^2 where the correction is applied. For such bins, the average value of the relative systematic uncertainty is 0.4%, which is rather marginal.

7.3.5 Radiative corrections

As a common practice in studies of the double-pion cross sections with CLAS [15–19, 21–23], a 5% global uncertainty is assigned to the cross section due to the inclusive radiative correction procedure (see Sect. 5.2).

7.3.6 Total systematic uncertainty

The average values of integral systematic errors with their sources are presented in Tab. 7.1. The uncertainties due to these sources were summed up in quadrature in each W and Q^2 bin to obtain the total systematic uncertainty for the integral cross sections. The common value of the total systematic uncertainty in the bin is $\sim 7\%$ (it is, however, higher near the threshold).

Table 7.1: Average values of integral systematic uncertainties.

Source	Average value
Normalization and electron identification	5%
Integration over three sets of hadron variables	1.7%
Relative efficiency uncertainty cut	0.6%
Correction due to FSI-background admixture	0.4%
Radiative corrections	5%
Total	**7.4%**

7.4 Summary for the cross section uncertainties

Finally, the model dependent uncertainties $\delta_{\text{model}}^{\text{cells}}(\Delta X)$ and $\delta_{\text{model}}^{\text{unfold}}(\Delta X)$ defined by Eq. (7.2.3) and Eq. (7.2.5), respectively, are combined with the total statistical uncertainty $\delta_{\text{stat}}^{\text{tot}}(\Delta X)$ defined in Sect. 7.1 as the following.

$$\delta_{\text{stat,mod}}^{\text{tot}}(\Delta X) = \sqrt{\left(\delta_{\text{stat}}^{\text{tot}}\right)^2 + \left(\delta_{\text{model}}^{\text{cells}}\right)^2 + \left(\delta_{\text{model}}^{\text{unfold}}\right)^2}. \tag{7.4.1}$$

The extracted cross sections are reported with the uncertainty $\delta^{\mathrm{tot}}_{\mathrm{stat,mod}}$, which for the single-differential distributions is given by Eq. (7.4.1), while for the integral cross sections is obtained from the uncertainty of the single-differential distributions according to the standard error propagation rules[4].

For the majority of $(W,\ Q^2)$ points of the integral cross sections the uncertainty $\delta^{\mathrm{tot}}_{\mathrm{stat,mod}}$ stays on a level of $\sim$ 4%-6%.

It should be mentioned that to combine the statistical uncertainty with the uncertainty of the model dependence and to report the final cross sections with the resulting uncertainty $\delta^{\mathrm{tot}}_{\mathrm{stat,mod}}$ have become conventional for the studies of double-pion production cross sections [15–19, 21–23].

In addition to the uncertainty $\delta^{\mathrm{tot}}_{\mathrm{stat,mod}}$, for the integral cross sections the total systematic uncertainty is also reported as a separate quantity. If necessary, the relative systematic uncertainty $(\varepsilon_{\mathrm{sys}})$ in each W and Q^2 bin can be propagated as a global factor to the corresponding single-differential distributions.

In this study the uncertainty $\delta^{\mathrm{tot}}_{\mathrm{stat,mod}}$ is less than the total systematic uncertainty for the majority of $(W,\ Q^2)$ points, exceeding it only near the threshold (for $W \lesssim$ 1.4 GeV). This happens because the former rises close to the threshold due to small experimental statistics, large contribution of the empty cells (see Sect. 5.1), and pronounced impact of the unfolding correction (see Sect. 5.3).

---

[4] Note that for the integral cross sections the value of $\delta^{\mathrm{tot}}_{\mathrm{stat,mod}}$ was averaged (as arithmetic mean) among the three sets of final hadron variables.

Chapter 8

Some other issues

8.1   The cross section beam energy dependence

The φ-integrated virtual photoproduction cross section σ_v can be decomposed into the combination of the structure functions [3, 39],

$$\sigma_v = \sigma_T + \varepsilon_L \sigma_L \quad \text{with} \quad \varepsilon_L = \frac{Q^2}{\nu^2}\varepsilon_T, \tag{8.1.1}$$

where σ_T and σ_L are the transverse and longitudinal structure functions, respectively, and ε_L the longitudinal polarization of the virtual photon with ε_T given by Eq. (4.5.4).

Being decomposed in this way, the cross section σ_v has a specific beam energy dependence, which is incorporated into the coefficient ε_L. The structure functions themselves, meanwhile, do not depend on the beam energy. A single experiment conducted with a certain beam energy allows for the extraction of σ_v as a whole without accessing the separate structure functions. Thus, the beam energy dependence turns out to be implicitly incorporated into the extracted cross sections.

Although the experiment is conducted with a fixed value of the laboratory beam energy, the actual energy of the incoming electron involved in the reaction turns out to alter and differ from the fixed laboratory value due to (i) the radiative effects that electrons undergo and (ii) the Fermi motion of the target proton. As a consequence, the extracted cross section cannot be associated with a distinct value of the electron beam energy, and this may complicate the interpretation of the results. Below these issues are addressed in more detail.

(i) The incoming and scattered electrons can emit photons thus reducing their energy. Due to the change of the incoming electron energy, the extracted cross sections correspond to the superposition of various beam energies. The correction due to this effect is included into the radiative corrections (see Sect. 5.2).

(ii) The experiment off the moving proton with fixed laboratory beam energy corresponds to that off the proton at rest performed with varying effective beam energies [24]. As a result, the extracted cross sections off moving protons are convoluted with the dependence of the quantity ε_L on the beam energy (see Eq. (8.1.1)). A study in Ref. [24], however, proves that this effect has an insignificant influence on the cross section. The correction due to this effect (which is negligible anyway) is automatically included into the procedure of unfolding the effects of the target motion (see Sect. 5.3)[1].

Being corrected, the cross sections extracted in this analysis may be assigned to the distinct value of the laboratory beam energy of $E_{beam} = 2.039$ GeV.

8.2   Off-shell effects

The target proton is bound in the deuterium nucleus and thus undergoes nucleon-nucleon interactions. The nucleon mass, however, is thought to be an interaction-dependent quantity, i.e. the nucleon's physical mass in a nucleus is smaller than that of a free nucleon [14]. In other words, the target proton bound in the deuteron is off-shell, which means that its four-momentum squared is not equal to its mass squared.

In the study [56], which aimed at π^- electroproduction off the neutron in deuterium, the impact of the off-shell effects on the measured cross sections was shown to be marginal. In this study the off-shell effects are ignored.

---

[1] Note that the radiative effects decrease the beam energy, while the Fermi motion leads to a symmetrical spread of the effective beam energy around the laboratory value.

Chapter 9

Discussion on final state interactions

9.1   Introduction to FSI for $\gamma_v p(n) \rightarrow p'(n')\pi^+\pi^-$

Hadrons produced in exclusive reactions are subject to Final State Interactions (FSI). The nature of this phenomenon is complicated due to numerous mechanisms being involved, most of which are driven by the strong interaction. If the reaction happens off nucleons contained in nuclei, then one can separate FSI into two general types:

- interactions between the final hadrons[1] and

- interaction of the final hadrons with the spectator nucleons[2].

Both FSI types can involve simple momentum exchanges between the hadrons as well as far more complicated processes such as nucleon resonance excitations.

Apparently, FSI in the reactions off a free proton are limited to the first type.

Interactions of the final hadrons with the spectator nucleons are thought to be far more pronounced than their interactions with each other. The arguments for that are the following. In general, the probability to interact in the final state depends on the distance between hadrons and their relative velocity, i.e. for slower and closer traveling particles the chance to interact is higher than for fast-moving and distant ones [57]. Final state hadrons are produced in one vertex, which means that in the

---

[1] Here the term "final hadrons" denotes p', π^+, and π^-, which define the reaction final state.

[2] Here the term "spectator" is related to a spectator of the original exclusive reaction, which is the neutron.

beginning, they are very close to each other and therefore have a high chance to interact as their wavefunctions are overlapping largely. However, immediately after the production, they start to fly apart from the vertex in radial directions increasing the distance between each other, which causes the interaction probability drop rapidly.

Meanwhile, the presence of a spectator nucleon changes the situation drastically. The neutron, which initially was not involved in the reaction of hadron production, is located slightly aside of the interaction vertex, but at the same time very close to it, so that the flying-off final hadrons can impact the neutron. In addition to that, the neutron also moves with Fermi momentum, which turns FSI into usual hadron-hadron collisions with the full range of related mechanisms being involved. Thus, hadron-hadron collisions, which are unlikely to occur in the reaction off the free proton as the final hadrons fly apart from one point, start to play a role in the reaction off the bound proton in the presence of the neutron. As a result, interactions with the spectator nucleons turn out to be more pronounced compared to interactions between the final hadrons.

Figure 9.1 schematically sketches the leading contributors to the process of the double-pion production off the proton bound in deuterium. The process (a) corresponds to the situation when the final hadrons manage to avoid any interaction with the neutron. In this case, the reaction is considered to occur in a so-called "quasi-free regime". Meanwhile, the processes (b-d) illustrate the situation when one of the final hadrons was involved in the interaction with the neutron. Such interactions represent the main components of FSI for the considered exclusive channel.

In fact, the process (b) in Fig. 9.1 corresponds the proton-neutron scattering [57, 58], while the processes (c) and (d) correspond to the pion-neutron scattering [59–61]. Therefore, FSI with spectator nucleons in the double-pion production channel represent a superposition of a broad spectrum of mechanisms inherent for these two scattering types.
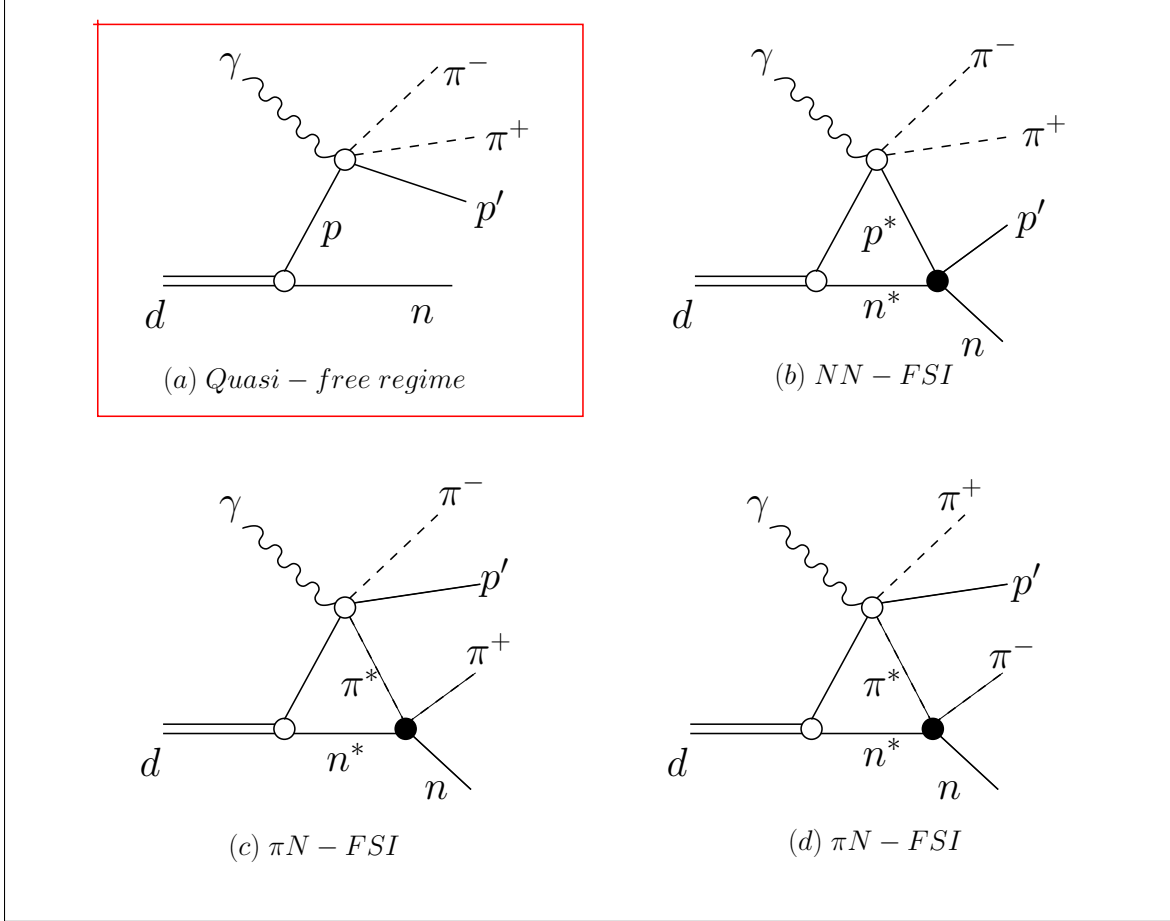
Figure 9.1: Illustration of the leading contributors to the process of the double-pion production off the proton bound in deuteron. (a) Quasi-free regime, (b) NN-FSI, and (c-d) πN-FSI.

One mechanism of the proton-neutron scattering seems to be very interesting in the context of this study, i.e. the charge exchange mechanism, in which proton and neutron can exchange their characteristics, literally turning one into another. This may complicate the interpretation of the experimentally collected information. For example, some protons of the original exclusive reaction are not registered as they have undergone the exchange transformation to neutrons. Furthermore, some registered protons may turn out to be actually "transformed" neutrons from an exclusive reaction off neutrons bound in deuterium.

The pion-nucleon scattering also involves a remarkable mechanism that deserves special attention, namely, the pion to neutron coupling with resonance formation. Section 9.5 of this chapter explores manifestations of this mechanism in the analyzed experimental data.

Among the main FSI components shown in Fig. 9.1, proton-neutron interactions, which correspond to the process (b), are thought to dominate over the pion-neutron interactions, sketched in (c) and (d). Using the "black disk" analogy, this ranking can be understood from the fact that a proton, being larger than a pion, has higher chances to spatially overlap with the neutron while traveling away from the vertex. In addition to that, due to the large difference in mass, protons and pions of a same momentum differ significantly in their velocity with the former being much slower. This makes the protons spend more time near the vertex (and hence near the neutron), which increases the interaction probability.

Due to the relatively low energy of the final hadrons, the majority of FSI in the investigated reaction are thought to happen elastically, which implies that (i) the quantum numbers of the participating hadrons do not change and (ii) no new particles are produced in such interactions. Note that the aforementioned mechanisms of the charge exchange in the proton-neutron scattering and the resonance formation in the process $\pi n \to \pi n$ are still attributed to elastic mechanisms. The minority of FSI in this reaction then evolves via inelastic scenarios [57].

The main goal of this study is to extract the double-pion cross sections in the quasi-free regime. Such an approach implies that quasi-free events that correspond to the process (a) in Fig. 9.1 are of interest, while events with FSI are treated as undesirable background and have to be eliminated. The analysis, therefore, was seeking special methods of separating these two types of events and correcting for the remaining admixture of events with FSI if the complete separation was not possible. These methods are described in detail in Sect. 3.5.

Thus, being attributed to the background and hence subjected to elimination, events with FSI were deprived of attention throughout the analysis. These events, therefore, were lacking detailed investigation, which they definitely deserve as FSI effects represent an essential issue in studies of any exclusive reaction, especially off nuclei. To regain fairness and balance into the analysis, this particular chapter is fully focused on the events with FSI and is devoted to the discussion of their peculiar features and manifestations.

9.2 Probing FSI kinematically

Recall that in general one can distinguish between two FSI types: (i) interactions between the final hadrons and (ii) interactions with spectator nucleons. These two FSI types, both driven by the strong interaction, seem to be similar to each other from the point of view of involved FSI mechanisms. Meanwhile, from the point of view of the reaction kinematics they differ. To discern this difference, let's consider each FSI type in more detail.

In general, all interactions that possibly could happen between the hadrons share the following three features,

- they preserve the total momentum of the participating hadrons, thus maintaining energy-momentum conservation between them,

- after FSI the participating hadrons are left on their mass shell, and

- the momentum of each participating hadron is altered and thus does not match its value before FSI.

These features deliver the following important conclusion: interactions between the final hadrons do not alter missing mass distributions[3]. As an interesting example, one can consider the situation when in a missing hadron topology FSI happens

---

[3] If new particles are not produced in these interactions.

between a registered hadron and the unregistered one. In this case, the calculated four-vector of a missing particle matches its actual four-momentum after FSI (in the absence of other factors, such as detector resolution, radiative effects, etc.) because the interaction keeps the energy-momentum conservation between the reaction particles. Then, as the unregistered particle ends up being on-shell after FSI, the calculated missing mass turns out to match the particle rest mass.

Although having no impact on the missing mass distributions, FSI between final hadrons nonetheless affect the experimentally extracted cross sections. This happens due to the following reason. Let's suppose that in the reaction of the double-pion production, two final hadrons interact with each other, while the third one avoids any interactions. In this case, the two interacting hadrons change their four-momenta (keeping their cumulative momentum unchanged though), while the third one manages to reach the detector unaltered. Then, for such an event, the calculated final hadron variables will differ from their true values before FSI. Specifically, the invariant mass of the pair of interacting hadrons will be preserved (due to the conservation of their cumulative four-momentum), whereas the invariant masses of an interacting hadron and the unaltered one will change. Moreover, the spatial angles of the unaltered hadron will be preserved, whereas the angles of both interacting hadrons will change. Such an event then will contribute to the "wrong" point of the reaction phase-space that is different from the point it is supposed to contribute without FSI. As a result, the measured cross sections acquire disturbances.

This issue with the cross section disturbances can hardly be avoided on the level of the experimental data analysis due to the insensitivity of the missing mass distributions to interactions of the final hadrons with each other. Therefore, measured cross sections (no matter whether off a free or bound nucleon) are inevitably convoluted with effects of this FSI type. This issue is supposed to be treated on the level of theoretical/phenomenological cross section interpretation.

Meanwhile, FSI with spectator nucleons have one distinctive feature, which differentiate them from FSI between the final hadrons. Specifically, as the spectator nucleon is extrinsic to the original exclusive reaction, any FSI with it causes in/out momentum flows, thus breaking the energy-momentum conservation imposed on the reaction particles. This means that after FSI the total energy/momentum of the reaction final hadrons is different from what they had before FSI as some part of it was either given to or taken from the neutron. As a consequence, for events with FSI, the missing mass technique gives faulty results for both the fully exclusive event sample or the one with a missing hadron, which means that FSI with the spectator introduce disturbances into the missing mass distributions.

Note that interactions between one of the final hadrons and the spectator neutron should anyway comply with the three above features, which implies not only the energy-momentum conservation in this particular interaction, but also the on-shellness of both interacting particles after the interaction happens.

The revealed specificity of FSI with spectator neutrons (i.e. the ability to disturb missing mass distributions), allows for a kinematic probing of this FSI type, which is unfortunately not possible for the case of final hadrons interacting with each other. Seeking to exploit this unique opportunity offered by "e1e" deuteron target experiment, the rest of this chapter is devoted to the kinematic examination of FSI with spectator nucleons in the reaction of the double-pion electroproduction off protons bound in deuterium nuclei. This implies that hereinafter whenever FSI is mentioned, the processes (b-d) of Fig. 9.1 are assumed unless specified otherwise.

It is convenient to start kinematic probing of FSI by recalling a few general facts.

First, it is worthwhile to recall that the amount of events produced in an exclusive reaction depends on a certain number of independent variables, which in the case of double-pion electroproduction is seven as described in Sect. 4.3. The yields of quasi-free events and events with FSI represent complementary portions of the total

number of reaction events, and hence both of them depend on these variables as well. Therefore, it is reasonable to consider the relative spread of events with FSI, which implies that the amount of events affected by FSI in any part of the reaction phase space is analyzed with respect to the corresponding amount of quasi-free events.

Meanwhile, the portion of events with FSI is not expected to be the same along the reaction phase space. Instead, their relative spread is anticipated to rise in the region of small hadron momenta as slower traveling hadrons have higher interaction probability. Meanwhile, in the acceptance of the CLAS detector the region of large polar angles corresponds mostly to low-momentum hadrons[4]. Therefore, a relative excess of events with FSI is also expected with increasing hadron polar angles. In addition to that, as various reaction topologies cover different ranges of hadron momenta and angles, the relative spread of events with FSI acquires topology dependence.

It is also important to emphasize that in general final state interactions are very complicated and involve numerous mechanisms. Their complete theoretical description requires application of the theory of the strong interactions and so far is not fully accomplished. However, all mechanisms that possibly could happen during FSI have one simple feature in common, i.e. they alter the momentum of the participating hadrons.

With regards to alterations of hadron momenta in collisions with the spectator neutrons, the following kinematic aspects should be taken into consideration. The neutrons move with the Fermi momentum, which for the vast majority of events is less than $\sim$250 MeV, but rarely can be higher. Meanwhile, in the analyzed experiment, the momentum of all final hadron types can be as high as $\sim$1.5 GeV. Therefore, in collisions with neutrons, rapid final hadrons are expected to mostly lose their momentum, whereas for slow hadrons a momentum gain is quite likely to occur. Here

---

[4] The mentioned correlation between the momentum and the polar angles of the final hadrons can be observed in the θ versus momentum distributions provided in Sect. 3.4.1.

one should also take into account that due to the presence of registration thresholds, pions slower than $\sim$100 MeV and protons slower than $\sim$300 MeV are not registered.

Now, having highlighted important general facts, it is worthwhile to recapitulate those features of FSI with spectator nucleons, which form the basis of the kinematic examination of FSI effects presented further in this chapter. Specifically, FSI with spectator nucleons (i) alter the momentum of the participating particles and (ii) do not preserve energy-momentum conservation between the final hadrons of the initial exclusive reaction. As a result, distributions of kinematic quantities calculated from the registered final hadron four-momenta acquire disturbances caused by agglomerations of events with FSI. These disturbances can be better visually distinguished, if the corresponding distributions of pure quasi-free events are used as reference.

The outlined effect was already exploited in this analysis on the quasi-free event selection level as described in detail in Sect. 3.5. The disturbances caused by events with FSI were observed in the distributions of missing quantities P_X, $M^2_{X[0]}$, and $M^2_{X[\pi^-]}$, which were used to establish the exclusivity cuts. However, the examination conducted in Sect. 3.5 was mostly concentrated on quasi-free events as they were the main point of interest for the analysis, while events with FSI lacked consideration. In this chapter, the distributions of missing quantities are examined once again with attention focused on FSI induced disturbances.

The two reaction topologies are again considered separately as FSI effects turn out to be topology dependent. The fully exclusive topology is addressed first as it benefits from capturing FSI for all three final hadrons including the π^-.

9.3   FSI in the fully exclusive topology

9.3.1   Relative spread of FSI events along the phase space

For the fully exclusive topology, the distributions of the following quantities are examined[5]: the missing momentum P_X for the reaction $ep(n) \rightarrow e'p'(n')\pi^+\pi^- X$ and the missing mass squared $M^2_{X[\pi^-]}$ for the reaction $ep(n) \rightarrow e'p'(n')\pi^+ X$. These quantities are defined by

$$\begin{aligned}
P_X &= |\overrightarrow{P}_e - \overrightarrow{P}_{e'} - \overrightarrow{P}_{p'} - \overrightarrow{P}_{\pi^+} - \overrightarrow{P}_{\pi^-}|, \\
M^2_{X[\pi^-]} &= [P^\mu_{\pi^-\ miss}]^2 = [P^\mu_e + P^\mu_p - P^\mu_{e'} - P^\mu_{p'} - P^\mu_{\pi^+}]^2,
\end{aligned} \tag{9.1}$$

where P^μ_i are the four-momenta and $\overrightarrow{P}_i$ the three-momenta of the particle i. Both quantities are calculated under the target-at-rest-assumption, i.e. considering $P^\mu_p = (0,\ 0,\ 0,\ m_p)$, where m_p is the proton mass.

As reference distributions of pure quasi-free events, the distributions of the same quantities plotted for the Monte Carlo simulation are used. The Monte Carlo simulation was performed on the basis of the TWOPEG-D event generator [24], which nicely reproduces the Fermi smearing of the missing quantities, but does not include FSI effects. The comparison of the FSI disturbed experimental distributions with these reference histograms reveals the features of events with FSI.

In the first step, the relative spread of events with FSI along the magnitude of the final hadron momenta is examined. Figures 9.2, 9.3, and 9.4 show the distributions of the quantities P_X (first row) and $M^2_{X[\pi^-]}$ (second row) plotted in different ranges of π^-, π^+, and proton momentum magnitudes, respectively. The relative spread of events with FSI can be visually judged by the mismatch between the experimental (black) and simulated (blue) histograms. The considered ranges of the hadron momenta are specified for each plot. Note that these ranges are not equidistant and were chosen in

---

[5] The quantity $M^2_{X[0]}$ is not examined here as it was shown in Ref. [41] to be quite insensitive to FSI with spectator nucleons.

such a way that the relative amount of events with FSI does not change significantly within each range. The distributions are plotted for events from the fully exclusive topology and normalized in a way that the maxima of the main peaks are equal to one.

As follows from Fig. 9.2, events with low π^- momenta ($\lesssim 0.5$ GeV) contain a considerable fraction of events with FSI, while events with higher π^- momenta ($\gtrsim 0.5$ GeV) are mostly quasi-free. However, the relative spread of events with FSI along the π^+ momentum demonstrates a different tendency as shown in Fig. 9.3, i.e. the fraction of events with FSI does not vary significantly along the π^+ momentum, staying sizable for all momentum values.

Figure 9.2: Relative spread of events with FSI among different ranges of the π^- momentum magnitude is demonstrated by the mismatch between the experimental (black) and the simulated (blue) distributions of the quantities P_X (first row) and $M^2_{X[\pi^-]}$ (second row) defined by Eqs. (9.1). The corresponding ranges of the π^- momentum are specified above the plots. Note that these ranges are not equidistant and were chosen in a way that the relative amount of events with FSI does not change significantly within each range. The distributions are plotted for events from the fully exclusive topology and normalized in a way that the maxima of the main peaks are equal to one. The presented statistics corresponds to the experimental data.

Meanwhile, the relative spread of events with FSI varies dramatically along the proton momentum as illustrated by Fig. 9.4. In the region of low proton momenta $\lesssim 0.4$ GeV no quasi-free events are present[6]. As the proton momentum grows up

---

[6] Note that in this region an admixture of spectator protons from the reaction off neutrons may be present. Also, in CLAS, reconstruction of protons with $p_{p'} \lesssim 0.4$ GeV is in general not quite reliable.

Figure 9.3: Relative spread of events with FSI among different ranges of the π^+ momentum magnitude is demonstrated by the mismatch between the experimental (black) and the simulated (blue) distributions of the quantities P_X (first row) and $M^2_{X[\pi^-]}$ (second row) defined by Eqs. (9.1). The corresponding ranges of the π^+ momentum are specified above the plots. Note that these ranges are not equidistant and were chosen in a way that the relative amount of events with FSI does not change significantly within each range. The distributions are plotted for events from the fully exclusive topology and normalized in a way that the maxima of the main peaks are equal to one. The presented statistics corresponds to the experimental data.

Figure 9.4: Relative spread of events with FSI among different ranges of the proton momentum magnitude is demonstrated by the mismatch between the experimental (black) and the simulated (blue) distributions of the quantities P_X (first row) and $M^2_{X[\pi^-]}$ (second row) defined by Eqs. (9.1). The corresponding ranges of the proton momentum are specified above the plots. Note that these ranges are not equidistant and were chosen in a way that the relative amount of events with FSI does not change significantly within each range. The distributions are plotted for events from the fully exclusive topology and normalized in a way that the maxima of the main peaks are equal to one. The presented statistics corresponds to the experimental data.

139

to ~0.5 GeV quasi-free events begin to appear in the sample, which is however still dominated by events with FSI. Then, in the region $\gtrsim 0.5$ GeV quasi-free events begin to prevail, but the fraction of events with FSI is still essential up to the values of $\gtrsim 0.6$ GeV. As the proton momentum grows further, the admixture of events with FSI is mitigated and for the values $\gtrsim 0.7$ GeV mostly quasi-free events are left.
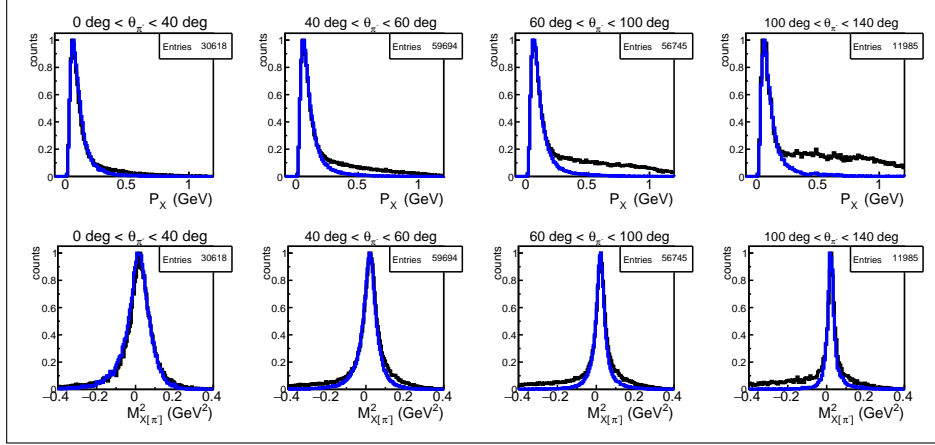
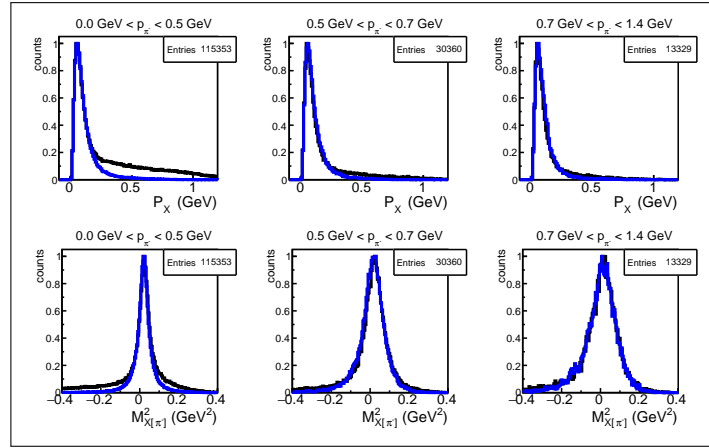Figure 9.5: Relative spread of events with FSI among different ranges of the π^- polar angle is demonstrated by the mismatch between the experimental (black) and the simulated (blue) distributions of the quantities P_X (first row) and $M^2_{X[\pi^-]}$ (second row) defined by Eqs. (9.1). The corresponding ranges of the π^- polar angle are specified above the plots. Note that these ranges are not equidistant and were chosen in a way that the relative amount of events with FSI does not change significantly within each range. The distributions are plotted for events from the fully exclusive topology and normalized in a way that the maxima of the main peaks are equal to one. The presented statistics corresponds to the experimental data.

In the next step, the relative spread of events with FSI along the polar angle of the final hadrons is examined in the same way. Figures 9.5, 9.6, and 9.7 show the distributions of the quantities P_X (first row) and $M^2_{X[\pi^-]}$ (second row) plotted in different ranges of π^-, π^+, and proton polar angle, respectively. The relative spread of events with FSI is again demonstrated by the mismatch between the experimental (black) and simulated (blue) histograms and the considered ranges of hadron polar angles are specified for each plot. These ranges are again not equidistant and as they were chosen in such a way that the relative amount of events with FSI does not change significantly within each range.
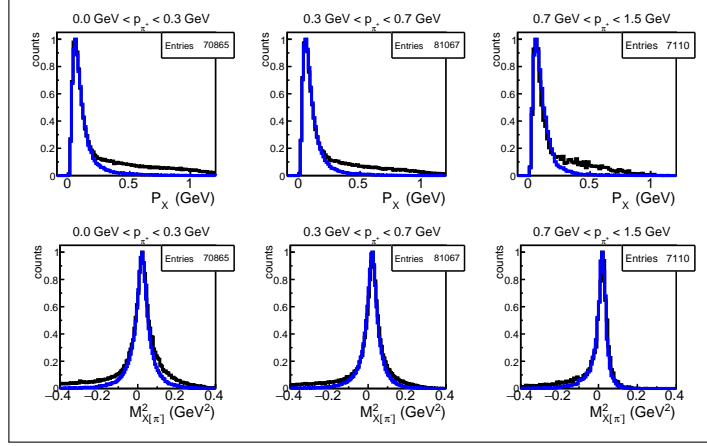
Figure 9.6: Relative spread of events with FSI among different ranges of the π^+ polar angle is demonstrated by the mismatch between the experimental (black) and the simulated (blue) distributions of the quantities P_X (first row) and $M^2_{X[\pi^-]}$ (second row) defined by Eqs. (9.1). The corresponding ranges of the π^+ polar angle are specified above the plots. Note that these ranges are not equidistant and were chosen in a way that the relative amount of events with FSI does not change significantly within each range. The distributions are plotted for events from the fully exclusive topology and normalized in a way that the maxima of the main peaks are equal to one. The presented statistics corresponds to the experimental data.
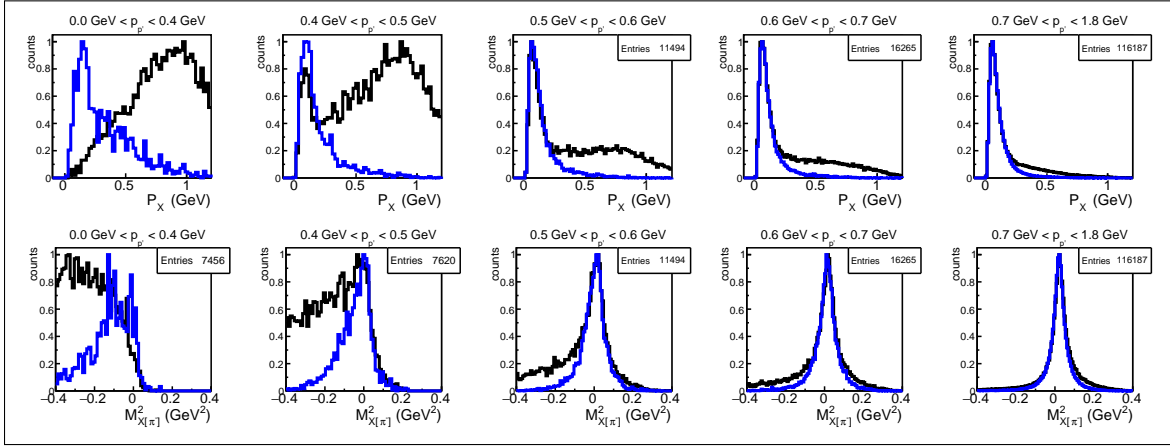

Figure 9.7: Relative spread of events with FSI among different ranges of the proton polar angle is demonstrated by the mismatch between the experimental (black) and the simulated (blue) distributions of the quantities P_X (first row) and $M^2_{X[\pi^-]}$ (second row) defined by Eqs. (9.1). The corresponding ranges of the proton polar angle are specified above the plots. Note that these ranges are not equidistant and were chosen in a way that the relative amount of events with FSI does not change significantly within each range. The distributions are plotted for events from the fully exclusive topology and normalized in a way that the maxima of the main peaks are equal to one. The presented statistics corresponds to the experimental data.

141

As follows from Fig. 9.5, events with low values of the π^- polar angle $\lesssim 40°$ are mostly quasi-free, while in the region $\gtrsim 40°$ a discernible fraction of events with FSI appears. This fraction gradually grows with increasing polar angle and in the region of $120° < \theta_{\pi^-} < 140°$ becomes considerable.
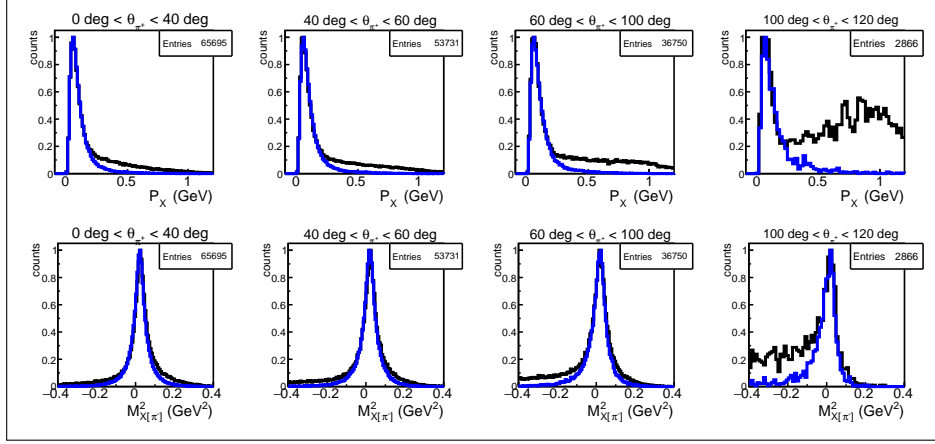
The relative spread of events with FSI along the π^+ polar angle again demonstrates a slightly different tendency, as seen in Fig. 9.6. The fraction of events with FSI turns out to be discernible for all values of the π^+ polar angle, showing a mild growth as the angle increases up to $100°$. Then, in the region of $100° < \theta_{\pi^+} < 120°$ the number of events with FSI rises suddenly up to a rather essential portion.

The correlation between the fraction of events with FSI and the proton polar angle is again more dramatic. As seen in Fig. 9.7, in the region $\theta_p < 35°$, which contains the majority of registered protons, the portion of events with FSI is discernible but small. However, for higher polar angles a rather steep rise of this portion takes place, i.e. in the narrow slice of $35° < \theta_p < 40°$ it becomes considerable and in the next $5°$-range – very large. Finally, for $\theta_p > 45°$ quasi-free events turn out to vanish, while events with FSI prevail.

The examination performed above confirms the expected increase in the relative amount of events with FSI in the regions of low momentum and large polar angles, which is observed for all final hadrons, to one extent or another. The anticipated dominance of proton-neutron interactions over the pion-neutron interactions is also in agreement with the observations. In addition to these general statements, the following more specific conclusions can be made.

- The fraction of events with FSI is strongly correlated with the proton kinematics, giving steep rises in the low-momentum region as well as for the region of large polar angles.

- The correlation with the π^- kinematics is mild with no steep alterations seen.

- The correlation with the π^+ kinematics is quite weak, with the only one exception of an essential rise for $\theta_{\pi^+} > 100°$.

- In the regions of the π^- momentum $\gtrsim 0.5$ GeV and the π^- polar angle $\lesssim 40°$ the event sample is completely dominated by quasi-free events.

- In the regions of the proton momentum $\lesssim 0.4$ GeV and the proton polar angle $\gtrsim 45°$ the event sample is completely dominated by events with FSI.

Note that the above observations are to a high degree determined by experimental conditions, as for instance, by the hardware threshold on the minimal detectable hadron momenta, which affects manifestations of proton and pion FSI in a different way. The point is that protons and pions that carry equal momenta differ significantly in their velocity: the former turn out to be much slower than the latter due to the difference in their mass. As a result, pions with potentially high probability of FSI have a tendency to be located in the region of extremely low momenta, which lies below the registration threshold. Meanwhile, protons with high probability of FSI turn out to be located in the region of moderately low momenta, comparable with the threshold value. Thus, the majority of pions that experienced FSI failed to be registered, while for protons the situation is different as the large number of them cross the threshold and hence managed to be registered.

The following several aspects are also noteworthy in the examination described above. First, the examination was performed for hadron momenta and polar angles defined in the laboratory system because this system is the only one that offers a sensible, unambiguous, and the most accurate determination of these quantities for events with FSI (which here are the main focus of interest). The arguments for this statement are given below.

The point is that the typically performed transformation to the CMS remains sensible only for quasi-free events, while for events with FSI it is no longer relevant.

This happens because once participating in FSI, events do not further keep the kinematics of the initial reaction and hence formally do not belong to "reaction events" anymore as in fact they were not produced off the target proton that defines the reaction CMS. Therefore, the usual CMS turns out to be an ill-defined system for events with FSI, and the transformation to this system would introduce further ambiguity into the examination.

In addition to that, the proper transformation to the reaction CMS requires the knowledge of the Fermi momentum of the initial proton for each event. The fully exclusive topology in general allows the reconstruction of this momentum as missing, which actually outputs the quantity P_X. However, being reconstructed in such a way this momentum not only suffers from poor resolution, but is also in fact incorrect for events with FSI as their initial kinematics is altered. Another option, i.e. performing the transformation under the target-at-rest assumption, convolutes the transformed quantities with effects of the target motion and hence lacks enough accuracy as well[7]. Therefore, being transformed to CMS, hadron momenta and angles would acquire an unnecessary systematic uncertainty, which would tangle the examination.

Taking into account all above arguments, the laboratory system was considered to give the best possible opportunity for the examination of features and manifestations of FSI effects.

The performed examination was conducted on a qualitative level without giving any definitive quantitative conclusions on the observed percentage of events with FSI in the analyzed event sample. This examination style is determined by the fact that the interrelation between the quasi-free events and events with FSI is strongly dependent on experimental conditions, detector acceptance/efficiency, the chosen reaction topology, the event selection employed in the analysis, etc. Therefore, any quantitative conclusion on the revealed ratio of quasi-free and FSI-affected events

---

[7] For the purpose of calculating quasi-free cross sections in the main analysis this option was considered adequate as it was accompanied by the corresponding correction. See Sects. 4.2 and 5.3.

144

would have been very condition-specific and thus misleading. Meanwhile, general tendencies observed in the spreading of FSI events along the reaction phase-space are thought to be more universal and stable, and therefore gain the main focus of this kinematic examination.

Meanwhile, sensible quantitative conclusions on this matter should be established on the cross section level other than on a level of event yields. An excellent opportunity to achieve this goal opens up with the completion of this analysis as now the newly extracted quasi-free cross sections can be compared with the analogous double-pion cross sections off free protons obtained in Ref. [22, 23]. In this way, a condition-independent impartial estimation of the relative contribution of events with FSI to the total amount of reaction events can be made.

9.3.2 Revealing details on hadron momentum alterations

Another noteworthy aspect of the performed examination is that one should be careful when considering the amount of events that fall within a certain range of hadron momentum/angle. One should remember that quasi-free events carry the actual values of these variables, i.e. the same as they had once been produced. However, for events with FSI, the hadron momentum/angle values are those they acquire after they underwent FSI, while the actual values for them are no longer known. Therefore, the "fraction of events with FSI" referred above does not reflect the portion of reaction events that were affected by FSI within the considered ranges of hadron momentum/angles, but corresponds to the portion of events that after FSI acquire such momentum/angle values which under the given experimental conditions fall into a certain range defined for quasi-free events (or for initial reaction events).

With regards to this point, one should recall that during FSI, both momentum loss and gain for affected hadrons are in general possible. In collisions with the spectator neutron, the type of the momentum alteration (gain/loss) depends on the relation

between the final hadron momentum and the neutron Fermi momentum. Here one of the fundamental differences between the two considered missing quantities becomes evident. Specifically, in the P_X distributions, FSI-affected events with a hadron momentum gain and loss are intermixed and no visual separation between them is possible. Whereas, the $M^2_{X[\pi^-]}$ distributions turn out to be more sophisticated in this sense as they allow one to distinguish between these two situations, at least to some extent.

For further discussion the examination performed in Ref. [41] can be of great use. The study [41] explores the influence of different factors on missing mass distributions and includes an attempt of naive modeling of kinematic effects of FSI with spectator nucleons for the case of double-pion production off bound protons. According to this modeling, the distributions of the quantity $M^2_{X[\pi^-]}$ (defined in the same way as here) demonstrate different structure depending on (i) the type of the hadron affected by FSI, (ii) kinematics of the affected hadron, (iii) the degree and type (gain/loss) of the hadron momentum alteration, and (iv) the relative spread of events with different degrees of momentum alterations within the event sample.

Specifically, Ref. [41] demonstrates that the left-side tail of the $M^2_{X[\pi^-]}$ distribution turns out to accumulate those FSI events, in which (i) relativistic hadrons gain the momentum in FSI and (ii) non-relativistic hadrons lose the momentum in FSI. Meanwhile, the right-side tail contains those events, in which (i) relativistic hadrons lose the momentum in FSI and (ii) non-relativistic hadrons gain the momentum in FSI, see more details in Ref. [41].

When applying these discoveries of Ref. [41] to this particular study, several aspects should be accounted for. The Fermi smearing of the $M^2_{X[\pi^-]}$ distributions, which was not considered in the FSI modeling in Ref. [41], is one of them. Being associated with event shuffling, Fermi smearing blurs the patterns of the FSI-event allocation described above. Beside this general impact, it has a few more specific effects on miss-

ing mass distributions that may interfere with FSI manifestations. One thing is that the Fermi smearing is W dependent, i.e. it increases as W grows from the threshold.

The other thing about the Fermi smearing, which is more important in the context of this study, is the following. If isolated from other effects, the Fermi smearing leads to a W-dependent asymmetry of the $M^2_{X[\pi^-]}$ distributions. Specifically, near the threshold more events are tossed to the left, then the asymmetry decreases with the growth of W, and at W~1.7-1.8 GeV the distributions regain their symmetry. This effect alters the common appearance of the $M^2_{X[\pi^-]}$ distributions, familiar from the free proton studies, with the asymmetric right-side tail caused mostly by the radiative effects (see Ref. [22, 23]). In contrast, the Fermi smeared distributions, if radiated, still keep a slight left-sided asymmetry near the threshold, which becomes smaller with growing W, leading to the visually symmetric distributions at W~1.6-1.7 GeV.

The outlined features of the Fermi smearing can be seen in Figs. 3.27, 3.29 and 3.30 from Sect. 3.5 as well as in those given below here. The simulated distributions show the influence of the Fermi smearing on quasi-free events, while its influence on events with FSI is not known. One may however anticipate them to follow the revealed tendency, thus forming an event excess at the left, which gradually vanishes as W grows from the threshold.

The next aspect to consider is related to the kinematics of the "e1e" experiment. To be more specific, in this experiment, pions registered in the detector are mostly relativistic as the momentum of the vast majority of non-relativistic pions turns out to be lower than the registration threshold. Meanwhile, the momentum range of non-relativistic protons extends far beyond the registration threshold, which (together with the low beam energy of the experiment) causes the major part of registered protons to be non-relativistic.

Finally, one should keep in mind that for rapid hadrons it is unlikely to gain the momentum through the momentum exchange with spectator neutrons as this

requires high values of the spectator Fermi momentum, which is a rare occasion. Although for some other mechanisms (e.g. resonance formations in the process $\pi n \to \pi n$) such gain is in general possible, the process of rapid hadrons gaining their momentum in FSI is not expected to belong to the leading contributors.

Taking into account all above arguments, the following consistent pattern can be stated for the allocation of events with FSI in the $M^2_{X[\pi^-]}$ distribution. The left-side tail is dominated by FSI events, in which non-relativistic protons lose their momentum. Meanwhile, the tail at the right is mostly populated by FSI events, in which relativistic protons and pions lose the momentum as well with those, in which non-relativistic protons gain the momentum[8]. This pattern is blurred by the Fermi smearing, which not only widens with W, but also promotes gradual event flow from the left tail to the right side as W grows from the threshold.

Considering the pattern described above, one can now examine the $M^2_{X[\pi^-]}$ distributions shown in Figs. 9.2–9.7 paying more attention to the right and left tails as they have been proven to provide some information on momentum alterations of FSI-affected hadrons.

This examination reveals that in those regions, where the fraction of events with FSI gives a steep rise (such as low proton momentum and high angles of protons and π^+), a very prominent left-side tail is observed in the $M^2_{X[\pi^-]}$ distributions with the almost complete absence of the right-side tail. Whereas, in the regions with small and moderate contributions from FSI events, both left and right tails are mild. This situation indicates that in the regions with large FSI contribution kinematically available in this experiment, FSI are dominated by the processes, in which non-relativistic protons lose their momentum. Meanwhile, events that correspond to other kinematic mechanisms of potentially comparable overall intensity either fall into kinematically not available regions (e.g. events with FSI-affected

---

[8] See Figs. 3.5 and 3.6 from Ref. [41] for better visualization of the described pattern.

low momentum pions, which fall below the registration threshold) or have a more homogeneous distribution along the reaction phase space.

At this point, it is worthwhile to mention again the low beam energy of the analyzed dataset, which promotes the abundance of non-relativistic protons. With increasing beam energy of an experiment, FSI effects are thought to become dominated with the momentum loss of relativistic hadrons. Then a different population of the $M^2_{X[\pi^-]}$ distribution tails is expected, with the right tail growing in size and the left tail dissolving.

9.3.3   Isolating FSI of various final hadrons

Now the second fundamental difference between the two considered missing quantities can be highlighted. It is remarkable that the quantity P_X, being calculated using the four-momenta of all registered final hadrons, incorporates information on FSI of each hadron type (p, π^+, and π^-). Whereas the quantity $M^2_{X[\pi^-]}$ absorbs only information on the proton and π^+ interactions as the information on the π^- interactions turns out to be missing together with its four-momentum as the latter is not used in the calculation of $M^2_{X[\pi^-]}$. This point should be taken into account when investigating the distributions shown in Figs. 9.2–9.7.

This remarkable feature offers the opportunity of isolating FSI contributions from various pairs of final hadrons considering the missing masses related to the corresponding third hadron. This opportunity is exploited in Fig. 9.8, which presents the distributions of the missing quantities $M^2_{X[\pi^-]}$ (first row), $M^2_{X[\pi^+]}$ (second row), and $M^2_{X[p']}$ (third row), with the first one defined in Eq. (9.1) and the others defined analogously. The relative spread of events with FSI in five 100-MeV-wide bins in W is again demonstrated by the mismatch between the experimental (black) and the simulated (blue) histograms. The distributions are plotted for events from the fully exclusive topology and normalized in a way that the maxima of the main peaks are equal to one.

They are however zoomed in on the range [0, 0.25] on the y-axis to better visualize the mismatch. Note also that the distributions from the first and second rows have the same limits on the x-axis, while for the third row the limits are chosen so that the distribution widths and relative positions are visually similar to those of the former.
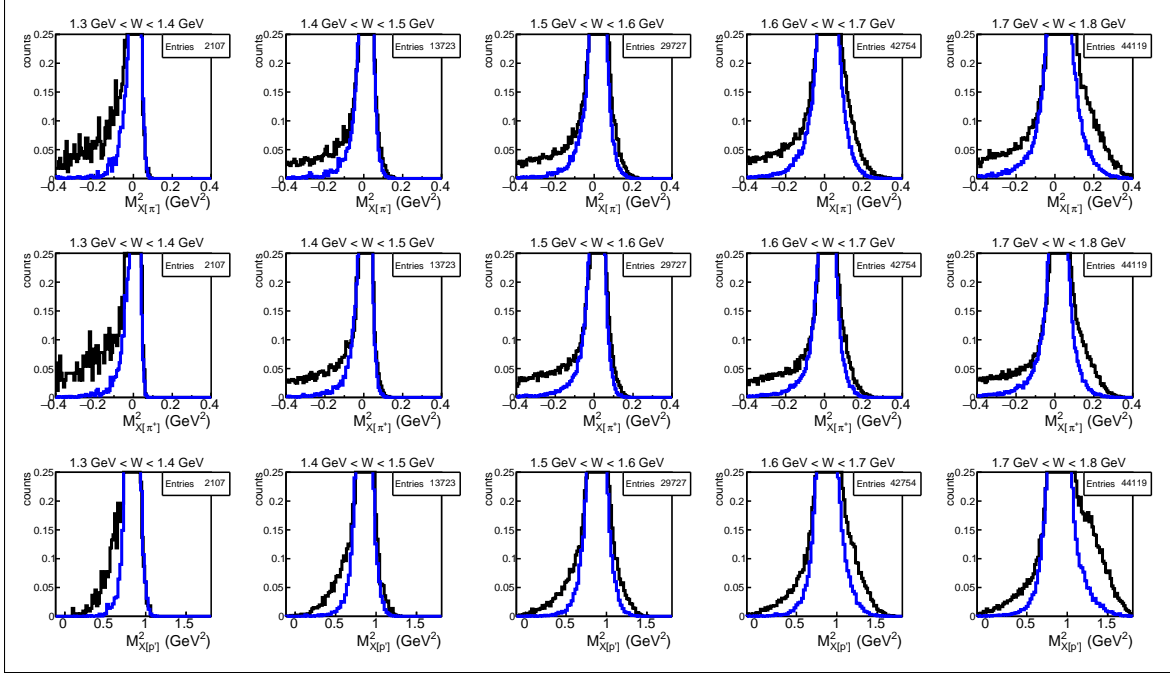

Figure 9.8: Distributions of the quantities $M^2_{X[\pi^-]}$ (first row), $M^2_{X[\pi^+]}$ (second row), and $M^2_{X[p']}$ (third row) defined in (or analogously to) Eq. (9.1). The relative spread of events with FSI in five 100-MeV-wide bins in W is demonstrated by the mismatch between the experimental (black) and the simulated (blue) histograms. The distributions are plotted for events from the fully exclusive topology and normalized in a way that the peak maxima are equal to one. They are however zoomed in on the range [0, 0.25] on the y-axis to better visualize the mismatch. The shown statistics corresponds to the unzoomed experimental distributions.

The distributions from Fig. 9.8 illustrate the cumulative contribution from FSI for the π^+ and proton (first row), π^- and proton (second row), and π^+ and π^- (third row). They share several global distinctive features. Specifically, for all distributions the left-side tail does not show any W dependence staying on a constant substantial level throughout the whole W range, being though a bit more prominent in the first bin. The tail at the right side, in turn, is absent for low W and gradually increases as W grows. This is thought to be driven by the following reasons.

150

First, the left-side tail was proven to contain a large portion of events, in which non-relativistic protons lose their momentum through FSI. Meanwhile, the majority of registered protons in this experiment is non-relativistic, which ensures the stable saturation of the left-side tail throughout the whole W range (for distributions from the first and second rows). At the same time, the right-side tail was proven to contain a large portion of events, in which relativistic hadrons (which are mostly pions) lose their momentum through FSI. This portion, in turn, grows with W, which leads to gradual emergence of the right-side tail.

The slight prominence of the left-side tail and the complete absence of the tail at the right in the first W bin is then due to (i) the abundance of the low-momentum hadrons near the threshold, (ii) the deficiency of the high-momentum hadrons there, and (iii) the most prominent asymmetry of the Fermi smearing in this region.

Once the main similarities of the distributions from Fig. 9.8 are addressed, one can discuss their differences and other related features. Thus, the right-side tail, although keeping nearly the same structure for all distribution types, demonstrates different intensity manifestation, which is the smallest for $M^2_{X[\pi^+]}$ (second row), greater for $M^2_{X[\pi^-]}$ (first row), and the largest for $M^2_{X[p']}$ (third row). This allows for the following conclusion: in the considered event sample the cumulative amount of relativistic π^- and protons that lose their momentum in FSI is smaller than that of π^+ and protons, which in turn is smaller than the corresponding amount of π^+ and π^-. Note that this conclusion is very likely to be dependent on the experimental conditions.

The next feature is related to the left-side tail, which although keeping generally the same W dependence and intensity manifestation for all distributions, demonstrates some structural variations. Thus, for the first two rows, the left-side tail is long and its structure is flat, while for the third row the tail is shorter (relative to the main peak) and has a steeper shape. This observation allows for the following interesting conclusion.

The point is that distributions from the first and second rows include the contributions from the proton FSI as well as from FSI of one type of pion, whereas the distributions from the third row isolate the FSI contribution from both pion types. Therefore, for the first two rows, the left-side tail is dominated with events, in which non-relativistic protons lose the momentum. Meanwhile, for the third row, where such events are not present, the left side-tail is populated with events, in which (i) relativistic pions gain their momentum and (ii) non-relativistic pions lose their momentum. Both these event types do not happen very often, so the $M^2_{X[p']}$ distributions offer a great opportunity to isolate them. One should also keep in mind that some part of the events in the left tail is tossed there from the right side by the Fermi smearing.

Note that the distributions from the first and second rows contain the aforementioned two types of rarer FSI events as well, but only for one type of pion, which means around a half of them. Their manifestation then turns out to be masked by events with the momentum loss of non-relativistic protons, which is the dominant type of FSI events in the left-side tail.

Additionally, from the structure of the left-side tails of distributions in Fig. 9.8, one can suggest that events with proton FSI are subject to a larger spread along the x-axis than events with pion FSI. This observation is confirmed by Ref. [41] as it demonstrates that, when the same variation in the momentum magnitude for pions and protons is considered, the distortions in the $M^2_{X[\pi^-]}$ distributions caused by the proton FSI are larger (i.e. their structure is flatter and the spread along the x-axis is of a larger extent) than those for the case of the pion FSI.

9.4 FSI in topologies with a missing hadron

As follows from the findings revealed above, the set of missing quantities $M^2_{X[i]}$ (where i corresponds to the missing hadron) offers great opportunities for studying kinematic manifestations of FSI effects because each $M^2_{X[i]}$ is capable of isolating the FSI contributions from the corresponding pair of registered hadrons. However, this advantage is mostly related to the fully exclusive topology, where all three available quantities $M^2_{X[i]}$ are auxiliary with respect to the primary quantity $M^2_{X[0]}$ that incorporates information of all registered final hadrons and hence is typically used to isolate the reaction channel. Meanwhile, for topologies with one unregistered hadron, the corresponding quantity $M^2_{X[i]}$, being the only one available, has to be used for the channel identification. Under these conditions, the aforementioned ability of $M^2_{X[i]}$ to isolate FSI contributions from the pair of registered hadrons results in some complications, as described below.

In general, when dealing with topologies with one unregistered hadron, the four-momentum of this hadron is typically reconstructed as missing using the four-momenta of registered particles and then the exclusivity cut on the corresponding distribution of $M^2_{X[i]}$ is performed for isolating the channel. The success of this conventional method is based on the fact that particles produced in one reaction are not independent as they share the same reaction kinematics, which imposes some reaction-specific constraints on their four-momenta. As a result, the particle four-momenta entangle, making the information on one particle to be incorporated into the kinematics of the others.

This method, however, works smoothly only for quasi-free events, while for events with FSI it, in fact, gives an incorrect output because (as was already mentioned) once participating in FSI, hadrons do not further keep the kinematics of the initial reaction and formally can no longer be attributed to this reaction.

To be more specific, the following three possibilities can be distinguished for events from the topologies with an unregistered hadron (assuming that only one final hadron in an event interacts with the neutron).

1. All final hadrons in an event avoided FSI with the neutron. Then this event is a true quasi-free event and the four-momentum of the unregistered hadron can be successfully reconstructed as missing by means of the conventional procedure.

2. The unregistered hadron avoided FSI, while one of the registered hadrons interacted in the final state, changing in this way its four-momentum and hence losing its kinematic affiliation to the initial reaction. This does not allow the proper reconstruction of the missing hadron four-momentum, causing the event to contribute to the FSI-background in the distributions of $M^2_{X[i]}$.

3. The unregistered hadron experienced FSI with the neutron and the registered hadrons avoided them. In this case, the missing four-momentum of the unregistered hadron corresponds to its four-momentum before FSI. Such an event is then falsely treated as quasi-free.

The given disposition reveals some important issues. First, the hadron four-momentum turns out to be the only one source of information on FSI (with the spectator nucleon) this hadron may undergo. If the hadron is not registered, the information on its interaction turns out to be lost beyond reconstruction as the other particles are not aware of this happening.

The next important thing to mention is that in reactions off bound nucleons, topologies with a missing hadron are revealed to suffer from miscounting of both quasi-free events and events with FSI as their separation is inaccurate. Specifically, the amount of quasi-free events is systematically overestimated because events of the third type are considered to be quasi-free, whereas they are actually events with FSI. Although the overestimation is not expected to be dramatic, this issue should

be carefully considered as it may have an impact on the interpretation of the final results of a data analysis.

With that said, one can pay closer attention to the π^--missing topology of this particular analysis[9]. Figure 9.9 shows the distributions of the missing quantity $M^2_{X[\pi^-]}$ plotted for this topology. The relative spread of events with FSI in five 100-MeV-wide bins in W is demonstrated by the mismatch between the experimental (black) and the simulated (blue) histograms. The distributions are normalized in a way that the peak maxima are equal to one and then zoomed in on the range $[0, 0.25]$ on the y-axis, to better visualize the mismatch and for consistency with the distributions in Fig. 9.8.
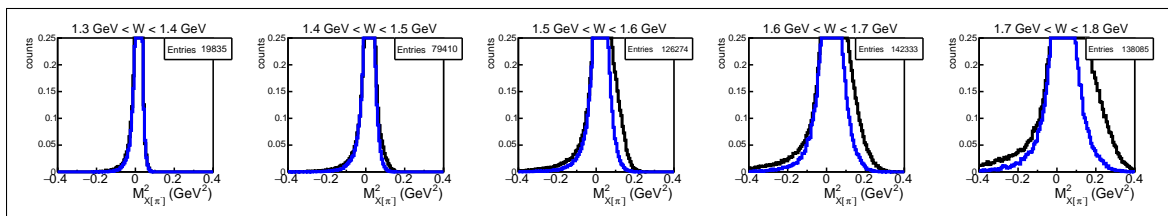

Figure 9.9: Distributions of the missing quantity $M^2_{X[\pi^-]}$ plotted for the π^--missing topology. The relative spread of events with FSI in five 100-MeV-wide bins in W is demonstrated by the mismatch between the experimental (black) and the simulated (blue) histograms. The distributions are normalized in a way that the peak maxima are equal to one and then zoomed in on the range $[0, 0.25]$ on the y-axis, to better visualize the mismatch. The presented statistics corresponds to the unzoomed experimental distributions.

The distributions in Fig. 9.9 reflect the contributions from FSI of the proton and π^+ and do not include the information on the π^- interactions, being analogous in that sense to the distributions in the first row of Fig. 9.8 related to the fully exclusive topology. This analogy advantages their comparison.

As seen in Fig. 9.9, for $W \lesssim 1.5$ GeV no significant mismatch between the experimental (black) and the simulated (blue) distributions is present. The explanation of this effect, which is not observed in the first row of Fig. 9.8, lies in the kinematic differences between the two topologies.

---

[9] Note that the π^--missing topology is the main analysis topology, the fully exclusive topology is a complementary one, while the two other topologies are not used. See more details in Sect. 3.5.

The point is that the π^--missing topology contains mostly events with negative pions of low momentum as they escape through the forward acceptance hole. Meanwhile, the fully exclusive topology includes events, in which the π^- momentum varies from moderate to high as they manage to be registered. Consequently, in the fully exclusive topology, the momenta of the proton and the π^+ are on average lower than in the π^--missing topology. This situation turns out to influence the relative spread of FSI affected events.

First, the dominant contribution to the left-side tail of the $M^2_{X[\pi^-]}$ distribution was shown to be formed by FSI events, in which non-relativistic protons lose their momentum. Meanwhile, the π^- topology happens to lack this kind of events as their major part belongs to the fully exclusive topology.

Another consequence is related to the fact that the probability to interact in the final state depends on the relative velocity of the interacting hadrons, i.e. for slower traveling hadrons the chance to interact is higher than for rapid hadrons. As a result, the two topologies turn out to have different distributions of the interaction probability among the final hadrons due to the difference in their momenta. Specifically, negative pions attributed to the π^--missing topology have higher probability to interact than those attributed to the fully exclusive topology. Meanwhile, for protons and positive pions the situation is the opposite, i.e. their chances to interact are higher for the fully exclusive topology.

Therefore, if compared with the π^--missing topology, the fully exclusive one contains larger number of events with alterations in the proton and π^+ four-momenta caused by FSI, which results in more disturbances seen in the $M^2_{X[\pi^-]}$ distributions as these four-momenta are used to calculate this missing quantity.

At the same time, the π^--missing topology accumulates more events with the π^- FSI than the fully exclusive topology. However, the quantity $M^2_{X[\pi^-]}$ does not reflect the information on the π^- interactions as its four-momentum is excluded from the

calculation of this quantity. This, in turn, promotes the presence of falsely defined quasi-free events in the $M^2_{X[\pi^-]}$ distributions, and their amount correlates with the aforementioned probability of the π^- interactions. This effect causes the distributions of the π^--missing topology to acquire fewer distortions than their fully exclusive analogues, with the maximum difference achieved near the threshold.

The combination of these effects explains the good match between the experimental and simulated distributions of $M^2_{X[\pi^-]}$ observed in the π^--missing topology for $W \lesssim 1.5$ GeV, which is not achieved in the fully exclusive topology.

A further comparison of distributions in Figs. 9.8 and 9.9 also reveals that the left-side tail of the $M^2_{X[\pi^-]}$ distributions in the π^--missing topology differs from its analogue from the fully exclusive topology both in intensity and in W dependence. Specifically, being completely absent near the threshold, it shows a constant, but rather mild growth with W, staying on a still very moderate level even in the last W bin. Meanwhile, the right-side tails for both cases are very alike, though for the π^--missing topology it shows more intensive growth with W.

The understanding again lies in the fact that the π^--missing topology lacks low momentum protons and π^+, having instead an excess of high-momentum hadrons of these types, with all the consequences addressed above. This causes the lack of FSI events with the momentum loss for non-relativistic hadrons and the corresponding abundance of events with the momentum loss for relativistic hadrons, which in turn results in the suppression of the left-side tail and some affluence of the tail at the right.

It is also important to pay closer attention to the issue with the falsely defined quasi-free events that contribute to the $M^2_{X[\pi^-]}$ distributions of the π^--missing topology. As was already stated above, in this topology many unregistered π^- experience FSI due to their very low momentum, leaving the registered protons and π^+ of the corresponding event to remain quasi-free. This effect is very pronounced near the threshold and is mitigated with growing W as proven by the gradually emerging disturbances

in the $M^2_{X[\pi^-]}$ distributions in Fig. 9.9, which indicate more registered hadrons experiencing FSI and hence more quasi-free unregistered π^-. As a result, the amount of falsely defined quasi-free events is maximal near the reaction threshold and declines for higher W. Although such a miscounting itself is inevitable for any topology with a missing hadron in reactions off bound nucleons, the amount of the miscounted events, and its spread along W is to a high degree determined by experimental conditions.

9.5   Resonance formation in pion-neutron FSI

So far the main attention of this investigation has concentrated on the momentum alterations that final hadrons undergo via FSI as a universal criterion for distinguishing events with FSI from regular quasi-free events, without any particular focus on the interaction mechanism itself. Meanwhile, the strong interaction, which drives FSI, offers a very broad spectrum of these mechanisms. Although this study mostly concentrates on kinematic effects and hence does not claim any attempt of a full description of any particular mechanism, it is interesting to dig into one more promising direction in order to fully exploit the opportunities provided by this experimental dataset for a better understanding of FSI.

First, it is worthwhile to recall that in the analyzed reaction, FSI are dominated by elastic scattering of final hadrons off spectator neutrons, i.e. by interactions, in which (i) the quantum numbers of the participating hadrons do not change and (ii) no new particles are produced. Inelastic mechanisms, which do not satisfy these two criteria, are meanwhile less pronounced.

This particular Section examines the process, in which a final hadron (h) couples with the spectator neutron (n), producing nucleon resonances (R) in the intermediate state. This can be represented as $hn \rightarrow R \rightarrow \sum_i h'_i$, where h'_i are the resonance decay products, which are registered by the detector afterwards. In this situation very inter-

esting things may happen, i.e. depending on the resonance decay mode, the registered hadrons may differ from those that form the resonance, both in their type and/or amount. Such processes then can contribute to both elastic and inelastic FSI parts.

To dig into this issue, advantages offered by the fully exclusive topology can again be of use. Specifically, with the four-momenta of all final hadrons available, one can reconstruct the four-momentum of the spectator neutron as missing. Although such reconstruction is inaccurate for events with FSI and also suffers from the Fermi smearing, the resulting four-momentum still suits the purpose of this examination. Specifically, the following set of the invariant masses can be calculated,

$$
\begin{aligned}
M_{n'\pi^-} &= \sqrt{(P^\mu_{n'} + P^\mu_{\pi^-})^2}, \\
M_{n'\pi^+} &= \sqrt{(P^\mu_{n'} + P^\mu_{\pi^+})^2}, \qquad \text{and} \\
M_{n'p'} &= \sqrt{(P^\mu_{n'} + P^\mu_{p'})^2},
\end{aligned}
\tag{9.2}
$$

where $P^\mu_{n'}$ is the four-momentum of the spectator neutron calculated as missing under the target-at-rest assumption, while $P^\mu_{\pi^-}$, $P^\mu_{\pi^+}$, and $P^\mu_{p'}$ are the four-momenta of the final hadrons registered by the detector.

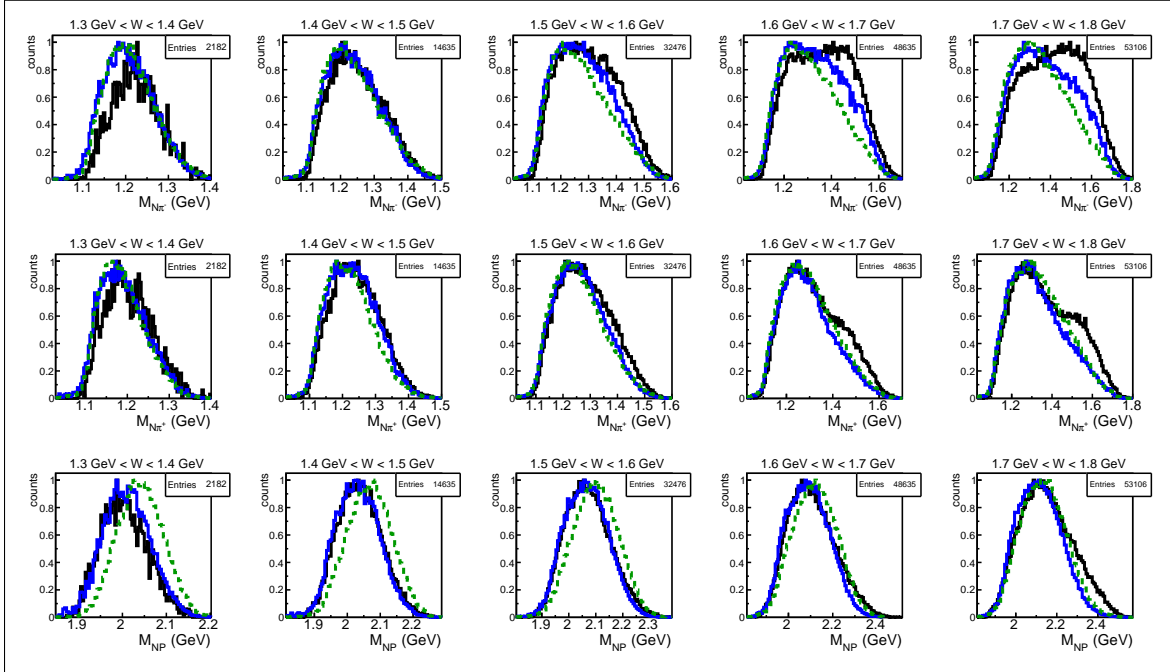Figure 9.10 shows the distributions of the invariant masses $M_{n'\pi^-}$ (first row), $M_{n'\pi^+}$ (second row), and $M_{n'p'}$ (third row) from Eqs. (9.2) plotted for the experimental data (black histograms) and the regular Monte-Carlo simulation (blue histograms). The dashed green histograms are auxiliary as they correspond to the same simulation, but with the cross section weights ignored, which means that phase-space distributions are assumed for all kinematic variables instead of the regular realistic distributions [24, 39]. These green histograms are intended to visualize the impact of the assumptions for the cross section shape implemented into the event generator [24].

In general, invariant mass distributions are very helpful in checking for the presence of an unstable particle, whose decay causes the emission of particles involved in the invariant mass calculation. If this is the case, then the invariant mass distributions acquire a peak at the position of the mass of this unstable particle.

Therefore, if an unstable particle was formed during FSI, then it should be seen as an agglomeration of events with FSI in the corresponding invariant mass distribution, which again can be visually spotted as a mismatch between the experiment and the simulation. Keeping that in mind, one can now examine the invariant mass distributions shown in Fig. 9.10. Note that in Fig. 9.10 all histograms are normalized in a way that their peak maxima are equal to one.

Figure 9.10: Distributions of the invariant masses $M_{n'\pi^-}$ (first row), $M_{n'\pi^+}$ (second row), and $M_{n'p'}$ (third row) from Eqs. (9.2) plotted for experimental data (black histograms) and regular Monte-Carlo simulation (blue histograms). The dashed green histograms are auxiliary as they correspond to the same simulation, but with the cross section weights ignored, which means that phase-space distributions of all kinematic variables are used instead of the regular realistic distributions [24, 39]. The mismatch between the data and the simulation is indicative of the agglomeration of events with FSI. All histograms are normalized in a way that the peak maxima are equal to one. The presented statistics corresponds to the experimental data.

The final proton and the spectator neutron are not expected to couple to each other with the formation of an unstable particle in the intermediate state as both of them are baryons. This conclusion is confirmed by the invariant mass distributions shown in the third row of Fig. 9.10, where the experimental and the simulated histograms agree with each other, both replicating the shape typical for the case of the phase-space distribution of all kinematic variables.

The situation is however different for the invariant masses $M_{n'\pi^-}$ and $M_{n'\pi^+}$ as the neutron can willingly couple to either π^- or π^+ forming a nucleon resonance, and the resonance mass is then determined by the cumulative energy of the coupled pair. Thus, for low W, the formation of the Δ resonances is only possible, while for higher W other resonances with larger masses will compete for the formation.

The visual spotting of the Δ resonances in the distributions of the invariant masses comes meanwhile with some difficulties. They originate from the fact that Δ resonances peak around $\sim$1.2 GeV, and the phase-space invariant mass distribution behaves similarly at low W. Therefore, as long as the width of the invariant mass distribution is comparable with the width of the Δ resonance (which is around 120 MeV), it is difficult to visually distinguish between resonant and non-resonant events as they form the same invariant mass structure. This effect is seen in the first and second rows of Fig. 9.10, where the experiment matches the simulation for $W \lesssim 1.6$ GeV, although the formation of Δ resonances is highly expected.

For higher W however the situation simplifies as the spread of the invariant mass distribution is now sufficient for observing the structures with lower width. Thus, for $W \gtrsim 1.6$ GeV the observed mismatch between the data and the simulation reveals the agglomeration of events with FSI at invariant mass values $\gtrsim 1.4$ GeV, which correspond to the masses of the resonances from the second resonance region. The contribution from the Δ resonance is, however, still hard to judge due to the overall normalization of the distributions.

Thus, the invariant mass distributions in Fig. 9.10 may serve as evidence that both π^- and π^+ do couple to the spectator neutron in the final state with the formation of several resonances, including those from the second resonance region. And moreover, the chance for the neutron and π^- pair to originate from the decay of the resonances from the second resonance region is much higher than that for the neutron and π^+ pair as confirmed by the much larger mismatch observed in the $M_{n'\pi^-}$ distributions (first row) comparing with the $M_{n'\pi^+}$ distributions (second row).

These findings allow for several interesting processes to be traced. First, for the neutron to pion coupling with the formation of Δ resonances, the following options are available. If the neutron couples to the π^-, then the $\Delta^-(1232)$ resonance is formed, which then decays with the emission of the same hadron pair that was involved in its formation (the original momenta are however not kept). Meanwhile, if the neutron couples to the π^+, then the Δ^+ resonance is formed, which has two decay options, i.e. either to the $n\pi^+$ or $p\pi^0$ final states. In the former case, the emitted hadrons are of the same type as the initial, with the different momentum though. However, in the latter case, both emitted hadrons differ from those in the FSI initial state.

The situation complicates further if the formation of the resonances of the second resonance region is considered. In this case, the decaying resonance may emit mesons different than pions (such as ρ, σ, etc.) or even baryons different than nucleons (such as Λ, Σ). The latter is however not expected to happen in this experiment due to its low beam energy, which does not allow for the formation of the resonances with this decay mode as they have too large masses.

Additionally, the resonances of the second resonance region can produce more than two decay products, and the decay to the $N\pi\pi$ final state is the most probable mode of this kind. In this case the resonance decay products differ from the hadrons involved in its formation not only in their type but also in amount.

Besides this, one more impact of FSI on the reaction final state becomes evident, when considering the resonances of the second resonance region decaying to the $N\pi\pi$ final state. In this case, several options for the types of the nucleon and the pions in the FSI final state are in general possible with the following two processes being the most remarkable, i.e. $n\pi^- \to R \to n\pi^-\pi^0$ and $n\pi^+ \to R \to n\pi^+\pi^0$, where R corresponds to a resonance. Although in these processes the neutron and pion maintain their types throughout the resonance formation and decay, their momenta are now affected beyond the level of individual alterations, i.e. their total momentum is not conserved as it leaks out via the π^0 emission.

Thus, one can conclude that the neutron-pion coupling with the resonance formation, which takes place during FSI, in general resolves in the following options[10],

- the types of the particles involved in FSI are kept, their momenta alter but the total momentum of the interacting pair is conserved,

- the types of the particles involved in FSI are kept, their momenta alter, but the cumulative momentum leaks via the emission of an additional particle, and

- the types of the particles involved in FSI are not kept.

The first option then corresponds to elastic interactions, while the second and the third belong to inelastic. It is also essential that manifestations of these options in analyses of experimental data off bound nucleons have some specificities, which are briefly addressed below.

Specifically, events that correspond to the first option turn out to be kinematically identical to those events, in which pions change their momenta through non-resonant rescattering off the spectator nucleon as in both cases pions experience either momentum gain or loss. Therefore, events of both kinds share the same kinematic behavior, which was discussed above.

---

[10] Note that all these options are also relevant for interactions of the final hadrons with each other.

If the process with the momentum leak occurs (the second option), then the chances are high that the corresponding π^- or π^+, if registered, would still be attributed to the original channel during the data analysis, especially taking into account the very poor efficiency of the π^0 registration in CLAS. In that case, such an event can not be distinguished from FSI events with the momentum alterations that conserve the total momentum of the interacting pair, like in the process $n\pi^- \to \Delta^- \to n\pi^-$ or in a simple momentum exchange, which are events of the first type. This is because the neutron (which is withal not registered) is extrinsic with respect to the original exclusive channel (which happens off protons) and hence is not included in its kinematics. Therefore, from the point of view of the original reaction, events with the momentum leak are FSI events with the pion momentum loss and hence comply with the patterns derived above for such kind of events.

Meanwhile, the third scenario leads to the modification of the final state of the original reaction due to FSI, which causes the registered particles to be attributed to a wrong exclusive channel with the consequence of miscounting events selected for a particular reaction. This problem can be however resolved to a very high degree on the level of the exclusivity cut on a missing mass distribution that is typically used for the channel identification. The majority of falsely defined events will not survive this cut because such events will fail to contribute to the main missing mass peak, as they do not keep the kinematics inherent for the channel that is subject to the selection.

At this point, the examination being conducted seems to exploit to a very high degree the opportunities offered by this experimental dataset for a better understanding of FSI effects, which occur in the reaction of the double-pion production off protons in deuterium. Therefore, considering the objectives set to this chapter being fulfilled, one can conclude the whole discussion of FSI effects, which accompanies the main analysis.

Chapter 10
Results and conclusion

This study experimentally explores the process of charged double-pion electroproduction off protons bound in deuterium nuclei. The exploration became possible owing to the experiment of electron scattering off a deuterium target conducted in Hall B at Jefferson Lab with the CLAS detector [4]. The data collected in this experiment incorporates information on a broad range of physical phenomena that represent important blocks in our understanding of nuclear and particle interactions. Some of these phenomena are inherent in reactions off free protons as well, whereas others are unique for reactions off bound nucleons.

In order to exploit to a higher degree opportunities offered by this deuteron target experiment, this study extends beyond the scope of observable extraction and represents an attempt at a broader and more detailed exploration of the features observed during the analysis. To facilitate understanding and interpretation of these features, the study [22, 23], which analyzed the same exclusive reaction off free protons under the same experimental conditions, was used as a reference point.

As the main result of this study, the integral and single-differential cross sections of the reaction $\gamma_v p(n) \rightarrow p'(n')\pi^+\pi^-$ in the kinematic region of the invariant mass W from 1.3 GeV to 1.825 GeV and photon virtuality Q^2 from 0.4 GeV^2 to 1 GeV^2 have been obtained. The cross sections were extracted in the quasi-free regime, which means that the admixture of events with FSI was kinematically reduced to the achievable minimum.
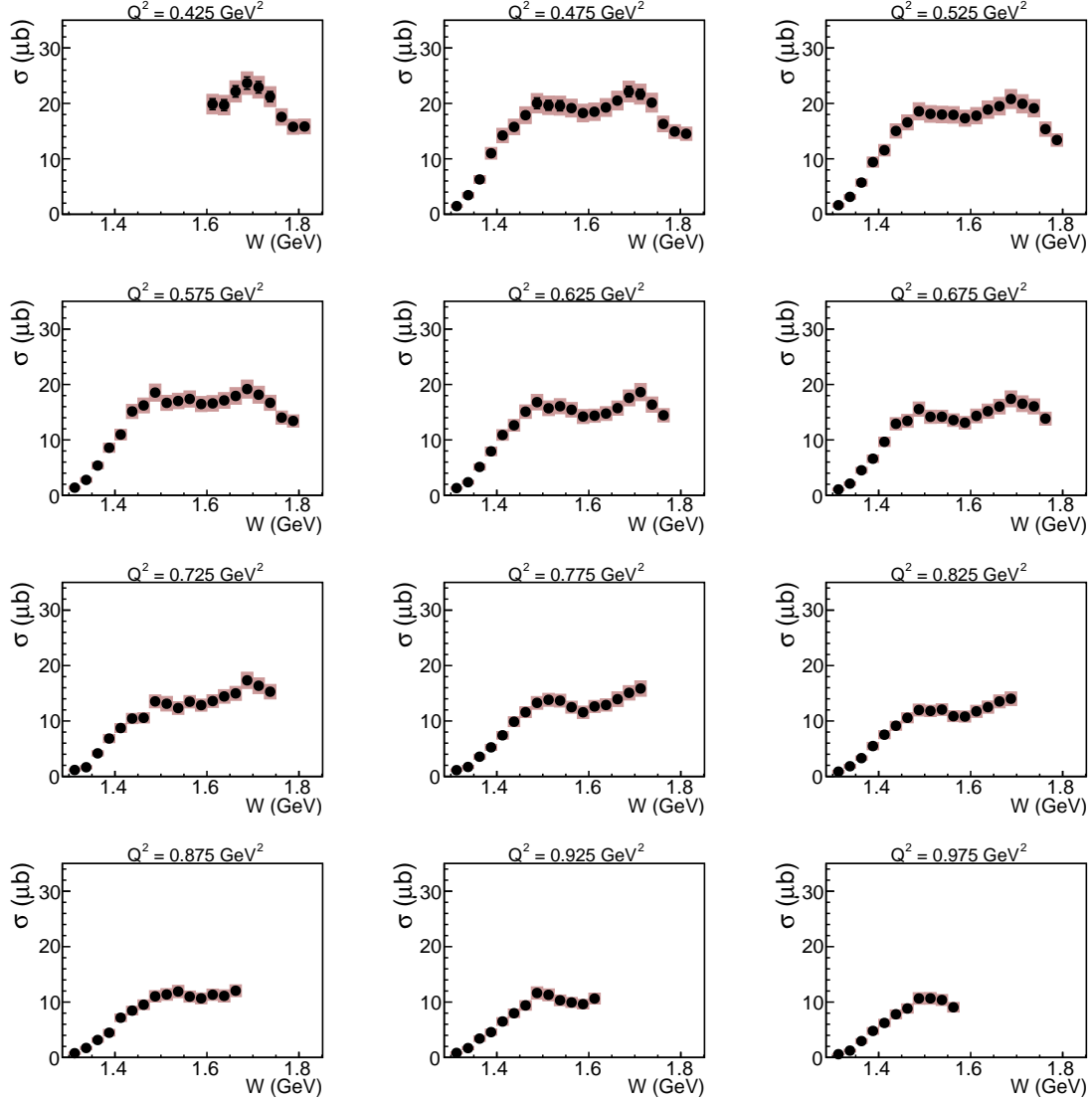
Figure 10.1: W dependences of the extracted integral cross sections in various bins in Q^2. The pink shadowed area for each point is the total cross section uncertainty, which is the uncertainty $\delta_{\text{stat,mod}}^{\text{tot}}$ (see Sect. 7.4) summed in quadrature with the total systematic uncertainty (see Sect. 7.3). The error bars that correspond to the $\delta_{\text{stat,mod}}^{\text{tot}}$ uncertainty only, are smaller than the symbol size.
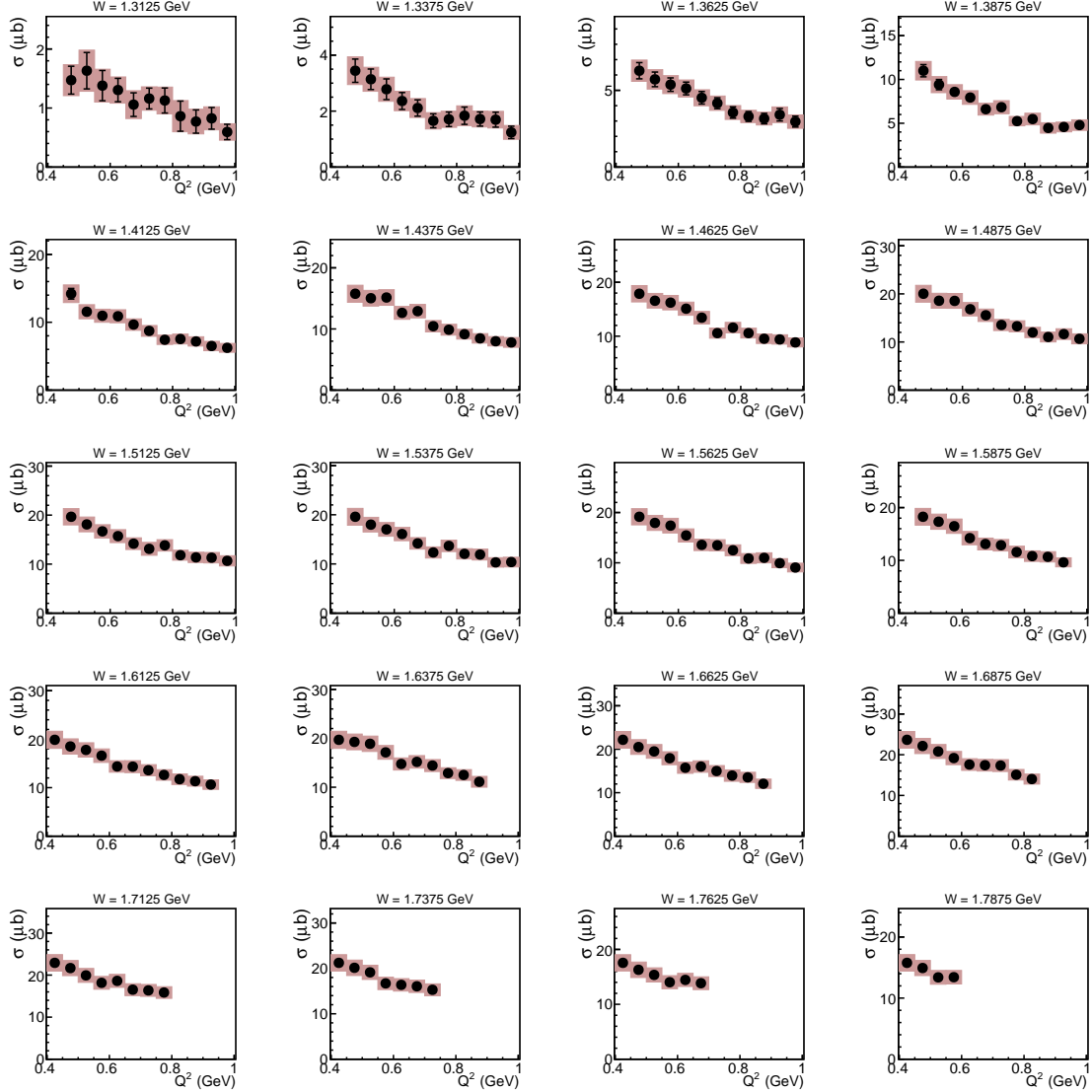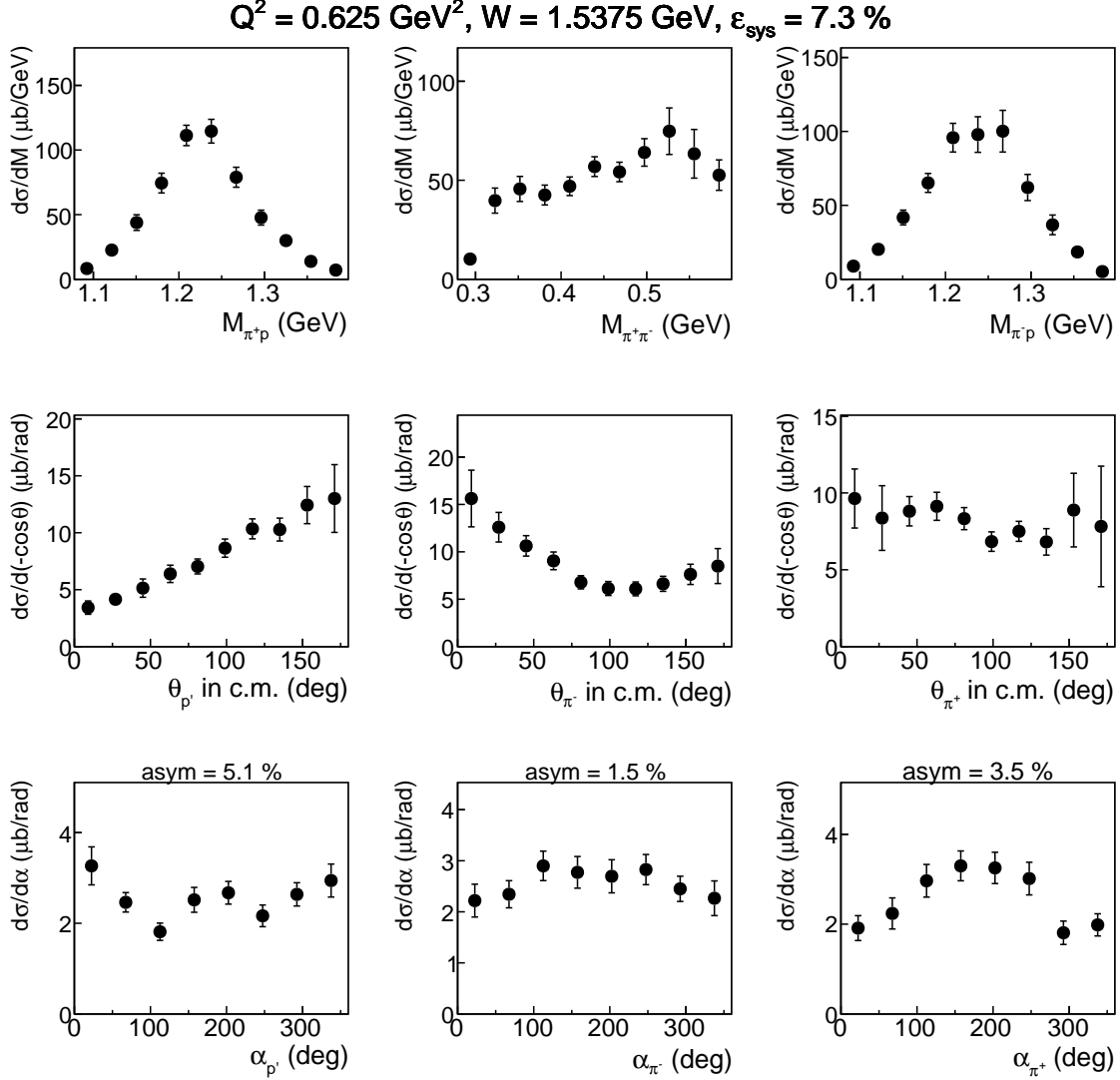
Figure 10.2: Q^2 dependences of the extracted integral cross sections in various bins in W. The pink shadowed area for each point is the total cross section uncertainty, which is the uncertainty $\delta_{\text{stat,mod}}^{\text{tot}}$ (see Sect. 7.4) summed in quadrature with the total systematic uncertainty (see Sect. 7.3). The error bars correspond to the $\delta_{\text{stat,mod}}^{\text{tot}}$ uncertainty only and for most of the points are smaller than the symbol size.

Figure 10.3: Single-differential cross sections for $W = 1.5375$ GeV and $Q^2 = 0.625$ GeV^2. The cross sections are shown with the uncertainty $\delta^{\text{tot}}_{\text{stat,mod}}$ represented by the error bars (see Sect. 7.4). The relative integral systematic uncertainty ε_{sys} for this (W, Q^2) point is specified in the plot title. The definition of the average asymmetry factor specified above each α distribution, is given in App. D.

Figure 10.1 shows the W dependences of the extracted integral cross sections in various bins in Q^2, while Figure 10.2 shows their Q^2 dependences in various bins in W. The pink shadowed area for each point is the total cross section uncertainty, which is the uncertainty $\delta^{\text{tot}}_{\text{stat,mod}}$ (see Sect. 7.4) summed in quadrature with the total systematic uncertainty (see Sect. 7.3). The error bars correspond to the $\delta^{\text{tot}}_{\text{stat,mod}}$ uncertainty only and for most of the points are smaller than the symbol size.

For each integral cross section point, the set of nine single-differential cross sections has been obtained. As an example, Figure 10.3 shows the single-differential cross sections for $W = 1.5375$ GeV and $Q^2 = 0.625$ GeV^2. The cross sections are reported with the uncertainty $\delta^{\text{tot}}_{\text{stat,mod}}$ represented by the error bars. The value of the relative integral systematic uncertainty ε_{sys} for this (W, Q^2) point is specified in the plot title. The full set of extracted single-differential cross sections is available in App. D accompanied by some explanatory remarks on the presentation format.

Note that FSI-background admixture left after the exclusivity cut in the π^--missing topology (see Sect. 3.5.2), being corrected only in an integral sense, may potentially impact the shape of extracted single-differential distributions (mostly angular). However, since this admixture is present only for events from the π^--missing topology for $W > 1.4625$ GeV and stays there on the level of 3-7%, its impact is not thought to be discernible against the total cross section uncertainty.

The cross section extraction analysis has undergone CLAS Collaboration Review by the Hadron Spectroscopy Working Group committee and been approved.

The other outcome of this study consists in the performed kinematic examination of FSI between the reaction final hadrons and the spectator neutron for the process of $\pi^+\pi^-$ electroproduction off protons bound in deuterium nuclei. This examination counterbalances the main cross section extraction analysis, which was mainly focused on quasi-free events.

The underlying idea of this examination stems from the fact that spectator nucleons are extrinsic to the original exclusive reaction, and therefore any interaction with them breaks the energy-momentum conservation imposed on the reaction particles. As a consequence, FSI with spectator nucleons introduce disturbances to the distributions of missing quantities, which can be examined along the reaction phase space. In this way, kinematic probing of this FSI type can be carried out.

In the performed examination, the increase in the relative amount of events with FSI in the regions of low momentum and large polar angles was observed for all final hadrons, to one extent or another. The dominance of proton-neutron interactions over the pion-neutron interactions was also revealed. Besides this, in the regions with large FSI contribution kinematically available in this experiment, FSI were found to be dominated by the processes, in which non-relativistic protons lose their momentum.

In addition to that, pion-neutron FSI were shown to willingly evolve through the formation of resonances in the intermediate state, including those from the second resonance region. Due to multiple decay options available for the latter, such processes can then contribute to both elastic and inelastic FSI parts.

Further on, FSI manifestations were found to differ strongly depending on the reaction topology. This is because the probability to experience FSI differs for hadrons attributed to various topologies due to their non-identical geometrical acceptance.

It is also important that in reactions off bound nucleons, topologies with a missing hadron are revealed to suffer from miscounting of both quasi-free events and events with FSI as their separation is inaccurate. This inaccuracy originate from the fact that in such topologies the only quantity available for the channel identification and isolation of quasi free events is the missing mass of the unregistered particle, which does not reflect information on FSI of the missing hadron.

Meanwhile, the latter conclusion reveals one more potential uncertainty source for the extracted quasi-free cross sections. Specifically, for the π^--topology, which

170

is the main analysis topology, some of events with the π^- FSI are falsely identified as quasi-free. The portion of such events is thought to be maximal near the reaction threshold and decline with growing W. Unfortunately, as true quasi-free events are kinematically identical to those that are falsely identified, this miscounting seems to be inevitable for any topology with a missing hadron in reactions off bound nucleons.

Another useful result of this analysis consists in exploring the effects of the initial proton motion. These effects turned out to be intertwined with many analysis aspects: they not only cause the smearing of some kinematic quantities, but also lead to the blurring of the boundaries of the Q^2 versus W distributions, alter the common procedure of the Lab to CMS transformation, affect the population of the multi-dimensional cells, and more. On top of that, they affect the extracted quasi-free cross sections, causing the need to perform a special unfolding correction. These issues were subjected to a careful investigation, which to a high degree relied on the Monte Carlo simulation. The latter, meanwhile, was performed by means of the TWOPEG-D event generator [24], which was specially developed to deal with the effects of the initial proton motion in this study.

Finally, in addition to the direct results summarized above, it is worthwhile to mention that this study initiated a set of related studies and developments. Among them are the development of the TWOPEG and TWOPEG-D event generators [24, 39], testing parameterizations of the deuteron quasi-elastic peak [47], and exploration of peculiar features of missing mass distributions that includes an attempt of kinematic modeling of FSI effects [41]. Besides this, Ref. [38] and Ref. [3] were also inspired by this analysis as well.

Bibliography

[1] B. Krusche and S. Schadmand, "Study of nonstrange baryon resonances with meson photoproduction," *Prog. Part. Nucl. Phys.*, vol. 51, pp. 399–485, 2003.

[2] I. G. Aznauryan and V. D. Burkert, "Electroexcitation of nucleon resonances," *Prog. Part. Nucl. Phys.*, vol. 67, pp. 1–54, 2012.

[3] Iu. A. Skorodumina *et al.*, "Nucleon resonances in exclusive reactions of photo- and electroproduction of mesons," *Moscow Univ. Phys. Bull.*, vol. 70, no. 6, pp. 429–447, 2015. [Vestn. Mosk. Univ.,no.6,3(2015)].

[4] B. A. Mecking *et al.*, "The CEBAF Large Acceptance Spectrometer (CLAS)," *Nucl. Instrum. Meth.*, vol. A503, pp. 513–553, 2003.

[5] "CLAS physics database." `http://clas.sinp.msu.ru/cgi-bin/jlab/db.cgi`.

[6] V. I. Mokeev, E. Santopinto, M. M. Giannini, and G. Ricco, "The Influence of the nuclear medium on the baryon resonance excitation," *Int. J. Mod. Phys.*, vol. E4, pp. 607–624, 1995
[see also Refs.[1-5] there].

[7] N. Bianchi *et al.*, "Absolute total photoabsorption cross-sections on nuclei in the nucleon resonance region," *Phys. Lett.*, vol. B325, pp. 333–336, 1994.

[8] J. Ahrens, "The Total Absorption of Photons by Nuclei," *Nucl. Phys.*, vol. A446, pp. 229C–239C, 1985.

[9] M. Osipenko *et al.*, " The deuteron structure function F2 with CLAS," CLAS-NOTE-2005-013, arXiv:hep-ex/0507098, 2005.

[10] M. Osipenko *et al.*, "Measurement of the deuteron structure function F(2) in the resonance region and evaluation of its moments," *Phys. Rev.*, vol. C73, p. 045205, 2006.

[11] M. Osipenko *et al.*, "Measurement of the Nucleon Structure Function F2 in the Nuclear Medium and Evaluation of its Moments," *Nucl. Phys.*, vol. A845, pp. 1–32, 2010.

[12] M. Osipenko *et al.*, "A Kinematically complete measurement of the proton structure function F(2) in the resonance region and evaluation of its moments," *Phys. Rev.*, vol. D67, p. 092001, 2003.

[13] B. Krusche, "Photoproduction of mesons from nuclei: In-medium properties of hadrons," *Prog. Part. Nucl. Phys.*, vol. 55, pp. 46–70, 2005.

[14] J. V. Noble, "Modification of the nucleon's properties in nuclear matter," *Phys. Rev. Lett.*, vol. 46, pp. 412–415, 1981.

[15] M. Ripani *et al.*, "Measurement of Two Pion Decay of Electroproduced Light Quark Baryon States with CLAS," *CLAS-Analysis-2002-109*, 2002.

[16] M. Ripani *et al.*, "Measurement of $ep \rightarrow e'p\pi^+\pi^-$ and baryon resonance analysis," *Phys. Rev. Lett.*, vol. 91, p. 022002, 2003.

[17] G. V. Fedotov *et al.*, "Analysis report on the $ep \rightarrow e'p\pi^+\pi^-$ reaction in the CLAS detector with a 1.515 GeV beam for $0.2 < Q^2 < 0.6$ GeV^2 and $1.3 < W < 1.6$ GeV," *CLAS-Analysis-2007-117*, 2007.

[18] G. V. Fedotov *et al.*, "Electroproduction of $p\pi^+\pi^-$ off protons at $0.2 < Q^2 < 0.6$ GeV^2 and $1.3 < W < 1.57$ GeV with CLAS," *Phys. Rev.*, vol. C79, p. 015204, 2009.

[19] E. L. Isupov *et al.*, "Measurements of $ep \rightarrow e'\pi^+\pi^-p'$ Cross Sections with CLAS at 1.40 Gev $< W < 2.0$ GeV and 2.0 GeV$^2 < Q^2 < 5.0$ GeV^2," *Phys. Rev.*, vol. C96, no. 2, p. 025209, 2017.

[20] E. Golovatch *et al.*, "First results on nucleon resonance photocouplings from the $\gamma p \rightarrow \pi^+\pi^-p$ reaction," *Phys. Lett.*, vol. B788, pp. 371–379, 2019.

[21] A. Trivedi and R. W. Gothe, "Measurement of New Observables from the $p\pi^+\pi^-$ Electroproduction off the Proton," *CLAS-Analysis-2019-102*, 2018.

[22] G. V. Fedotov *et al.*, "Analysis report on the $ep \rightarrow e'p\pi^+\pi^-$ reaction in the CLAS detector with a 2.039 GeV," *CLAS-Analysis-2017-101 (CLAS-NOTE-2018-001)*, 2017.

[23] G. V. Fedotov *et al.*, "Measurements of the $\gamma_v p \rightarrow p'\pi^+\pi^-$ cross section with the CLAS detector for 0.4 GeV$^2 < Q^2 < 1.0$ GeV^2 and 1.3 GeV $< W < 1.825$ GeV," *Phys. Rev.*, vol. C98, no. 2, p. 025203, 2018.

[24] Iu. Skorodumina, G. V. Fedotov, and R. W. Gothe, "TWOPEG-D: An Extension of TWOPEG for the Case of a Moving Proton Target," *CLAS12-NOTE-2017-014*, 2017, arXiv:1712.07712.

[25] "e1e target assembly." `https://userweb.jlab.org/~skorodum/e1e_target/tar_e1e_web.pdf`.

[26] M. Amarian *et al.*, "The CLAS forward electromagnetic calorimeter," *Nucl. Instrum. Meth.*, vol. A460, pp. 239–265, 2001.

[27] G. Adams *et al.*, "The CLAS Cherenkov detector," *Nucl. Instrum. Meth.*, vol. A465, pp. 414–427, 2001.

[28] E. S. Smith *et al.*, "The time-of-flight system for CLAS," *Nucl. Instrum. Meth.*, vol. A432, pp. 265–298, 1999.

[29] S. T. G. Mutcler and E. Smith, "CLAS TOF Scintillator Positions," CLAS-NOTE-1998-008, 1998.

[30] *http://clasweb.jlab.org/bos/browsebos.php.*

[31] S. Stepanyan, "Proposal for the Production of the DST's to Distribute CLAS Data," *CLAS-NOTE-99-002*, 1999.

[32] I. A. Skorodumina *et al.*, "Quasi-free cross section measurements for the $\pi^+\pi^-$ electroproduction off the proton in deuterium with CLAS and a 2.039 GeV beam," *CLAS-Analysis-2021*, 2020.

[33] K. Egiyan *et al.*, "Determination of electron energy cut due to the CLAS EC threshold," *CLAS-NOTE-99-007*, 1999.

[34] M. Osipenko, A. Vlassov, and M. Taiuti, "Matching between the electron candidate track and Cherenkov counter hit," *CLAS-NOTE-2004-020*, 2004.

[35] P. K. Khetarpal, *NEAR THRESHOLD NEUTRAL PION ELECTRO-PRODUCTION AT HIGH MOMENTUM TRANSFERS.* Ph. D. Thesis: https://www.jlab.org/Hall-B/general/thesis/Khetarpal_thesis.pdf.

[36] M. Ungaro and K. Joo, *e1-6 Electron Identification.* CLAS web page: https://userweb.jlab.org/~ungaro/maureepage/proj/pi0/e_pid/e_pid.html.

[37] K. Park *et al.*, "Kinematics Corrections for CLAS," *CLAS-Note-2003-012*, 2003.

[38] Yu. Skorodumina *et al.*, "Investigating of the exclusive reaction of $\pi^+\pi$ pair electroproduction on a proton bound in a deuteron," *Bull. Russ. Acad. Sci. Phys.*, vol. 79, no. 4, pp. 532–536, 2015. [Izv. Ross. Akad. Nauk Ser. Fiz.79,no.4,575(2015)].

[39] Iu. Skorodumina, G. V. Fedotov, *et al.*, "TWOPEG: An Event Generator for Charged Double Pion Electroproduction off Proton," *CLAS12-NOTE-2017-001*, 2017, arXiv:1703.08081.

[40] R. Machleidt, K. Holinde, and C. Elster, "The Bonn Meson Exchange Model for the Nucleon Nucleon Interaction," *Phys. Rept.*, vol. 149, pp. 1–89, 1987.

[41] Iu. Skorodumina, G. V. Fedotov, and R. W. Gothe, "Peculiar features of missing mass distributions in studies of exclusive reactions," *CLAS12-NOTE-2021-002*, 2021.

[42] E. Byckling and K. Kajantie, *Particle Kinematics.* Jyvaskyla, Finland: University of Jyvaskyla, 1971.

[43] L. W. Mo and Y.-S. Tsai, "Radiative Corrections to Elastic and Inelastic ep and μp Scattering," *Rev.Mod.Phys.*, vol. 41, pp. 205–235, 1969.

[44] N. Markov *et al.*, "Single π^0 Electroproduction off the Proton in the Resonance region," *CLAS-Analysis-2014-106*, 2014.

[45] B. Laforge and L. Schoeffel, "Elements of statistical methods in high-energy physics analyses," *Nucl. Instrum. Meth.*, vol. A394, pp. 115–120, 1997.

[46] E. N. Golovach *et al.* `http://depni.sinp.msu.ru/~golovach/EG/`.

[47] Iu. Skorodumina, G. V. Fedotov, and R. W. Gothe, "Testing Parameterizations of the Deuteron Quasi-Elastic Peak," *CLAS12-NOTE-2019-003*, 2019, arXiv:2003.02337.

[48] P. Bosted *et al.* `https://userweb.jlab.org/~bosted/fits.html`.

[49] P. E. Bosted and M. E. Christy, "Empirical fit to inelastic electron-deuteron and electron-neutron resonance region transverse cross-sections," *Phys. Rev.*, vol. C77, p. 065206, 2008.

[50] K. M. Hanson, J. R. Dunning, M. Goitein, T. Kirk, L. E. Price, and R. Wilson, "Large angle quasielastic electron-deuteron scattering," *Phys. Rev.*, vol. D8, pp. 753–778, 1973.

[51] S. Rock, R. G. Arnold, P. E. Bosted, B. T. Chertok, B. A. Mecking, I. A. Schmidt, Z. M. Szalata, R. York, and R. Zdarko, "Measurement of elastic electron - neutron scattering and inelastic electron - deuteron scattering cross-sections at high momentum transfer," *Phys. Rev.*, vol. D46, pp. 24–44, 1992.

[52] S. Rock *et al.*, "Measurement of elastic electron - neutron scattering and inelastic electron - deuteron scattering cross-sections at high momentum transfer," *SLAC-PUB-5239*, 1991.

[53] A. Bodek, M. E. Christy, and B. Coopersmith, "Effective Spectral Function for Quasielastic Scattering on Nuclei," *Eur. Phys. J.*, vol. C74, no. 10, p. 3091, 2014.

[54] L. Durand, "Inelastic Electron-Deuteron Scattering Cross Sections at High Energies. 2. Final-State Interactions and Relativistic Corrections," *Phys. Rev.*, vol. 123, pp. 1393–1422, 1961.

[55] P. E. Bosted, "An Empirical fit to the nucleon electromagnetic form-factors," *Phys. Rev.*, vol. C51, pp. 409–411, 1995.

[56] Y. Tian and R. W. Gothe, "Exclusive π^- Electroproduction off the Neutron in Deuterium in the Resonance Region," *CLAS-Analysis-2021-101*, 2020.

[57] Yu. M. Shirokov and N. P. Yudin, *Yadernaya fizika (Nuclear Physics)*. Moscow: Nauka, 1980.

[58] F. Rohrlich and J. Eisenstein, "Neutron-proton and neutron-neutron scattering at high energies," *Phys. Rev.*, vol. 75, pp. 705–724, Mar 1949.

[59] R. E. Cutkosky, R. E. Hendrick, J. W. Alcock, Y. A. Chao, R. G. Lipes, J. C. Sandusky, and R. L. Kelly, "Pion-nucleon partial-wave analysis," *Phys. Rev. D*, vol. 20, pp. 2804–2838, Dec 1979.

[60] A. M. Gasparyan, J. Haidenbauer, C. Hanhart, and J. Speth, "Pion nucleon scattering in a meson exchange model," *Phys. Rev. C*, vol. 68, p. 045207, 2003.

[61] T. P. Vrana, S. A. Dytman, and T. S. H. Lee, "Baryon resonance extraction from pi N data using a unitary multichannel model," *Phys. Rept.*, vol. 328, pp. 181–236, 2000.

Appendix A

Lab to CMS transformation

Here the procedure of the Lab to CMS transformation for an electroproduction experiment off the proton at rest (bottom left illustration in Fig. 4.2) is described [22]. In this case the CMS axis orientation is different for each reaction event and is specified by the direction of the scattered electron. The transformation from Lab to CMS includes the following steps[1]:

A. The xy-plane of the Lab system is rotated around the z-axis (given by the incoming electron direction) to make the x-axis lying in the electron scattering plane (see Fig. A.1). This rotation transforms the four-momentum as $P' = P \cdot R_1(\varphi_{e'})$, with

$$R_1(\varphi_{e'}) = \begin{pmatrix} \cos \varphi_{e'} & -\sin \varphi_{e'} & 0 & 0 \\ \sin \varphi_{e'} & \cos \varphi_{e'} & 0 & 0 \\ 0 & 0 & 1 & 0 \\ 0 & 0 & 0 & 1 \end{pmatrix}, \tag{A.1}$$

where $\varphi_{e'}$ is the azimuthal angle of the scattered electron.

After this rotation $\varphi_{e'} = 0$, while $\varphi_{\gamma_v} = \pi$ with respect to the intermediate reference frame.

---

[1] In all derivations the energy is assumed to be the last component of the four-momentum and the four-momentum to be a row vector.
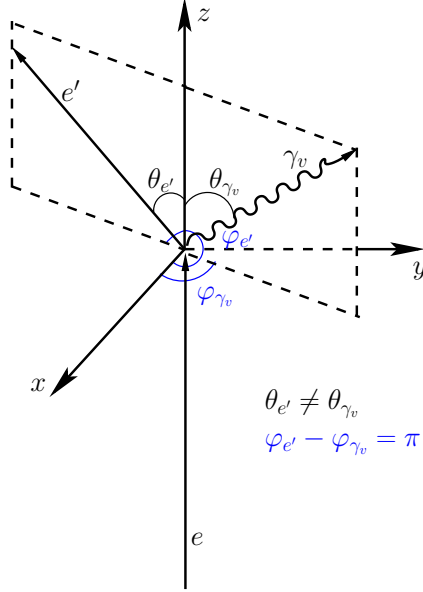
Figure A.1: Virtual photon and scattered electron angles θ and φ in the Lab frame for the proton at rest experiment.

B. The Lab system is then rotated to align the z-axis with the virtual photon direction. The four-momentum transformation for this rotation is given by $P'' = P' \cdot R_2(\theta_{\gamma_v})$, with

$$R_2(\theta_{\gamma_v}) = \begin{pmatrix} \cos\theta_{\gamma_v} & 0 & -\sin\theta_{\gamma_v} & 0 \\ 0 & 1 & 0 & 0 \\ \sin\theta_{\gamma_v} & 0 & \cos\theta_{\gamma_v} & 0 \\ 0 & 0 & 0 & 1 \end{pmatrix}, \tag{A.2}$$

where θ_{γ_v} is the polar angle of the virtual photon[2].

---

[2] Using embedded ROOT functions, both rotations can be coded using the unit vectors TVector3 uz = P4_gamma.Vect().Unit() and TVector3 ux = (P4_EL.Vect().Cross(P4_ELP.Vect())).Unit(), where P4_gamma, P4_EL, and P4_ELP are the four-momenta of the virtual photon, initial and final electrons, respectively. The axis vector ux needs to be rotated according to ux.Rotate(3.*M_PI/2,uz). Finally the rotation is defined as rot.SetZAxis(uz,ux).Invert() and needs to be applied to the four-momentum (P4) of each particle: P4.Transform(rot).

C. Finally, a boost into the CM frame of the *virtual photon – initial proton* system is performed. It is given by the formula $P''' = P'' \cdot R_3(\beta)$, with

$$R_3(\beta) = \begin{pmatrix} 1 & 0 & 0 & 0 \\ 0 & 1 & 0 & 0 \\ 0 & 0 & \gamma & -\gamma\beta \\ 0 & 0 & -\gamma\beta & \gamma \end{pmatrix}, \quad \beta = \frac{|\vec{q}|}{E_\gamma + m_{proton}} = \frac{\sqrt{E_\gamma^2 + Q^2}}{E_\gamma + m_{proton}}, \quad \gamma = \frac{1}{\sqrt{1-\beta^2}},$$

(A.3)

where $|\vec{q}|$ is the magnitude of the three-vector of the virtual photon and β the magnitude and z-component of the three-vector[3] $\vec{\beta} = (0, 0, \beta)$.

---

[3] Note: if you use the ROOT function .Boost, you should change the sign of the z-component of β-vector as .Boost(0,0,-β).

Appendix B

The reaction phase-space

The phase-space of the reaction $ep \rightarrow e'p'\pi^+\pi^-$ is determined by seven kinematic variables, i.e. W, Q^2, $M_{h_1h_2}$, $M_{h_2h_3}$, θ_{h_1}, φ_{h_1}, and α_{h_1} (see Sect. 4.3 for details). The kinematic coverage for various variables has the following specificities.

- In the W and Q^2 variables it depends on the electron beam energy and experimental conditions and is fixed for a particular experiment.

- The angular variables θ_{h_1}, φ_{h1}, and α_{h1} vary in the fixed limits of $[0, \pi]$, $[0, 2\pi]$, and $[0, 2\pi]$, respectively.

- In the invariant masses $M_{h_1h_2}$ and $M_{h_2h_3}$ the coverage depends on W and broadens as W grows.
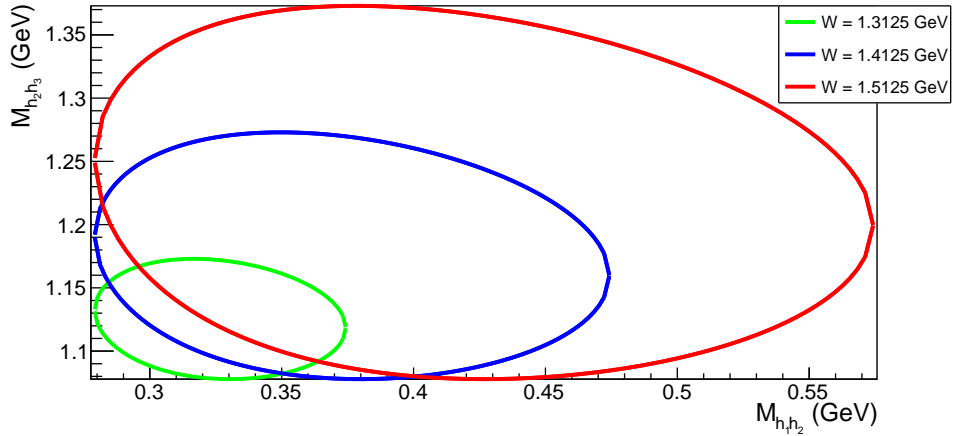
Figure B.1: Boundary of the $M_{h_2h_3}$ versus $M_{h_1h_2}$ distribution for several distinct values of W specified in the plot.

The shape of the reaction phase-space in the invariant masses is determined by the condition $B(M^2_{h_1 h_2}, M^2_{h_2 h_3}, W^2, m^2_{h_2}, m^2_{h_1}, m^2_{h_3}) = 0$, where $B(x, y, z, u, v, w)$ is the Byckling function [42] given by

$$\begin{aligned} B(x, y, z, u, v, w) =&\, x^2 y + xy^2 + z^2 u + zu^2 + v^2 w + vw^2 + \\ & xzw + xuv + yzv + yuw - xy(z + u + v + w) - \\ & zu(x + y + v + w) - vw(x + y + z + u). \end{aligned} \tag{B.1}$$

Figure B.1 shows the boundary of the $M_{h_2 h_3}$ versus $M_{h_1 h_2}$ distribution for several values of W specified in the plot and visually demonstrates the effect of the phase-space broadening with the increase of W.

Appendix C
Uncertainties for indirect measurements

Some useful examples of the error propagation for indirect measurements are described here. In these examples one assumes that $a > 0$, $b > 0$, and $c > 0$.

- If independent variables x_1 and x_2 have absolute uncertainties Δx_1 and Δx_2, respectively, then the absolute uncertainty of the variable $y = c(\frac{x_1}{a} - \frac{x_2}{b})$ is

$$\Delta y = c \sqrt{\left(\frac{\Delta x_1}{a}\right)^2 + \left(\frac{\Delta x_2}{b}\right)^2}. \tag{C.1}$$

- If the variable x has an absolute uncertainty Δx, then the absolute uncertainty of the variable $y = \frac{a}{x}$ is

$$\Delta y = \frac{a}{x^2} \cdot \Delta x = y \cdot \frac{\Delta x}{x}. \tag{C.2}$$

- If the variable x has an absolute uncertainty Δx, then the absolute uncertainty of the variable $y = \frac{a \cdot x + b}{c}$ is

$$\Delta y = \frac{a \cdot \Delta x}{c}. \tag{C.3}$$

- If there is a set of measurements x_1, x_2, ..., x_n with the arithmetic mean $\overline{x}$, then the absolute standard error of the arithmetic mean is

$$\Delta \overline{x} = \sqrt{\frac{\sum\limits_{i=1}^{n}(x_i - \overline{x})^2}{n \cdot (n-1)}}. \tag{C.4}$$

Appendix D

Measured single-differential cross sections

This Appendix contains the full set of single-differential cross sections measured in the current analysis. The cross sections are reported with the uncertainty $\delta_{\mathrm{stat,mod}}^{\mathrm{tot}}$ shown by the error bars (see Sect. 7.4). The central point of the corresponding W and Q^2 bin is specified in the title of each figure together with the value of the relative integral systematic uncertainty $\varepsilon_{\mathrm{sys}}$ that can be propagated as a global factor to the corresponding single-differential cross sections (see Sect. 7.3).

Note that the invariant mass distributions are shown in the range from M_{lower} to M_{upper}, both given by Eq. (4.4.1) with the latter calculated using the central value of the W bin. One, therefore, should take into consideration that, for each invariant mass, the cross section is equal to zero on both sides of the range. Also note that the invariant mass distributions contain one bin less than specified in Tab. 4.1, since the cross section in the last mass bins is not reported. This happens due to the special arrangement of thhe mass bins used in the analysis, which forces the last bin to be situated out of the specified range (see Sect. 4.4 for details).

It is also noteworthy that α angular distributions of the double-pion cross sections should be symmetrical with respect to $\alpha = 180^{\circ}$, when integrated over φ. However, the experimentally measured α distributions acquire some asymmetry. To judge more quantitatively the asymmetry degree, the average asymmetry factor was estimated for each extracted α distribution as

$$\text{asym} = \frac{1}{\text{int}[n/2]} \sum_{i=1}^{\text{int}[n/2]} \left| 1 - \frac{2\sigma_i}{\sigma_i + \sigma_{n-i}} \right|, \qquad (D.1)$$

where n is the number of bins in the distribution and σ_i the cross section value in the bin i.

The average asymmetry factor estimated by Eq. (D.1) is specified in the plots above each α distribution to facilitate visual judgement of the distribution shape and its inherent systematic inaccuracy.
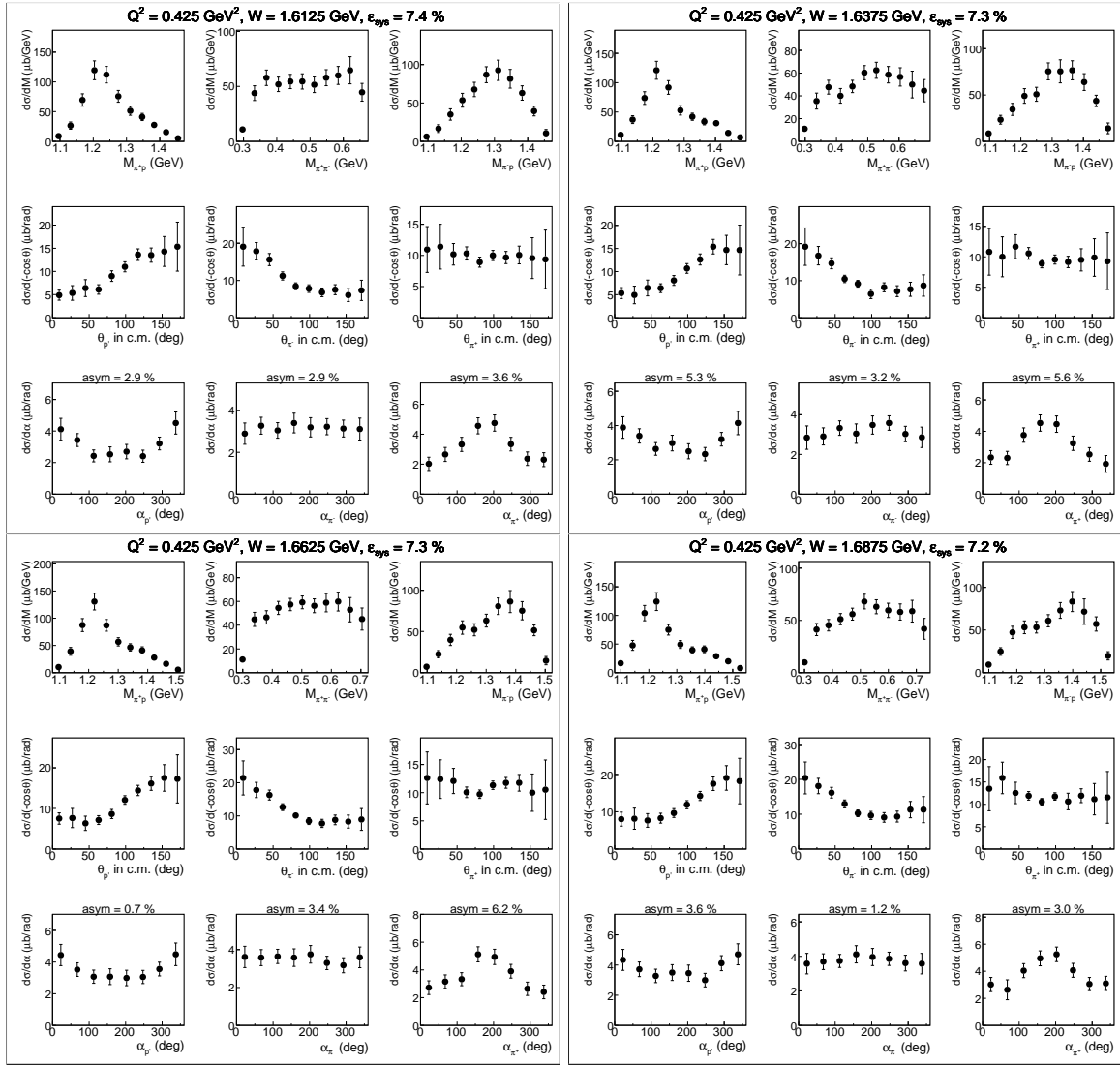
Figure D.1: Measured single-differential cross sections.
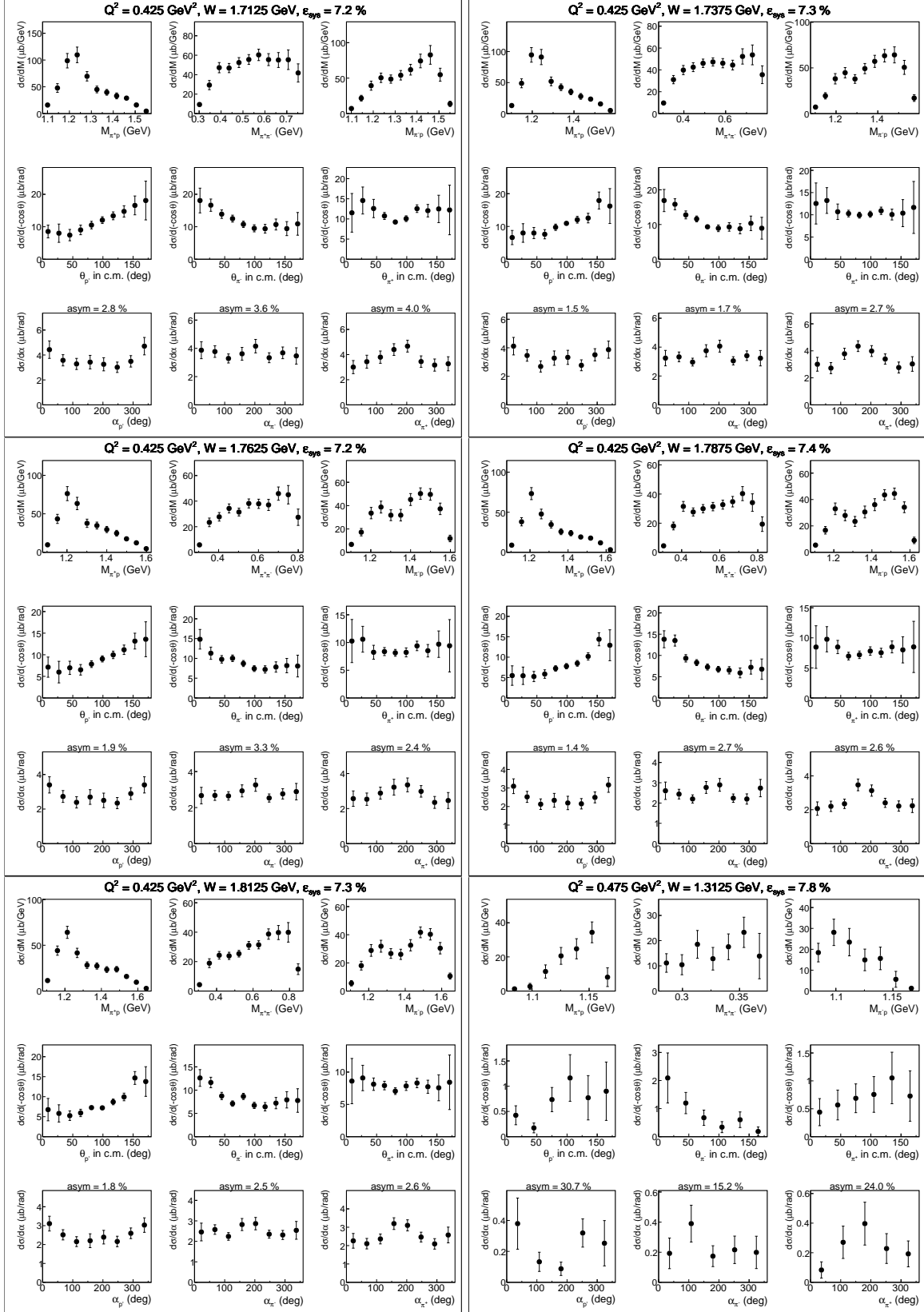
Figure D.2: Measured single-differential cross sections.
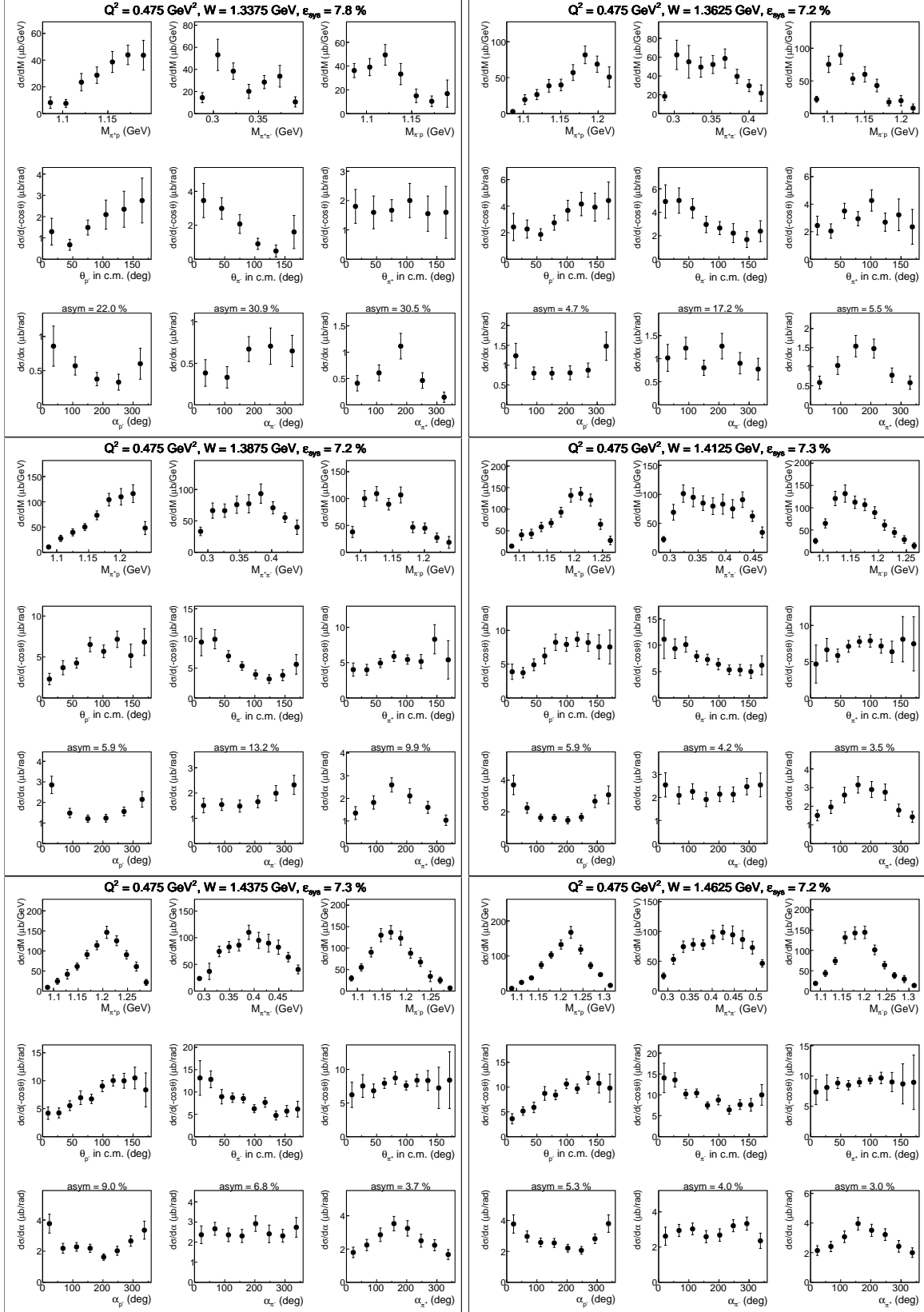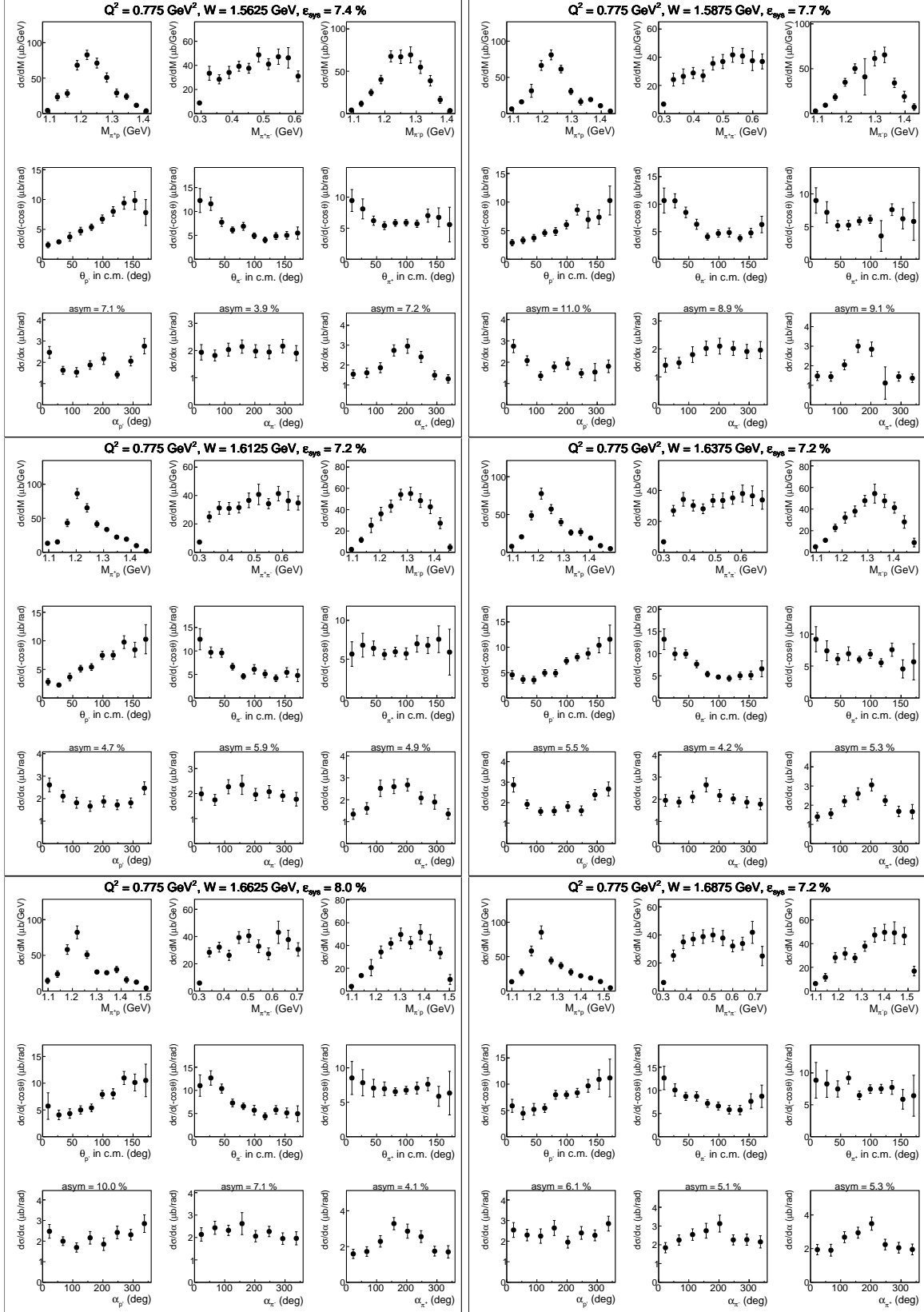
Figure D.3: Measured single-differential cross sections.
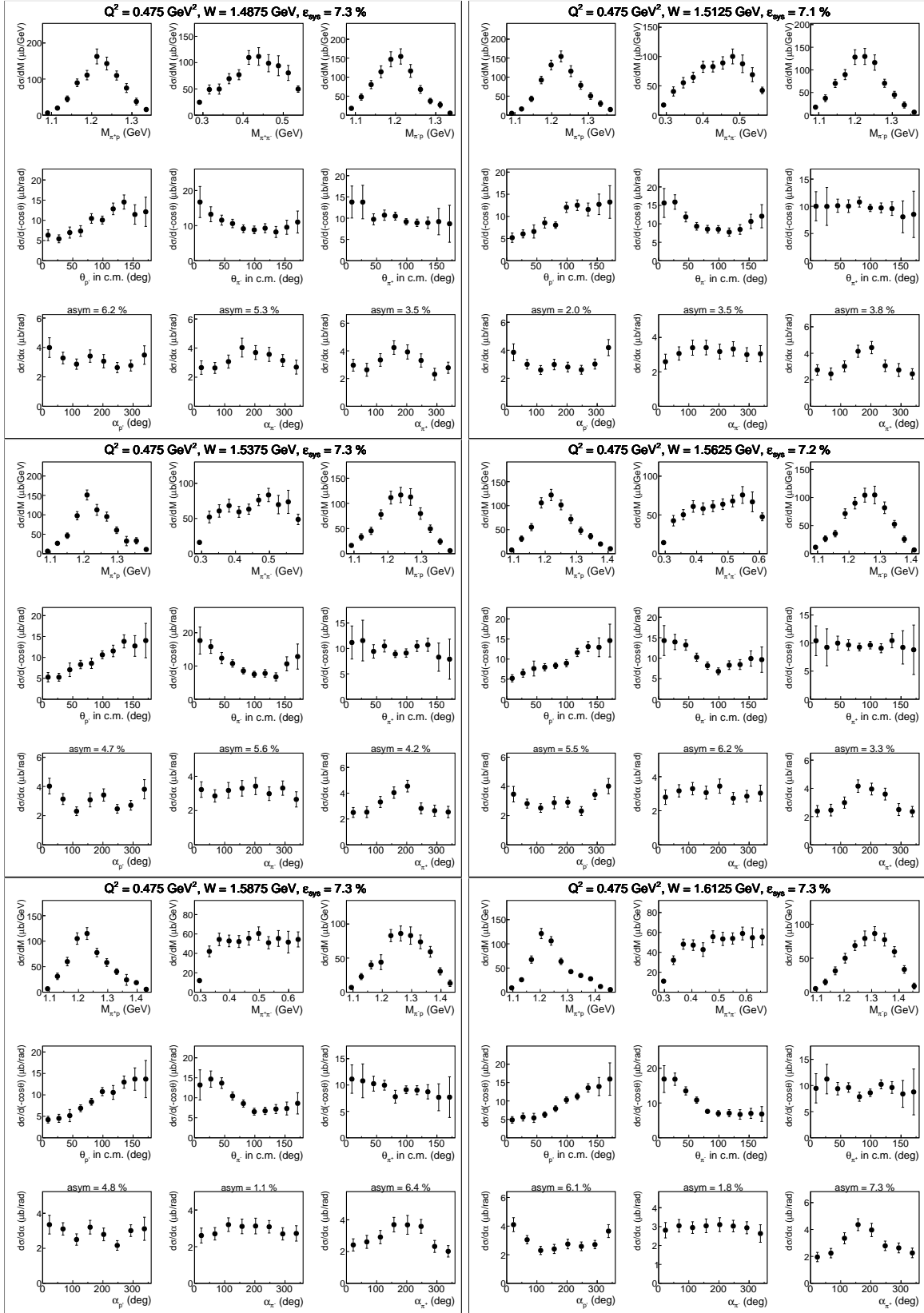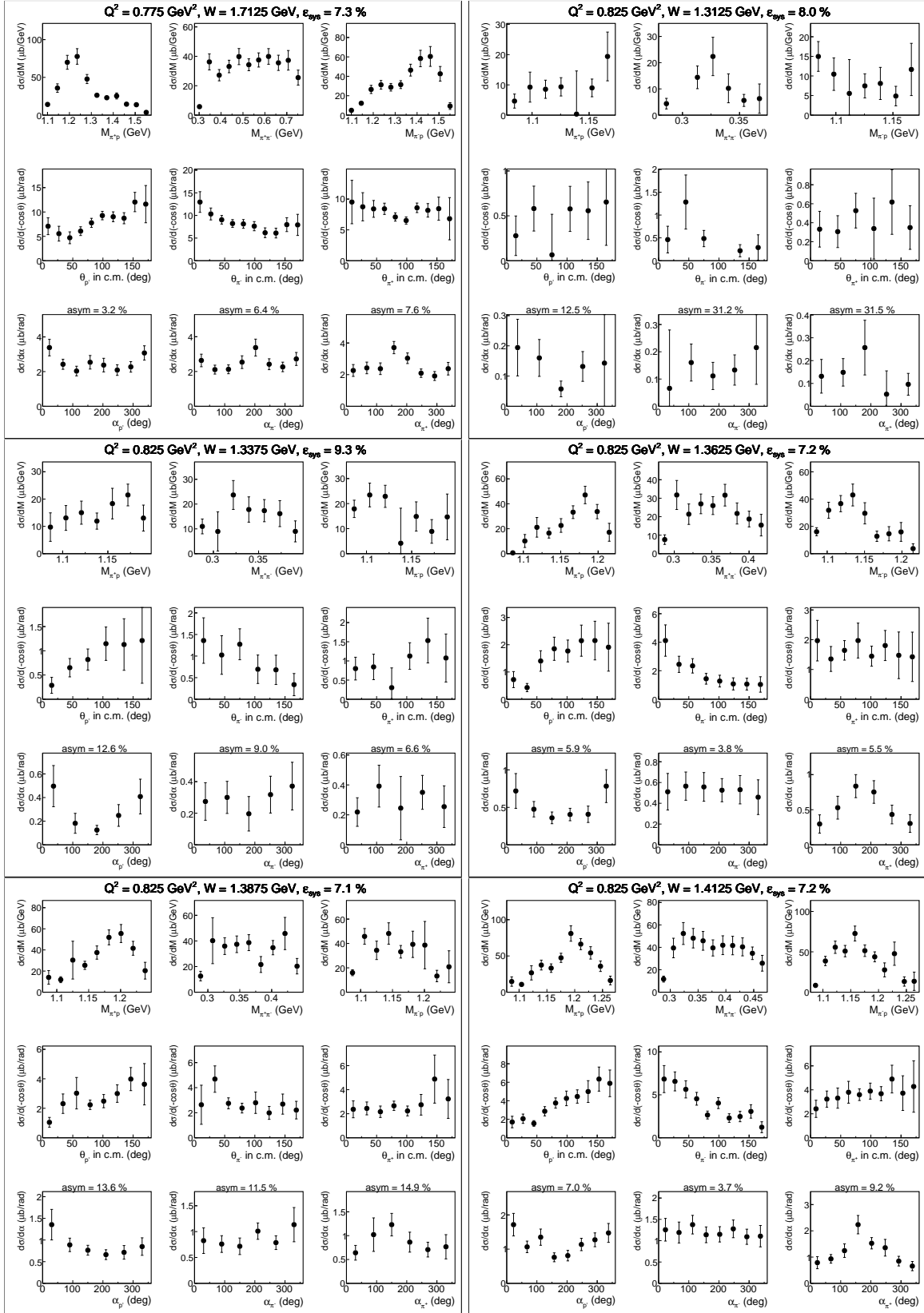
Figure D.4: Measured single-differential cross sections.
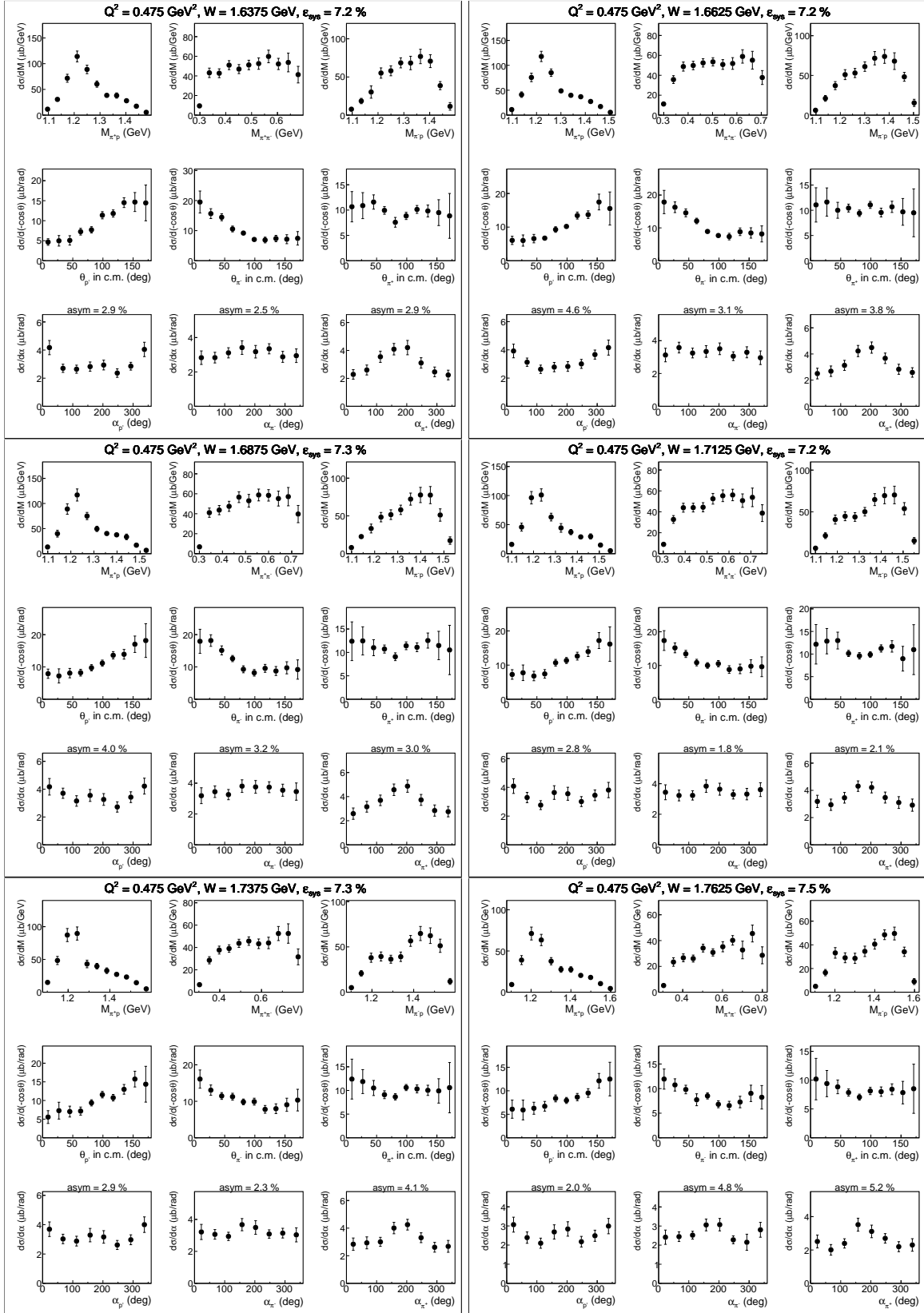
Figure D.5: Measured single-differential cross sections.
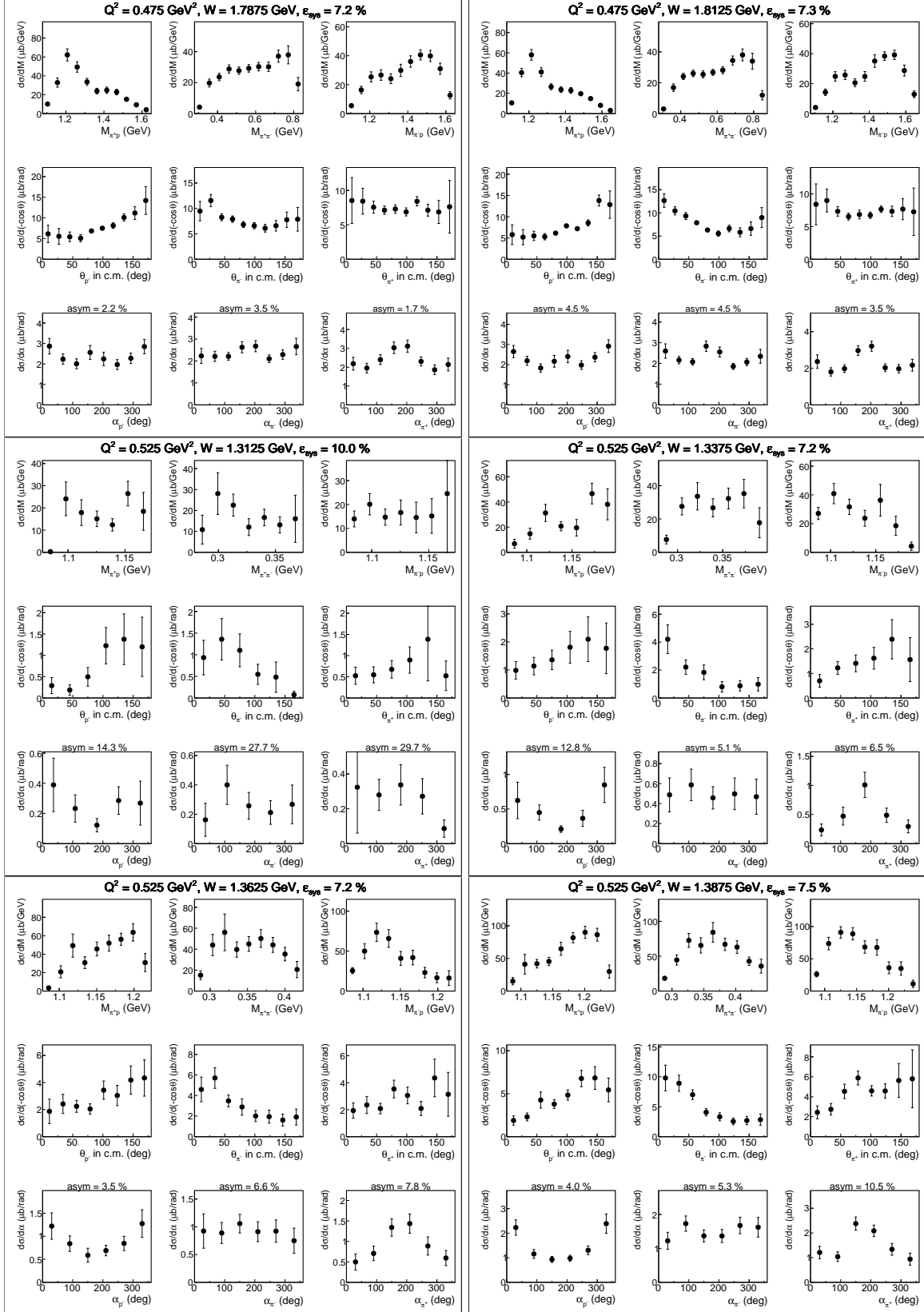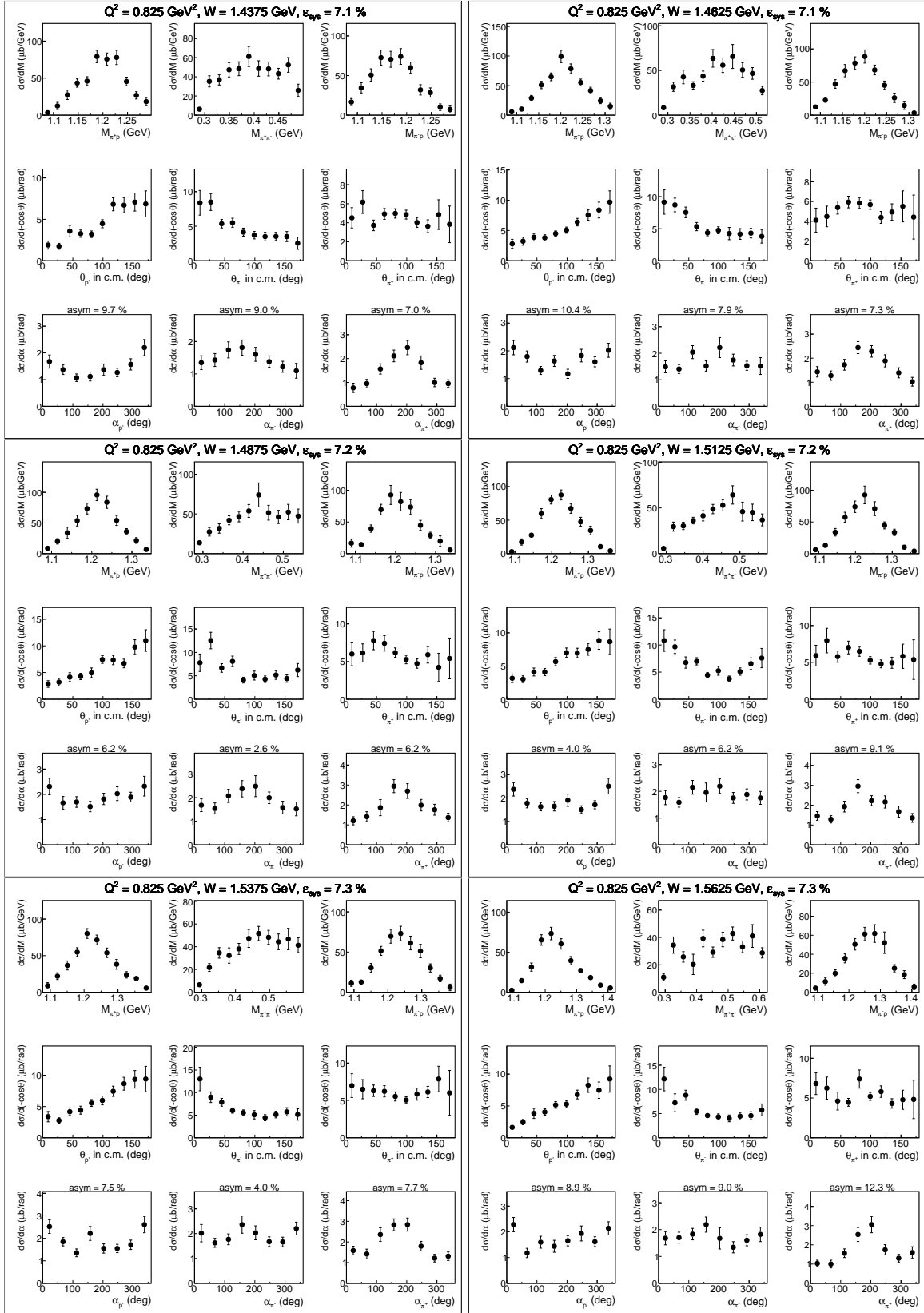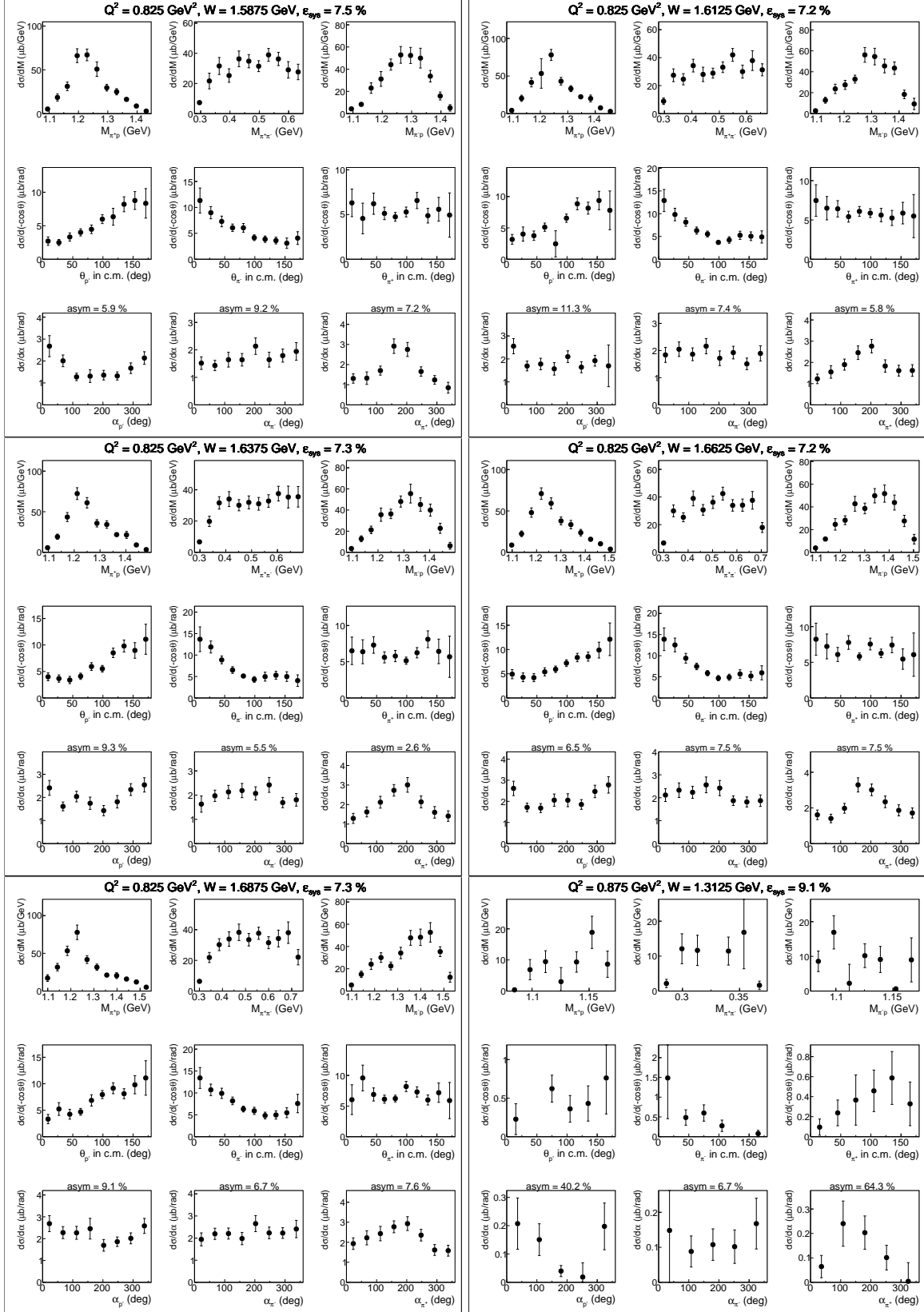
Figure D.6: Measured single-differential cross sections.
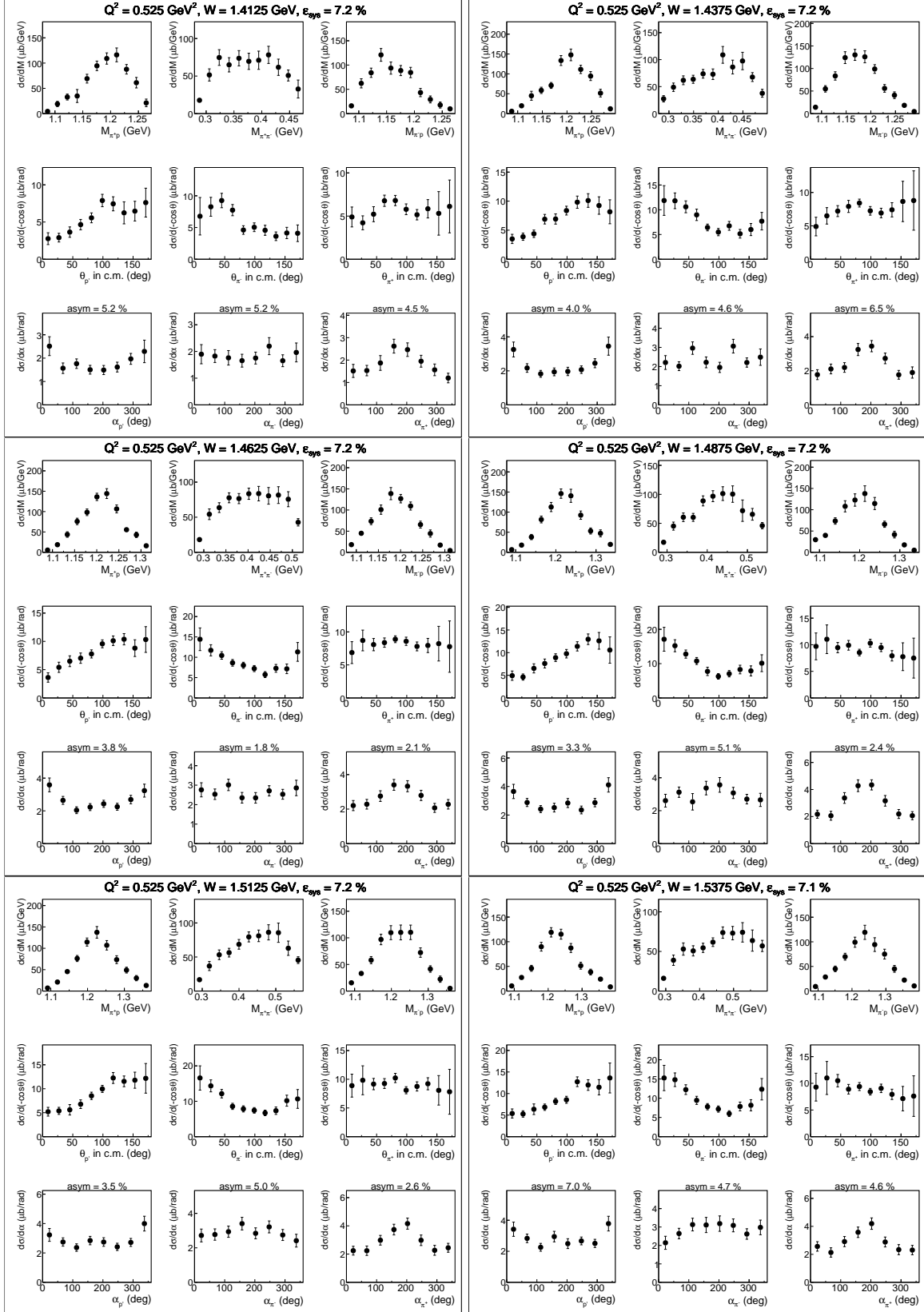
Figure D.7: Measured single-differential cross sections.
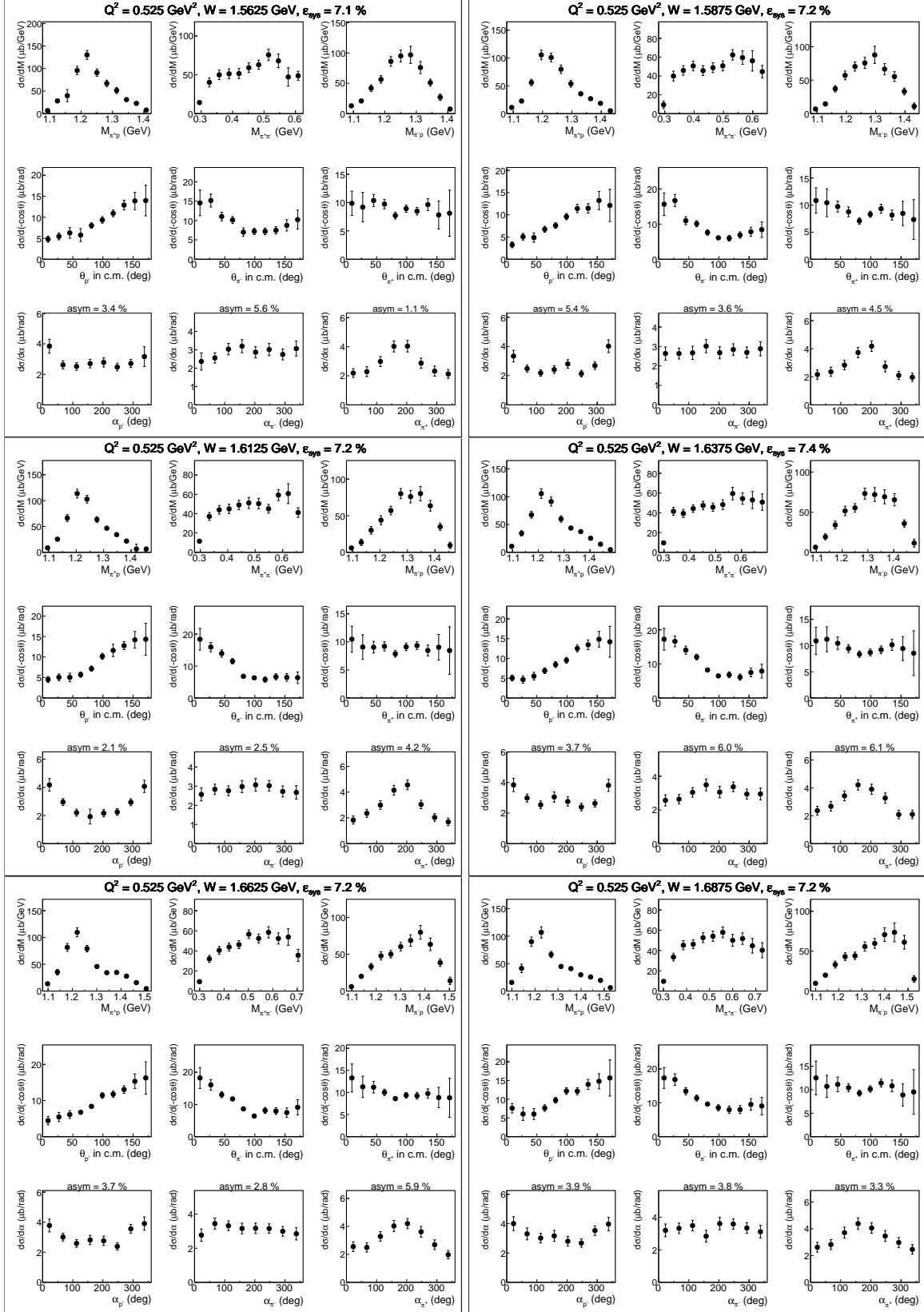
Figure D.8: Measured single-differential cross sections.
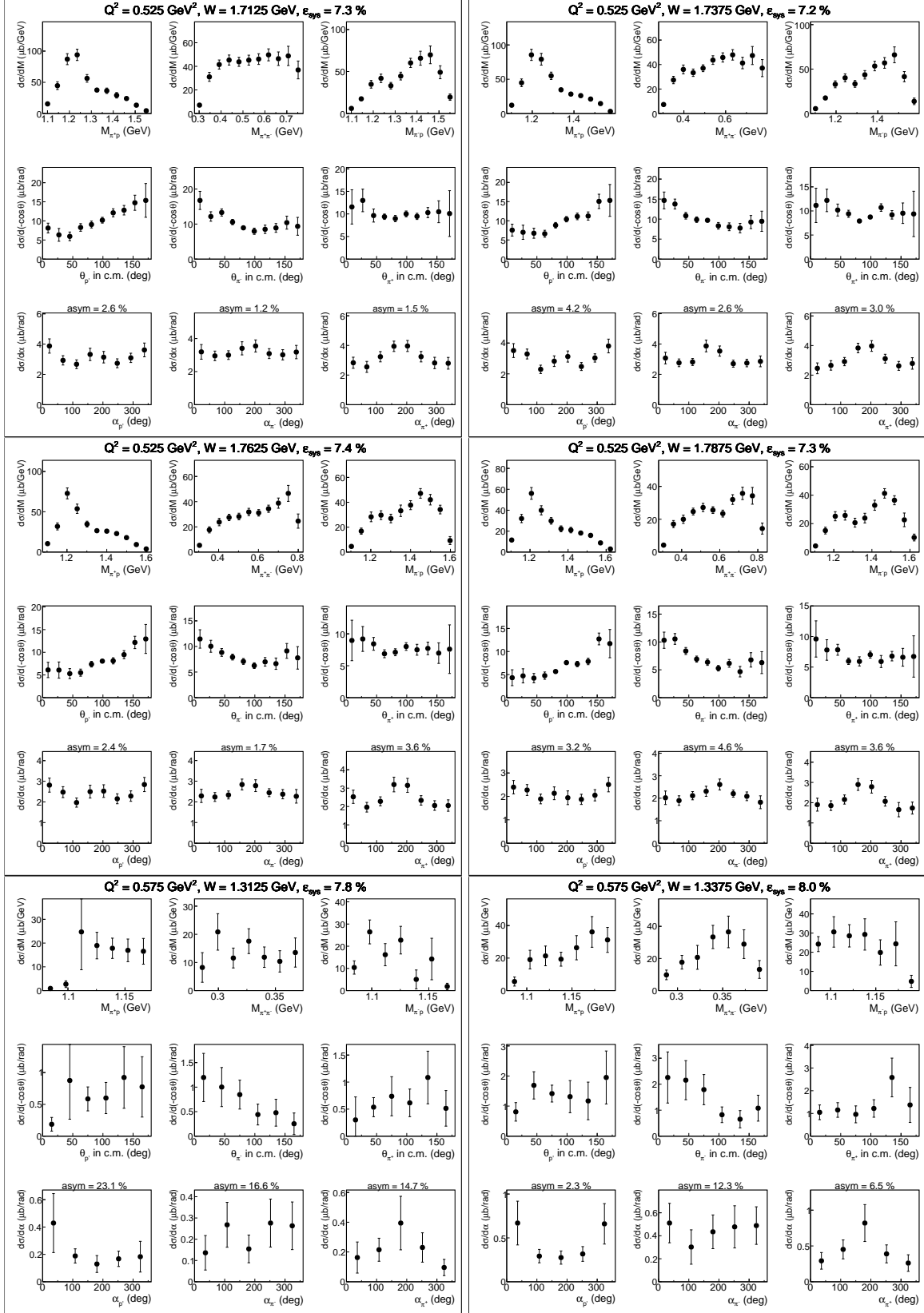
Figure D.9: Measured single-differential cross sections.
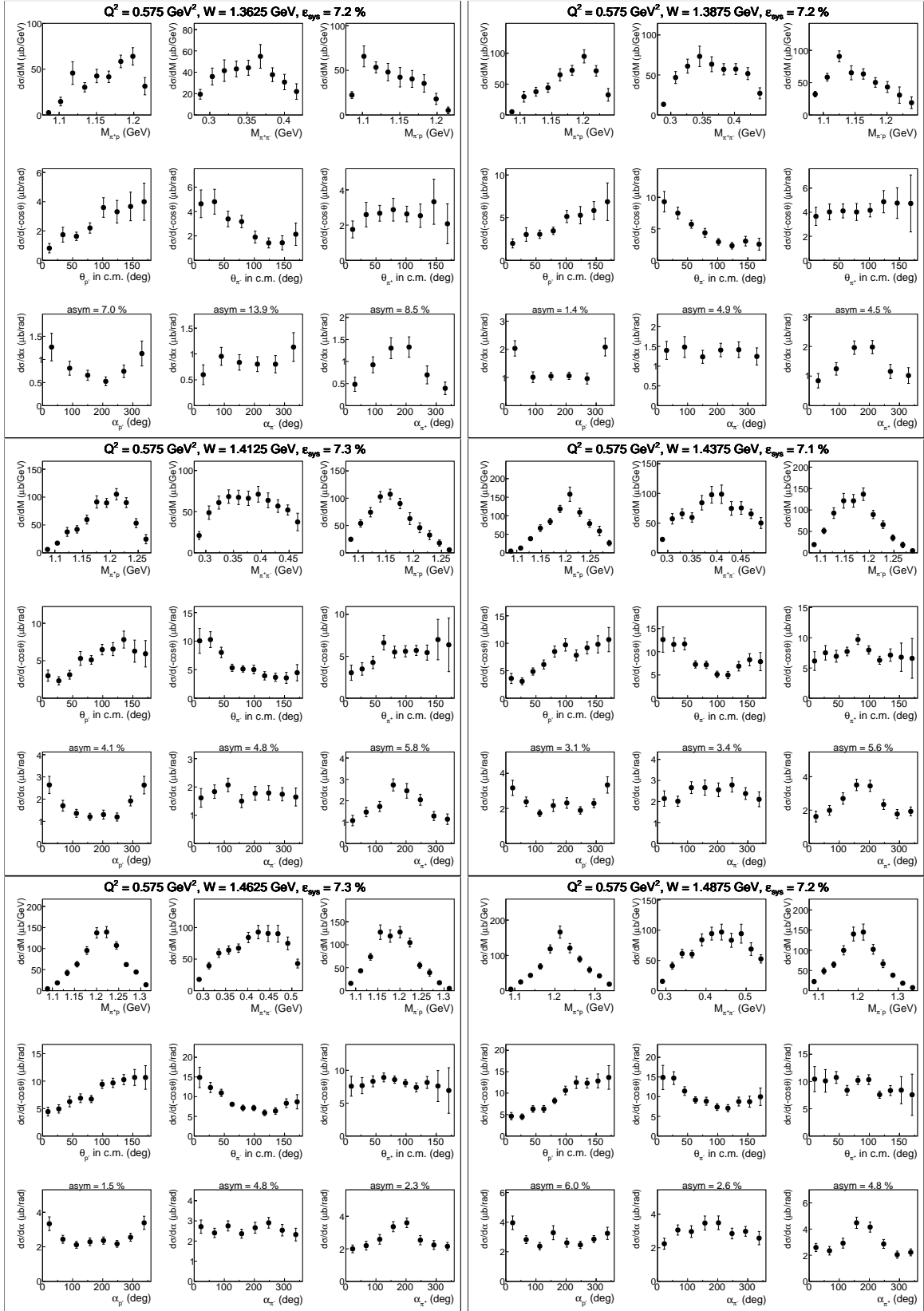
Figure D.10: Measured single-differential cross sections.
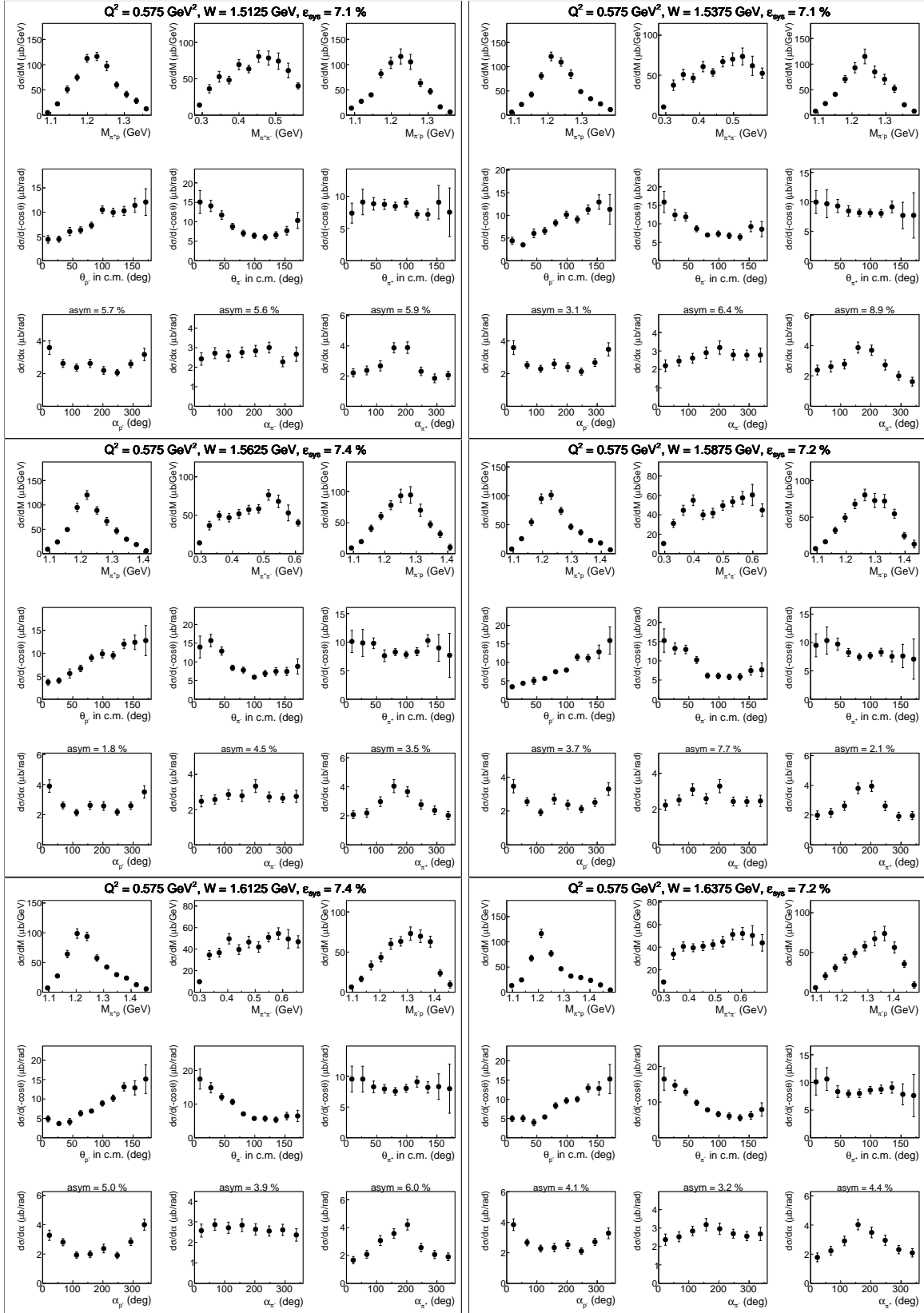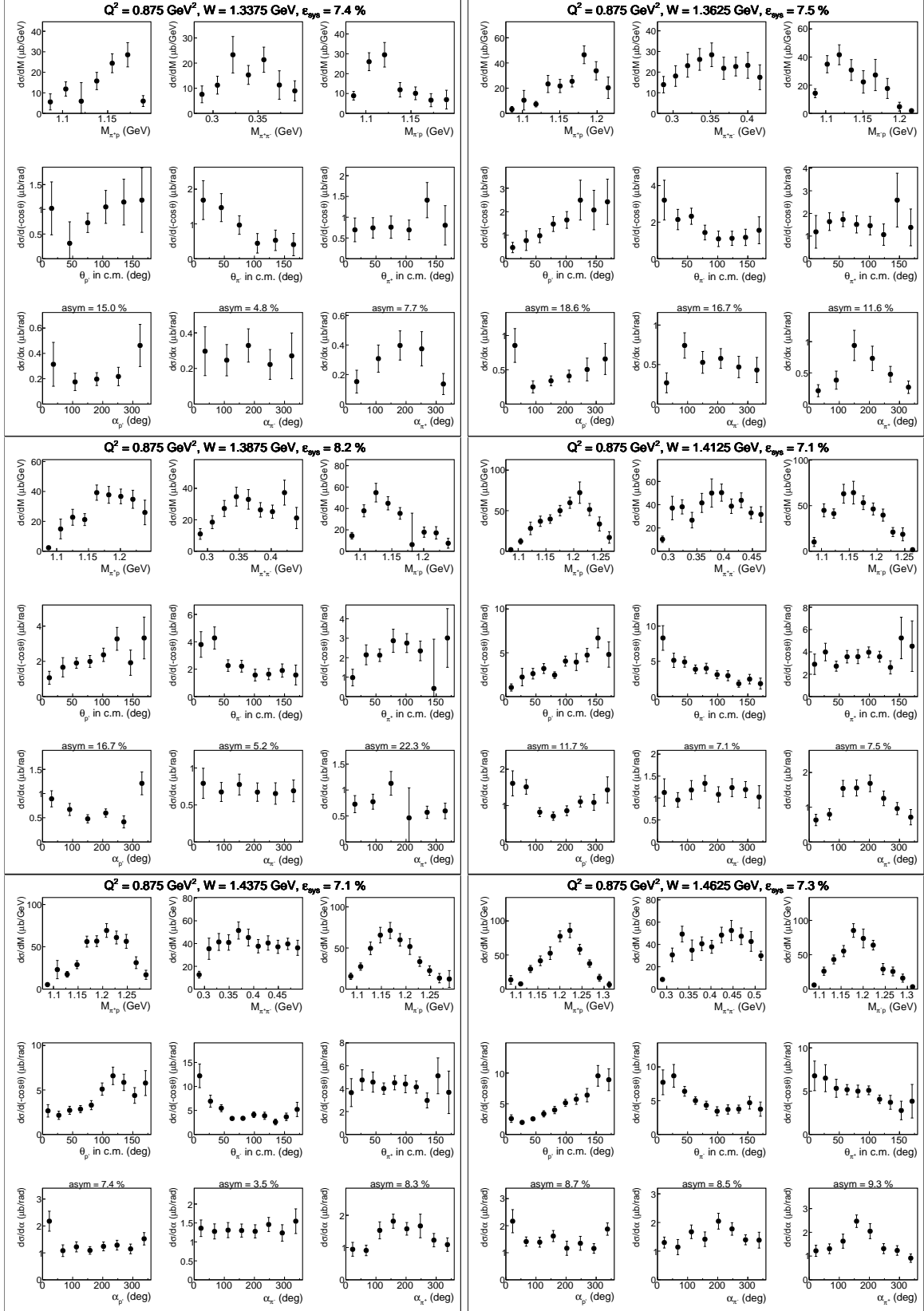
Figure D.11: Measured single-differential cross sections.

194
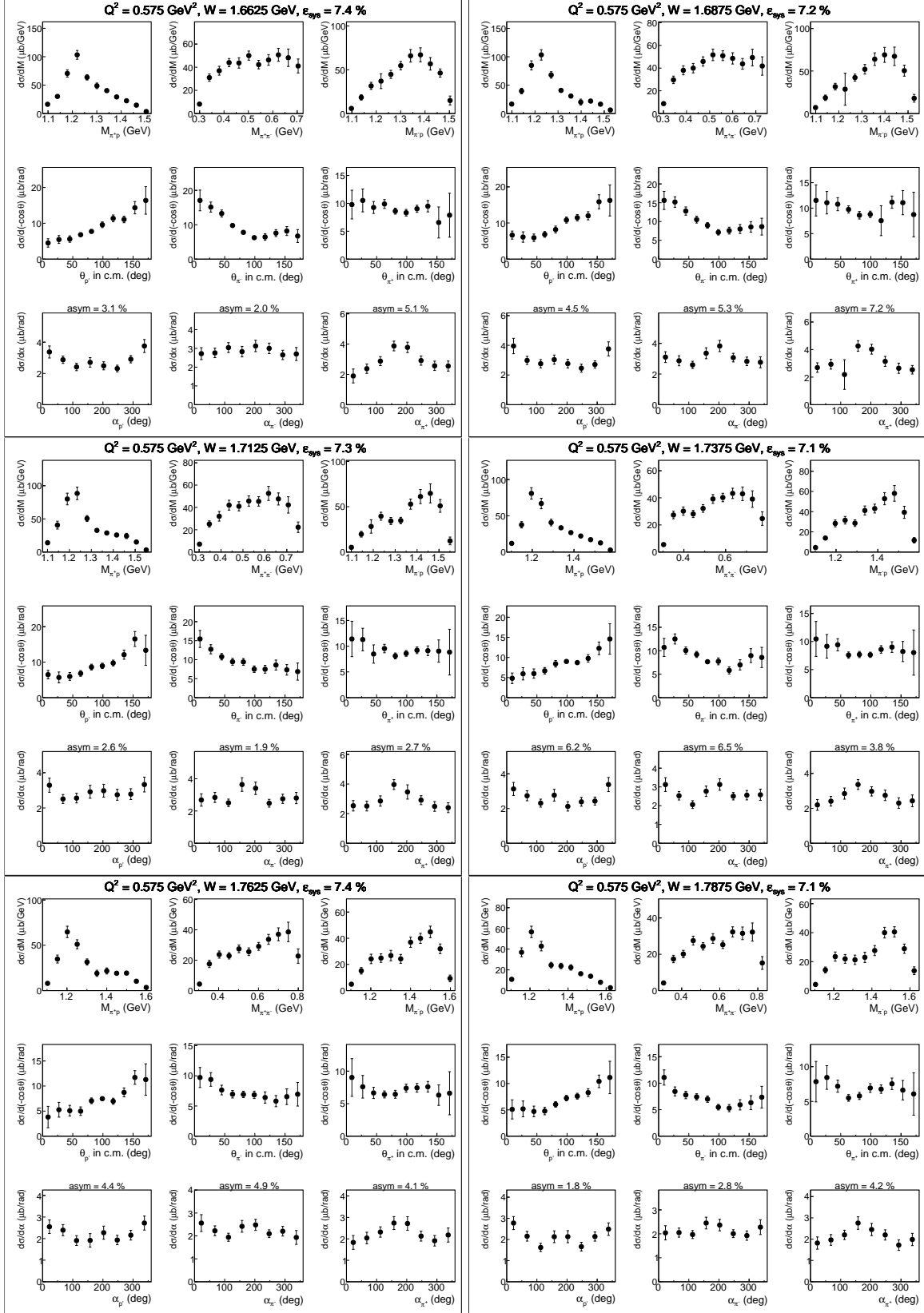
Figure D.12: Measured single-differential cross sections.

195
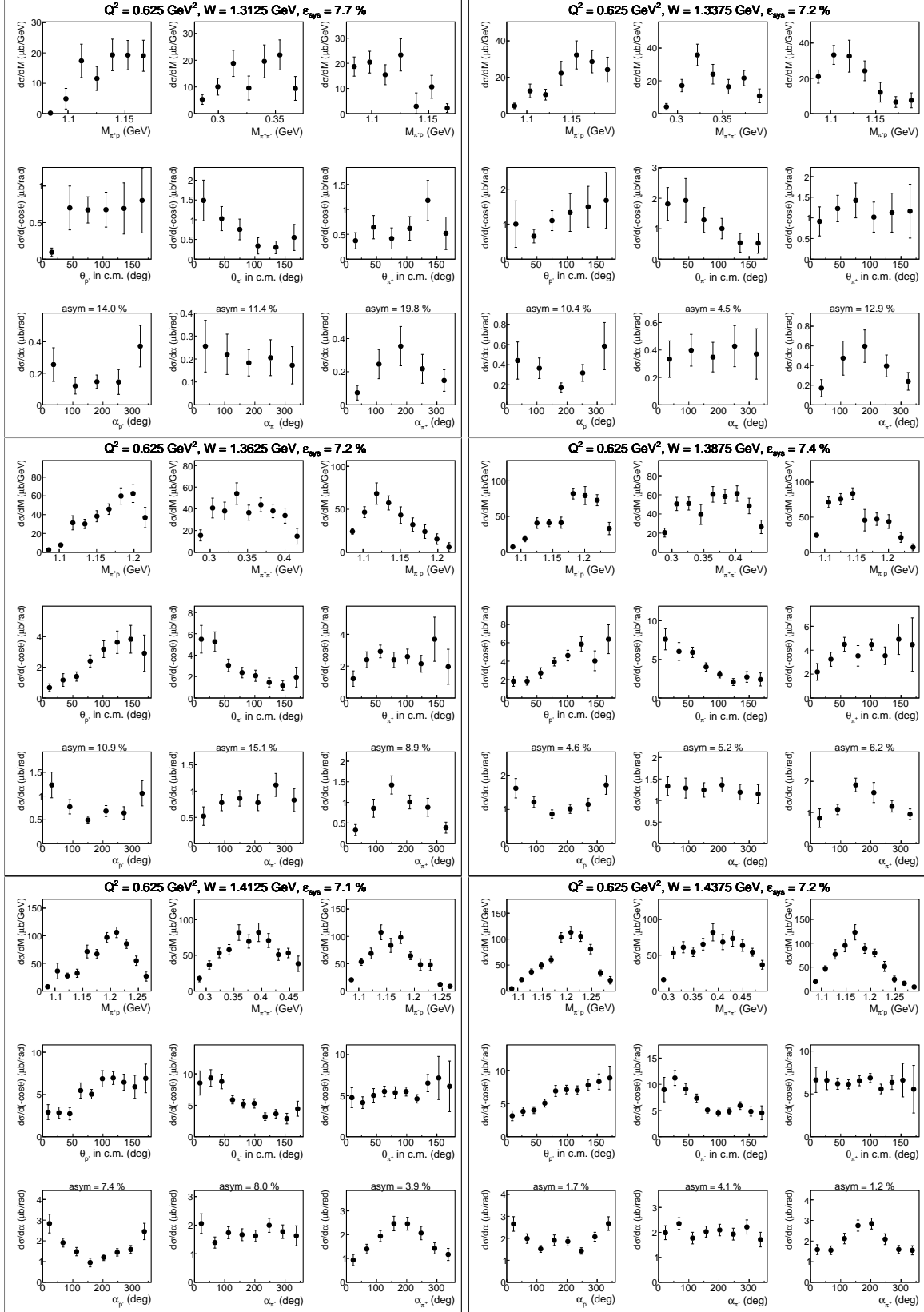
Figure D.13: Measured single-differential cross sections.
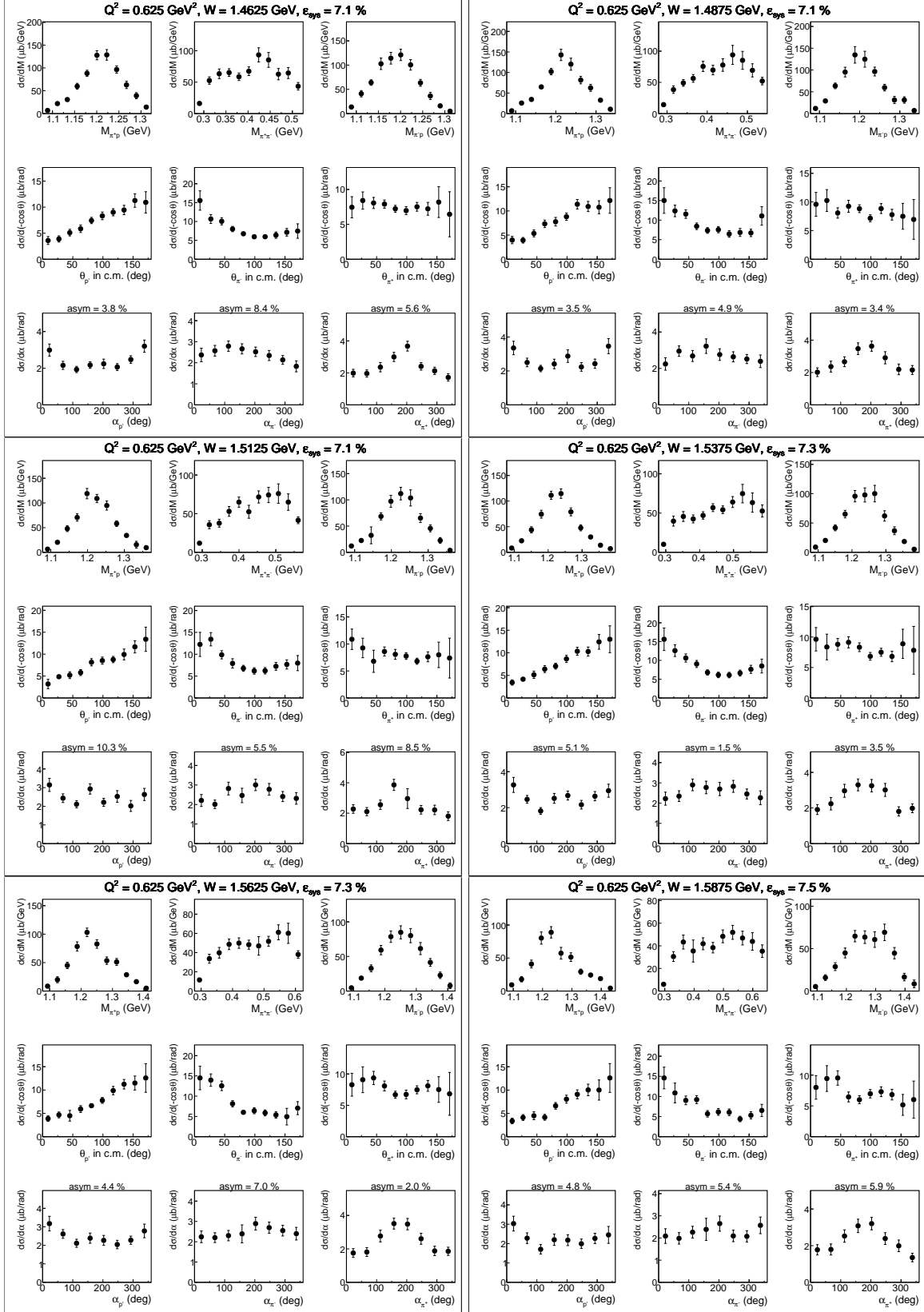
Figure D.14: Measured single-differential cross sections.
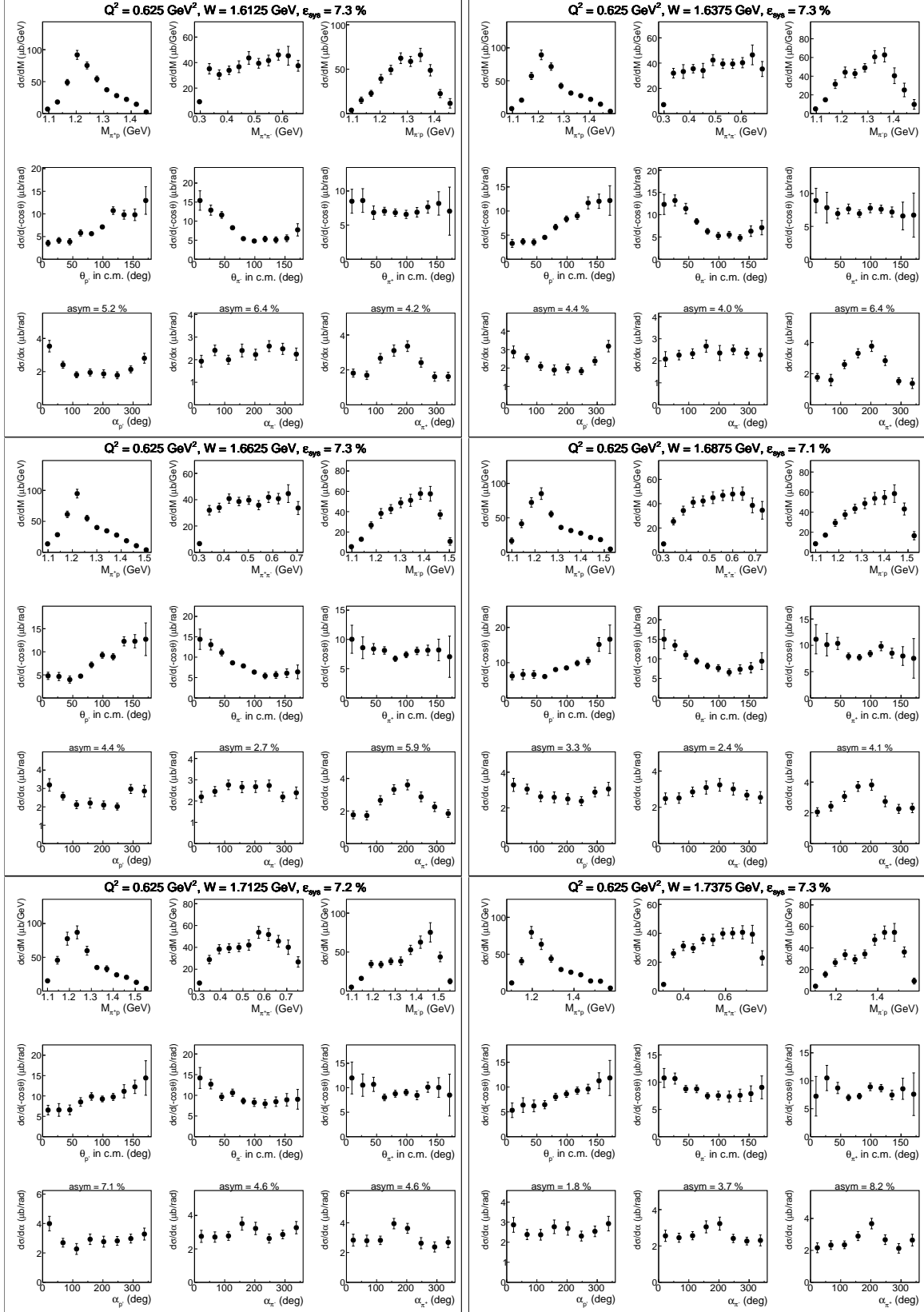
Figure D.15: Measured single-differential cross sections.
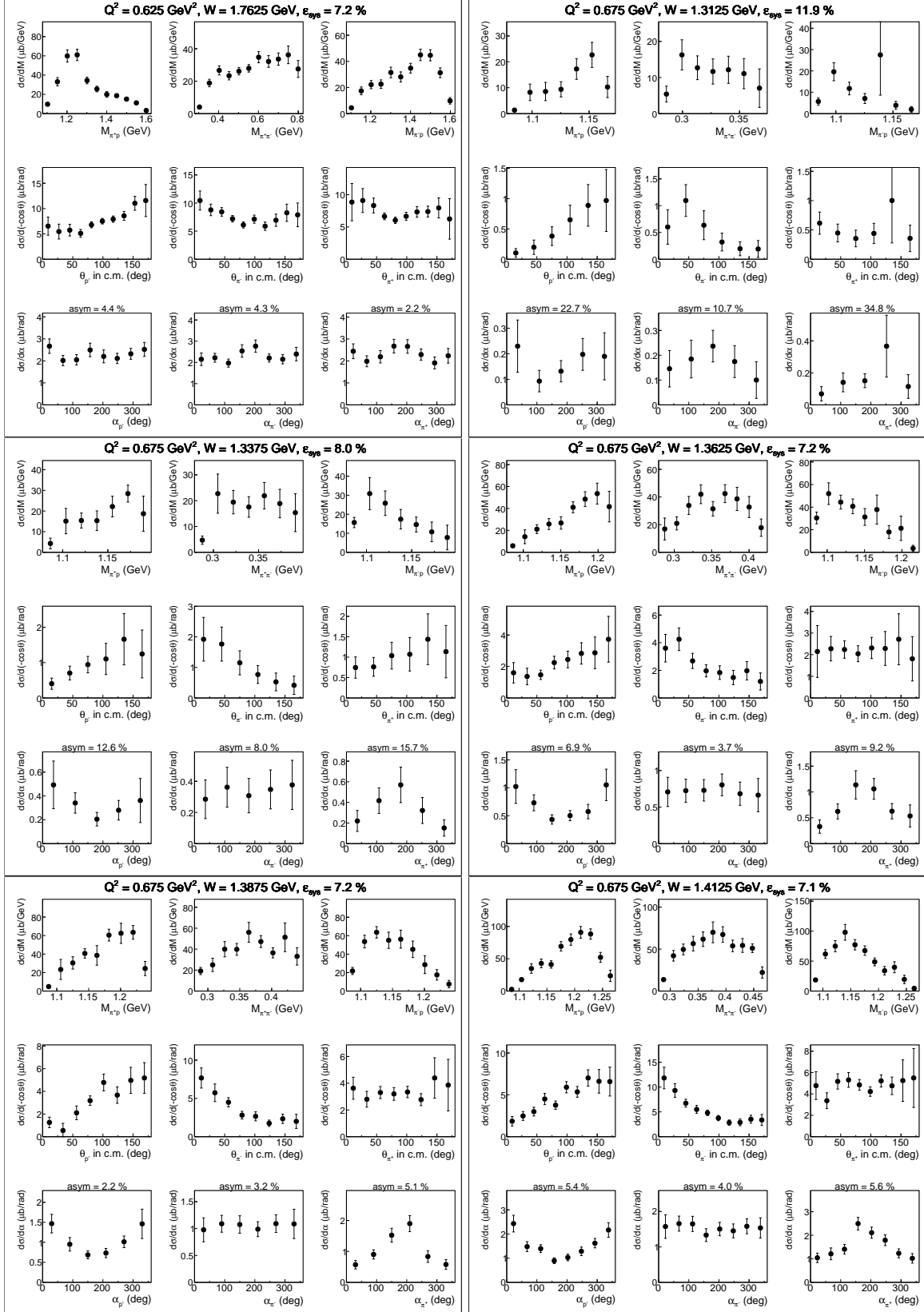
Figure D.16: Measured single-differential cross sections.
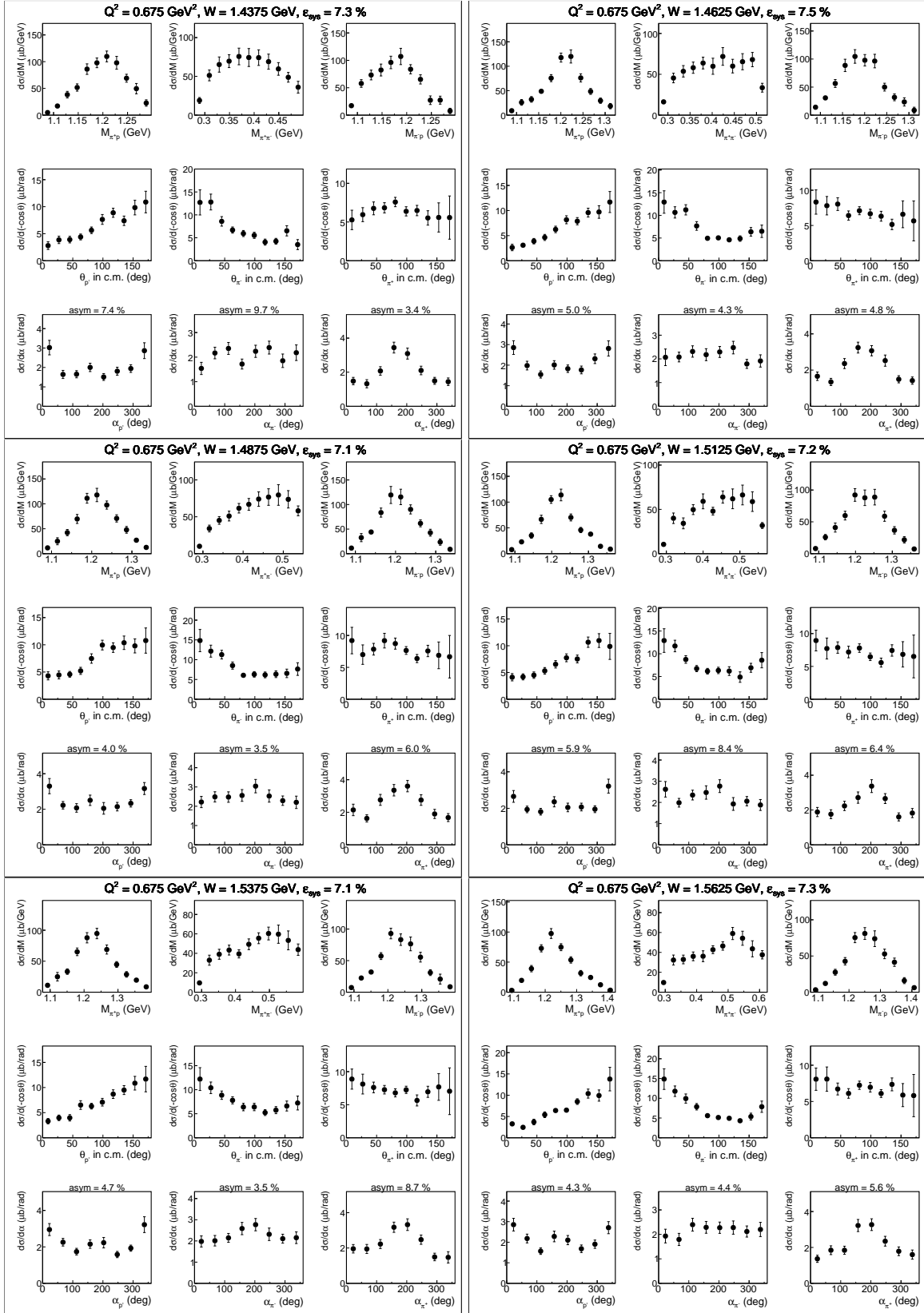
Figure D.17: Measured single-differential cross sections.
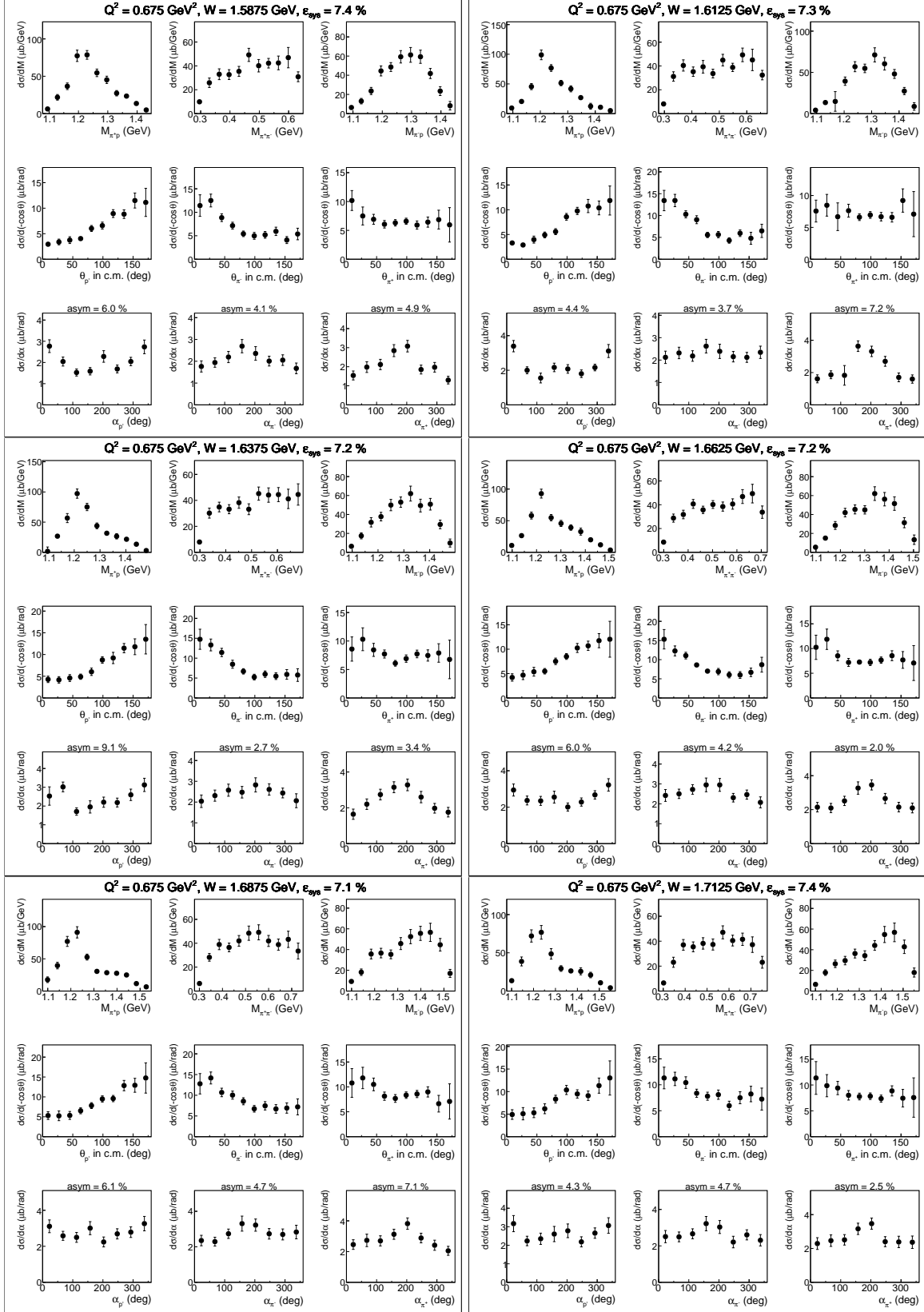
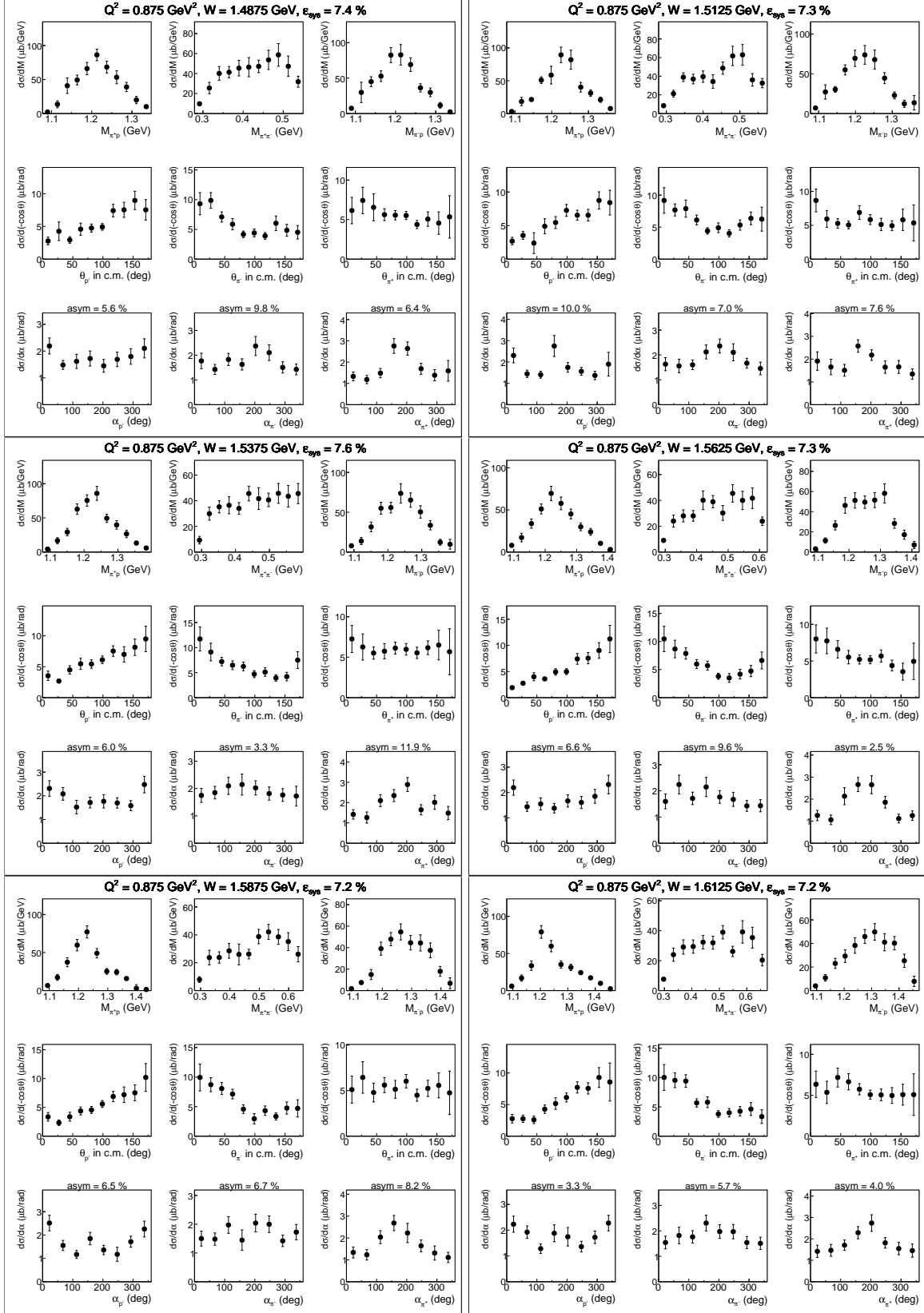Figure D.18: Measured single-differential cross sections.
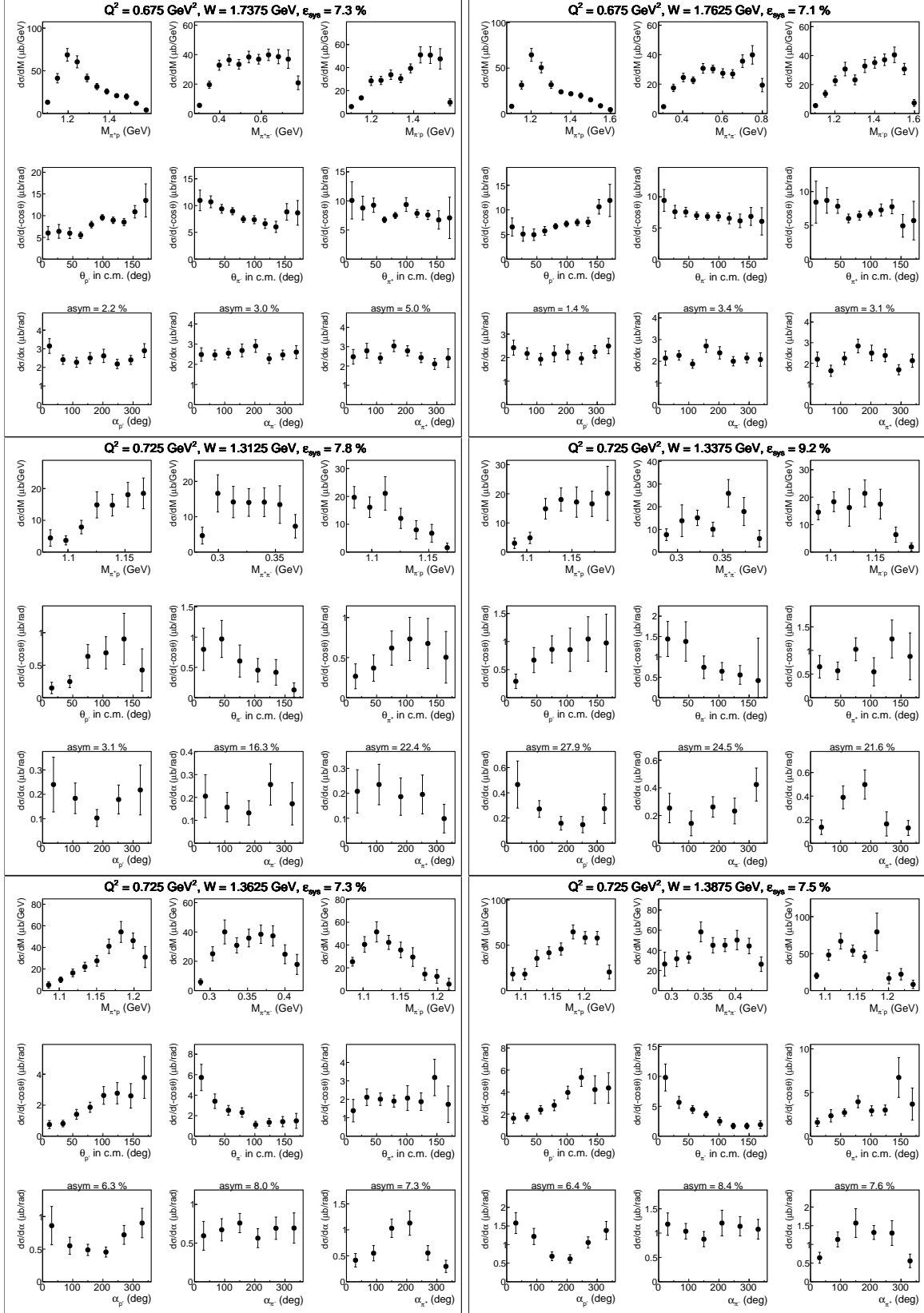
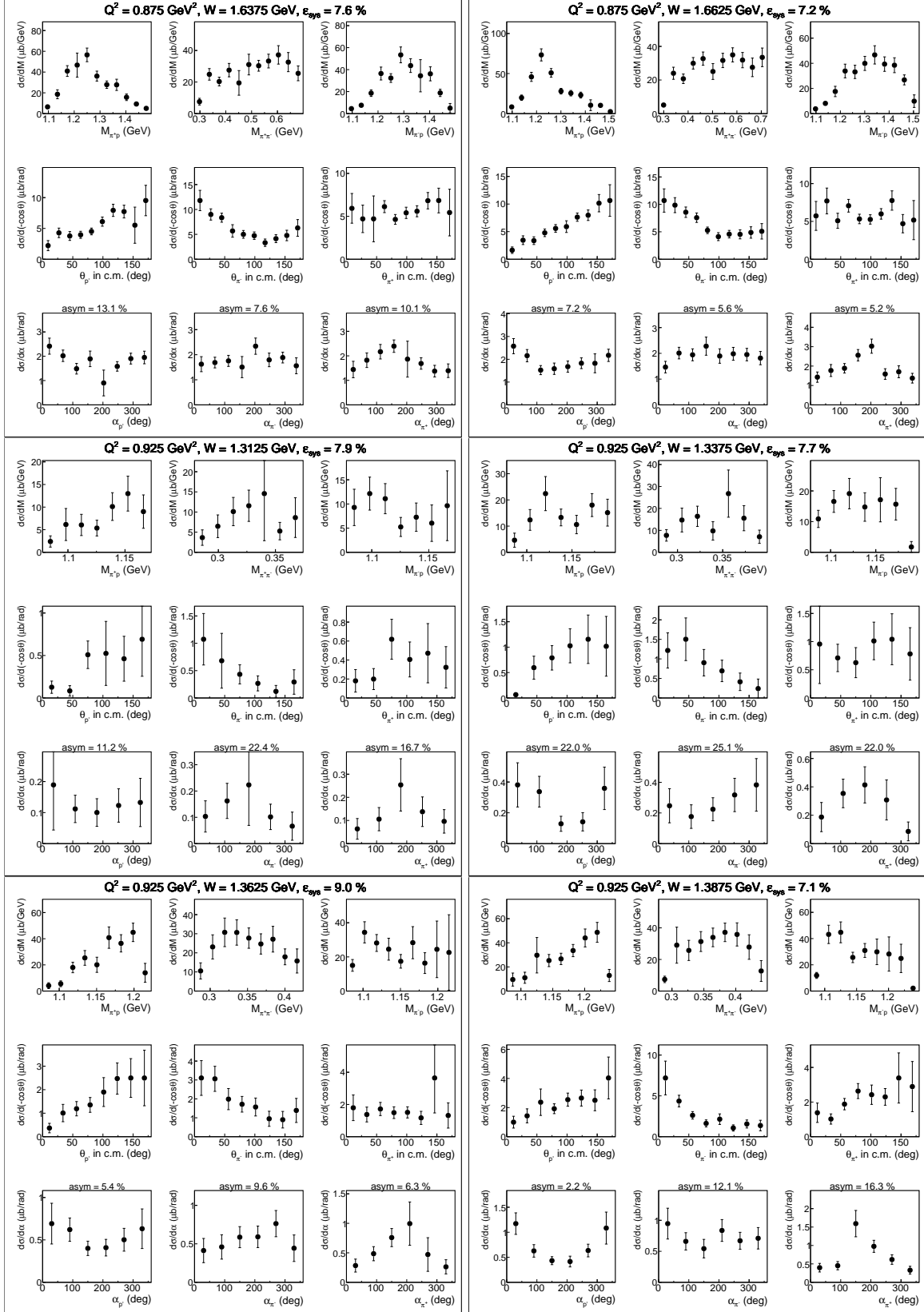Figure D.19: Measured single-differential cross sections.
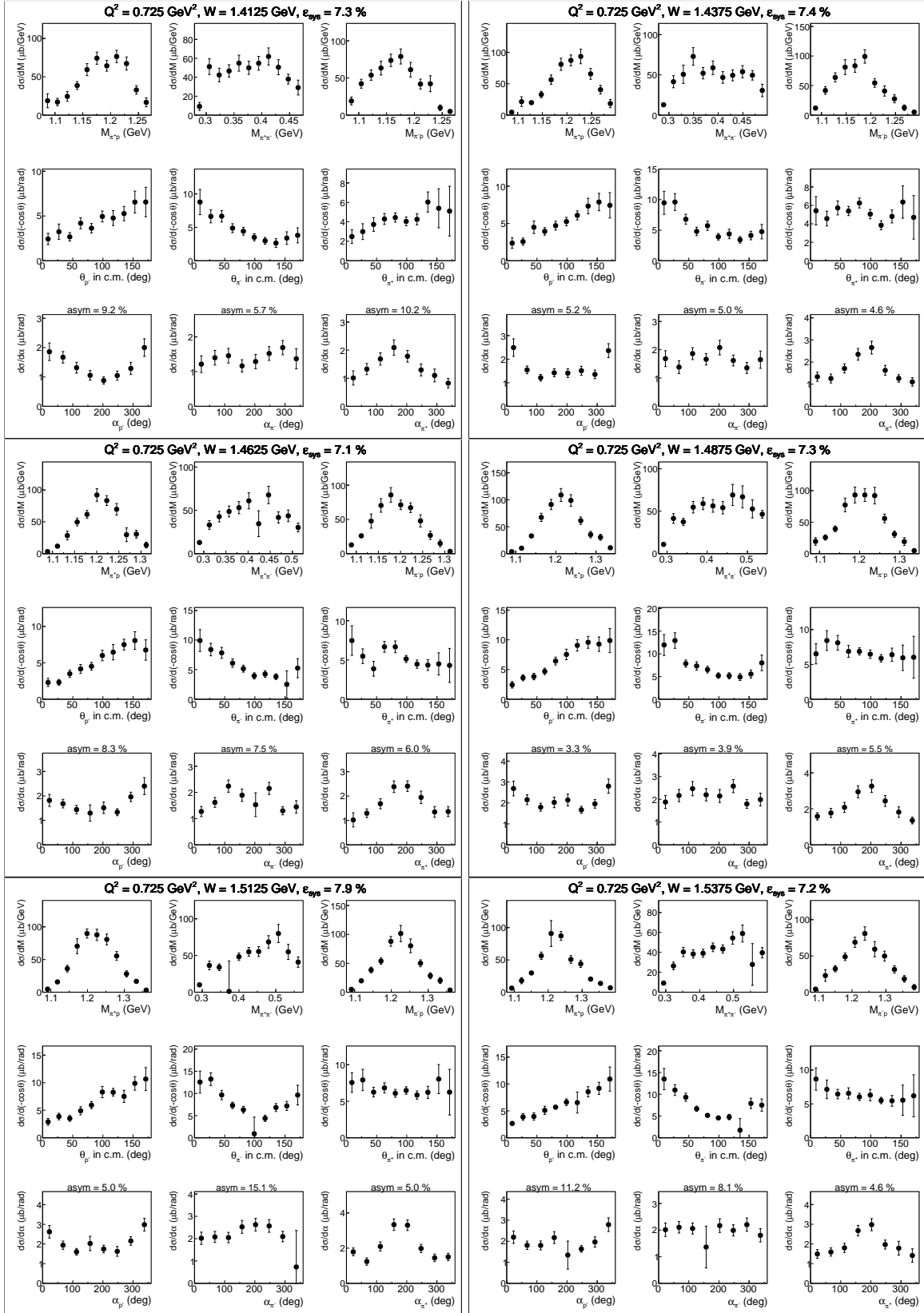
Figure D.20: Measured single-differential cross sections.
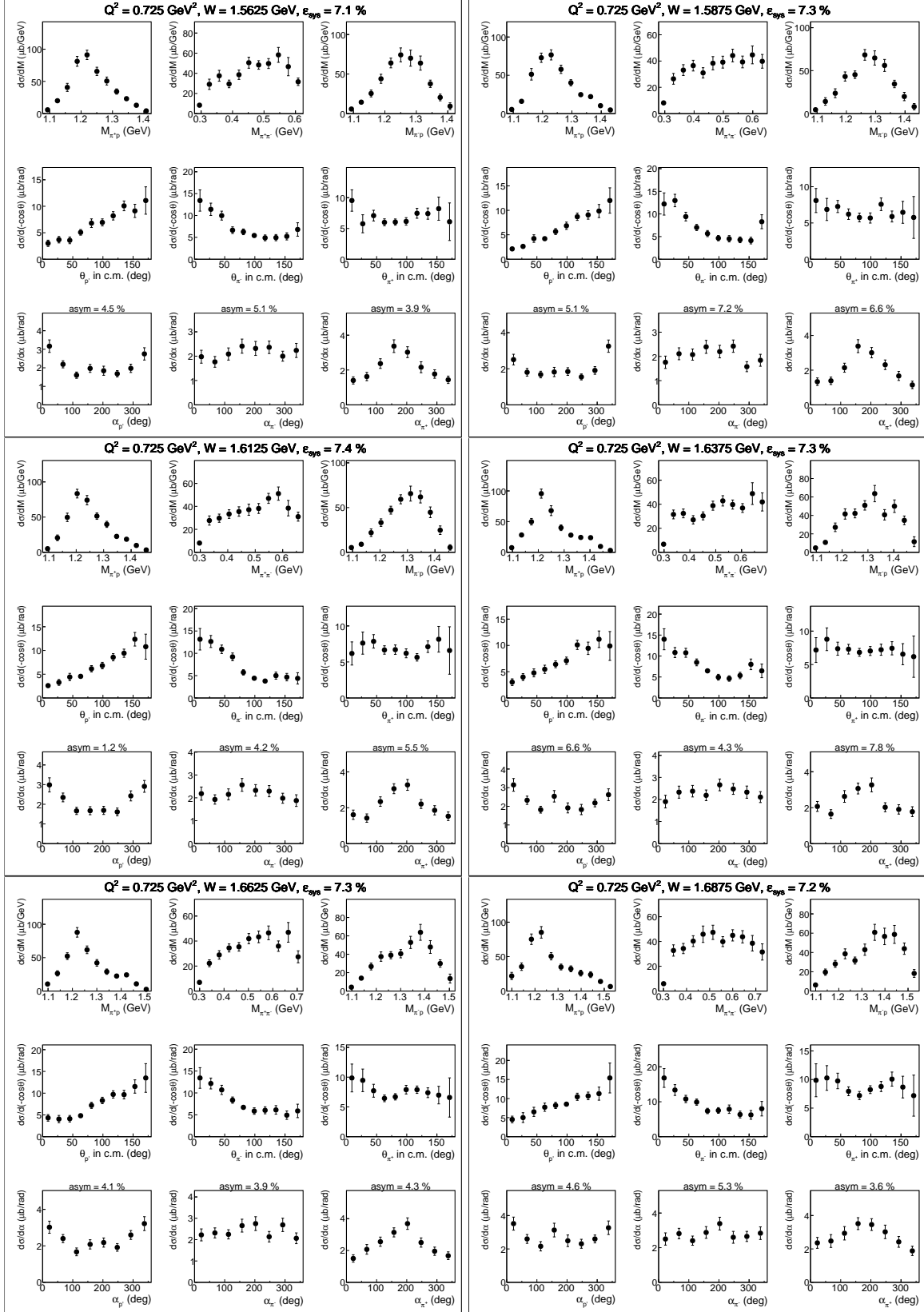
Figure D.21: Measured single-differential cross sections.
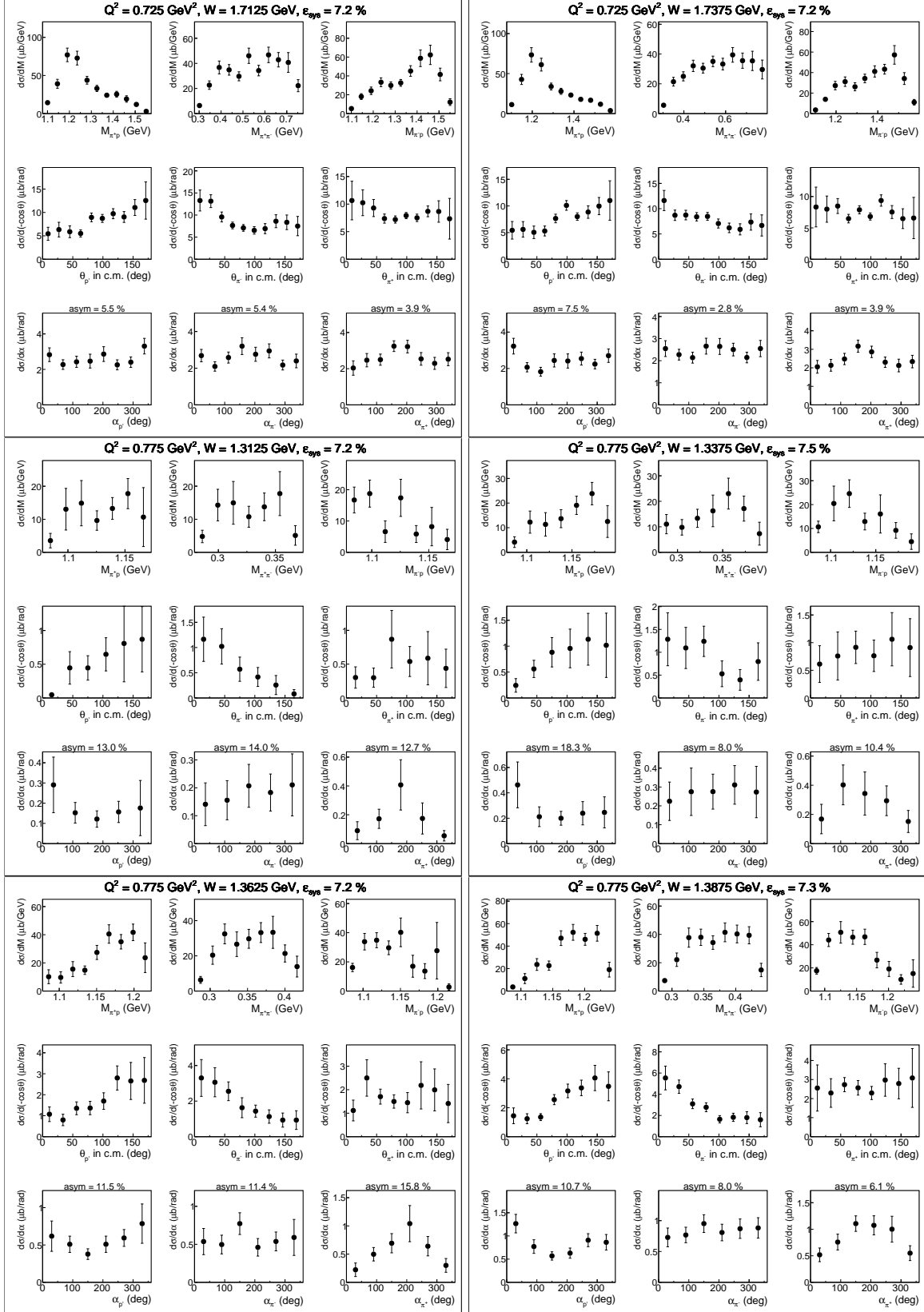
Figure D.22: Measured single-differential cross sections.
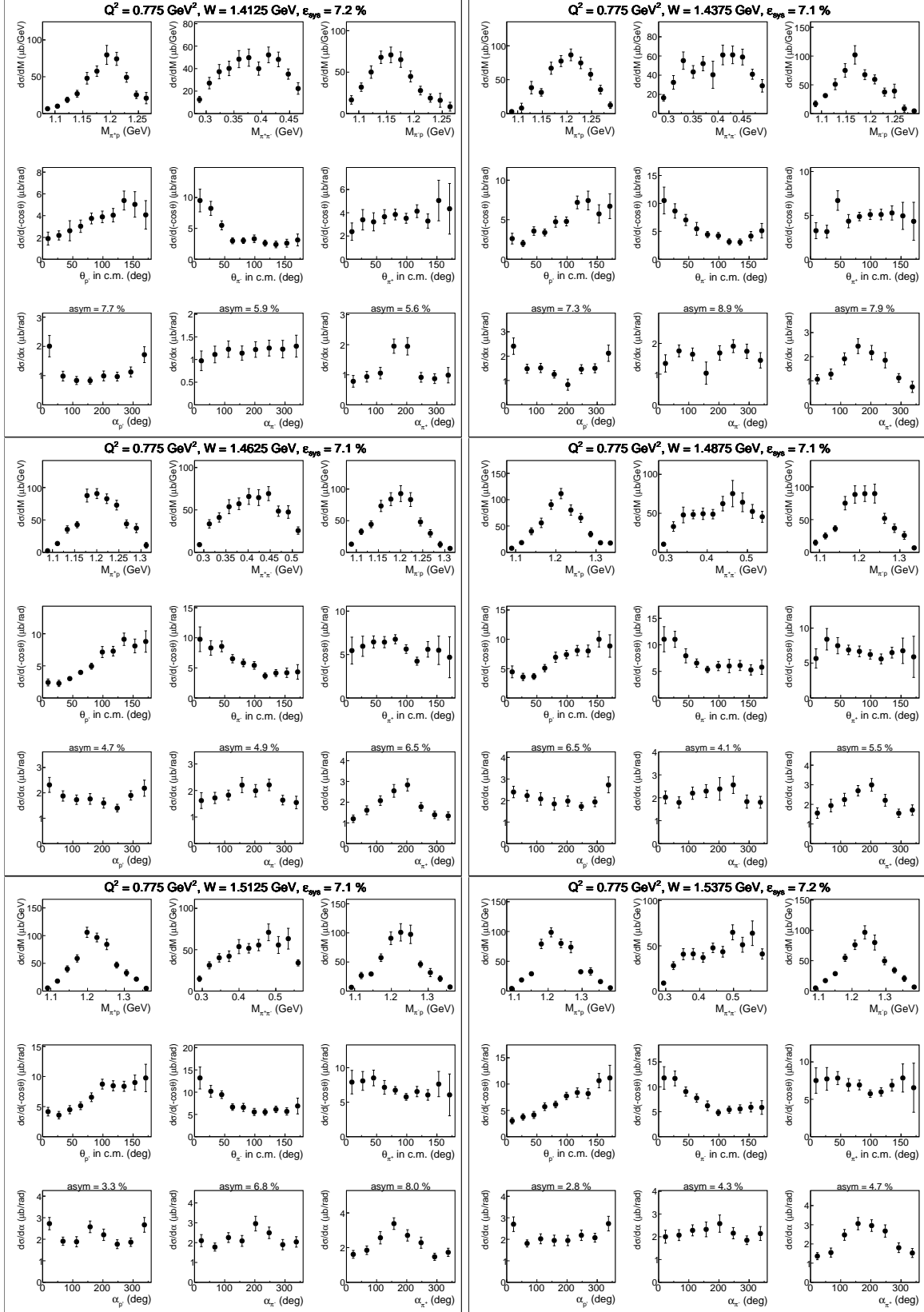
Figure D.23: Measured single-differential cross sections.
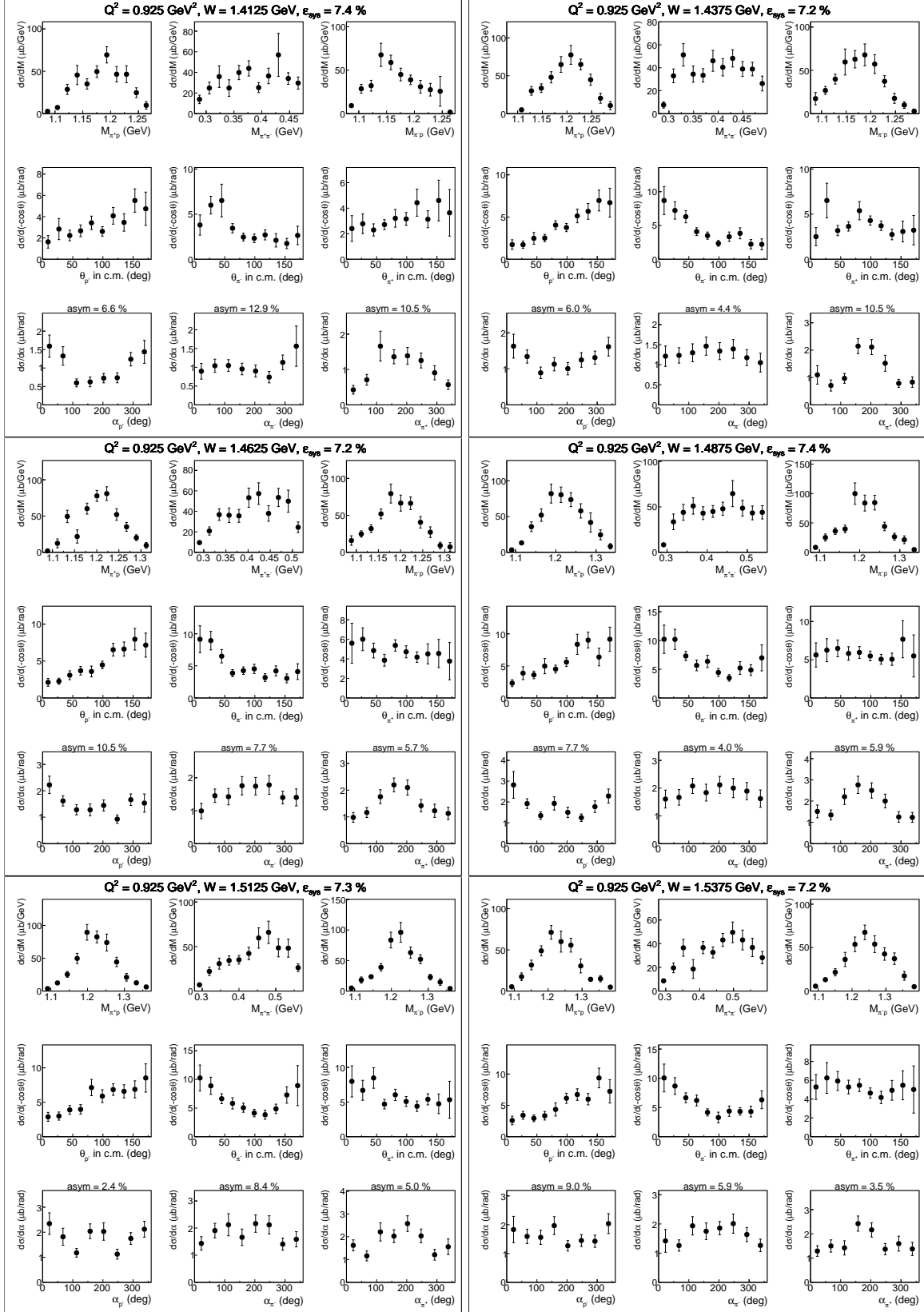
206

Figure D.24: Measured single-differential cross sections.

Figure D.25: Measured single-differential cross sections.

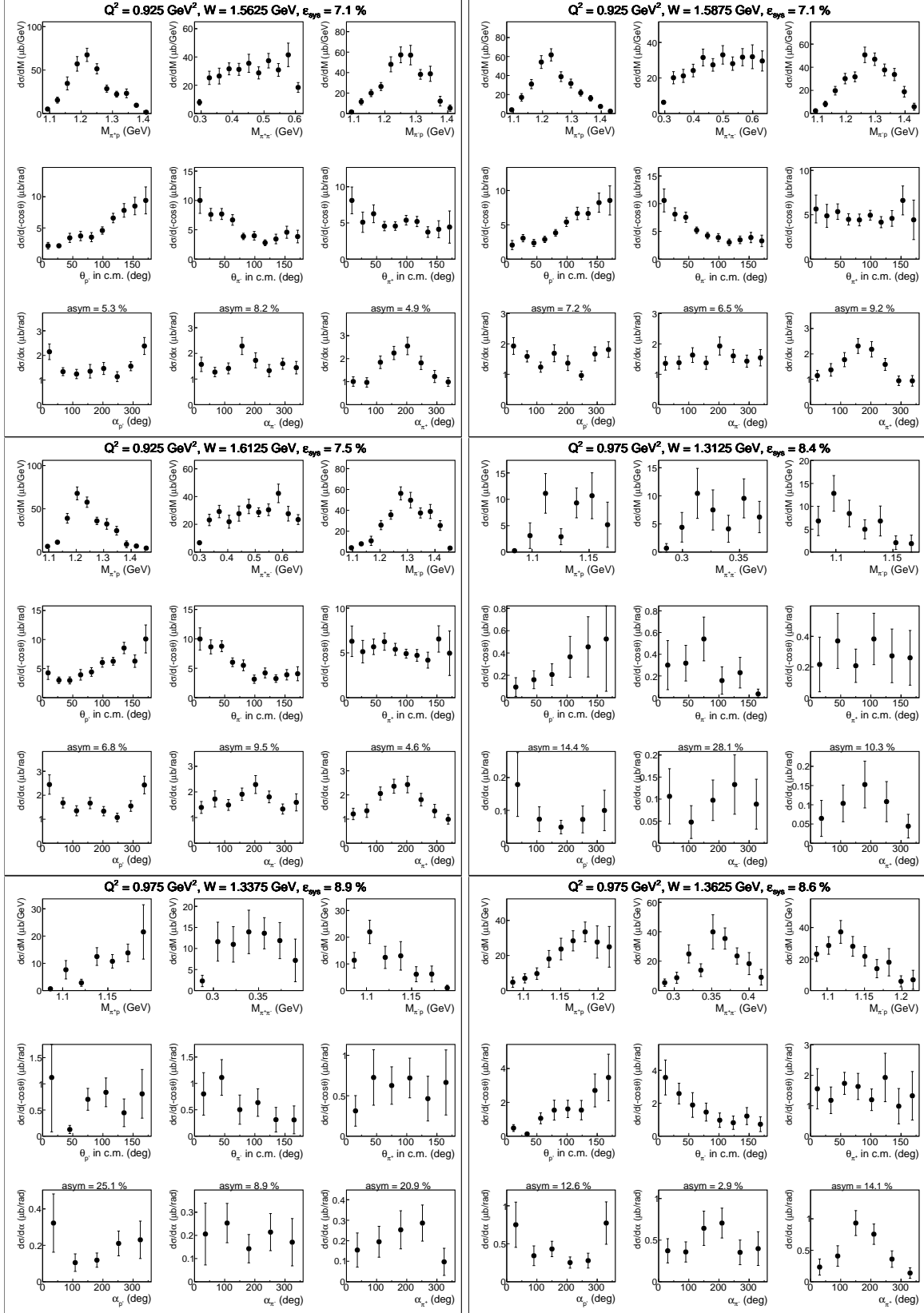Figure D.26: Measured single-differential cross sections.

Figure D.27: Measured single-differential cross sections.

Figure D.28: Measured single-differential cross sections.

Figure D.29: Measured single-differential cross sections.

Figure D.30: Measured single-differential cross sections.

Figure D.31: Measured single-differential cross sections.

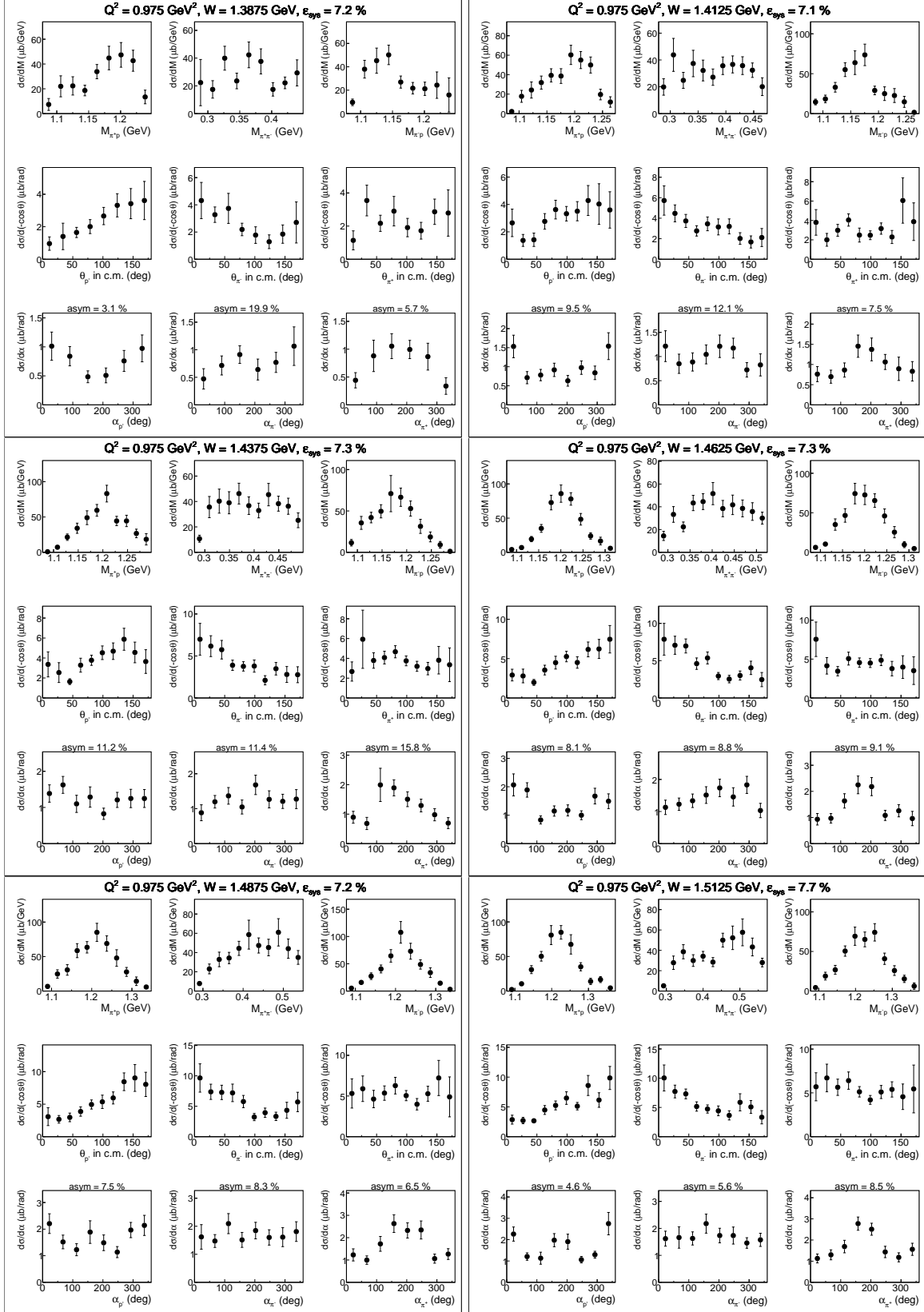Figure D.32: Measured single-differential cross sections.
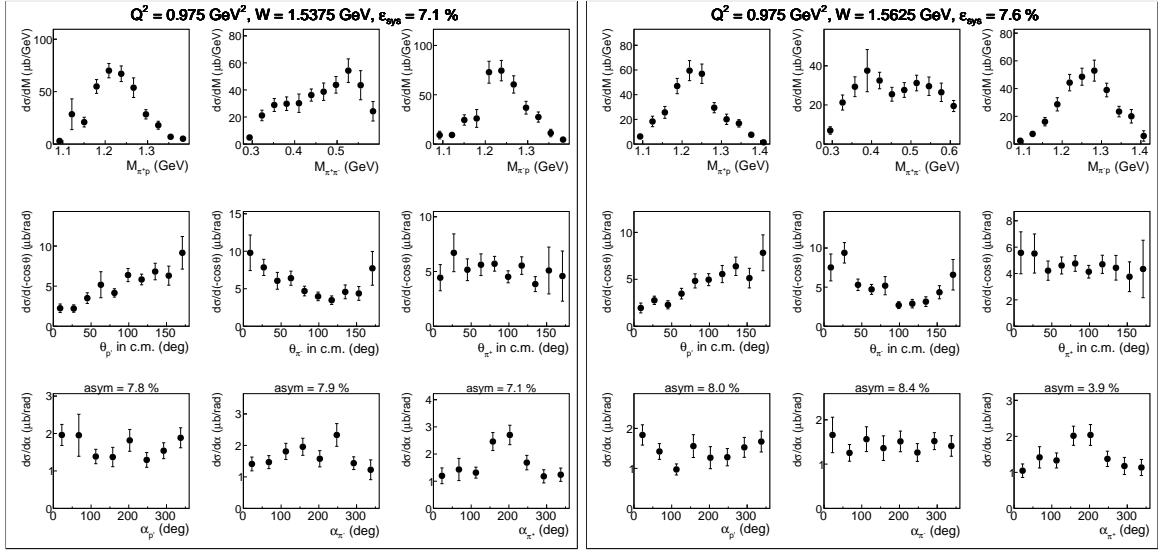
Figure D.33: Measured single-differential cross sections.

Figure D.34: Measured single-differential cross sections.